Many-Body Perturbation Theory with Slater Type Orbitals

Förster, Arno Titus Lorenz

2022

document version
Publisher's PDF, also known as Version of record

VRIJE UNIVERSITEIT

Many-Body Perturbation Theory with Slater Type Orbitals

ACADEMISCH PROEFSCHRIFT

ter verkrijging van de graad Doctor of Philosophy aan de Vrije
Universiteit Amsterdam,
op gezag van de rector magnificus
prof.dr. J.J.G. Geurts,
in het openbaar te verdedigen
ten overstaan van de promotiecommissie
van de Faculteit der Bètawetenschappen
op vrijdag 9 december 2022 om 9.45 uur
in een bijeenkomst van de universiteit,
De Boelelaan 1105

door

Arno Titus Lorenz Förster

geboren te Hanau, Duitsland

promotor:	prof.dr. L. Visscher
copromotor:	dr. K. Giesbertz
promotiecommisie:	prof.dr. P. Gori Giorgi prof.dr. W. Klopper prof.dr. K. Schoutens dr. L. Leppert dr. B. Baumeier prof.dr. P. Rinke

Contents

Chapter 1

Introduction

Quantum chemistry is concerned with calculating measurable physical properties of molecules. This becomes challenging for molecules containing hundreds or even thousands of electrons. Relevant examples of such systems include DNA oligomers,[1] chromophores in the reaction centers of photosystems,[2,3] large organic acceptor molecules which can be used in photovoltaic devices,[4] metal-organic frameworks[5] and many more (see ref. [6] and references therein). In such cases, finding a good compromise between the computational effort required to calculate a certain observable and the necessary accuracy becomes a balancing act.

Molecules consist of electrons and positively charged nuclei which interact by exchanging photons. The physics of such systems is described by quantum electrodynamics (QED). The resulting equations are complicated and impossible to solve numerically, let alone analytically, for more than a few particles.[7] In non-relativistic electronic structure theory on instead focuses on solving a time-independent, non-relativistic electronic Schrödinger equation describing N electrons subject to an external potential. Physical properties of molecules, called observables, are then given as expectation values of operators with respect to these $N-$electron states. The number of degrees of freedom of the resulting equations grows exponentially with system size and therefore their solution by exact diagonalization techniques[8–11] is only possible for systems with a few electrons.

While the dimensionality of the N-electron states grows exponentially, the amount of information they contain might not,[12,13] allowing for the compression of the N-electron states and ultimately the solution of the many-body problem in polynomial time. Some examples of compression techniques include Quantum Monte Carlo methods,[14,15] the density matrix renormalization group,[16,17] matrix product states[18,19] and tensor networks,[20,21] dynamical mean field theory,[22–24] selected configuration interaction[25,26] or artificial neural networks.[27–29]

The possibly most radical compression method is many-body perturbation theory (MBPT) - which can also be combined with non-perturbative approaches.[30–33] This thesis exclusively deals with MBPT. Building on insights from quantum field theory, the techniques of MBPT have been formalized mostly in the 1950s and 1960s. They are based on the assumption that the

many-electron system can be described, at least qualitatively, as a system of non-interacting renormalized electrons, or quasielectrons. The resulting equations are complicated and the formalism frequently breaks down in case the picture of non-interacting renormalized electrons is not valid.[34] However, in contrast to the non-perturbative approaches MBPT can potentially be applied to much larger systems with often sufficient accuracy. In this thesis, we describe the design and implementation of MBPT based algorithms which are capable to calculate electron-electron interaction energies, ionization energies, electron attachment energies and photoabsorption energies for systems with thousands of electrons.

The remainder of this thesis consists of five chapters: Chapter 2 consists of three sections in which we introduce the theoretical foundations on which this thesis is based. We introduce the basic equations of MBPT in section 2.1. These equations are not immediately useful and in section 2.2 we will show how they can be turned into more useful expressions using resummation techniques. In section 2.3 we will then highlight the physical content of these equations and introduce and discuss common approximations to these equations in section. 2.4

Chapter 3, is based on refs. [35–39]. It contains the main results of this thesis: We will introduce numerical approximations with which equations of MBPT can be implemented in an efficient way and with low scaling with system size, so that also large systems with up to thousands of electrons are computationally tractable. Chapter 4 is based on refs. [37, 38, 40]. In this chapter, we will then compare the results obtained using these approximations to ones from other codes implementing the same equations with different numerical approximations. Section 5 is based on ref. [40] and ref. [41] and is concerned with the assessment of the accuracy of these approximations for the calculation of single-particle excitations and electron-electron correlation energies. Chapter 6 is based on ref. [38] and ref. [39]. In this chapter, we will present some applications to the photoionization of DNA oligomers, as well as to the calculation of optical spectra in the reaction center of photosystem II. Finally, chapter 7 summarizes and concludes this work.

Chapter 2

Many-Body Perturbation Theory

Many-body perturbation theory is a set of techniques connecting expectation values with respect to the true N-electron ground state to expectation values with respect to the ground state of a fictitious system of N non-interacting electrons. Under certain assumptions,[42] this connection is exact and allows for the evaluation of expectation values without knowledge of the interacting ground-state.

Typically, we are interested in the expectation values of time-ordered products of operators. We call such expectation values correlators. Non-interacting correlators are correlators with respect to the ground state of the fictitious system of N non-interacting electrons. We call this state the non-interacting ground state. Interacting correlators are correlators evaluated with respect to the $N-$electron ground state. In this thesis, three correlators play a central role: The electron-electron interaction part of the $N-$electron Hamiltonian, the one-particle Green's function and the two-particle Green's function.

Based on earlier developments in quantum field theory,[43–47] the foundations of MBPT for many-electron systems have been laid in the 1950s. These consist of three theorems: 1) The Gell-Mann–Low theorem[42] expresses time-ordered products of Heisenberg operators in terms of non-interacting correlators in the interaction picture, divided by the expectation value of the $S-$matrix.[44] 2) Wick's theorem[1][48,49] is then used to bring these correlators into normal order. 3) Finally, the linked-cluster theorem[50–54] states that the unlinked terms arising from the application of Wick's theorem equal the expectation value of the $S-$matrix and therefore do not contribute to the interacting correlators. These theorems are the subject of section 2.1.

Together, these theorems allow to expand the interacting correlators as a series in the electron-electron interaction which can be evaluated term by term. This is neither feasible nor desirable.[55] In section 2.2 we will show how these series can be resummed to give more useful expressions. These resummations have been introduced in the early 1960s by Luttinger and Ward[56], Klein[57], Baym and Kadanoff,[58] and Baym[59]. The crucial points here are the renormalization of the single-particle Green's function[56] via Dyson's equation[45] and of the 2-particle vertex function

[1] Which has apparently not been discovered by Wick but by Houriet and Kind,[48] at least according to Wick[49]

via a Bethe-Salpeter equation (BSE)[60]. Systematic ways to evaluate the vertex are the parquet formalism due to De Dominicis and Martin,[61] the Coupled cluster (CC)[62–66] method and the $GW\Gamma$ approach by Hedin,[67] typically referred to as Hedin's equations. In Hedin's formalism the screening of the electron-electron interaction[52,68], conceptually related to photon renormalization, plays a decisive role as well.

All three formalisms are closely related and are based on the Dyson equation for single-particle Green's function. They mainly differ in the expression for the vertex. The aim of section 2.2 is derivation of Hedin's equations. Starke and Kresse[69] have formulated a hierarchy of equations completely equivalent to the Hedin ones using a a 4-point vertex. Even though they are apparently better known in their formulation by Hedin, in the form by Starke and Kresse they are valid in any orthonormal basis of the one-particle Hilbert space.[69] Therefore they are more suitable for numerical implementations. They also allow for a unified treatment of one-particle and two-particle Green's functions. We will derive here a set of equations which are equivalent to the ones by Hedin and Starke and Kresse but assume a different form. We believe that this form of the equations is most suitable for numerical implementations and for the derivation of the approximations to them we will introduce later on.

In section 2.3, we will relate this theoretical framework to the concept of quasiparticles (QP). Non-interacting QPs are one of the most important concepts in chemistry: They provide a theoretical justification of the concept of the chemical bond and the simple picture of Lewis structures[70] and also the excited states of molecules can often be interpreted in terms of individual QPs. QPs have first been introduced by Landau[71–73] who argued that there is a one-to-one correspondence between the elementary excitations of a gas of non-interacting electrons (Fermi gas) and a gas of interacting electrons (Fermi liquid). Landau realized that the Fermi liquid can be described in terms of non-interacting QPs, which are obtained from the non-interacting particles by renormalization. In fact, this is the physical picture behind MBPT as shown first by Abrikosov and Khalatnikov[74] and Abrikosov, Gorkov and Dzyaloshinskii[75] and also by Nozières and Luttinger.[76] The concept of QPs is closely linked to the properties of Green's functions which we will discuss thoroughly as well.

In the last section of this chapter, section 2.4, we will discuss common approximations to the equations above which can be implemented in practice. Kohn-Sham (KS) density functional theory (DFT) by Hohenberg and Kohn[77] and Kohn and Sham,[78] as well as Hartree-Fock (HF) theory, already developed in the 1930s by Hartree,[79] Slater[80,81] and Fock[82] are both examples of QP theories and are introduced as special cases of the formalism which will be developed in the next sections. For the present work, they are mostly used to simplify the implementation of more advanced approximations to MBPT, the GW and also the $GW + G3W2$ approximations which we will introduced as well. Section 2.4 therefore sets the stage for chapter 3 where we will focus on the (efficient) implementation of these equations.

2.1 Foundations

2.1.1 Second Quantization

A system of non-relativistic interacting electrons subject to an external potential can be described by the following Hamiltonian,

$$\hat{H} = \hat{H}_0 + \hat{V} \ , \tag{2.1}$$

with

$$\hat{H}_0 = \sum_i^N \hat{h}_1(\boldsymbol{r}_i) \ , \tag{2.2}$$

and

$$\hat{V} = \frac{1}{2} \sum_{i \neq j}^N v(\boldsymbol{r}_i, \boldsymbol{r}_j) \ . \tag{2.3}$$

$$\hat{h}_1(\boldsymbol{r}) = -\frac{1}{2}\nabla^2 + v_{ext}(\boldsymbol{r}) \ , \tag{2.4}$$

describes a single electron with kinetic energy $\hat{t} = -\frac{1}{2}\nabla^2$ in the presence of an external potential v_{ext}. $\boldsymbol{r}$ denotes a set of spatial coordinates and v is the electron electron interaction,

$$v(\boldsymbol{r}, \boldsymbol{r}') = \frac{1}{|\boldsymbol{r} - \boldsymbol{r}'|} \ . \tag{2.5}$$

We can find the eigenstates of this Hamiltonian by a suitable discretization (see chapter 3) and subsequent diagonalization. This becomes quickly intractable for more than a few electrons. However, for non-interacting electrons, i.e. when $\hat{H} = \hat{H}_0$, the diagonalization of $\hat{H}$ reduces to the problem of diagonalizing $\hat{h}_1$. Since electrons are indistinguishable all $\hat{h}_1(\boldsymbol{r}_i)$ are equivalent.

In addition to their spatial degrees of freedom, electrons have an additional degree of freedom, called spin. The spin-degree of freedom can be probed by the spin-operator

$$\begin{aligned} \hat{s} =& \frac{1}{2} \left(\hat{\sigma}_x \ , \hat{\sigma}_x \ , \hat{\sigma}_z \right) \\ \hat{\sigma}_x = \begin{pmatrix} 0 & 1 \\ 1 & 0 \end{pmatrix} \ , & \hat{\sigma}_y = \begin{pmatrix} 0 & -i \\ i & 0 \end{pmatrix} \ , \hat{\sigma}_z = \begin{pmatrix} 1 & 0 \\ 0 & -1 \end{pmatrix} \ . \end{aligned} \tag{2.6}$$

The eigenvalues of $\hat{\sigma}_z$ are then conveniently chosen to quantize the spin-degree of freedom, $\sigma = \pm\frac{1}{2}$. To denote the spin-dependence of the electrons, we now define the composite index $x = (\boldsymbol{r}, \sigma)$. In non-relativistic quantum mechanics, the spin-dependence of the electron needs to be introduced in an *ad hoc* fashion. The simplest way to do so is to introduce spin-orbitals. They can be constructed by solving the spin-less single-particle problem

$$\hat{h}_1 \left| \varphi_k(\boldsymbol{r}) \right\rangle = \epsilon_k \left| \varphi_k(\boldsymbol{r}) \right\rangle \ , \tag{2.7}$$

where the φ_i are called spatial orbitals. The spin-orbitals are then obtained by combing the spatial orbitals with the eigenfunctions of $\hat{\sigma}_z$, which we denote by

$$s(\alpha) = \begin{pmatrix} 1 \\ 0 \end{pmatrix} \quad s(\beta) = \begin{pmatrix} 0 \\ 1 \end{pmatrix} \ , \tag{2.8}$$

and which are orthonormal to each other,

$$s(\sigma)s^*(\sigma') = \delta_{\sigma,\sigma'} \tag{2.9}$$

We have then

$$|\phi_k(x)\rangle = |\phi_k(\boldsymbol{r},\sigma)\rangle = \begin{cases} |\varphi_k(\boldsymbol{r})\rangle\, s(\alpha) & \sigma = \alpha \\ |\varphi_k(\boldsymbol{r})\rangle\, s(\beta) & \sigma = \beta \ . \end{cases} \tag{2.10}$$

In this equation, k labels a spatial orbital. It is however convenient to define k as a composite index which also includes the spin-variable σ. Therefore, we will often write $\phi_k(\boldsymbol{r})$ instead of $\phi_k(x)$.

The eigenstates of the single-particle Hamiltonian $\hat{h}_1$ can now be used to construct eigenstates of $\hat{H}_0$. As a first step, one might introduce a simple product state of the form

$$\left|\Phi_0^{(N)}\right\rangle = \bigotimes_{i=1}^{N} |\phi(x_k)\rangle_k \ , \tag{2.11}$$

where $|\phi_k\rangle_{k'}$ is the eigenstate with quantum number k of the k'th particle. However, a physical eigenstate of $\hat{H}_0$ can not be written in the form of (2.11). This is due to the fact that a Fermionic wave function needs to change sign when two particles are exchanged, i.e, the wave function needs to fulfill

$$\Psi(x_1,\dots,x_k,\dots,x_{k'},\dots) \stackrel{!}{=} -\Psi(x_1,\dots,x_{k'},\dots,x_k,\dots) \ , \tag{2.12}$$

or, for the product of two single-particle states,

$$\phi_k(x_k)\phi_{k'}(x_{k'}) = -\phi_k(x_{k'})\phi_{k'}(x_k) \ . \tag{2.13}$$

Therefore, we have to take into account all possible ways to distribute N electrons in N eigenstates of $\hat{h}_1$, considering (2.12). This leads to

$$\begin{aligned} \left|\Phi^{(N)}\left[\{x_1,\dots,x_N\}\right]\right\rangle =& \frac{1}{\sqrt{N!}} \sum_{\pi\in\mathcal{S}_N} (-1)^\pi \bigotimes_{i=1}^{N} |\phi\rangle_{\pi(i)} \\ =& \frac{1}{\sqrt{N!}} \sum_{\pi\in\mathcal{S}_N} (-1)^\pi \, |\phi\rangle_{\pi(1)} \otimes |\phi\rangle_{\pi(2)} \otimes \cdots \otimes |\phi\rangle_{\pi(N)} \ , \end{aligned} \tag{2.14}$$

where π runs over all possible permutations and $\mathcal{S}_N$ is the symmetric group of order N. A state of the form (2.14) is called Slater determinant.[2] The states which can be constructed in this way from N eigenstates of $\hat{h}_1$ form a Hilbert space,

$$\bigwedge^N \mathbb{H} = \text{span}\left\{ \left| \Phi^{(N)}\left[\{x_1, \ldots, x_N\}\right] \right\rangle \right\} , \tag{2.15}$$

i.e. the Fermionic N-particle Hilbert space is the antisymmetrized Tensor product $\bigwedge$ of N single-particle Hilbert spaces. The direct sum of all $N-$particle Hilbert spaces is called Fock space[86],

$$\mathbb{F} = \bigoplus_{N=0}^{\infty} \bigwedge^N \mathbb{H} . \tag{2.16}$$

It consist of all possible Slater determinants with all possible numbers of particles and fulfills the completeness relation

$$1 = \sum_{n=0}^{\infty} \left| \Psi_n^{(N)} \right\rangle \left\langle \Psi_n^{(N)} \right| . \tag{2.17}$$

Fock space is useful for our purpose, since it provides a convenient framework to describe processes in which the number of particles in a system change. We can now introduce so-called ladder operators which allow to climb up and down from different sectors of Fock space. Lowering operators map from the $N-$electron Hilbert space to the $N-1-$electron Hilbert space

$$\hat{c}_k : \bigwedge^N \mathbb{H} \mapsto \bigwedge^{N-1} \mathbb{H} , \tag{2.18}$$

and raising operators map from the $N-1$-electron Hilbert space to the N-electron Hilbert space

$$\hat{c}_k^\dagger : \bigwedge^{N-1} \mathbb{H} \mapsto \bigwedge^N \mathbb{H} . \tag{2.19}$$

The null element of Fock space, $|0\rangle$, is called bare vacuum and it is the state containing 0 particles. Lowering operators anihilate the bare vacuum,

$$\hat{c}_k |0\rangle = 0 . \tag{2.20}$$

Physically, the operator $\hat{c}_k^\dagger$ creates an electron with quantum number k, while $\hat{c}_k$ annihilates an electron with quantum number k. This is equivalent to saying that $\hat{c}_k$ creates a hole with quantum numbers k. All states in Fock space can be represented as linear combinations of strings of raising and lowering operators acting on the bare vacuum. $\hat{c}_k$ and $\hat{c}_{k'}^\dagger$ obey the anticommutation relation

$$\left[\hat{c}_k \hat{c}_{k'}^\dagger + \hat{c}_{k'}^\dagger \hat{c}_k\right] \left| \Psi^{(N)} \right\rangle = \delta_{kk'} \left| \Psi^{(N)} \right\rangle , \tag{2.21}$$

[2] While the Slater determinant is named after John C. Slater who introduced this form of the wave function in 1929[83], it has apparently appeared first in articles by Dirac and Heisenberg a few years earlier.[84,85]

for an arbitrary state $|\Psi\rangle$. Furthermore, the application of multiple ladder operators needs to preserve the Fermionic structure of Fock space. When two particles with quantum numbers k, k' are created (anihilated), interchanging the order of operations needs to change the sign of the resulting wave-function,

$$\hat{c}_k \hat{c}_{k'} \left|\Psi^{(N)}\right\rangle = -\hat{c}_{k'} \hat{c}_k \left|\Psi^{(N)}\right\rangle \ , \tag{2.22}$$

and

$$\hat{c}_k^\dagger \hat{c}_{k'}^\dagger \left|\Psi^{(N)}\right\rangle = -\hat{c}_{k'}^\dagger \hat{c}_k^\dagger \left|\Psi^{(N)}\right\rangle \ . \tag{2.23}$$

It is rather cumbersome to create all states from the bare vacuum. Therefore, it is convenient to redefine the vacuum as the N-particle state which is constructed from the N lowest eigenstates of $\hat{h}_1$. This is the ground state of $\hat{H}_0$, $\left|\Phi_0^{(N)}\right\rangle$ and we call this state the Fermi vacuum. Let us introduce the sequence of real numbers

$$\epsilon_1 \leq \epsilon_2 \cdots \leq \epsilon_N < \mu < \epsilon_{N+1} \leq \epsilon_{N+2} \cdots \in \mathbb{R} \ , \tag{2.24}$$

where ϵ_i is the eigenvalue corresponding to the single-particle state ϕ_i,

$$\hat{h}_1 \phi_i(x) = \epsilon \phi_i(x).$$

Since $\hat{h}_1$ is bounded below and self-adjoint, the sequence (2.24) exists.[3] Furthermore, since we are dealing with finite systems, there is a gap between ϵ_N and ϵ_{N+1}. This gap will be called the fundamental gap. The number μ is called chemical potential. Its precise value is not important, as long as it has the property (2.24). We can now introduce a new set of operators, defined by

$$\hat{b}_k \, |\Phi_0^{(N)}\rangle = 0 \ . \tag{2.25}$$

There is no electron in any single-particle state corresponding to eigenvalues higher than the chemical potential, and there are no holes in single-particle states corresponding to eigenvalues below the chemical potential. Therefore,

$$\begin{aligned}
\hat{c}_k \left|\Phi_0^{(N)}\right\rangle &= 0 \quad \text{if } \epsilon_k > \mu \\
\hat{c}_k^\dagger \left|\Phi_0^{(N)}\right\rangle &= 0 \quad \text{if } \epsilon_k < \mu \\
\left\langle\Phi_0^{(N)}\right| \hat{c}_k &= 0 \quad \text{if } \epsilon_k < \mu \\
\left\langle\Phi_0^{(N)}\right| \hat{c}_k^\dagger &= 0 \quad \text{if } \epsilon_k > \mu \ ,
\end{aligned} \tag{2.26}$$

[3] Additionally, it is required that the potential $v(x)$ in (2.1) vanishes at infinity. For periodic potentials the situation is quite different. For instance, the highest occupied and the lowest unoccupied bands may overlap. For a more general discussion see ref. [87].

and the operators defined in (2.25) can be written as

$$\begin{aligned}\hat{b}_k =&\Theta(\epsilon_k-\mu)\hat{c}_k+\Theta(\mu-\epsilon_k)\hat{c}_k^\dagger\\ \hat{b}_k^\dagger =&\Theta(\epsilon_k-\mu)\hat{c}_k^\dagger+\Theta(\mu-\epsilon_k)\hat{c}_k\ ,\end{aligned}\tag{2.27}$$

In (2.27), the Heaviside step-function

$$\Theta(t)=\begin{cases}1 & \text{if } t>0\\ 0 & \text{if } t<0\end{cases}\tag{2.28}$$

appears. It is important to note, that $\Theta(0)$ is not defined.[4]

Finally, we introduce a real space representation of ladder operators which we call field operators,

$$\begin{aligned}\hat{\psi}(x) =&\sum_k \phi_k(x)\hat{b}_k\\ \hat{\psi}^\dagger(x) =&\sum_k \phi_k^*(x)\hat{b}_k^\dagger\ ,\end{aligned}\tag{2.29}$$

where the expansion coefficients

$$\phi_k(x)=\left\langle x\middle|\phi_k\right\rangle$$

are the projections of the eigenstates of the single-particle Hamiltonian on spin and real space. The field operator inherits the properties of $\hat{b}_k$, i.e. $\hat{\psi}(x)$ has a zero Fermi vacuum expectation value but its vacuum expectation value is generally different from zero. Using (2.27), we can write

$$\begin{aligned}\hat{\psi}(x) =&\hat{\psi}_>(x)+\hat{\psi}_<^\dagger(x)\\ =&\sum_k \phi_k(x)\Theta(\epsilon_k-\mu)\hat{c}_k+\sum_k \phi_k(x)\Theta(\mu-\epsilon_k)\hat{c}_k^\dagger\ ,\end{aligned}\tag{2.30}$$

and

$$\begin{aligned}\hat{\psi}^\dagger(x) =&\hat{\psi}_>^\dagger(x)+\hat{\psi}_<(x)\\ =&\sum_k \phi_k^*(x)\Theta(\epsilon_k-\mu)\hat{c}_k^\dagger+\sum_k \phi_k^*(x)\Theta(\mu-\epsilon_k)\hat{c}_k\ .\end{aligned}\tag{2.31}$$

The two components of the field operators represent the following physical processes:

$$\begin{aligned}\hat{\psi}_>(x):&\quad \text{anihilates electron at position } x \text{ with energy greater than } \mu\\ \hat{\psi}_<(x):&\quad \text{anihilates hole at position } x \text{ with energy lesser than } \mu\\ \hat{\psi}_>^\dagger(x):&\quad \text{creates electron at position } x \text{ with energy greater than } \mu\\ \hat{\psi}_<^\dagger(x):&\quad \text{creates hole at position } x \text{ with energy lesser than } \mu\ .\end{aligned}\tag{2.32}$$

[4] Later in this chapter, to derive the COHSEX approximation, we will need to cheat a little bit and redefine $\Theta(0)=\frac{1}{2}$ for a short moment.

Therefore, the field components with the superscript $>$ are called greater components and the ones with the superscript $<$ are called lesser components. The important relations

$$\begin{aligned}\hat{\psi}_{>}(x)\,|\Phi_0^{(N)}\rangle &= 0\\ \hat{\psi}_{<}(x)\,|\Phi_0^{(N)}\rangle &= 0\\ \left\langle \Phi_0^{(N)}\right|\hat{\psi}_{>}^{\dagger}(x) &= 0\\ \left\langle \Phi_0^{(N)}\right|\hat{\psi}_{<}^{\dagger}(x) &= 0\end{aligned} \tag{2.33}$$

follow directly from (2.26).

Field operators allow us to express the process of particle addition or removal as expectation values of correlators over a suitable N-particle state. It is convenient to introduce transformations which makes these operators time-dependent since this allows to discuss time-dependent particle addition and removal processes. Such transformations are called picture transformations. In the Heisenberg representation operators are time-dependent and states are time-independent while in the Schrödinger representation operators are time-independent and states are time-dependent. In the interaction picture which is very useful for perturbation theory, both states and operators are time-dependent. In the following discussion, we will use the subscripts S,H and I to distinguish between these pictures whenever necessary.

2.1.2 Pictures and Picture Transformations

The time evolution of a state of a system with Hamiltonian (2.1) is described by the time-dependent Schrödinger equation,

$$i\frac{\partial}{\partial t}\left|\Psi^{(N)}(t)\right\rangle_S = \hat{H}_S\left|\Psi^{(N)}(t)\right\rangle_S . \tag{2.34}$$

Since

$$\left\langle\Psi(t)\middle|\Psi(t)\right\rangle \stackrel{!}{=} 1 ,$$

the time-evolution of a state is given by a unitary transformation

$$\left|\Psi^{(N)}(t)\right\rangle_S = U(t,t')\left|\Psi^{(N)}(t')\right\rangle_S . \tag{2.35}$$

From (2.34), the equation-of-motion (EOM) for U follows,

$$i\frac{\partial}{\partial t}U(t,t') = \hat{H}_S U(t,t') , \tag{2.36}$$

and we can also write down its adjoint form, using $U(t,t')^{\dagger} = U(t',t)$,

$$-i\frac{\partial}{\partial t}U(t',t) = U(t',t)\hat{H}_S . \tag{2.37}$$

Since $\hat{H}_S$ is time-independent and using the boundary condition $U(t,t) = 1$, the solution of (2.36) is

$$U_S(t,t') = e^{-i\hat{H}_S(t-t')} \ . \tag{2.38}$$

Setting $t' = 0$, we can then define

$$\left|\Psi^{(N)}\right\rangle_S = U_S^\dagger(t,0) \left|\Psi^{(N)}(t)\right\rangle_S = U_S(0,t) \left|\Psi^{(N)}(t)\right\rangle_S = \left|\Psi^{(N)}(0)\right\rangle_S \ . \tag{2.39}$$

The Hamiltonian in the Schrödinger picture is time-independent. The same is true for all other operators. Using the just defined transformation, we obtain the time-dependent operators in the Heisenberg picture,

$$\hat{A}_H(t) = U_S^\dagger(t,0)\hat{A}_S U_S(t,0) \ . \tag{2.40}$$

Introducing the abbreviation $U(t) = U(t,0)$, the field operators assume the form

$$\begin{aligned} U_S^\dagger(t_1)\hat{\psi}_S(x_1)U_S(t_1) =& \hat{\psi}_H(x_1,t_1) \equiv \hat{\psi}_H(1) \\ U_S^\dagger(t_1)\hat{\psi}_S^\dagger(x_1)U_S(t_1) =& \hat{\psi}_H^\dagger(x_1,t_1) \equiv \hat{\psi}_H^\dagger(1) \ . \end{aligned} \tag{2.41}$$

In the development of the MBPT formalism below, we will use the time-dependent form of the field operators. To simplify the notation, we have introduced the notation $1 = (x_1, t_1)$. From now on, we will drop the subscripts S and H from the field operators, with the understanding that the ones with a time argument always denote Heisenberg operators. We can then use (2.36) and (2.37) and calculate the time-derivative of the Heisenberg-operator (2.40). This gives the Heisenberg EOM,

$$i\frac{\partial}{\partial t}\hat{A}_H(t) = \left[\hat{A}_H(t), \hat{H}_S\right] \ . \tag{2.42}$$

Now, we introduce the interaction picture. The interaction picture is very useful when the Hamiltonian (2.1) cannot be solved exactly and, starting from $\hat{H}_0$, one wishes to obtain a solution in terms of an expansion in $\hat{V}$. We define the state

$$\left|\Psi^{(N)}(t)\right\rangle_I = e^{iH_0 t} \left|\Psi^{(N)}(t)\right\rangle_S \ , \tag{2.43}$$

and insert it into the time-dependent Schrödinger equation. This gives

$$\hat{H}_0 e^{-i\hat{H}_0 t} \left|\Psi^{(N)}(t)\right\rangle_I + e^{-i\hat{H}_0 t} i\frac{\partial}{\partial t} \left|\Psi^{(N)}(t)\right\rangle_I = \left[\hat{H}_0 + \hat{V}\right] \left|\Psi^{(N)}(t)\right\rangle_I \ , \tag{2.44}$$

which reduces to

$$i\frac{\partial}{\partial t} \left|\Psi^{(N)}(t)\right\rangle_I = \hat{V}_I \left|\Psi^{(N)}(t)\right\rangle_I \ , \tag{2.45}$$

where we have defined

$$\hat{A}_I(t) = e^{i\hat{H}_0 t}\hat{A}_S(t)e^{-i\hat{H}_0 t} \ , \tag{2.46}$$

for some time-dependent Schrödinger operator $\hat{A}(\mathrm{t})$. This operator is of the same form as the Heisenberg operators for the non-interacting system, while the states satisfy a Schrödinger equation (2.45), with the full Hamiltonian replaced by the interaction part of the Hamiltonian. Equations (2.43) and (2.46) define states and operators in the interaction picture. We can also write down the EOM for the time-evolution operator by inserting the definition (similar to eq. (2.46))

$$U_I(t,t') = e^{i\hat{H}_0 t} U_S(t,t') e^{-i\hat{H}_0 t} \tag{2.47}$$

into (2.36). Through (2.46) this gives

$$i\frac{\partial}{\partial t} U_I(t,t') = e^{iH_0 t}\hat{V}_S e^{-iH_0 t'} U_I(t,t') = \hat{V}_I U_I(t,t') \;, \tag{2.48}$$

the Tomonaga-Schwinger equation[88]. Its integrated form,

$$U_I(t,t') = 1 - i\int_{t_0}^{t} dt_1 \hat{V}_I(t_1) U_I(t_1,t') \tag{2.49}$$

is a Fredholm equation of the second kind[89,90] whose solution can be written as an infinite series, the Liouville-Neumann series,[15,91]

$$\begin{aligned} U_I(t,t') =& 1 - i\int_{t'}^{t} \hat{V}_I(t_1)dt_1 - \int_{t'}^{t} dt_1 \int_{t'}^{t_1} dt_2 \hat{V}_I(t_1)\hat{V}_I(t_2) + \;\ldots \\ &+ (-i)^n \int_{t'}^{t} dt_1 \int_{t'}^{t_1} dt_2 \cdots \int_{t'}^{t_{n-1}} dt_n \hat{V}_I(t_1)\hat{V}_I(t_2)\ldots\hat{V}_I(t_n) \;. \end{aligned} \tag{2.50}$$

We would like to rewrite this series so that all integrals have equal limits. To do so, we first introduce the time-ordering operator $\mathcal{T}$, defined by

$$\mathcal{T}\left[\hat{A}(t_1)\hat{A}(t_2)\right] = \begin{cases} \hat{A}(t_1)\hat{A}(t_2) & t_1 > t_2 \\ -\hat{A}(t_2)\hat{A}(t_1) & t_1 < t_2 \end{cases} \;,$$

for Fermions and by

$$\mathcal{T}\left[\hat{A}(t_1)\hat{A}(t_2)\right] = \begin{cases} \hat{A}(t_1)\hat{A}(t_2) & t_1 > t_2 \\ \hat{A}(t_2)\hat{A}(t_1) & t_1 < t_2 \end{cases} \;,$$

for Bosons. $\mathcal{T}$ arranges a string of operators in a way that the ones acting on a state at earlier times are always on the right of the ones acting on the state at later times. This can also be written[15] as

$$\mathcal{T}\left[\hat{A}_1(t)\hat{A}_2(t')\right] = \Theta(t-t')\hat{A}_1(t)\hat{A}_2(t') - \Theta(t'-t)\hat{A}_2(t')\hat{A}_1(t) \tag{2.51}$$

for Fermions and as

$$\mathcal{T}\left[\hat{A}_1(t)\hat{A}_2(t')\right] = \Theta(t-t')\hat{A}_1(t)\hat{A}_2(t') + \Theta(t'-t)\hat{A}_2(t')\hat{A}_1(t) \tag{2.52}$$

for Bosons. Since

$$t > t_1 > t_2 > \cdots > t_n > t' \,, \tag{2.53}$$

the products in each term of (2.50) are time-ordered and the nth term can trivially be written as

$$U_I^{(n)}(t,t') = (-i)^n \int_{t'}^{t} dt_1 \int_{t'}^{t_1} dt_2 \cdots \int_{t'}^{t_{n-1}} dt_n \mathcal{T}\left[\hat{V}_I(t_1)\hat{V}_I(t_2)\ldots\hat{V}_I(t_n)\right] \,. \tag{2.54}$$

Now the integrand in each term is symmetric with respect to the exchange of two time variables and in the nth term there are $n!$ possibilities to permute the time arguments. Each of the possible permutations of time arguments is a sub-region of the integral

$$K_I^{(n)}(t,t') = (-i)^n \int_{t'}^{t} dt_1 \int_{t'}^{t} dt_2 \cdots \int_{t'}^{t} dt_n \mathcal{T}\left[\hat{V}_I(t_1)\hat{V}_I(t_2)\ldots\hat{V}_I(t_n)\right] \,, \tag{2.55}$$

which is obtained from (2.54) by changing the upper limits of all integrals to t. The nth term of (2.50) can thus be written as[92]

$$U_I^{(n)}(t,t') = (-i)^n \frac{1}{n!} \int_{t'}^{t} dt_1 dt_2 \ldots dt_n \mathcal{T}\left[\hat{V}_I(t_1), \hat{V}_I(t_2)\ldots\hat{V}_I(t_n)\right] \,, \tag{2.56}$$

and the full series eq. (2.50) becomes

$$U_I(t,t') = 1 + \sum_{n=1}^{\infty} \frac{1}{n!}(-i)^n \int_{t'}^{t} dt_1 \int_{t'}^{t} dt_2 \cdots \int_{t'}^{t} dt_n \mathcal{T}\left[\hat{V}_I(t_1)\hat{V}_I(t_2)\ldots\hat{V}_I(t_n)\right] \,, \tag{2.57}$$

which is known as Dyson series[44,45].

2.1.3 Non-interacting Correlators

We will now discuss properties of correlators in the non-interacting ground state using the Heisenberg representation. The most important correlators of this type are the N-particle Green's functions. These are expectation values of strings of $2n$ field operators where n operators are daggered and n are not. First, we introduce a few definitions: The expectation value of an operator $\hat{A}$ with respect to state $|\Psi\rangle$ is

$$\left\langle \hat{A}(t) \right\rangle = \left\langle \Psi \middle| \hat{A}(t) \middle| \Psi \right\rangle \,. \tag{2.58}$$

The form on the *l.h.s.* is used when the state with respect to which the expectation value is evaluated is not important. Otherwise, the *r.h.s.* is used. A correlator is the expectation value of a product of operators

$$C_{\hat{A}_1\hat{A}_2\ldots\hat{A}_N}(1,2,\ldots,N) = \left\langle \hat{A}_1(1)\hat{A}_2(2)\ldots\hat{A}_N(N) \right\rangle \,. \tag{2.59}$$

In case the correlator is time-dependent, it is called dynamic, otherwise it is called static.

Often, it is useful to arrange a product of operators in a way that all anihilation operators are on the right of all creation operators. Such a product is called *normal-ordered* and its expectation value is zero when evaluated with respect to the vacuum. In terms of fields, this means that all $\hat{\psi}_{\lessgtr}$ should be on the right of all $\hat{\psi}^\dagger_{\lessgtr}$. Let $\mathcal{N}$ denote the operator which brings a string of operators into normal order. We can then define the difference between the time-ordered and the normal-ordered product as

$$\overbrace{\hat{A}\hat{B}} = \mathcal{T}\left[\hat{A}\hat{B}\right] - \mathcal{N}\left[\hat{A}\hat{B}\right] \ . \tag{2.60}$$

This is called a *contraction*. Generalized Wick's theorem states,[49] that the time-ordered products of a system of N operators is equal to the normal-ordered product of operators plus all normal-ordered products with all possible contractions,[93–95]

$$\begin{aligned}\mathcal{T}\left[\prod_k^N \hat{A}_k\right] = \mathcal{N}\left[\prod_k^N \hat{A}_k\right] + \sum_{i<j}(-1)^{i+j-1}\overbrace{\hat{A}_i\hat{A}_j}\,\mathcal{N}\left[\prod_{k\neq i\neq j}^N \hat{A}_k\right] \\ + \frac{1}{2!}\sum_{i<j<k<l}(-1)^{i+j+k+l-1}\overbrace{\hat{A}_i\hat{A}_j}\overbrace{\hat{A}'_i\hat{A}'_j}\,\mathcal{N}\left[\prod_{k\neq i\neq j\neq i'\neq j'}^N \hat{A}_k\right] + \dots \ .\end{aligned} \tag{2.61}$$

In particular, this means, that all operators which are non-contracted are in normal order, i.e. only the terms in which all operators are contracted contribute to vacuum expectation values.

To proof this statement, consider a time-ordered product of $N+1$ operators and let us assume (2.61) is true for N operators. We already know that it is true for $N = 2$ and $N = 1$. Following our assumption, we can use (2.61) to write

$$\begin{aligned}\mathcal{T}\left[\prod_k^{N+1} \hat{A}_k\right] = \left(\hat{A}_{1_>} + \hat{A}^\dagger_{1_<}\right)\left\{\mathcal{N}\left[\prod_k^N \hat{A}_k\right] + \sum_{i<j}(-1)^{i+j-1}\overbrace{\hat{A}_i\hat{A}_j}\,\mathcal{N}\left[\prod_{k\neq i\neq j}^N \hat{A}_k\right]\right. \\ \left. + \frac{1}{2!}\sum_{i<j<k<l}(-1)^{i+j+k+l-1}\overbrace{\hat{A}_i\hat{A}_j}\overbrace{\hat{A}_{i'}\hat{A}_{j'}}\,\mathcal{N}\left[\prod_{k\neq i\neq j\neq i'\neq j'}^N \hat{A}_k\right] + \dots\right\} .\end{aligned} \tag{2.62}$$

We would now like to transform this expression so that $\hat{A}_{1_>}$ is on the right. We do not need to care about $\hat{A}^\dagger_{1_<}$ since all contractions involving it will be zero (The other operators in the term are already normal-ordered). Therefore, these contractions can be trivially added to the sum. However, $\hat{A}_{1_>}$ only needs to be pulled to the right of all uncontracted fields, since the contracted fields are just complex numbers which will commute with everything. Let us work this out for a

term with $m-1$ uncontracted fields by repeatedly applying (2.60), and (2.22). We obtain

$$\begin{aligned}
\hat{A}_{1_>}\mathcal{N}\left[\hat{A}_2\dots\hat{A}_m\right] =& \mathcal{N}\left[\hat{A}_{1_>}\hat{A}_2\dots\hat{A}_m\right] + \hat{A}_1\hat{A}_2\mathcal{N}\left[\hat{A}_3\dots\hat{A}_m\right] \\
=& \hat{A}_1\hat{A}_2\mathcal{N}\left[\hat{A}_3\dots\hat{A}_m\right] - \hat{A}^\dagger_{2_<}\hat{A}_{1_>}\hat{A}_3\mathcal{N}\left[\hat{A}_4\dots\hat{A}_m\right] \\
=& \hat{A}_1\hat{A}_2\mathcal{N}\left[\hat{A}_3\dots\hat{A}_m\right] - \hat{A}_1\hat{A}_3\mathcal{N}\left[\hat{A}_2\hat{A}_4\dots\hat{A}_m\right] \\
&+ \hat{A}^\dagger_{2_<}\hat{A}^\dagger_{3_<}\hat{A}_{1_>}\hat{A}_4\mathcal{N}\left[\hat{A}_5\dots\hat{A}_m\right] \\
=& \hat{A}_1\hat{A}_2\mathcal{N}\left[\hat{A}_3\dots\hat{A}_m\right] - \hat{A}_1\hat{A}_3\mathcal{N}\left[\hat{A}_2\hat{A}_4\dots\hat{A}_m\right] \\
&+ \hat{A}_1\hat{A}_4\mathcal{N}\left[\hat{A}_2\hat{A}_3\hat{A}_5\dots\hat{A}_m\right]\dots \\
=& \sum_{k=2}(-1)^k\hat{A}_1\hat{A}_k\mathcal{N}\left[\hat{A}_2\dots\hat{A}_{k-1}\hat{A}_{k+1}\dots\hat{A}_m\right] .
\end{aligned} \tag{2.63}$$

This shows, that all contractions of $\hat{A}_1$ with the N other fields are generated. The result does not change if we replace $\hat{A}_1$ by $\hat{A}^\dagger_1$ since in this case we would only need to replace $\hat{A}_{1_>}$ by $\hat{A}^\dagger_{1_>}$. Since all possible contractions between the N other operators are present by the assumption before, (2.61) holds, and since the statement is true for $N=1$, (2.61) is proven by induction.

We now use Wick's theorem to prove a corollary about particle conserving expectation values of products of $2n$ fields of the form

$$G^{(0)}_n(1,\dots,n,1',\dots,n') = (-i)^n\left\langle\Phi^{(N)}_0\middle|\mathcal{T}\left[\hat{\psi}(1)\dots\hat{\psi}(n)\hat{\psi}^\dagger(1')\dots\hat{\psi}^\dagger(n')\right]\middle|\Phi^{(N)}_0\right\rangle . \tag{2.64}$$

We call these quantities non-interacting n-particle Green's functions. The corollary we are about to proof allows us to express these expectation values (with respect to the non-interacting ground state) as a linear combination of $n!$ products of terms of the form

$$G^{(0)}(1,1') \equiv G^{(0)}(1,1') = -i\left\langle\Phi^{(N)}_0\middle|\mathcal{T}\left[\hat{\psi}(1)\hat{\psi}^\dagger(1')\right]\middle|\Phi^{(N)}_0\right\rangle , \tag{2.65}$$

which is identified as the $n=1$ case of (2.64). This quantity is called non-interacting single-particle Green's functions, or non-interacting electron propagator.[43,46,47] We will discuss its properties in some detail in section 2.3. At this point, it is only important to note that $G^{(0)}$ can be expressed in terms of the eigendecomposition of $\hat{h}_1$. Following ref. [95] we will prove that

$$\left\langle\Phi^{(N)}_0\middle|\mathcal{T}\left[\prod_k^n\left\{\hat{\psi}(k)\hat{\psi}^\dagger(k')\right\}\right]\middle|\Phi^{(N)}_0\right\rangle = \det\begin{pmatrix} G^{(0)}(1,1') & G^{(0)}(1,2') & \dots & G^{(0)}(1,n') \\ G^{(0)}(2,1') & G^{(0)}(2,2') & \dots & G^{(0)}(2,n') \\ \vdots & \vdots & \ddots & \vdots \\ G^{(0)}(n,1') & G^{(0)}(n,2') & \dots & G^{(0)}(n,n') \end{pmatrix} \tag{2.66}$$

for Fermionic fields. We assume (2.66) to be true for some n. For $n+1$, we can write

$$\begin{aligned} G^{(0)}_{n+1} &= \left\langle \Phi_0^{(N)} \middle| \mathcal{T}\left[\prod_k^{n+1}\left\{\hat{\psi}(k)\hat{\psi}^\dagger(k')\right\}\right] \middle| \Phi_0^{(N)} \right\rangle \\ &= \det \begin{pmatrix} G^{(0)}(1,1') & G^{(0)}(1,2') & \dots & G^{(0)}(1,(n+1)') \\ G^{(0)}(2,1') & G^{(0)}(2,2') & \dots & G^{(0)}(2,(n+1)') \\ \vdots & \vdots & \ddots & \vdots \\ G^{(0)}((n+1),1') & G^{(0)}((n+1),2') & \dots & G^{(0)}((n+1),(n+1)') \end{pmatrix} \end{aligned} \tag{2.67}$$

The determinant developed after the $(N+1)^{\text{th}}$ column is

$$\begin{aligned} G^{(0)}_{n+1} =& G^{(0)}(1,(n+1)') \det \begin{pmatrix} G^{(0)}(2,1') & G^{(0)}(2,2') & \dots & G^{(0)}(2,n') \\ \vdots & \vdots & \ddots & \vdots \\ G^{(0)}((n+1),1') & G^{(0)}((n+1),2') & \dots & G^{(0)}((n+1),n') \end{pmatrix} \\ &- G^{(0)}(2,(n+1)') \det \begin{pmatrix} G^{(0)}(1,1') & G^{(0)}(1,2') & \dots & G^{(0)}(1,n') \\ G^{(0)}(3,1') & G^{(0)}(3,2') & \dots & G^{(0)}(3,n') \\ \vdots & \vdots & \ddots & \vdots \\ G^{(0)}((n+1),1') & G^{(0)}((n+1),2') & \dots & G^{(0)}((n+1),n') \end{pmatrix} \\ &+ \dots \\ &+ G^{(0)}(n+1,(n+1)') \det \begin{pmatrix} G^{(0)}(1,1') & G^{(0)}(1,2') & \dots & G^{(0)}(1,n') \\ G^{(0)}(2,1') & G^{(0)}(2,2') & \dots & G^{(0)}(2,n') \\ \vdots & \vdots & \ddots & \vdots \\ G^{(0)}(n,1') & G^{(0)}(n,2') & \dots & G^{(0)}(n,n') \end{pmatrix}, \end{aligned} \tag{2.68}$$

Since electrons are indistinguishable we can rename the indices inside the determinants. From Wick's theorem, we also have

$$\begin{aligned} &\left\langle \Phi_0^{(N)} \middle| \mathcal{T}\left[\prod_k^{n+1}\left\{\hat{\psi}(k)\hat{\psi}^\dagger(k')\right\}\right] \middle| \Phi_0^{(N)} \right\rangle = \sum_i^{n+1} G^{(0)}(i,(n+1)') \\ &\times \left\langle \Phi_0^{(N)} \middle| \mathcal{T}\left[\prod_k^{n}\left\{\hat{\psi}(k)\hat{\psi}^\dagger(k')\right\}\right] \middle| \Phi_0^{(N)} \right\rangle, \end{aligned} \tag{2.69}$$

i.e.

$$G^{(0)}_{n+1} = G^{(0)}_n \sum_i^{n+1} G^{(0)}(i,(n+1)') \tag{2.70}$$

Following our assumption, the latter factor can be written in the form (2.66), so (2.66) is true for $N+1$. Since for $N=1$ (2.66)it is true by definition, this proves (2.66) by induction. In

particular, the order of operators in (2.66) is irrelevant: According to (2.51), permutation of 2 operators simply leads to a sign-change. However, this just corresponds to interchanging two columns in the determinant which changes the sign of the determinant as well.

2.1.4 Interacting Correlators

After having discussed non-interacting correlators, we will discuss interacting correlators. For this purpose, it is useful for work in the Heisenberg picture. In second quantized form, the one-body part of is (2.1) given by the expression

$$\hat{H}_0 = \int d1 \hat{\psi}^\dagger(x) h(x) \hat{\psi}(x) = \int \left[\frac{1}{2} \nabla \hat{\psi}^\dagger(x) \nabla \hat{\psi}(x) + \hat{v}_{ext}(\boldsymbol{r}) \hat{\psi}^\dagger(x) \hat{\psi}(x) \right] \tag{2.71}$$

and the two-body part is given by

$$\hat{V}_S = \frac{1}{2} \sum_{\sigma,\sigma'} \int d\boldsymbol{r} d\boldsymbol{r}' \hat{\psi}^\dagger(x) \hat{\psi}^\dagger(x') v_c(x,x') \hat{\psi}(x') \hat{\psi}(x) \tag{2.72}$$

in the Schrödinger picture. Through (2.29) this can also be written as

$$\hat{V}_S = \frac{1}{2} \sum_{klmn} \hat{b}_k^\dagger \hat{b}_l^\dagger v_{knlm} \hat{b}_m \hat{b}_n \tag{2.73}$$

where k, l, m, n are composite indices labeling spin-orbitals and, in Mulliken notation,

$$v_{knlm} = \int d\boldsymbol{r} d\boldsymbol{r}' \phi_k^*(\boldsymbol{r}) \phi_n(\boldsymbol{r}) v_c(\boldsymbol{r}, \boldsymbol{r}') \phi_l^*(\boldsymbol{r}') \phi_m(\boldsymbol{r}') \ . \tag{2.74}$$

In the Heisenberg picture, the electron-electron interaction reads

$$\begin{aligned} \hat{V}_H(t) =& \frac{1}{2} \sum_{\sigma\sigma'} \int d\boldsymbol{r} d\boldsymbol{r}' \hat{\psi}^\dagger(x,t) \hat{\psi}^\dagger(x',t) v_c(\boldsymbol{r}, \boldsymbol{r}') \hat{\psi}(x',t) \hat{\psi}(x,t) \\ =& \frac{1}{2} \int d1 d2 \hat{\psi}^\dagger(1) \hat{\psi}^\dagger(2) W^{(0)}(1,2) \hat{\psi}(2) \hat{\psi}(1) \ , \end{aligned} \tag{2.75}$$

where we have defined

$$W^{(0)}(1,2) = \lim_{\eta \to 0^+} v_c(1,2) \delta(t_1 - t_2 + \eta) \delta_{\sigma,\sigma'} \ . \tag{2.76}$$

Later on, it will also become useful to define a four-point interaction

$$W^{(0)}(1,2,3,4) = W^{(0)}(1,3) \delta(1-2) \delta(3-4) \tag{2.77}$$

with which we can write

$$\hat{V}_H(t) = \frac{1}{2} \int d1 d2 d3 d4 \hat{\psi}^\dagger(1) \hat{\psi}^\dagger(4) W^{(0)}(1,2,3,4) \hat{\psi}(3) \hat{\psi}(2) \ . \tag{2.78}$$

We now wish to calculate these correlators without explicitly constructing the interacting $N-$electron ground state. We will use perturbation theory instead. The key properties of the interacting correlators which allows us to do so is their adiabatic connection to their non-interacting counterparts.

We are primarily interested in the following correlators:

- The electron-electron correlation energies are given by the expectation value of the operator defined in (2.75), or equivalently (2.78), with respect to the interacting ground state,

$$\left\langle \Psi_0^{(N)} \middle| \hat{V}_H(t) \middle| \Psi_0^{(N)} \right\rangle \ . \tag{2.79}$$

- The relevant correlator to obtain electron addition and removal energies (also called single-particle excitations) is the one-particle Green's function

$$G(1,1') \equiv G_1(1,1') = -i \left\langle \Psi_0^{(N)} \middle| \mathcal{T}\left[\hat{\psi}(1)\hat{\psi}^\dagger(1')\right] \middle| \Psi_0^{(N)} \right\rangle \ . \tag{2.80}$$

- For the calculation of optical, or neutral excitations (excitonic states) we additionally need the two-particle Green's function

$$G_2(1,2,1',2') = -\left\langle \Psi_0^{(N)} \middle| \mathcal{T}\left[\hat{\psi}(1)\hat{\psi}(2)\hat{\psi}^\dagger(2')\hat{\psi}^\dagger(1')\right] \middle| \Psi_0^{(N)} \right\rangle \ . \tag{2.81}$$

Other interesting quantities as for instance density-density response functions or one-particle reduced density matrices can easily be obtained from these correlators. Equations (2.80) and (2.81) are identified as special cases of the interacting counterpart of the n-particle Green's function defined in eqs. 2.64,

$$G_n(1,\dots n,1'\dots n') = (-i)^n \left\langle \Psi_0^{(N)} \middle| \mathcal{T}\left[\hat{\psi}(1)\dots\hat{\psi}(n)\hat{\psi}^\dagger(1')\dots\hat{\psi}^\dagger(n')\right] \middle| \Psi_0^{(N)} \right\rangle \ . \tag{2.82}$$

The adiabatic connection between an interacting and a non-interacting correlators is formalized by the Gell-Mann–Low theorem.[42] Suppose we have a Hamiltonian of the form (2.1), where we vary the charge of the electron as a function of time,

$$\hat{V} = g\hat{V}_\eta(t) \ , \tag{2.83}$$

with g being a coupling constant and

$$v_\eta(t) = \lim_{\eta\to 0+} W^{(0)} e^{-\eta|t|} \ , \tag{2.84}$$

i.e. for $t = \pm\infty$, this potential vanishes, and for $t = 0$, the true Coulomb potential is recovered. Further suppose that for $\eta \to 0^+$ the limit

$$|\Psi_\eta^{(\pm)}\rangle = \frac{U_{\eta,I}(0,\pm\infty)\,|\phi_0^{(N)}\rangle}{\left\langle \phi_0^{(N)} \middle| U_{\eta,I}(0,\pm\infty) \middle| \phi_0^{(N)} \right\rangle} \tag{2.85}$$

exists. Then the Gell-Mann–Low theorem states[96] that the $|\Psi_\eta^{(\pm)}\rangle$ are eigenstates of $\hat{H}_\eta$ and fulfill

$$\hat{H}_\eta^{(\pm)} |\Psi_\eta^{(\pm)}\rangle = E_\eta^{(\pm)} |\Psi_\eta^{(\pm)}\rangle \ , \tag{2.86}$$

where

$$E_\eta^{(\pm)} = \left\langle \Phi_0^{(N)} \middle| \hat{H}_\eta^{(\pm)} \middle| \Psi_\eta^{(\pm)} \right\rangle \ . \tag{2.87}$$

In particular, this implies that in the limit $\eta \to 0^+$

$$\lim_{\eta \to 0^\pm} \left(|\Psi_\eta^{(\pm)}\rangle , E_\eta^{(\pm)} \right) = \left(|\Psi\rangle , E \right) \ . \tag{2.88}$$

The Gell-Mann–Low theorem does not imply that the non-interacting ground state is transformed into the interacting ground state. $(|\Psi\rangle , E)$ is an *arbitrary* eigenpair of $\hat{H}$. Following ref. [96], the Gell-Mann–Low theorem can be proven by considering the Hamiltonian (2.83) with $g = e^{\eta\theta}$,

$$\hat{H}_\eta = \hat{H}_0 + W^{(0)} e^{\eta(\theta - |t|)} \ , \tag{2.89}$$

and

$$\hat{H}^\pm = \hat{H}_0 + W^{(0)} e^{\pm\eta|t|} \ , \tag{2.90}$$

with corresponding time-evolution operators $U^{(\pm)}$ In analogy to (2.49), we can then write for the time-evolution operators

$$\begin{aligned} U_\eta(t,t') =& 1 - i \int_{t'}^{t} ds \left(\hat{H}_0 + W^{(0)} e^{\eta(\theta - |s|)} \right) U(s,t') \\ =& 1 - i \int_{t'+\theta}^{t+\theta} d\tau \left(\hat{H}_0 + W^{(0)} e^{\eta|\tau|} \right) U(t_1 - \theta, t') \\ =& U^{(\pm)}(t \pm \theta, t' \pm \theta) \end{aligned} \tag{2.91}$$

where we have used $\theta = \tau - s$ in the second equation and we have

$$U_\eta(t,t') = \begin{cases} U^{(+)}(t+\theta, t'+\theta) & t < t' \\ U^{(-)}(t-\theta, t'-\theta) & t > t' \ . \end{cases} \tag{2.92}$$

We then obtain

$$\frac{\partial}{\partial\theta} U_\eta(t,t') = \pm \frac{\partial}{\partial t} U_\eta(t,t') \pm \frac{\partial}{\partial t'} U_\eta(t,t') \ . \tag{2.93}$$

We can then add (for the + case) or subtract (for the − case) (2.36) and (2.37) which gives for Schrödinger and interaction picture

$$i\eta g \frac{\partial}{\partial g} U_{S/I_\eta}(t,t') = \begin{cases} \hat{H}_{S/I_\eta} U_{S/I_\eta}(t,t') - U_{S/I_\eta}(t',t) \hat{H}_{S/I_\eta} & t < t' \\ U_{S/I_\eta}(t',t) \hat{H}_{S/I_\eta} - \hat{H}_{S/I_\eta} U_{S/I_\eta}(t,t') & t > t' \ . \end{cases} \tag{2.94}$$

We then obtain ($\hat{H}_\eta = \hat{H}_{S_\eta}(t=0)$)

$$\left[\hat{H}_\eta - E_0\right] U_{I_\eta}(0,\pm\infty)\left|\Phi_0^{(N)}\right\rangle = \mp i\eta g \frac{\partial}{\partial g} U_{I_\eta}(0,\pm\infty)\left|\Phi_0^{(N)}\right\rangle . \tag{2.95}$$

We now need to prove that this implies

$$\left[\hat{H}_\eta - E_\eta^{(\pm)}\right]\left|\Psi_\eta^{(\pm)}\right\rangle = \mp i\eta g \frac{\partial}{\partial g} U_{I_\eta}(0,\pm\infty)\left|\Psi_\eta^{(\pm)}\right\rangle , \tag{2.96}$$

since then we can take the limit $\eta \to 0^\pm$ which gives then (2.86). Since $|\Phi_0^{(N)}\rangle$ does not depend on g, we can write

$$\left\langle \Phi_0^{(N)}\right| \frac{\partial}{\partial g} U_{I_\eta}(0,\pm\infty)\left|\Phi_0^{(N)}\right\rangle = \frac{\partial}{\partial g}\left\langle \Phi_0^{(N)}\right| U_{I_\eta}(0,\pm\infty)\left|\Phi_0^{(N)}\right\rangle , \tag{2.97}$$

and therefore, using (2.95) and (2.85) ,

$$\begin{aligned}
\frac{\partial}{\partial g}\left|\Psi_\eta^{(\pm)}\right\rangle =& \frac{\partial}{\partial g}\left\{ \frac{U_{\eta,I}(0,\pm\infty)\left|\phi_0^{(N)}\right\rangle}{\left\langle \phi_0^{(N)}\right| U_{\eta,I}(0,\pm\infty)\left|\phi_0^{(N)}\right\rangle} \right\} \\
=& \frac{1}{\left\langle \phi_0^{(N)}\right| U_{\eta,I}(0,\pm\infty)\left|\phi_0^{(N)}\right\rangle} \frac{\partial}{\partial g}\left\{ U_{\eta,I}(0,\pm\infty)\left|\phi_0^{(N)}\right\rangle \right\} \\
&+ \frac{\partial}{\partial g}\left\{ \frac{1}{\left\langle \phi_0^{(N)}\right| U_{\eta,I}(0,\pm\infty)\left|\phi_0^{(N)}\right\rangle} \right\} U_{\eta,I}(0,\pm\infty)\left|\phi_0^{(N)}\right\rangle \\
=& \frac{1}{\left\langle \Phi_0^{(N)}\right| U_{\eta,I}(0,\pm\infty)\Phi_0^{(N)}\right\rangle} \left[\hat{H}_\eta - E_0\right] U_{\eta,I}(0,\pm\infty)\left|\Phi_0^{(N)}\right\rangle \\
&- \left\{ \frac{\left\langle \Phi_0^{(N)}\right| \hat{H}_\eta - E_0 \left| U_{\eta,I}(0,\pm\infty)\Phi_0^{(N)}\right\rangle}{\left\langle \Phi_0^{(N)}\right| U_{\eta,I}(0,\pm\infty)\left|\Phi_0^{(N)}\right\rangle^2} \right\} U_{\eta,I}(0,\pm\infty)\left|\Phi_0^{(N)}\right\rangle \\
=& \left[\hat{H}_\eta - E_0\right]\left|\Psi_\eta^{(\pm)}\right\rangle - \left|\Psi_\eta^{(\pm)}\right\rangle\left\langle \Phi_0^{(N)}\right|\left[\hat{H}_\eta - E_0\right]\left|\Psi_\eta^{(\pm)}\right\rangle \\
=& \left[\hat{H}_\eta - E_\eta^{(\pm)}\right]\left|\Psi_\eta^{(\pm)}\right\rangle .
\end{aligned} \tag{2.98}$$

This gives directly (2.96) and taking the limit $\epsilon \to 0^\pm$ completes the proof.

Together with Wick's theorem, we now have a tool at hand to express any time-ordered product of operators with respect to the non-interacting ground state as a linear combination of products of non-interacting single-particle Green's functions. Before we proceed with writing down explicit expressions for interacting correlators, we comment on the assumptions entering the Gell-Man–Low theorem and its implications.

First, the Gell-Mann and Low formula is not applicable in the case of Hamiltonians with a degenerate ground state.[97] (See ref. [98, 99] for generalizations of the Gell-Man–Low theorem to degenerate ground states.) As a rule of thumb, perturbation theory is not applicable when the perturbation V is too large compared to the non-interacting reference Hamiltonian. It is then not possible to single out a non-interacting reference system whose ground state is a single Slater determinant and perturbation theory needs to be applied to a many-determinant ground state. Systems for which such problems occur are called multi-reference problems and are frequently encountered in chemistry, for instance in coupled spins in open-shell transition metal complexes or bond-breaking processes (a prime example being the dissociation of the Hydrogen molecule).[13,100,101]

Second, when applying the Gell-Man–Low theorem, we will always need to assume that the ground-state of the non-interacting system is connected to the one of the interacting system. Third, we also need to assume that it is possible to switch on the interaction adiabatically. The second and third requirement have been verified for simple model Hamiltonians,[97] but it is in no way guaranteed that they hold for realistic systems.

In this work, we assume throughout the validity of the single QP picture. In the same way as the Gell-Mann–Low theorem assumes continuity between the non-interacting and the interacting system, Fermi liquid theory assumes that the ground state of a Fermi gas, upon switching on the interaction between the particles, is adiabatically transformed into the ground state of the interacting system. Thus, the Gell-Man–Low theorem indeed provides the theoretical framework to transform free particles into QPs.

Explicit expression for expectation values

Using (2.85) we can write down an explicit expression for correlators with respect to the interacting ground-state,

$$\begin{aligned}\left\langle \Psi_0^{(N)} \middle| \hat{A}_H(t) \middle| \Psi_0^{(N)} \right\rangle &= \lim_{\eta\to 0} \left\langle \Psi_\eta^{(+)} \middle| \hat{A}_H \middle| \Psi_\eta^{(-)} \right\rangle \\ &= \lim_{\eta\to 0} \frac{\left\langle \Phi_0^{(N)} \middle| U_{\eta,I}(\infty,t)\hat{A}_H(t)U_{\eta,I}(t',-\infty) \middle| \Phi_0^{(N)} \right\rangle}{\left\langle \Phi_0^{(N)} \middle| U_{\eta,I}(\infty,-\infty) \middle| \Phi_0^{(N)} \right\rangle} ,\end{aligned} \tag{2.99}$$

where $\hat{A}_H$ can be any time-ordered product of operators. We have chosen to follow the time contour from $-\infty$ to ∞. This is a convenient choice since it simplifies working with time-ordered

operators[15]. Using the definition of the time-evolution operator (2.57) we can then write

$$\begin{aligned}
&\lim_{\eta\to 0}\left\langle \Psi_\eta^{(+)}\middle|\hat{\psi}(x,t)\hat{\psi}^\dagger(x',t')\middle|\Psi_\eta^{(-)}\right\rangle \\
&=\lim_{\eta\to 0}\left\{1+\sum_{n=1}^{\infty}(-1)^n\frac{1}{n!}\int dt_1\dots dt_n e^{\eta(|t_1|+\dots|t_n)}\right. \\
&\qquad\left.\times\frac{\left\langle \Phi_0^{(N)}\middle|\mathcal{T}\left[\hat{V}_I(t_1)\dots\hat{V}_I(t_n)\hat{A}_I(t)\right]\middle|\Phi_0^{(N)}\right\rangle}{\left\langle \Psi_\eta^{(+)}\middle|U_{\eta,I}(\infty,-\infty)\middle|\Psi_\eta^{(-)}\right\rangle}\right\}
\end{aligned} \tag{2.100}$$

and taking the limit $\eta\to 0$ and with the definition of the S-matrix[44],

$$\hat{S}=\lim_{\eta\to\infty}U_{\eta,I}(\infty,-\infty)\;, \tag{2.101}$$

we obtain

$$\begin{aligned}
\left\langle \Psi_0^{(N)}\middle|\hat{A}_H(t)\middle|\Psi_0^{(N)}\right\rangle =&\frac{\left\langle \Phi_0^{(N)}\middle|\mathcal{T}\left[\hat{A}_I(t)\hat{S}\right]\middle|\Phi_0^{(N)}\right\rangle}{\left\langle \Phi_0^{(N)}\middle|\hat{S}\middle|\Phi_0^{(N)}\right\rangle} \\
=&\frac{\sum_{n=0}^{\infty}\frac{1}{n!}(-i)^n\int dt_1\dots dt_n\left\langle \Phi_0^{(N)}\middle|\mathcal{T}\left[\hat{V}(t_1)\dots\hat{V}(t_n)\hat{A}(t)\right]\middle|\Phi_0^{(N)}\right\rangle}{\sum_{n=0}^{\infty}\frac{1}{n!}(-i)^n\int dt_1\dots dt_n\left\langle \Phi_0^{(N)}\middle|\mathcal{T}\left[\hat{V}(t_1)\dots\hat{V}(t_n)\right]\middle|\Phi_0^{(N)}\right\rangle}\;.
\end{aligned} \tag{2.102}$$

For the special case of the single-particle Green's function, (2.102) is

$$\begin{aligned}
G(1,1') =& -i\left\langle \Psi_0^{(N)}\middle|\hat{\psi}(x,t)\hat{\psi}^\dagger(x',t')\middle|\Psi_0^{(N)}\right\rangle \\
=& -i\frac{\left\langle \Phi_0^{(N)}\middle|T\left[\hat{\psi}(x,t)\hat{\psi}^\dagger(x',t')\hat{S}\right]\middle|\Phi_0^{(N)}\right\rangle}{\left\langle \Phi_0^{(N)}\middle|\hat{S}\middle|\Phi_0^{(N)}\right\rangle}\;.
\end{aligned} \tag{2.103}$$

Let us look at the first few terms in the nominator,

$$\begin{aligned}
&\left\langle \Phi_0^{(N)}\middle|T\left[\hat{\psi}(1)\hat{\psi}^\dagger(1')\hat{S}\right]\middle|\Phi_0^{(N)}\right\rangle \\
&=C^{(0)}(1,1'))+C^{(1)}(1,1')+\;\dots\;+C^{(n)}(1,1')\dots\;,
\end{aligned} \tag{2.104}$$

where the zeroth-order term is clearly the non-interacting propagator

$$C^{(0)}(1,1')=G^{(0)}(1,1')=-i\left\langle \Phi_0^{(N)}\middle|\mathcal{T}\left[\hat{\psi}(1)\hat{\psi}^\dagger(1')\right]\middle|\Phi_0^{(N)}\right\rangle\;. \tag{2.105}$$

To evaluate higher-order terms, we use Wick's theorem (2.66) together with the definition of the electron-electron interaction eq. (2.75) to obtain to first order in C (recall that the 3-particle Green's function contains a prefactor of $(-i)^3)^5$,

$$\begin{aligned} C^{(1)}(1,1') =& -i\int dt_1 \left\langle \Phi_0^{(N)} \middle| \mathcal{T}\left[\hat{V}(t_1)\hat{\psi}(1)\hat{\psi}^\dagger(1')\right] \middle| \Phi_0^{(N)} \right\rangle \\ =& \frac{i}{2}\int d2d2' W^{(0)}(2,2') G_3(1,2,2',1',2^+,2'^+) \\ =& \frac{i}{2}\int d2d2' W^{(0)}(2,2') \det \begin{pmatrix} G^{(0)}(1,1') & G^{(0)}(1,2) & G^{(0)}(1,2') \\ G^{(0)}(2,1') & G^{(0)}(2,2^+) & G^{(0)}(2,2') \\ G^{(0)}(2,1') & G^{(0)}(2',2) & G^{(0)}(2',2'^+) \end{pmatrix} . \end{aligned} \tag{2.107}$$

The single-particle Green's function in the upper left corner and the interaction term $W^{(0)}$ do not share a coordinate. Therefore, we can factor out this contribution to $C^{(1)}$,

$$\begin{aligned} C^{(1)}(1,1') =& \frac{i}{2}\int d2d2' W^{(0)}(2,2') \det \begin{pmatrix} 0 & G^{(0)}(1,2) & G^{(0)}(1,2') \\ G^{(0)}(2,1') & G^{(0)}(2,2^+) & G^{(0)}(2,2') \\ G^{(0)}(2,1') & G^{(0)}(2',2) & G^{(0)}(2',2'^+) \end{pmatrix} \\ &+ \int dt_1 \left\langle \Phi_0^{(N)} \middle| \mathcal{T}\left[\hat{V}(t_1)\right] \middle| \Phi_0^{(N)} \right\rangle \left\langle \Phi_0^{(N)} \middle| \mathcal{T}\left[\hat{\psi}(1)\hat{\psi}^\dagger(1')\right] \middle| \Phi_0^{(N)} \right\rangle . \end{aligned} \tag{2.108}$$

To second order in $\hat{V}$, we have

$$\begin{aligned} C^{(2)}(1,1') =& -\frac{1}{2}\int dt_2 dt_3 \left\langle \Phi_0^{(N)} \middle| \mathcal{T}\left[\hat{V}(t_2)\hat{V}(t_3)\hat{\psi}(1)\hat{\psi}^\dagger(1')\right] \middle| \Phi_0^{(N)} \right\rangle \\ =& -\frac{1}{8}\int d2d2'd3d3' W^{(0)}(2,2') W^{(0)}(3,3') \\ & \times \det \begin{pmatrix} G^{(0)}(1,1') & G^{(0)}(2,1') & G^{(0)}(2',1') & G^{(0)}(3,1') & G^{(0)}(3',1') \\ G^{(0)}(1,2) & G^{(0)}(2,2^+) & G^{(0)}(2',2) & G^{(0)}(3,2) & G^{(0)}(3',2) \\ G^{(0)}(1,2') & G^{(0)}(2,2'^+) & G^{(0)}(2',2') & G^{(0)}(3,2') & G^{(0)}(3',2') \\ G^{(0)}(1,3) & G^{(0)}(2,3) & G^{(0)}(2',3) & G^{(0)}(3,3^+) & G^{(0)}(3',3) \\ G^{(0)}(1,3') & G^{(0)}(2,3') & G^{(0)}(2',3') & G^{(0)}(3,3') & G^{(0)}(3',3'^+) \end{pmatrix} , \end{aligned} \tag{2.109}$$

[5] Generally, we have

$$(-i)^{n+m} = (-i)^{2n+m} * i^n \tag{2.106}$$

since

$$(-i)^{2n+m} * i^n = (-1)^m (-i)^{2n} * i^{n+m} = (-1)^m * (-1)^n * i^{n+m} = (-i)^{n+m} ,$$

which can also be written as

$$
\begin{aligned}
\hat{C^{(2)}} = &-\frac{1}{8}\int d2d2'd3d3'W^{(0)}(2,2')W^{(0)}(3,3') \\
&\times \det\begin{pmatrix} 0 & G^{(0)}(1,1') & G^{(0)}(1',1') & G^{(0)}(3,1') & G^{(0)}(3',1') \\ G^{(0)}(1,2) & 0 & 0 & G^{(0)}(3,2) & G^{(0)}(3',2) \\ G^{(0)}(1,2') & 0 & 0 & G^{(0)}(3,2') & G^{(0)}(3',2') \\ G^{(0)}(1,3) & G^{(0)}(2,3) & G^{(0)}(2',3) & 0 & 0 \\ G^{(0)}(1,3') & G^{(0)}(2,3') & G^{(0)}(2',3') & 0 & 0 \end{pmatrix} \\
&-\frac{1}{2}\int dt_2 \int dt_3 \left\langle \Phi_0^{(N)} \middle| \mathcal{T}\left[\hat{V}(t_2)\hat{V}(t_3)\right] \middle| \Phi_0^{(N)} \right\rangle \left\langle \Phi_0^{(N)} \middle| \mathcal{T}\left[\hat{\psi}(1)\hat{\psi}^\dagger(1')\right] \middle| \Phi_0^{(N)} \right\rangle \\
&-\frac{1}{2}\int dt_2 \left\langle \Phi_0^{(N)} \middle| \mathcal{T}\left[\hat{V}(t_2)\right] \middle| \Phi_0^{(N)} \right\rangle \int dt_3 \left\langle \Phi_0^{(N)} \middle| \mathcal{T}\left[\hat{V}(t_3)\hat{\psi}(1)\hat{\psi}^\dagger(1')\right] \middle| \Phi_0^{(N)} \right\rangle \\
&-\frac{1}{2}\int dt_3 \left\langle \Phi_0^{(N)} \middle| \mathcal{T}\left[\hat{V}(t_3)\right] \middle| \Phi_0^{(N)} \right\rangle \int dt_2 \left\langle \Phi_0^{(N)} \middle| \mathcal{T}\left[\hat{V}(t_2)\hat{\psi}(1)\hat{\psi}^\dagger(1')\right] \middle| \Phi_0^{(N)} \right\rangle \ .
\end{aligned}
\tag{2.110}
$$

In both contributions, we have written the terms separately which can be factorized as the product of more than one time-ordered product of expectation values. If we were to represent these terms as diagrams in which $G^{(0)}(n,n')$ is depicted as a line connecting points n and n', these are all terms which give diagrams in which not all points $2, 2' \ldots n, n'$ are connected to the external points $1, 1'$ by a line. Therefore, we call these terms *disconnected*. All the other terms are called *connected*. Note, that the last two terms on the *r.h.s.* of the last equation in (2.110) are just the first-order terms (2.107) multiplied with a single $\hat{V}$ expectation value. In general, the term in (2.104) of the order $m+1$ will always give m terms of the form

$$
\begin{aligned}
&\int dt_k \left\langle \Phi_0^{(N)} \middle| \mathcal{T}\left[\hat{V}(t_k)\right] \middle| \Phi_0^{(N)} \right\rangle \\
&\times \int dt_1 \ldots dt_{k-1} dt_{k+1} \ldots dt_m \left\langle \Phi_0^{(N)} \middle| \mathcal{T}\left[\hat{V}(t_1)\hat{V}(t_{k-1})\hat{V}(t_{k+1})\hat{V}(t_m)\hat{\psi}(x,t)\hat{\psi}^\dagger(x',t')\right] \middle| \Phi_0^{(N)} \right\rangle
\end{aligned}
\tag{2.111}
$$

because there are m different $\hat{V}$ which can be pulled out, and the term of order $m+2$ will give $(m+1)m/2$ terms with two $\hat{V}$ pulled out, and the term $m+k$ will give

$$
\frac{(m+k-1)(m+k-2)(m+k-3)\ldots}{k!} = \frac{(m+k-1)!}{m!k!} \tag{2.112}
$$

terms with k $\hat{V}$ pulled out. Let us define the quantity $D^{(m)}$ as the sum of all the contributions to the nominator of (2.102) which contain at least one connected diagram of order m. These are all connected diagram from the mth term in (2.104) times any connected factors of order m

coming from all $m+k$th order terms in (2.104) with $m+k>m$,

$$\begin{aligned} D^{(m)} =& \frac{1}{m!}(-1)^m \int dt_1 \dots dt_m \left\langle \Phi_0^{(N)} \middle| \mathcal{T}\left[\hat{V}(t_1)\dots\hat{V}(t_m)\hat{\psi}(x,t)\hat{\psi}^\dagger(x',t')\right] \middle| \Phi_0^{(N)} \right\rangle_{con} \\ & \times \frac{1}{m!}(-i)^m \left\{ 1 + \int dt_{m+1} \left\langle \Phi_0^{(N)} \middle| \mathcal{T}\left[\hat{V}(t_{m+1})\right] \middle| \Phi_0^{(N)} \right\rangle \right. \\ & \left. + \int dt_{m+1} \int dt_{m+2} \left\langle \Phi_0^{(N)} \middle| \mathcal{T}\left[\hat{V}(t_{m+1})\hat{V}(t_{m+2})\right] \middle| \Phi_0^{(N)} \right\rangle \dots \right\} . \end{aligned} \tag{2.113}$$

Since the index runs to infinity, we can simply shift the index, so that the term in curly parentheses becomes

$$\begin{aligned} & 1 + i\int dt_1 \left\langle \Phi_0^{(N)} \middle| \mathcal{T}\left[\hat{V}(t_1)\right] \middle| \Phi_0^{(N)} \right\rangle - \frac{1}{2}\int dt_1 \int dt_2 \left\langle \Phi_0^{(N)} \middle| \mathcal{T}\left[\hat{V}(t_1)\hat{V}(t_2)\right] \middle| \Phi_0^{(N)} \right\rangle + \dots \\ =& 1 + \sum_{n=1}^{\infty} \frac{i^n}{n!} \int dt_1 \dots dt_n \left\langle \Phi_0^{(N)} \middle| \mathcal{T}\left[\hat{V}(t_1)\hat{V}\dots(t_n)\right] \middle| \Phi_0^{(N)} \right\rangle , \end{aligned} \tag{2.114}$$

which is just the expectation value of the S-matrix, the denominator in (2.102). Eq. (2.113) is of course valid for all terms with $m=n=0\dots\infty$. Therefore, we just proved the *linked-diagram theorem*: In (2.102), the disconnected terms in the nominator cancel exactly with the expectation value of the S-matrix. Using eqs. (2.66), (2.75), (2.102) and (2.106) and the definition

$$G^{con} = G - \text{all unlinked terms} , \tag{2.115}$$

we arrive arrive at the expression

$$\begin{aligned} G(c,c') =& -i \left\langle \Phi_0^{(N)} \middle| \mathcal{T}\left[\hat{\psi}(1)\hat{\psi}^\dagger(1')\hat{S}\right] \middle| \Phi_0^{(N)} \right\rangle_{con} \\ =& G^{(0)}(c,c') + \sum_{n=1}^{\infty} \left(\frac{i}{2}\right)^n \frac{1}{n!} \int d1d1' \dots dndn' W^{(0)}(1,1') \dots W^{(0)}(n,n') \\ & \times G^{(0),con}_{2n+1}(c,1,1',\dots,n,n';c',1^+,1'^+\dots,n^+,n'^+) \end{aligned} \tag{2.116}$$

for the single-particle Green's function.

Furthermore, we see that all terms which can be generated from each other by permuting the internal indices contribute identically to the correlator. For each order n there are $2^n n!$ possible permutations. The factor of 2 comes here from the fact that the Coulomb potential is symmetric, $W^{(0)}(1,1') = W^{(0)}(1',1)$ and therefore integration over n and n' contribute equivalently to each term. Therefore, we can express the single-particle Green's function as

$$\begin{aligned} G(c,c') =& G^{(0)}(c,c') + \sum_{n=1}^{\infty} i^n \int d1d1' \dots dndn' W^{(0)}(1,1') \dots W^{(0)}(n,n') \\ & \times G^{(0),cd}_{2n+1}(c,1,1',\dots,n,n';c',1^+,1'^+\dots,n^+,n'^+) \end{aligned} \tag{2.117}$$

Note, that we have never resorted explicitly to the form of the expectation value. Therefore, this result is valid in general and also applied to the two-particle Green's function, for which we then obtain

$$\begin{aligned} G_2(c,d,c',d') =& G^{(0)}(c,c')G^{(0)}(d,d') - G^{(0)}(c,d')G^{(0)}(d,c') \\ &+ \sum_{n=1}^{\infty} i^n \int d1d1' \dots dndn' W^{(0)}(1,1') \dots W^{(0)}(n,n') \\ &\times G^{(0),cd}_{2n+2}(c,d,1,1',\dots,n,n';c',d',1^+,1'^+\dots,n^+,n'^+) \ , \end{aligned} \tag{2.118}$$

where we have already used (2.66) for the non-interacting 2-particle Green's function. The third expectation value which is important for this work is the one for the electron-electron interaction. Written as in eq. 2.78 it is

$$\begin{aligned} E_{ee} =& \sum_{n=1}^{\infty} i^n \int d1d1' \dots dndn' W^{(0)}(1,1') \dots W^{(0)}(n,n') \\ &\times G^{(0),cd}_{2n}(1,1',\dots,n,n';1,1'\dots,n,n') \ . \end{aligned} \tag{2.119}$$

The electron-electron interaction energy is therefore often referred to as the 0-particle propagator. Notice, that the expectation value of the electron-electron interaction with respect to the non-interacting ground state is zero. i.e. unlike the expansions eqs. (2.117) and (2.118) (2.119) does not contain a zeroth-order term with is independent of the Coulomb potential. The ground state energy of the interacting system is then

$$E_{tot} = E_0 + E_{ee} \ , \tag{2.120}$$

where E_0 is the sum of the energies of the non-interacting particles. For reasons explained below, the electron-electron interaction energy is often referred to as Hartree (H)-exchange-correlation (xc) energy.

2.2 Resummation

2.2.1 The 2-point Vertex function

The 2-Point Vertex $\Sigma\left[G^{(0)}, W^{(0)}\right]$

It is useful to introduce a graphical representation of the terms appearing in eqs. (2.117) and (2.118) in terms of diagrams, originally introduced by Feynman.[43] The diagrams we use here are due to Goldstone.[51] For each term appearing in eqs. (2.117)–(2.119), we introduce the following rules:

1. For each nth-order term, draw n horizontal wiggly interaction (photon propagator) lines.
2. Each end point of an interaction line is a vertex.

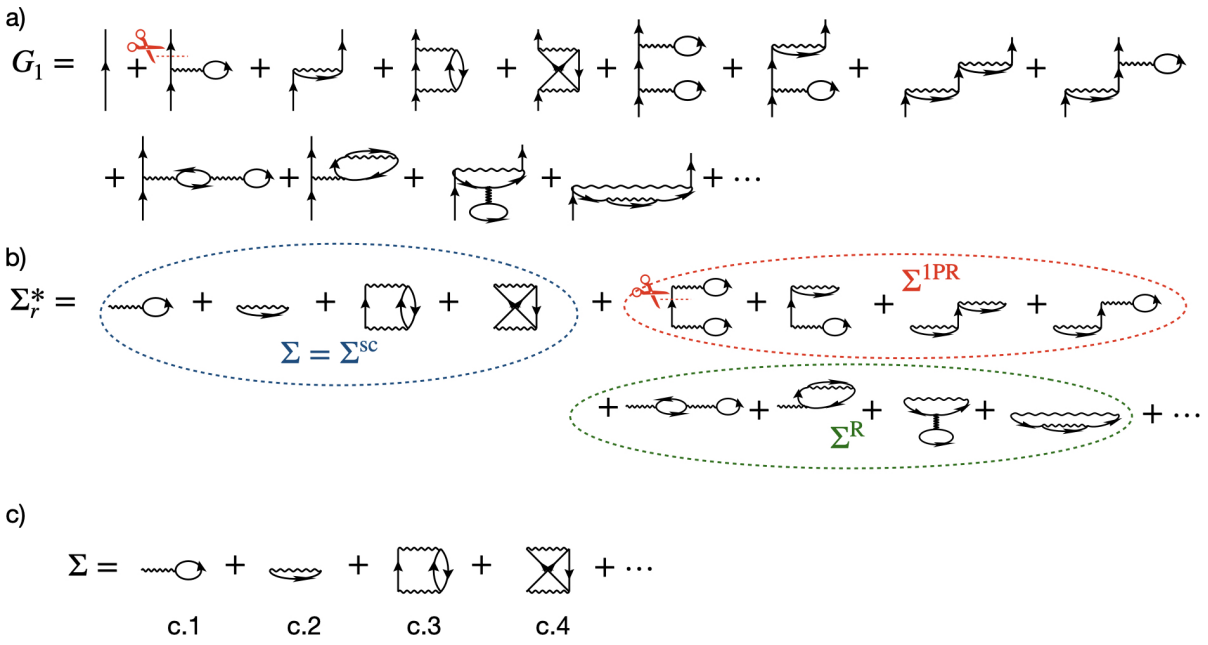

Figure 2.1: a) Diagrammatic representation of the perturbation series for the single-particle Green's function up to second order in $W^{(0)}$. b) Diagrammatic representation of the 2-point vertex containing three distinct classes of diagrams. c) The irreducible part of the self-energy up to second order in $W^{(0)}$.

3. At each vertex, momentum needs to be conserved.

4. Each vertex connects two propagators. These can either be electron or photon propagators.

5. A interacting propagator is represented by a double line.

6. A non-interacting propagator is represented by a single line.

These rules here are very loosely formulated since we only use them for illustrative purposes. They do not allow to convert diagrams into programmable expressions. For stricter rules which allow the direct translation of diagrams into equations, see for instance ref. [102].

Using these rules, to second order in $W^{(0)}$ (2.117) can be represented as depicted in figure 2.1a). From figure 2.1 a) it can be seen that each term in (2.117) (except for the non-interacting propagator) contains two external propagator lines. If we remove these lines as indicated in the first first-order term on the *r.h.s.* of the equation in figure 2.1a), we arrive at the so-called one-particle reducible (1PR) 2-point vertex function Σ_r^*. Generally, a reducible diagram be decomposed into equivalent building blocks by removing certain propagator lines. Depending on what type of lines are to be removed to decompose the diagram into smaller parts one distinguishes different channels. In case of 1PR diagrams there are only two possibilities: A diagram can be reducible in the particle or in the hole channel. However, these channels are related by symmetry. Σ_r^* is shown in figure 2.1b). Using this quantity, (2.117) can be written as

$$G(1,1') = G_1^{(0)}(1,1') = G_1^{(0)}(1,2)\Sigma_r^*(2,2')G_1^{(0)}(2',1') \; . \tag{2.121}$$

In this and also in the following equations repeated variables are integrated, unless they appear on both sides of the equation. In figure 2.1 b) it is also indicated that the 2-particle vertex can be decomposed as

$$\Sigma_r^* = \Sigma + \Sigma^{\mathrm{1PR}} + \Sigma^{\mathrm{R}} \; . \tag{2.122}$$

The first of these terms, the skeleton part of Σ_r^*, is the most important contribution and is usually called irreducible self-energy and abbreviated by Σ. It contains the building blocks of all other diagrams in the series expansion of Σ_r^*. This is most easily seen from the expansion of the single-particle Green's function in figure 2.1a). There are only two first-order diagrams but there are ten second-order diagrams. The first two of the second-order diagrams translate into the skeleton diagrams c.3 and c.4 in figure 2.1c). All other diagrams can be generated from the first-order diagrams by inserting them into themselves. For example, the third second-order diagram in figure 2.1a) is obtained by replacing one of the upwards pointing lines in the first first-order diagram (the one with the scissor) by itself. There are four possibilities to replace one of the upwards pointing lines in each of the first-order diagrams by themselves. However, figure 2.1a) only contains four of them, because replacing the upper or the lower line does not generate topologically distinct diagrams. It is not shown here, that the first-order diagrams can then again be inserted into the second-order diagrams, resulting in third-order diagrams, until diagrams to infinite order in $W^{(0)}$ are generated. When the external lines are amputated, one

ends up with the Σ^{1PR} class of diagrams in fig. 2.1b). These diagrams can be decomposed into two diagrams by removing a single propagator line. This process is indicated by the scissor in the first diagram of Σ^{1PR}. With these considerations, we can rewrite (2.117) again. If we restrict Σ_r^* in (2.121) to the skeleton and 1PR part only, we see that

$$\begin{aligned} G(1,1') =& G_1^{(0)}(1,1') + G_1^{(0)}(1,2)\left\{\Sigma\left[G_1^{(0)}\right] + \Sigma^{\text{1PR}}\left[G_1^{(0)}\right]\right\}(2,2')G_1^{(0)}(2',1') \\ =& G_1^{(0)}(1,2)\Sigma\left[G_1^{(0)}\right](2,2')G_1^{(0)}(2',1') \\ &+ G_1^{(0)}(1,2)\Sigma\left[G_1^{(0)}\right](2,2')G_1^{(0)}(2',3)\Sigma\left[G_1^{(0)}\right](3,3')G_1^{(0)}(3',1') + \dots \\ =& G_1^{(0)}(1,2)\sum_{n=0}^{\infty}\left[\Sigma\left[G_1^{(0)}\right]\times G_1^{(0)}\right]^n(2,1') \,. \end{aligned} \tag{2.123}$$

Since $1/(1-x) = \sum_{n=0}^{\infty} x^n$, the last equation can be written as[103]

$$\begin{aligned} G(1,1') =& G_1^{(0)}(1,2)[1-\Sigma\left[G_1^{(0)}\right]G_1^{(0)}]^{-1}(2,1') \\ =& \left\{\left[G^{(0)}\right]^{-1} - \Sigma\left[G_1^{(0)}\right]\right\}^{-1} \,. \end{aligned} \tag{2.124}$$

We can write this symbolically as

$$G(1,1') = G_1^{(0)}(1,1') + G_1^{(0)}(1,2)\Sigma\left[G_1^{(0)}\right](2,2')G(2',1') \,. \tag{2.125}$$

This shows that we only need the skeleton part of Σ_r^* to generate all of its 1PR diagrams as well. This relation can also be expressed as

$$\widetilde{\Sigma}(1,2) = \Sigma(1,2) + \Sigma(1,3)G^{(0)}(3,4)\widetilde{\Sigma}(4,2) \,, \tag{2.126}$$

where we have introduced the 1PR self-energy $\widetilde{\Sigma}$. This is a general result. Whenever we have a Dyson equation

$$X = X^{(0)} + X^{(0)}KX \,, \tag{2.127}$$

connecting a non-interacting quantity $X^{(0)}$ to an interacting quantity X, there is always a corresponding Dyson equation which connects the interaction kernel K to it's reducible counterpart $\widetilde{K}$,

$$\widetilde{K} = K + KX^{(0)}\widetilde{K} \,. \tag{2.128}$$

The reducible kernel can then used to rewrite the Dyson equation as

$$X = X^{(0)} + X^{(0)}\widetilde{K}X^{(0)} \,. \tag{2.129}$$

Comparison of (2.129) and (2.128) implies that

$$\widetilde{K}X^{(0)} = KX \,. \tag{2.130}$$

We will encounter these relations more often in the course of this section. Also note, that we have assumed here that the interacting single-particle Green's function can be inverted. However, it is not clear whether this is always true.

The 2-Point Vertex $\Sigma\left[G, W^{(0)}\right]$

The last class of diagrams belonging to the 2-particle vertex is denoted by Σ^{R}. These diagrams are obtained from the last four diagrams in fig. 2.1. They can not be decomposed into two parts by removing one propagator lines and therefore they are not generated from eq. (2.125). However, these diagrams can be obtained by replacing the non-interacting propagator lines in the first-order contributions to Σ_r^* by one of the first-order contributions to G. This result is valid also for higher-order contributions: In eq. (2.125), Σ is a functional of the non-interacting propagator. If Σ in (2.125) is made a functional of the interacting propagator instead of the non-interacting one, all terms of (2.117) (or equivalently (2.121)) are obtained. This has first been realized by Luttinger and Ward[56] in 1960 and leads to the famous Dyson equation for the single-particle Green's function,

$$G(1,1') = G^{(0)}(1,1') + G^{(0)}(1,2)\Sigma\left[G\right](2,2')G(2',1') \;, \tag{2.131}$$

depicted schematically in figure 2.2 a). All the complexity of the perturbative expansion of the interacting single-particle Green's function (2.117) is now hidden in the skeleton expansion of the self-energy, a frequency- and momentum-dependent self-consistent field experienced by the particles encoding their mutual interaction. The price we had to pay is that we have transformed a linear equation (2.117) to a non-linear one (2.131). We can rewrite (2.131) as

$$G^{-1}(1,1') = \left[G^{(0)}\right]^{-1}(1,1') - \Sigma(1,1') \;, \tag{2.132}$$

which essentially shows that we do not longer expand the Green's function but rather the inverse of the Green's function in powers of the interaction. The inverse of a n-particle Green's function is closely related to a n-particle Hamiltonian. In particular, we have

$$\left[G^{(0)}\right]^{-1}(\boldsymbol{r},\boldsymbol{r}',z) = z - \hat{h}_1(\boldsymbol{r})\delta(\boldsymbol{r}-\boldsymbol{r}') \;. \tag{2.133}$$

Therefore, (2.132) describes rather the expansion of an effective single-particle Hamiltonian than of a Green's function, where the zeroth-order term is simply the non-interacting Hamiltonian. It should be noted that in some MBPT based approaches the Green's function is expanded directly, for instance in the CC Green's function method.[104–106]

Formally, we can write the self-energy as a sum of distinct contributions

$$\Sigma(1,2) = \sum_{n=1}^{\infty} \Sigma^{(n)}(1,2) \;, \tag{2.134}$$

where n can correspond to a certain order of Σ in $W^{(0)}$, but this is not necessary. The decomposition is completely arbitrary. We now assume[6] that the order in which we dress the

[6]It should be noted that any resummation of the series expansion assumes that the series expansion (2.117)

non-interacting Green's function line with self-energy diagrams is not important. We can for example decide, to first dress $G^{(0)}$ with the first-order terms of Σ (the first 2 diagrams in figure 2.1 c)) only and then to generate all reducible self-energy diagrams using (2.131). We then obtain

$$G_1^{(1)}(1,1') = G_1^{(0)}(1,1') + G_1^{(0)}(1,2)\Sigma^{(1)}(2,2')G_1^{(1)}(2',1') \; , \tag{2.136}$$

where $G^{(1)}$ contains all 1PR contributions which can be generated from the first two-terms in the irreducible self-energy only. In a next step, we could then include all diagrams which can be obtained from the second-order terms of the irreducible self-energy. Continuing this process, we can obtain an infinite hierarchy of Dyson equations,

$$\begin{aligned} G_1^{(1)}(1,1') =& G_1^{(0)}(1,1') + G_1^{(0)}(1,2)\Sigma^{(1)}(2,2')G_1^{(1)}(2',1') \\ G_1^{(2)}(1,1') =& G_1^{(1)}(1,1') + G_1^{(1)}(1,2)\Sigma^{(2)}(2,2')G_1^{(1)}(2',1') \\ & \dots \\ G_1^{(n)}(1,1') =& G_1^{(n-1)}(1,1') + G_1^{(n-1)}(1,2)\Sigma^{(n)}(2,2')G_1^{(n)}(2',1') \; , \end{aligned} \tag{2.137}$$

until we finally obtain

$$G(1,1') = \lim_{n\to\infty} G_1^{(n)}(1,1') \; .$$

This property of the Dyson equation is of utmost importance in practice and we will use it extensively in the following chapters. In quantum chemistry, one typically first solves a Dyson equation with Σ in the HF approximation and then includes additional diagrams, either perturbatively or self-consistently. Each step in (2.137) can be seen as a redefinition of the Fermi vacuum.

As in (2.123), we can also expand the Dyson equation in powers of Σ,

$$G(1,1') = G^{(0)}(1,1') + G^{(0)}(1,2)\Sigma(2,2')G^{(0)}(2',1') + \mathcal{O}\left(\Sigma^2\right) \; . \tag{2.138}$$

Retaining only the first order term in this expansion, the linearized Dyson equation is obtained. As can be seen from figure 2.1, the linearized Dyson equation does not give the contributions to G which are obtained from Σ^{R} and therefore replacing (2.131) by (2.138) leads to an incomplete expansion of G. Nevertheless, it is important in practice as it is much simpler to solve than (2.131) and it is therefore often used as a starting point for approximations.[110]

(and equivalently for all other series expansions based on the Gell-Man–Low theorem) is absolutely convergent. Otherwise, according to the Riemann series theorem, the terms of the series can be arranged so that the new series converges to an arbitrary real number or even diverges. A given expression for the self-energy can be interpreted as a mapping of the form

$$\Sigma : G^{(0)} \mapsto G \; . \tag{2.135}$$

Therefore, it might be possible that resummation of Σ will map the same $G^{(0)}$ to different G (or the other way around). The possibility of this to happen has already been demonstrated for Hubbard like systems.[107–109] The resummation of the series expansion of the single-particle Green's function (2.117) to the form (2.131) seems to be a very successful one; the resulting G aligns very well with experimental observations. It is not clear at all why this is the case.

The skeleton expansion of the self-energy can be made more robust. In fact, in many interesting situations, this expansion will fail, as for example for a uniform gas of electrons[111,112] or metals,[113] or at least show an erratic behavior. For finite systems this failure is best known for the electron-electron interaction energy (See ref. [114] for a review). When solving (2.131), the self-energy is dressed by the interacting propagator lines. The skeleton series $\Sigma[G]$ can then be interpreted as the sum of all possible ways in which the electron in the *interacting* systems (the renormalized electrons) interact with each other via $W^{(0)}$. It can be argued that $W^{(0)}$ is not the most suitable quantity to describe the interactions between the renormalized particles.

Why is this the case? The renormalized electrons also contain the effect of their interactions with all other electrons via the self-energy which results in their charge being screened. Therefore, the Coulomb interactions between them are weaker than in the case of non-interacting particles. Interestingly, even prior to the work of Luttinger and Ward, Hubbard suggested that a weaker, or screened, Coulomb interaction might therefore be a more suitable expansion parameter to describe the electron-electron interactions.[52] This idea has been formalized later on by Hedin.[67] In fact, it can then be shown that an expansion of the irreducible self-energy in terms of the renormalized Green's function and a renormalized (screened) electron-electron interaction, makes (2.131) even more robust[112] than the replacement

$$\Sigma\left[G^{(0)}, W^{(0)}\right] \to \Sigma\left[G, W^{(0)}\right]$$

we have just introduced. This new expansion is just another resummation. Symbolically, we can introduce this expansion by the replacement

$$\Sigma\left[G, W^{(0)}\right] \to \Sigma\left[G, W\right] \ .$$

In the following, we will formally introduce this form of the self-energy, which leads to a set of equations which are not identical, but equivalent to the ones of Hedin.[67] The success of this resummation scheme in practical applications is the subject of chapter 5 and chapter 6. It will turn out, that for a quantitative description of the screening of the electron-electron interaction the two-particle Green's function is needed.

2.2.2 The Bethe-Salpeter equation for the 4-point Vertex function

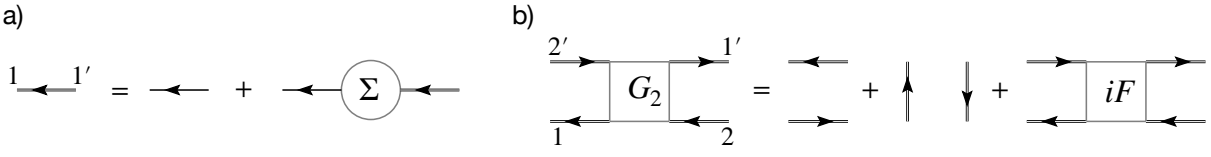

Figure 2.2: a) Dyson equation (2.131) for the single-particle Green's function. b) Definition of the 2-particle Green's function (2.140) via the reducible 4-point vertex iF

Using (2.66) for (2.118) one can see that we can always factor out 4 propagator lines in each term of the expansion, leading to

$$\begin{aligned} G_2(1,2,1',2') =& G^{(0)}(1,1')G^{(0)}(2,2') - G^{(0)}(1,2')G^{(0)}(1',2) \\ &+ iG^{(0)}(1,3)G^{(0)}(2,4)F[G^{(0)}](3,4,5,6)G^{(0)}(5,1')G^{(0)}(6,2') \ . \end{aligned} \tag{2.139}$$

The first two terms on the *r.h.s* of (2.139) are the contributions to $G_2^{(0)}$ and third term describes all possible scattering processes between two in-going and two out-going free electrons. The quantity F is called the 4-point vertex (sometimes it is also called scattering amplitude).[115] This expression is also valid when all non-interacting propagators are replaced by interacting ones. In (2.139), F contains not only the interactions between the renormalized particles but also renormalizes the non-interacting particles. Following the same arguments leading to the Dyson equation for the single-particle Green's function (2.131), it is more convenient to replace the bare particles in (2.139) by renormalized ones,

$$\begin{aligned} G_2(1,2,1',2') =& G(1,1')G(2,2') - G(1,2')G(1',2) \\ &+ iG(1,3)G(2,4)F[G](3,4,5,6)G(5,1')G(6,2') \ . \end{aligned} \tag{2.140}$$

Now, the redefined 4-point vertex F only contains the scattering processes between two incoming and two out-going renormalized electrons. It is shown diagrammatically in figure 2.2b. F can further be decomposed as[115,116]

$$F = \Lambda + \Gamma^{ph} + \Gamma^{\overline{ph}} + \Gamma^{pp} \ . \tag{2.141}$$

In this decomposition Λ contains all 2-particle irreducible (2PI) diagrams and the three terms Γ contains all diagrams which are 2-particle reducible (2PR). There are four possibilities to reduce a 2PR diagram out which 2 are topologically equivalent: One can remove (i) two particle lines (equivalent to removing two hole lines) in a way that one of the two resulting diagrams contains two hole lines and the other one two particles lines. In our definition of the two-particle Green's function (compare to (2.82)) this corresponds to separating lines 1 and 2 from lines 1' and 2'. Diagrams of this type are said to be reducible in the particle-particle (pp) channel (sometimes referred to as the parallel channel). Next, there are two possibilities to remove two lines so that the remaining fragments both have one hole and one particle line: (ii) One can remove the lines in a way that lines 1 and 1' are separated from 2 and 2'. These diagrams are reducible in the(longitudinal) particle-hole (ph) channel (sometimes referred to as the transverse channel). (iii) One can remove the lines in a way that lines 1 and 2' are separated from 2 and 1'. These are reducible in the transverse particle-hole ($\overline{ph}$) channel.[116] This decomposition is known as Parquet decomposition[115,116] and shown diagrammatically in figure 2.3.[7] It should be noted that this decomposition is not unique and alternative partitionings of the full vertex have been suggested.[126]

[7]The fully irreducible and dressed vertex functions Λ and F are directly related to the self-energy via the

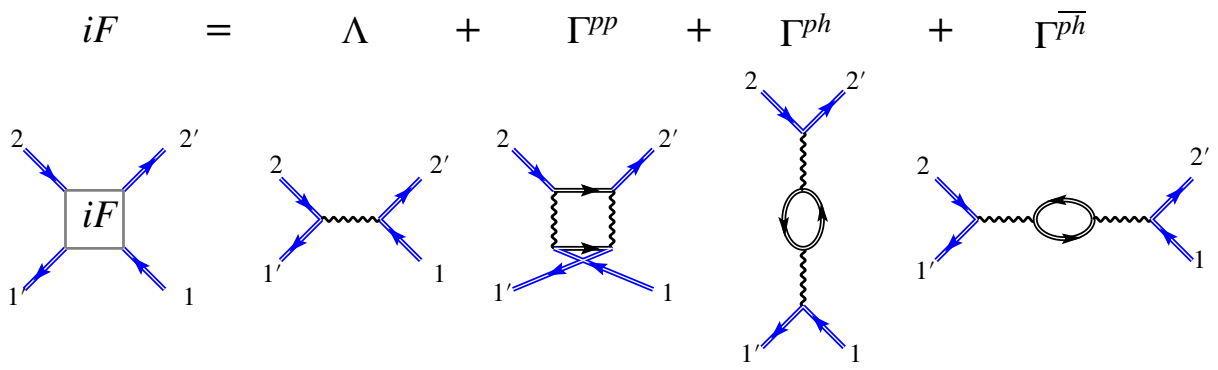

Figure 2.3: Parquet decomposition of the 4-point vertex function F. One of the lowest order diagrams of each class is shown. The black lines in each diagram belong to the 4-point vertex while he blue propagator lines are not part of the vertex but of the 2-particle Green's function.

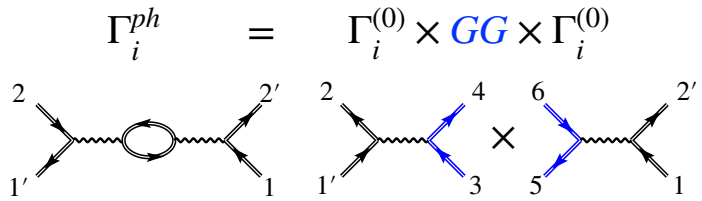

Figure 2.4: The ph-diagram shown in figure 2.3 is generated from two irreducible diagrams by inserting a propagator and a hole line.

Alternatively, one can write the Parquet decomposition as

$$F = \Gamma^{(0)} + \Gamma_l \quad l = ph, \overline{ph}, pp \,, \tag{2.142}$$

where F is partitioned into diagrams which are irreducible ($\Gamma^{(0)}_l$) or reducible ($F_{r,l}$) in channel l, for instance, when the ph-channel is chosen, comparison with (2.141) shows that

$$\begin{aligned} F =& \Gamma^{(0)} + \Gamma_{ph} \\ \Gamma^{(0)} =& \Lambda + \Gamma^{\overline{ph}} + \Gamma^{pp} \,. \end{aligned} \tag{2.143}$$

Schwinger-Dyson equation,[44,46,47]

$$\Sigma(1,1') = -\Lambda(1,2,1',2')G(2',2) - \frac{1}{2}\Lambda(1,2,3,4)G(2',2)G(4,4')G(3,3')F(4',3'1',2') \,.$$

The decomposition (2.141) allows then to represent Σ as the sum of the four contributions from each term in (2.141), the parquet decomposition of the self-energy.[115] To the best of our knowledge, applications have so far been limited to Hubbard models[116–120] and Anderson impurity models[121,122] but also to the Pariser–Parr-Pople model[123,124] of a Benzene molecule.[125] The main issue currently preventing its application to realistic systems seems to be the numerical complexity of the calculations.

The reducible diagrams can then be generated from the irreducible ones for a given channel by inserting the corresponding propagators.[69] To see this, we first define a contraction of 4-point functions,[69]

$$C(1,2,3,4) = A(1,5,3,6)B(6,2,5,4) \; . \tag{2.144}$$

For example, it is clear that the particle-hole diagram in figure 2.3 can be generated from the Λ diagram by inserting a particle and a hole line with the appropriate connectivity as shown in figure 2.4. In this way, we can then generate the vertex F in the particle-hole channel (here GG needs to be understood as the 4-point object $G(1,4)G(2,3) = G(1,2,3,4)$)

$$\begin{aligned} F(1,2,1',2') =& \Gamma^{(0)}(1,2,1',2') + i\Gamma^{(0)}(1,3,1',4)G(4,6)G(5,3)\Gamma^{(0)}(6,2,5,2') \\ &+ i^2\Gamma^{(0)}(1,3,1',4)G(4,6)G(5,3)\Gamma^{(0)}(6,5',5,6') \\ &\times G(6',7)G(5',8)\Gamma^{(0)}(8,2,7,2') + \dots \; . \end{aligned} \tag{2.145}$$

Using the same arguments leading to (2.124), we obtain the Bethe-Salpeter equation (BSE)[60,69]

$$\begin{aligned} F(1,2,1',2') =& \Gamma^{(0)}(1,2,1',2') + \Gamma_{ph}(1,2,1',2') \\ =& \Gamma^{(0)}(1,2,1',2') + i\Gamma^{(0)}(1,3,1',4)G(4,6)G(5,3)F(6,2,5,2') \; , \end{aligned} \tag{2.146}$$

for the reducible vertex in the particle-hole channel which relates the particle-hole reducible to the irreducible 4-point vertex function. Note the close similarity to the corresponding equation (2.126) for the 2-point vertex function. For the two other channels, different BSEs are obtained since the irreducible contributions to the vertex need to be connected in different ways. These other BSEs are irrelevant for this work. For the explicit expressions and their derivations, see for instance ref. [115].

2.2.3 Connecting the single- and two-particle Green's Functions

So far, the equations for the single- and two-particle Green's functions have been treated separately. Comparison of the 2-point vertex in figure 2.1 and of the 4-point vertex diagrams in figure 2.2 already suggests that there should be a close connection, since the 4-point vertex can apparently be obtained from the 2-point one by amputating a single propagator line. It will turn out that this can be done in three different ways, corresponding to the three channels in which contributions to the 4-point vertex can be irreducible. Again, we will focus only on the ph-channel.

To derive an expression for $\Gamma^{(0)}$, we consider an external source u which couples linearly to the single-particle Green's function. We therefore consider the time-dependent Hamiltonian,

$$\hat{H}(t) = \hat{H}_0 + \hat{V} + \hat{H}_{ext}(t) \; , \tag{2.147}$$

with ground state $\left|\Psi_0^{(N)'}\right\rangle$ where

$$\hat{H}_{ext}(t) = \int d1d2\hat{\psi}(1)u(1,2)\hat{\psi}^\dagger(2) \; . \tag{2.148}$$

We now want to calculate the response of the single-particle Green's function to the source. We assume that the external source is adiabatically switched on at some distant time in the past, $u(t, -\infty) = 0$. As in section 2.1.4 we can then relate the Green's function at time t to the one at time $t' = -\infty$ using the Gell-Mann–Low theorem. At time $t' = -\infty$, the Green's function is simply the Green's function of the interacting system. In analogy to (2.57), the corresponding $S-$matrix is

$$\hat{S} = \sum_{n=0}^{\infty} \frac{1}{n!}(-i)^n \int_{\infty}^{t} dt_1 dt_2 \dots dt_n \mathcal{T}\left[\hat{H}_{ext}(t_1)\hat{H}_{ext}(t_2)\dots\hat{H}_{ext}(t_n)\right] , \tag{2.149}$$

and we can write for the associated single-particle Green's function at time t

$$\begin{aligned} G^{(u)}(1,2) =& -i\left\langle \Psi_0^{(N)'}(t)\middle|\mathcal{T}\left[\hat{\psi}(1)\hat{\psi}^\dagger(2)\right]\middle|\Psi_0^{(N)'}(t)\right\rangle \\ =& -i\frac{\left\langle \Psi_0^{(N)}(-\infty)\middle|\mathcal{T}\left[\hat{\psi}(1)\hat{\psi}^\dagger(2)\hat{S}\right]\middle|\Psi_0^{(N)}(-\infty)\right\rangle}{\left\langle \Psi_0^{(N)}(-\infty)\middle|\hat{S}\middle|\Psi_0^{(N)}(-\infty)\right\rangle} . \end{aligned} \tag{2.150}$$

We now look at the linear response of the Green's function with respect to the external source. The derivative of the $S-$matrix with respect to the source is simply

$$\frac{\delta\hat{S}}{\delta u(2',2)} = i\mathcal{T}\left[\hat{S}\hat{\psi}(2)\hat{\psi}^\dagger(2')\right] , \tag{2.151}$$

and the derivatives of the fields are zero. With (2.150) and using (2.103) for the 2-particle Green's function (2.118) we therefore find for the linear response of the single-particle Green's function to an external perturbation

$$-i\frac{\delta G^{(u)}(1,1')}{\delta u(2',2)} = iG_2(1,2,1',2') - iG(1'1')G(2',2) \equiv \chi(1,2,1',2') . \tag{2.152}$$

The quantity χ is called the generalized susceptibility. Since it describes the response of the interacting single-particle Green's function with respect to an external field it is sometimes also called 4-point linear response function. χ obeys a BSE. Defining the non-interacting susceptibility,

$$\chi^{(0)}(1,2,1',2') = -iG(1,2')G(2,1') \tag{2.153}$$

and inserting (2.153) and (2.152) into (2.140), we obtain

$$\chi(1,2,1',2') = \chi^{(0)}(1,2,1'2') + \chi^{(0)}(1,4,1',3)F(3,5,4,6)\chi^{(0)}(6,2,5,2') , \tag{2.154}$$

and into (2.146), we obtain

$$F(1,2,1',2') = \Gamma^{(0)}(1,2,1',2') + \Gamma^{(0)}(1,3,1',4)\chi^{(0)}(4,5,3,6)F(6,2,5,2') . \tag{2.155}$$

Inserting (2.155) we obtain the BSE for the generalized susceptibility in the particle-hole channel[58,127,128] through (2.154),

$$\chi(1,2,1',2') = \chi^{(0)}(1,2,1',2') + \chi^{(0)}(1,3,1',4)\Gamma^{(0)}(4,5,3,6)\chi(6,2,5,2') \; , \tag{2.156}$$

or

$$\chi^{-1}(1,2,1',2') = \left[\chi^{(0)}\right]^{-1}(1,2,1',2') - \Gamma^{(0)}(1,2,1',2') \; . \tag{2.157}$$

Notice that the pair of equations eqs. (2.155) and (2.156) is another instance of the pair eqs. (2.127) and (2.128) of two interrelated Dyson equations for the response function and the kernel.

In principle, it is clear how to solve (2.131). We restrict the self-energy to a subset of skeleton diagrams, for example the set shown in figure 2.1c). We then diagonalize the single-particle Hamiltonian to obtain $G_1^{(0)}$ and evaluate $\Sigma\left[G_1^{(0)}\right]$. We then calculate G using (2.131). This yields already an infinite amount of the 1PR terms in (2.117). Then we use this G to evaluate $\Sigma[G]$. This gives us a fraction of the subset of terms belonging to Σ^{R} which can be obtained from the chosen subset of skeleton diagrams. If we repeat this procedure, we generate more of the terms in Σ^{R}. We can then do this a few times until we do not observe any changes in G any more.

We can use the G obtained in this way to construct $\chi^{(0)}$ and solve (2.156). We then need to make assumptions on the kernel $\Gamma^{(0)}$. We could again chose a subset of terms which are 2PI in the ph channel. The choice of terms is then not necessarily in agreement with the diagrams in Σ. However, there is a connection between I and Σ, which has been found by Baym and Kadanoff.[58] We augment the Dyson equation for G with the non-local source u,

$$G(1,2) = G^{(0)}(1,2) + G^{(0)}(1,3)\left[\Sigma(3,4) + u(3,4)\right]G(4,2) \; , \tag{2.158}$$

or equivalently

$$[G]^{-1}(1,2) = \left[G_1^{(0)}\right]^{-1} - \Sigma(1,2) - u(1,2) \; . \tag{2.159}$$

We can now invert the generalized susceptibility

$$\begin{aligned} \frac{\delta u(1,1')}{\delta G(2',2)} =& -i\chi^{-1}(1,2,1',2') \\ =& \frac{\delta}{\delta G(2',2)}\left\{\left[G_1^{(0)}\right]^{-1}(1,1') - [G]^{-1}(1,1') - \Sigma(1,1')\right\} \; . \end{aligned} \tag{2.160}$$

The first term on the *r.h.s.* vanishes since $G^{(0)}$ does not depend on G. Using

$$\int d4\,[G]^{-1}(1,4)G(4,2) = \delta(1,2) \tag{2.161}$$

for the second term, differentiation with respect to G gives the identity

$$-\frac{\delta\,[G]^{-1}(1,2)}{\delta G(4,3)} = -[G]^{-1}(1,4)\,[G]^{-1}(3,2) = -i\left[\chi^{(0)}\right]^{-1}(1,3,2,4) \; . \tag{2.162}$$

We therefore obtain for (2.160)

$$\chi^{-1}(1,3,2,4) = \left[\chi^{(0)}\right]^{-1}(1,3,2,4) - i\frac{\delta\Sigma(1,2)}{\delta G(4,3)} \; . \tag{2.163}$$

This is the same Dyson equation as (2.156), with the derivative of the self-energy with respect to the single-particle Green's function as its kernel. Comparison to (2.157) implies the identity

$$\Gamma^{(0)}(1,2,1',2') = i\frac{\delta\Sigma(1,1')}{\delta G(2',2)} \tag{2.164}$$

for the kernel of eq. (2.156).[8] There is now a fundamental difference between (2.131) and (2.156). The kernel of (2.156) as defined by (2.164) does not depend on its solution. After solving the Dyson equation for G as outlined above, we can then simply calculate the kernel (2.164) and solve (2.156). This already gives the generalized susceptibility within a single calculation.

Symmetries of the 4-Point Vertex

From the definition of the 2-particle Green's function (2.82) and the fact that the field operator anti-commutes with itself, it follows that

$$G_2(1,2,1',2') = -G_2(1',2,1,2') = -G_2(1,2',1',2) = G_2(1',2',1,2) \; , \tag{2.167}$$

known as crossing symmetry.[129] The crossing symmetry implies important symmetry relation for the different irreducible vertices. Let us first define the generalized susceptibility in the $\overline{ph}$-channel,

$$\chi^{(0)}_{\overline{ph}}(1,2,1',2') = iG(1,1')G(2,2') \; . \tag{2.168}$$

[8] Eq. (2.156) is often (for instance in ref.[15]) formulated in terms of the quantity

$$L(1,2,3,4) = -G_2(1,2,3,4) + G(1,3)G(2,4) \; ,$$

which is connected to the generalized susceptibility by

$$L(1,2,3,4) = i\chi(1,2,3,4) \quad L^{(0)}(1,2,3,4) = G(1,4)G(2,3) = i\chi^{(0)}(1,2,3,4) \; .$$

Multiplying (2.156) with a factor of i

$$i\chi = i\chi^{(0)} + i\chi^{(0)}i\frac{\delta\Sigma}{\delta G}\chi \tag{2.165}$$

shows that the BSE for L is

$$L = L^{(0)} + L^{(0)}\frac{\delta\Sigma}{\delta G}L \; , \tag{2.166}$$

where now the kernel $\Gamma^{(0)}$ differs to the one in (2.156) by a imaginary unit. Sometimes (for instance in ref[128] (2.156) is used but χ is called L. In ref. [69] the BSE is also formulated in terms of L, but L is defined with opposite sign.)

It is obtained from the non-interacting generalized susceptibility in the *ph*-channel by exchanging either the two in-going or the two out-going propagators. We then have the symmetry[9]

$$\chi^{(0)}_{\overline{ph}}(1,2,1',2') = -\chi^{(0)}_{ph}(1,2,2',1') \; , \tag{2.169}$$

and the same for the interacting susceptibilities,

$$\chi_{\overline{ph}}(1,2,1',2') = -\chi_{ph}(1,2,2',1') \; . \tag{2.170}$$

$\chi^{(0)}_{\overline{ph}}$ and $\chi_{\overline{ph}}$ are related by a BSE equivalent to (2.200). Therefore, (2.169) and (2.170) imply the crossing symmetry for the reducible vertex,

$$F(1,2,1',2') = F(2,1,2',1') \; , \tag{2.171}$$

and for the reducible vertex functions

$$\Gamma^{(0)}_{\overline{ph}}(1,2,1',2') = -\Gamma^{(0)}_{ph}(1,2,2',1') \; . \tag{2.172}$$

The irreducible vertex in the *pp*-channel fulfills a crossing symmetry on its own.[130] Eq. (2.172) is equivalent to[15]

$$\frac{\delta\Sigma(1,1')}{\delta G(2',2)} = \frac{\delta\Sigma(2,2')}{\delta G(1',1)} \; , \tag{2.173}$$

which is an important constraint when approximating the 4-point vertex.

The 2-point vertex $\Sigma\,[W,G]$

To turn (2.156) and (2.131) into a closed set of equations, we need to establish a dependence of the self-energy on χ. For this, we need the EOM for the single-particle Green's function. We start from (2.42) and use (2.1) to obtain the EOM for the field operator,

$$\left[i\frac{\partial}{\partial t} - \hat{h}_1(x) \right] \hat{\psi}(1) = \int d2 \hat{\psi}^\dagger(2)\hat{\psi}(2)W^{(0)}(2,1)\hat{\psi}(1) \; . \tag{2.174}$$

[9] Recall that we have here defined

$$\chi^{(0)}(1,2,1',2') \equiv \chi^{(0)}_{ph}(1,2,1',2') \; .$$

We can now calculate the time-derivative of the single-particle Green's function (2.80),

$$\begin{aligned} i\frac{\partial}{\partial t_1}G(1,2) =& \frac{\partial}{\partial t_1}\Theta(t_1-t_2)\left\langle \Psi_0^{(N)}\middle|\hat{\psi}(1)\hat{\psi}^\dagger(2)\middle|\Psi_0^{(N)}\right\rangle \\ &+ \Theta(t_1-t_2)\left\langle \Psi_0^{(N)}\middle|\frac{\partial\hat{\psi}(1)}{\partial t_1}\hat{\psi}^\dagger(2)\middle|\Psi_0^{(N)}\right\rangle \\ &- \frac{\partial}{\partial t_1}\Theta(t_2-t_1)\left\langle \Psi_0^{(N)}\middle|\hat{\psi}^\dagger(2)\hat{\psi}(1)\middle|\Psi_0^{(N)}\right\rangle \\ &- \Theta(t_2-t_1)\left\langle \Psi_0^{(N)}\middle|\hat{\psi}^\dagger(2)\frac{\partial\hat{\psi}(1)}{\partial t_1}\middle|\Psi_0^{(N)}\right\rangle , \end{aligned} \tag{2.175}$$

and use

$$\frac{\partial}{\partial t_1}\Theta(t_1-t_2) = \delta(t_1-t_2) = -\frac{\partial}{\partial t_1}\Theta(t_2-t_1) \tag{2.176}$$

together with (2.174) to obtain the identity

$$G(1,1') = G^{(0)}(1,1') - iG^{(0)}(1,2)W^{(0)}(2,3)G_2(2,3^+,1',3^{++}) \tag{2.177}$$

for the single-particle Green's function. Using (2.152) we can factor out an additional term,

$$\begin{aligned} G(1,1') =& G^{(0)}(1,1') - iG^{(0)}(1,2)W^{(0)}(2,3)G(2,1')G(3,3^+) \\ &- G^{(0)}(1,2)W^{(0)}(2,3)\chi(2,3^+,1',3^{++}) . \end{aligned} \tag{2.178}$$

the second term on the *r.h.s* is the first term in the series expansion of G in figure 2.1a) The corresponding contribution to the self-energy is the first term in figure 2.1b). This is the Hartree term,

$$\Sigma_H(1,2) = \delta(1,2)v_H(1) = -i\delta(1,2)\int d3W^{(0)}(1,3)G(3,3+) . \tag{2.179}$$

Eq. (2.178) becomes

$$\begin{aligned} G(1,1') =& G^{(0)}(1,1') + G^{(0)}(1,2)\Sigma_H(2,3)G(3,1') \\ &- G^{(0)}(1,2)W^{(0)}(2,3)\chi(2,3^+,1',3^{++}) . \end{aligned} \tag{2.180}$$

We now consider again the single-particle Green's function in the presence of the time-dependent source term,

$$\begin{aligned} G_u(1,1') =& G^{(0)}(1,1') + G^{(0)}(1,2)\left[u(2,3)+\Sigma_H(2,3)\right]G_u(2,1') \\ &+ iG^{(0)}(1,2)W^{(0)}(2,3)\frac{\delta G_u(2,1')}{\delta u(3^+,3)} . \end{aligned} \tag{2.181}$$

Following ref. [15], this is equivalent to

$$\begin{aligned} G_u^{-1}(1,1') =& \left[G^{(0)}\right]^{-1}(1,1') - \left[u(1,1')+\Sigma_H(1,1')\right] \\ &- iW^{(0)}(2,3)\frac{\delta G_u(1,2)}{\delta u(3^+,3)}G_u^{-1}(2,1') , \end{aligned} \tag{2.182}$$

and by comparison to the Dyson equation of the unperturbed interacting system, the self-energy is

$$\Sigma(1,1') = \Sigma_H(1,1') - iW^{(0)}(1,3)G(1,2)\frac{\delta G^{-1}(2,1')}{\delta u(3^+,3)} \ , \tag{2.183}$$

where the last factor in the last term becomes (using (2.159) in the first equation and (2.152) as well as (2.146) in the last equation)

$$\begin{aligned}\frac{G^{-1}(2,1')}{\delta u(3^+,3)} =& \frac{\left[G^{(0)}\right]^{-1}(2,1')}{\delta u(3^+,3)} - \frac{u(2,1')}{\delta u(3^+,3)} - \frac{\Sigma(2,1')}{\delta u(3^+,3)} \\ =& -\delta(2,1')\delta(2,3) - \frac{\delta\Sigma(2,1')}{\delta u(3^+,3)} \\ =& -\delta(2,1')\delta(2,3) - \frac{\delta\Sigma(2,1')}{\delta G(4,4')}\frac{\delta G(4,4')}{\delta u(3^+,3)} \\ =& -\delta(2,1')\delta(2,3) - \Gamma^{(0)}(2,4',1',4)\chi(4,3,4',3^+) \ .\end{aligned} \tag{2.184}$$

Inserting the last equation into (2.183) the first term becomes

$$\Sigma_x(1,1') \equiv iW^{(0)}(1,3)G(1,2)\delta(2,1')\delta(2,3) = iW^{(0)}(1,1')G(1,1') \ , \tag{2.185}$$

which is the second term in the series expansion in figure 2.1c), the so-called Fock term. The remainder is called correlation term,

$$\Sigma_c(1,1') \equiv +iW^{(0)}(1,3)G(1,2)\Gamma^{(0)}(2,4',1',4)\chi(4,3,4',3^+) \ , \tag{2.186}$$

$$\Sigma(1,1') = \Sigma_H(1,1') + \Sigma_x(1,1') + \Sigma_c(1,1') \ . \tag{2.187}$$

This does not seem to be useful since both Σ and its functional derivative with respect to G appear in the last expression. However, together with (2.131) and (2.156), (2.187) forms a closed hierarchy of equations. For example, after having solved for G^0, one could set, in a first step $\Gamma^0 = 0$ so that one has

$$\Sigma = \Sigma_H + \Sigma_x \ ,$$

with which (2.131) is solved. Afterwards, one can take the functional derivative with respect to the resulting Green's function, solve (2.156) and insert the resulting χ (together with Σ^0) into (2.187) which results in a more complicated expression for Σ. Repeating this procedure an infinite amount of times, the complete skeleton series for Σ will eventually be created and the exact G could be evaluated.

In practice, one typically takes one additional step. Decomposing the 4-point vertex

$$\begin{aligned}\Gamma^{(0)}(1,2,1',2') &= \Gamma^{(0)}_H(1,2,1',2') + \Gamma^{(0)}_{xc}(1,2,1',2') \\ &= i\frac{\Sigma_H(1,1')}{\delta G(2',2)} + i\frac{\Sigma_{xc}(1,1')}{\delta G(2',2)}\end{aligned} \tag{2.188}$$

substituting it into (2.187) and using (2.185), we obtain

$$\begin{aligned}\Sigma(1,1') =&\Sigma_H(1,1') + iW^0(1,1')G(1,1') \\ &+ iG(1,1')W^{(0)}(1,2)\chi(4',3,4,3^+)\delta(2,4')\delta(2,4)W^{(0)}(2,1') \\ &+ iG(1,1')W^{(0)}(1,3)\chi(4',3,4,3^+)\Gamma^{(0)}_{xc}(2,4,1',4') \ .\end{aligned} \tag{2.189}$$

This expression for Σ is equivalent to the expression given by Maggio and Kresse in ref. [131]. We can then factor out an additional term,

$$\begin{aligned}W(1,1') \equiv&W^0(1,1') + W^{(0)}(1,2)\chi(4',3,4,3^+)\delta(2,4')\delta(2,4)W^{(0)}(2,1') \\ =&W^{(0)}(1,2) + W^{(0)}(1,2)\chi^{(0)}(4',3,4,3^+)\delta(2,4')\delta(2,4)W(2,1') \ ,\end{aligned} \tag{2.190}$$

which takes the form of a Dyson equation. Writing out the kernel of the equation

$$\chi(6,4,5,4^+)\delta(3,6)\delta(3,5) = iG_2(3,4,3^+,4^+) - iG^{(0)}(3,3+)G^{(0)}(4,4^+) \ , \tag{2.191}$$

using (2.64) and identifying the density operator

$$\hat{n}(1) = \lim_{t_2 \to t_1^+} \int d2\hat{\psi}(1)\delta(\boldsymbol{r}_1 - \boldsymbol{r}_2)\delta_{\sigma\sigma'}\hat{\psi}^\dagger(2) \ , \tag{2.192}$$

we see that

$$\begin{aligned}P(3,4) =&\chi(6,4,5,4^+)\delta(3,6)\delta(3,5) \\ =&-\left\langle \Phi_0^{(N)} \middle| \hat{n}(3)\hat{n}(4) \middle| \Phi_0^{(N)} \right\rangle - \left\langle \Phi_0^{(N)} \middle| \hat{n}(3) \middle| \Phi_0^{(N)} \right\rangle \left\langle \Phi_0^{(N)} \middle| \hat{n}(4) \middle| \Phi_0^{(N)} \right\rangle\end{aligned} \tag{2.193}$$

describes how the charge density of the N-electron system is modified by an external perturbation. This quantity is also called density-density response, or polarizability. We can also define its irreducible counterpart,

$$P^{(0)}(1,2) = -iG(1,2)G(2,1^+) \ , \tag{2.194}$$

which follows directly from the definition of the non-interacting generalized susceptibility (2.153). Both quantities fulfill

$$P^{(0)}(1,2) = P^{(0)}(2,1) \tag{2.195}$$

and

$$P(1,2) = P(2,1) \ . \tag{2.196}$$

We can then rewrite (2.190) in the compact form

$$W(1,2) = W^{(0)}(1,2) + W^{(0)}(1,3)P(3,4)W^{(0)}(3,2) \tag{2.197}$$

$$W(1,2) = W^{(0)}(1,2) + W^{(0)}(1,3)P^{(0)}(3,4)W(3,2) \ . \tag{2.198}$$

The self-energy (2.187) can then be rewritten using this quantity and together with (2.156), (2.131), (2.197) (2.164) and (2.201), forms a closed set of equations. This set is the final result of this section and is summarized below:

$$G(1,2) = G^0(1,2) + G^{(0)}(1,3)\Sigma^{(0)}(3,4)G(4,2) \tag{2.199}$$

$$\chi(1,2,1',2') = \chi^{(0)}(1,2,1',2') + \chi^{(0)}(1,4,1',3)\Gamma^{(0)}(3,5,4,6)\chi(6,2,5,2') \tag{2.200}$$

$$P(1,2) = \chi(3,2,4,2^+)\delta(3,1)\delta(4,1) \tag{2.201}$$

$$W(1,2) = W^{(0)}(1,2) + W^{(0)}(1,3)P(3,4)W^{(0)}(3,2) \tag{2.202}$$

$$\Sigma(1,2) = \Sigma_H(1,2) + iG(1,2)W(1,2) + iG(1,3)W^{(0)}(1,4)\chi(6,4,5,4^+)\Gamma^{(0)}_{xc}(3,5,2,6) \tag{2.203}$$

This set of equations is equivalent to the four equations by Starke and Kresse, eqs. 32-34 and eq. 44 in ref. [69], and to Hedin's equations[67], as has been shown by Starke and Kresse[69].

2.3 Green's Functions and Quasiparticles

Before introducing some common approximations to the equations above, we discuss some properties of single- and two-particle Green's functions.

2.3.1 The Single-Particle Green's function

Using eqs. (2.32) and (2.51) and the identities (2.33), the single-particle Green's function defined in (2.117) can be written as

$$G(1,2) = \Theta(t_1 - t_2)G_>(1,2) - \Theta(t_2 - t_1)G_<(2,1) \ , \tag{2.204}$$

with

$$G_>(1,2) = -i\left\langle \Psi_0^{(N)} \middle| \hat{\psi}_>(1)\hat{\psi}^\dagger_>(2) \middle| \Psi_0^{(N)} \right\rangle \tag{2.205}$$

$$G_<(1,2) = -i\left\langle \Psi_0^{(N)} \middle| \hat{\psi}_<(1)\hat{\psi}^\dagger_<(2) \middle| \Psi_0^{(N)} \right\rangle \ . \tag{2.206}$$

$G_>$ and $G_<$ are respectively called greater and lesser Green's function. The greater component is the probability amplitude that an electron with energy higher than the chemical potential is created at space-time point 2 and destroyed at space-time point 1. The lesser component is the probability amplitude that a hole with energy lower than the chemical potential is created at space-time point 1 destroyed at space-time point 2. Note, that per definition $t_1 > t_2$. A hole going backwards in time is equivalent to an electron moving forward in time. Since the single-particle Green's function describes the propagation of an electron, it is also called electron propagator.

The single-particle propagator is zero for $\sigma_1 \neq \sigma_2$ due to conservation of spin. Therefore, we ignore spin in the following discussion. Using (2.205), (2.58), and (2.46), we obtain for the greater (2.205) and the lesser components (2.206)

$$\begin{aligned} G_>(1,2) &= -i\Big\langle \Psi_0^{(N)} \Big| e^{i\hat{H}t_1}\hat{\psi}_>(x_1)e^{-i\hat{H}t_1}e^{-i\hat{H}t_2}\hat{\psi}_>^\dagger(x_2)e^{i\hat{H}t_2}\Big|\Psi_0^{(N)}\Big\rangle \\ G_<(1,2) &= -i\Big\langle \Psi_0^{(N)} \Big| e^{i\hat{H}t_1}\hat{\psi}_<(x_1)e^{-i\hat{H}t_1}e^{-i\hat{H}t_2}\hat{\psi}_<^\dagger(x_2)e^{i\hat{H}t_2}\Big|\Psi_0^{(N)}\Big\rangle \end{aligned} \tag{2.207}$$

We can now insert the completeness relation of the Slater determinants (2.17) to obtain the Lehmann representations of both components

$$\begin{aligned} G_>(1,2) &= -i\sum_n^\infty \Big\langle \Psi_0^{(N)} \Big| e^{i\hat{H}t_1}\hat{\psi}_>(x_1)e^{-i\hat{H}t_1}\Big|\Psi_n^{(N')}\Big\rangle\Big\langle \Psi_n^{(N')} \Big| e^{-i\hat{H}t_2}\hat{\psi}_>^\dagger(x_2)e^{i\hat{H}t_2}\Big|\Psi_0^{(N)}\Big\rangle \\ G_<(1,2) &= -i\sum_n^\infty \Big\langle \Psi_0^{(N)} \Big| e^{i\hat{H}t_1}\hat{\psi}_<(x_1)e^{-i\hat{H}t_1}\Big|\Psi_n^{(N')}\Big\rangle\Big\langle \Psi_n^{(N')} \Big| e^{-i\hat{H}t_2}\hat{\psi}_<^\dagger(x_2)e^{i\hat{H}t_2}\Big|\Psi_0^{(N)}\Big\rangle \,. \end{aligned} \tag{2.208}$$

$|\Psi_n^{(N)}\rangle$ is an eigenstate of $\hat{H}$ with eigenvalue $E_n^{(N)}$ and from the series representation of the exponential it follows that

$$\begin{aligned} G_>(1,2) &= -i\sum_n^\infty e^{-i\left(E_0^{(N)}-E_n^{(N')}\right)(t_1-t_2)}\Big\langle \Psi_0^{(N)} \Big|\hat{\psi}_>(x_1)\Big|\Psi_n^{(N')}\Big\rangle\Big\langle \Psi_n^{(N')} \Big|\hat{\psi}_>^\dagger(x_2)\Big|\Psi_0^{(N)}\Big\rangle \\ G_<(1,2) &= -i\sum_n^\infty e^{-i\left(E_0^{(N)}-E_n^{(N')}\right)(t_1-t_2)}\Big\langle \Psi_0^{(N)} \Big|\hat{\psi}_<(x_1)\Big|\Psi_n^{(N')}\Big\rangle\Big\langle \Psi_n^{(N')} \Big|\hat{\psi}_<^\dagger(x_2)\Big|\Psi_0^{(N)}\Big\rangle \,. \end{aligned} \tag{2.209}$$

This implies that the single particle Green' function only depends on the time-difference,

$$G(1,2) = G(x_1, x_2, t_1 - t_2)\,. \tag{2.210}$$

Explicit expressions for the non-interacting Green's Function

Let us now evaluate the expectation values of the field operators. Inserting their definitions (2.30) and (2.31), and considering (2.18) and (2.19) we obtain in the non-interacting case for $N' = N \pm 1$

$$\begin{aligned} \Big\langle \Phi_n^{(N+1)} \Big|\hat{\psi}_>^\dagger(x)\Big|\Phi_0^{(N)}\Big\rangle &= \sum_k \phi_k^*(x)\Theta(\epsilon_k-\mu)\delta_{nk} \\ \Big\langle \Phi_0^{(N)} \Big|\hat{\psi}_>(x)\Big|\Phi_n^{(N+1)}\Big\rangle &= \sum_k \phi_k(x)\Theta(\epsilon_k-\mu)\delta_{nk} \\ \Big\langle \Phi_n^{(N-1)} \Big|\hat{\psi}_<^\dagger(x)\Big|\Phi_0^{(N)}\Big\rangle &= \sum_k \phi_k(x)\Theta(\mu-\epsilon_k)\delta_{nk} \\ \Big\langle \Phi_0^{(N)} \Big|\hat{\psi}_<(x)\Big|\Phi_n^{(N-1)}\Big\rangle &= \sum_k \phi_k^*(x)\Theta(\mu-\epsilon_k)\delta_{nk}\,. \end{aligned} \tag{2.211}$$

Since the overlap of Slater determinants corresponding to different N-particle sectors of Fock space is zero, all matrix elements in (2.209) with $N' \neq N \pm 1$ are zero. Finally, we can rewrite the exponential. We notice, that

$$E_0^{(N)} = \sum_n \epsilon_n, \quad \epsilon_n < \mu \ , \tag{2.212}$$

due to the Pauli exclusion principle. The $N+1$ particle system has one electron more, so the energy difference in the exponential is simply

$$E_0^{(N)} - E_k^{(N+1)} = -(\epsilon_k - \mu) < 0 \ . \tag{2.213}$$

The lesser component of the Green's function is obtained analogously. Putting everything together, we obtain in the non-interacting case

$$\begin{aligned} G_>^{(0)}(1,2) &= -i \sum_k \Theta(\epsilon_k - \mu) \phi_k(x_1) \phi_k^*(x_2) e^{-i(\epsilon_k - \mu)(t_1 - t_2)} \\ G_<^{(0)}(1,2) &= -i \sum_k \Theta(\mu - \epsilon_k) \phi_k^*(x_1) \phi_k(x_2) e^{-i(\epsilon_k - \mu)(t_1 - t_2)} \end{aligned} \tag{2.214}$$

and therefore the final form of the non-interacting time-ordered propagator is

$$\begin{aligned} G^{(0)}(x_1, x_2, t_1 - t_2) = &- i\Theta(t_1 - t_2) \sum_k \Theta(\epsilon_k - \mu) e^{-i(\epsilon_k - \mu)(t_1 - t_2)} \phi_k(x_1) \phi_k^*(x_2) \\ &+ i\Theta(t_2 - t_1) \sum_k \Theta(\mu - \epsilon_k) e^{-i(\epsilon_k - \mu)(t_1 - t_2)} \phi_k(x_1) \phi_k^*(x_2) \ . \end{aligned} \tag{2.215}$$

Let us now look at the single-particle Green's function in frequency space. The Fourier transform of (2.204) with respect to time is formally given as

$$G^{(0)}(x_1, x_2, \omega) = \int d(t_1 - t_2) e^{i\omega(t_1 - t_2)} G^{(0)}(x_1, x_2, t_1 - t_2) \ . \tag{2.216}$$

This expression is ill-defined, since the Fourier transform of the Heaviside step function is not a function, but a distribution. However, we can write the Fourier transform in terms of a two-sided Laplace transforms $\mathcal{L}$,

$$\mathcal{L}\left[f\right](s) = \int e^{-st} f(t) dt \ , \tag{2.217}$$

where we define

$$s = \lim_{\eta \to 0^+} i\omega \pm \eta \ . \tag{2.218}$$

In particular, the Laplace transform of the Heaviside step function is well defined and is given as

$$\int \theta(\pm t) e^{i\omega t \mp \eta t} = \frac{\pm i}{\omega \pm i\eta} \ . \tag{2.219}$$

We can now write

$$\begin{aligned}&\int dt e^{\omega t}\left[\Theta(t)-\Theta(-t)\right]e^{-ixt}\\&=\lim_{\eta\to 0^+}\int_0^\infty d(-t)\Theta(t)e^{(i\omega-ix+\eta)t}+\lim_{\eta\to 0^+}\int_0^\infty dt\Theta(-t)e^{(i\omega-ix+\eta)t}\,.\end{aligned}\tag{2.220}$$

Using (2.219), and (2.220), we obtain

$$\mathcal{L}\left\{\left[\Theta(t)-\Theta(-t)\right]e^{-ixt}\right\}(s)=\frac{i}{\omega-x+i\eta}-\frac{i}{\omega-x-i\eta}\,,\tag{2.221}$$

which implies

$$\lim_{\eta\to 0^+}\left[\frac{i}{\omega-x+i\eta}-\frac{i}{\omega-x-i\eta}\right]=2\pi\delta(\omega-x)\,.\tag{2.222}$$

With the substitution $x=\epsilon_k-\mu$ and with (2.214) we therefore obtain for non-interacting electrons

$$\begin{aligned}G^{(0)}(x_1,x_2,\omega)=&\lim_{\eta\to 0^+}\sum_k\phi_k(x_1)\phi_k^*(x_2)\Theta(\epsilon_k-\mu)\frac{1}{\omega-(\epsilon_k-\mu)+i\eta}\\&+\lim_{\eta\to 0^+}\sum_k\phi_k(x_1)\phi_k^*(x_2)\Theta(\mu-\epsilon_k)\frac{1}{\omega-(\epsilon_k-\mu)-i\eta}\,.\end{aligned}\tag{2.223}$$

Imaginary time and Imaginary Frequency Representations

The real time and real frequency representations of the Green's function are useful since they give it a clear physical meaning. Mathematically, working on the real axes is cumbersome. On the real frequency axis, the Green's function has poles. On the real time axis, the Green's function is oscillating. Informally, one can introduce an imaginary-time representation of the single-particle Green's function (2.209) by the replacement $t\to -i\tau$. Eq. (2.209) becomes

$$\begin{aligned}G_>(x_1,x_2,i\tau)=&-i\sum_n^\infty e^{-\left(E_0^{(N)}-E_n^{(N')}\right)\tau}\left\langle\Psi_0^{(N)}\left|\hat\psi_>(x_1)\right|\Psi_n^{(N')}\right\rangle\left\langle\Psi_n^{(N')}\left|\hat\psi_>^\dagger(x_2)\right|\Psi_0^{(N)}\right\rangle\\G_<(x_1,x_2,i\tau)=&-i\sum_n^\infty e^{-\left(E_0^{(N)}-E_n^{(N')}\right)\tau}\left\langle\Psi_0^{(N)}\left|\hat\psi_<(x_1)\right|\Psi_n^{(N')}\right\rangle\left\langle\Psi_n^{(N')}\left|\hat\psi_<^\dagger(x_2)\right|\Psi_0^{(N)}\right\rangle\,.\end{aligned}\tag{2.224}$$

Unlike in the non-interacting case, we can not obtain a simple analytical expression for the action of the field operators on $\left|\Psi_0^{(N)}\right\rangle$ since $\left|\Psi_0^{(N)}\right\rangle$ is not a single Slater-determinant. However, recalling the definition of the field operators eqs. (2.30)–(2.32) we know that for instance $\hat\psi_<^\dagger(x_2)\left|\Psi_0^{(N)}\right\rangle$ is an interacting $N-1$-particle state since $\hat\psi_<^\dagger$ creates a hole below the chemical potential. Therefore, we know that in the lesser propagator only the terms with $N'=N-1$ and

in the greater propagator only the terms with $N' = N + 1$ remain. We now define the Lehmann amplitudes

$$\begin{aligned}\psi_{-,k}(x) =& \left\langle \Phi_0^{(N)} \middle| \hat{\psi}(x)_< \middle| \Phi_k^{(N-1)} \right\rangle \\ \psi_{+,k}(x) =& \left\langle \Phi_0^{(N)} \middle| \hat{\psi}(x)_> \middle| \Phi_k^{(N+1)} \right\rangle\end{aligned} \tag{2.225}$$

and the energy differences

$$\begin{aligned}E_k^{(+)} =& E_0^{(N)} - E_k^{(N+1)} \\ E_k^{(-)} =& E_0^{(N)} - E_k^{(N-1)} \,,\end{aligned} \tag{2.226}$$

with which, together with eq. (2.224), we can write (2.204) as

$$G(x_1, x_2, i\tau) = -i\Theta(\tau) \sum_k e^{-E_k^{(+)}\tau} \psi_{+,k}(x_1)\psi^*_{+,k}(x_2) + i\Theta(-\tau) \sum_k e^{-E_k^{(-)}\tau} \psi_{-,k}(x_1)\psi^*_{-,k}(x_2) \,. \tag{2.227}$$

In the non-interacting case, eqs. (2.214) and (2.215) become

$$\begin{aligned}G^{(0)}_>(x_1, x_2, i\tau) &= -i \sum_k \Theta(\epsilon_k - \mu)\phi_k(x_1)\phi^*_k(x_2)e^{-(\epsilon_k-\mu)\tau} \\ G^{(0)}_<(x_1, x_2, i\tau) &= -i \sum_k \Theta(\mu - \epsilon_k)\phi^*_k(x_1)\phi_k(x_2)e^{-(\epsilon_k-\mu)\tau}\end{aligned} \tag{2.228}$$

and

$$\begin{aligned}G^{(0)}(x_1, x_2, i\tau) =& -i\Theta(\tau) \sum_k \Theta(\epsilon_k - \mu)e^{-(\epsilon_k-\mu)\tau}\phi_k(x_1)\phi^*_k(x_2) \\ &+ i\Theta(-\tau) \sum_k \Theta(\mu - \epsilon_k)e^{-(\epsilon_k-\mu)\tau}\phi_k(x_1)\phi^*_k(x_2) \,.\end{aligned} \tag{2.229}$$

These expression are useful since the Green's functions are exponentially decaying function of imaginary time. We can then transfer these expressions to the imaginary frequency axis using Laplace transforms followed by analytic continuation to the imaginary axis (for convenience we will refer to them often as Fourier transforms even though strictly speaking they are not).[132] For a general meromorphic function they can be written as

$$F(i\tau) = \frac{i}{2\pi} \int d\omega F(i\omega)e^{-i\omega\tau} \tag{2.230}$$

and

$$F(i\omega) = -i \int d\tau F(i\tau)e^{i\omega\tau} \,. \tag{2.231}$$

In particular, we can write (2.231) as

$$F(i\omega) = -i \int_0^\infty d\tau F(i\tau)e^{i\omega\tau} - i \int_0^\infty d\tau F(-i\tau)e^{-i\omega\tau} \,, \tag{2.232}$$

which is useful for functions involving step functions.

The expressions eqs. (2.230) and (2.231) are not uniquely defined and different conventions can be found in the literature for the signs of the arguments of the exponential. Also in our work, we have typically used these equations with opposite signs.[36,37,40] Both choices are fine in principle, but they need to yield the correct definition of the Green's function on the real frequency axis (see below). This means, they need to be compatible with the definition of the time-ordered Green's function in imaginary time eqs. (2.227) and (2.229). The correct definitions of eqs. (2.230) and (2.231) are of particular importance in implementations of MBPT using the space-time method[132,133] on which our implementation is based. In the space-time literature, conventions differ: For instance, Godby and coworkers[132] and also Wilhelm et al.[6] define eqs. (2.230) and (2.231) with opposite signs in the exponentials, but our notation agrees with Kresse and coworkers[134] (and also standard textbooks[135,136]). Importantly, in our first paper detailing the implementatinon of GW[36] we have defined the time-ordered propagators and the Fourier transforms in accordance with Godby and coworkers.[132] There are good reasons to adjust this choice here since the present definition of the time-ordered propagator follows naturally from MBPT. In contrast, it is not clear how the expression for the propagator given in[132] (eq. 3.3) can be derived. The time-ordered propagator in there is the anti-time-ordered Green's function[137] (which are exponentially increasing in imaginary time) but with opposite signs in the exponentials to make same exponentially decaying in imaginary time.

Using (2.232) we obtain the imaginary frequency representation of (2.227) as

$$G(x_1, x_2, i\omega) = \sum_k \frac{\psi_{+,k}(x_1)\psi^*_{+,k}(x_2)}{i\omega - E_k^{(+)}} + \sum_k \frac{\psi_{-,k}(x_1)\psi^*_{-,k}(x_2)}{i\omega - E_k^{(-)}} \,. \tag{2.233}$$

In the non-interacting case, we obtain

$$G^{(0)}(x_1, x_2, i\omega) = \sum_k \Theta(\epsilon_k - \mu)\frac{\phi_k(x_1)\phi^*_k(x_2)}{i\omega - (\epsilon_k - \mu)} + \sum_k \Theta(\mu - \epsilon_k)\frac{\phi_k(x_1)\phi^*_k(x_2)}{i\omega - (\epsilon_k - \mu)} \,, \tag{2.234}$$

which simplifies to

$$G^{(0)}(x_1, x_2, i\omega) = \sum_k \frac{\phi_k(x_1)\phi^*_k(x_2)}{i\omega - (\epsilon_k - \mu)} \tag{2.235}$$

since $\Theta(\epsilon_k - \mu) + \Theta(\mu - \epsilon_k) = 1$ for all k. By giving up the restriction to either real or imaginary frequency axis and analytical continuation of G to the complex plane,[15] we can also express (2.233) in an alternative spectral form,[138]

$$G(x_1, x_2, z) = \sum_k \frac{\psi_k(x_1, z)\psi^*_k(x_2, z)}{z - \epsilon_k^{QP}} \,, \tag{2.236}$$

which is more general than (2.233).

Spectral Functions

The non-interacting Green's function as defined in (2.223) becomes diagonal in the basis of single-particle states. By combination of (2.223) and the Dyson equation (2.131), we therefore obtain another important representation of the interacting single-particle Green's function,

$$G_{kk'}(\omega) = \lim_{\eta \to 0^+} \left[\omega - i\eta - \epsilon_k - \Sigma_{kk'}\right]^{-1} \ . \tag{2.237}$$

The spectral function A is defined by[15]

$$A_{kk'}(\omega) = -\frac{1}{\pi} \lim_{\eta \to 0^+} \text{Im } G_{kk'}(\omega + i\eta) \ . \tag{2.238}$$

or alternatively through the analytical continuation of the single-particle Green's function to the complex plane[15]

$$G(z) = \int d\omega \frac{A(\omega)}{z - \omega} \ . \tag{2.239}$$

Using (2.237) and splitting the self-energy into real and imaginary parts, we obtain for the diagonal elements of A,

$$A_{kk}(\omega) = -\frac{1}{\pi} \frac{\text{Im } \Sigma_{kk}(\omega)}{\left|\omega - \epsilon_k - \text{Re } \Sigma_{kk}(\omega)\right|^2 + \left|\text{Im } \Sigma_{kk}(\omega)\right|^2} \ . \tag{2.240}$$

We have already mentioned that QPs with energy ϵ^{QP} can be identified with poles in the single-particle Green's function. This motivates the definition of the QP dispersion relation

$$\epsilon_K^{QP} = \epsilon_k + \text{Re } \Sigma_{kk}(\epsilon_K^{QP}) \ . \tag{2.241}$$

In a Fermi liquid one then defines[139] the Fermi surface as

$$\epsilon_{\boldsymbol{k}_F} + \text{Re } \Sigma(0, \boldsymbol{k}_F) = 0 \ , \tag{2.242}$$

and therefore, by definition

$$\epsilon^{QP}(\boldsymbol{k}_F) = 0 \ . \tag{2.243}$$

We now need to assume that this behavior carries over to a finite system close to the chemical potential. Fermi liquid theory assumes that the self-energy is approximately linear around the Fermi level.[34] For finite systems, we assume that this implies that the self-energy is is approximately linear around the chemical potential. We can then also expand the frequency dependence of Σ around ϵ_k,

$$\Sigma_k(\epsilon_k^{QP}) = \text{Re } \Sigma_k(\epsilon_k) + \left.\frac{\partial \text{Re } \Sigma_k(\omega)}{\partial \omega}\right|_{\omega = \epsilon_k} \left(\epsilon_k^{QP} - \epsilon_k\right) + \dots \ , \tag{2.244}$$

and truncate after the first derivative. One then typically defines a renormalization factor Z as

$$Z_k(\omega) = \left(1 - \frac{\partial \text{Re } \Sigma_{kk}(\omega)}{\partial \omega} \mid_{\omega = E_k^{QP}}\right)^{-1} . \tag{2.245}$$

We can then write the QP dispersion relation in the vicinity of the chemical potential as

$$\epsilon_k^{QP} = \epsilon_k + Z_k(\epsilon_k) \text{Re } \Sigma_{kk}(\epsilon_k) , \quad \epsilon_K^{QP} \approx \mu . \tag{2.246}$$

We now also assume that a similar relation holds for the imaginary part of the self-energy close to the chemical potential, for which we write

$$- \text{Im } \Sigma_{kk}(\epsilon_K^{QP}) = \gamma_k \times \left(\epsilon_K^{QP}\right)^2 + \mathcal{O}\left(\left(\epsilon_K^{QP}\right)^4\right) , \quad \epsilon_K^{QP} \approx \mu . \tag{2.247}$$

Using this expansion as well as (2.246), we obtain through eq. (2.240),

$$A_{kk}(\omega) = \frac{1}{\pi} \frac{\gamma_k Z_k(\epsilon_K^{QP}) \left(\epsilon_K^{QP}\right)^2}{\left[\epsilon_k - \epsilon_K^{QP}\right]^2 + Z_k^2 \left(\epsilon_k^{QP}\right) \gamma_k^2 \left(\epsilon_K^{QP}\right)^4} , \tag{2.248}$$

which reduces to

$$A_{kk}(\omega) = Z_k(\epsilon_K^{QP}) \delta(\epsilon_k - \epsilon_K^{QP}) , \quad \epsilon_K^{QP} \approx \mu . \tag{2.249}$$

Therefore, the spectral function can be written as[140]

$$A_{kk}(\omega) = Z_k(\epsilon_K^{QP}) \delta(\epsilon_k - \epsilon_K^{QP}) + A_{kk}^{inc}(\omega) , \tag{2.250}$$

where A^{inc} describes the incoherent part of the spectral function beyond the linear terms in eqs. (2.246) and (2.247). Through (2.239), we finally obtain (defining $Z_k = Z_k(\epsilon_K^{QP})$)

$$G_{kk}(i\omega) = Z_k G_{kk}^{(0)} + G_{kk}^{inc}(i\omega) , \tag{2.251}$$

where G^{inc} is defined by (2.239) and denotes the incoherent part of the interacting single-particle propagator, i.e. the part which does not have QP character.[140–142]

Dyson's Equation as effective single-particle Equation

Eq. (2.236) allows us to rewrite Dyson's equation (2.199) as an effective single-particle equation. We first note that

$$i \frac{\partial}{\partial t_1} G^{(0)}(x_1, x_2, t_1 - t_2) = \delta(t_1 - t_2) \delta(x_1 - x_2) + h_1(x_1) G^{(0)}(x_1, x_2, t_1 - t_2) , \tag{2.252}$$

i.e. $G^{(0)}$ is the inverse of the time-dependent single-particle Schrödinger equation. This follows from the definition of the time-ordered $G^{(0)}$ together with

$$\frac{\partial \Theta(t-t')}{\partial t} = \delta(t-t') \; .$$

Upon rotation to the complex plane and subsequent Fourier transformation, eq. (2.252) becomes[143]

$$[z - h_1(\boldsymbol{r}_1)]\, G^{(0)}(x_1, x_2, z) = 1 \; . \tag{2.253}$$

Using this identity and multiplying by $\left[G^{(0)}\right]^{-1}$ from the left we obtain

$$[z - h_1(\boldsymbol{r}_1)]\, G(1,1') - \Sigma(1,3) G(3,1') = \delta(1,1') \tag{2.254}$$

through (2.199). With eqs. (2.129) and (2.130) we can also rewrite (2.199) in the form

$$G = G^{(0)} + G\Sigma G^{(0)} \tag{2.255}$$

and therefore we can also obtain the relation

$$G(1',1)\,[z - h_1(\boldsymbol{r}_1)] - G(1'3)\Sigma(3,1) = \delta(1,1') \; . \tag{2.256}$$

Inserting the spectral decomposition of G eq. (2.236) into (2.254) and using the analytical continuation of $G^{(0)}$ to the complex plane, we get

$$\sum_p \frac{\psi_p^*(\boldsymbol{r}_2)}{z - \epsilon_p^{QP}} \left\{ [z - h_1(\boldsymbol{r}_1)]\, \phi_p(\boldsymbol{r}_1) - \int d\boldsymbol{r}_3 \Sigma(\boldsymbol{r}_1, \boldsymbol{r}_3, z) \phi_p(\boldsymbol{r}_3) \right\} = \delta(\boldsymbol{r} - \boldsymbol{r}') \; . \tag{2.257}$$

With slight abuse of notation we have used the fact that Σ is diagonal in spin. In case p denotes a spatial orbital amd not a spin-orbital, the above relation holds for $\sigma = \alpha$ and $\sigma = \beta$ separately. Multiplying with $z - \epsilon_p^{QP}$ from the left and taking the limit $z \to \epsilon_p^{QP}$, we get

$$\begin{aligned} &\lim_{z \to \epsilon_p^{QP}} \left(z - \epsilon_p^{QP}\right) \sum_p \frac{\psi_p^*(\boldsymbol{r}_2)}{z - \epsilon_p^{QP}} \left\{ [z - h_1(\boldsymbol{r}_1)]\, \phi_p(\boldsymbol{r}_1) - \int d\boldsymbol{r}_3 \Sigma(\boldsymbol{r}_1, \boldsymbol{r}_3, z) \phi_p(\boldsymbol{r}_3) \right\} \\ &= \lim_{z \to \epsilon_p^{QP}} \left(z - \epsilon_p^{QP}\right) \delta(\boldsymbol{r} - \boldsymbol{r}') \; . \end{aligned} \tag{2.258}$$

The *r.h.s.* of this expression is clearly zero everywhere. However, the *l.h.s.* can only be zero if the term in curly brackets vanishes since $\psi_p^*(\boldsymbol{r}_2)$ is never zero for all $\boldsymbol{r}_2$. An analogous derivation starting from (2.256) leads to the same relation for the conjugated Dyson amplitudes. We therefore obtain the QP equations[144]

$$\begin{aligned} h_1(\boldsymbol{r}_1)\psi_p(\boldsymbol{r}_1) + \int d\boldsymbol{r}_3 \Sigma(\boldsymbol{r}_1, \boldsymbol{r}_3, \epsilon_p^{QP}) \psi_p(\boldsymbol{r}_3) &= \epsilon_p^{QP} \psi_p(\boldsymbol{r}_1) \\ \psi_p^*(\boldsymbol{r}_1) h_1(\boldsymbol{r}_1) + \int d\boldsymbol{r}_3 \psi_p^*(\boldsymbol{r}_3) \Sigma(\boldsymbol{r}_3, \boldsymbol{r}_1, \epsilon_p^{QP}) &= \psi_p^*(\boldsymbol{r}_1) \epsilon_p^{QP} \end{aligned} \tag{2.259}$$

Physical interpretation of (2.259)

Superficially, eq. (2.259) resembles the independent-particle Schrödinger equation (2.7), with h_1 replaced by $h_1+\Sigma$. However, the presence of the non-hermitian self-energy introduces important differences. First, the operator on the *l.h.s.* of (2.259) is diagonalized by a set of non-orthogonal eigenvectors. The ψ_k^* are the dual basis to ψ_k and therefore by definition[138] they satisfy an orthogonality condition. Additionally, we can require the ψ_k to be normalized which then results in the orthonormality condition

$$\int dx\ \psi_k^*(x,z)\psi_k'(x,z) = \delta_{kk'}\ . \tag{2.260}$$

Galitskii and Migdal[145] have shown that the energies and lifetimes of QPs are given by the poles of the single-particle propagator defined in (2.117). Using (2.259) this has for instance been discussed by Layzer[146] and Sham and Kohn.[144] Good discussion can also be found in ref. [138] and ref. [127]. If the equation

$$z - E_k(z) = 0 \tag{2.261}$$

has a solution, (2.236) has a pole in the complex plane. This signifies a true eigenstate of the $N+1$ or $N-1$ particle system, where the real part of z (or equivalently $E_k(z)$) can be identified with the energy of the QP while the imaginary part is proportional to the lifetime of the QP. In case the imaginary part of $E_k(z)$ is zero, the lifetime of the QP is infinite. It is also possible that (2.261) does not have a solution. In that case, one can search for the z which minimizes the residual of (2.259)

$$\min\left(z - E_k(z)\right)\ , \tag{2.262}$$

which then signify approximate eigenstates of the $N\pm1$ particle system.

The many-body eigenstates of an interacting system are not Slater determinants and therefore the eigenstates of (2.259) can not be interpreted as single-particle orbitals. However, the basic idea of perturbation theory was to transform the non-interacting particles into approximately non-interacting QPs. Therefore, we can think of the eigenstates of (2.259) as approximate single QP orbitals. The quality of this approximation can be quantified by calculating the norm of the QP orbital: We can ask to what extend the state $\Psi_k^{(N+1)}$ can be regarded as a single-particle excitation from the ground state. That is, we need to choose a (normalized) non-interacting single particle state ϕ_i in a way that the overlap

$$\left\langle \Psi_k^{(N+1)} \middle| \hat{c}_\phi^\dagger \middle| \Psi_k^{(N)} \right\rangle$$

is maximized, with the definition

$$\hat{c}_\phi^\dagger = \int dx \phi^*(x)\hat{\Psi}^\dagger(x)\ .$$

This translates into the condition

$$\|\psi_k\| = \max_\phi \left\{ \left\langle \Psi_k^{(N+1)} \middle| \hat{c}_\phi^\dagger \middle| \Psi_k^{(N)} \right\rangle\ ,\quad \|\phi\| = 1 \right\}\ . \tag{2.263}$$

The QP orbital corresponding to an excitation creating the $N+1$ ($N-1$) single-particle state is therefore the ψ_k which is created by injecting an electron into (removing an electron from) the orbital ϕ which maximizes its norm. Strictly speaking, the validity of the single QP picture implies the existence of a ϕ such that $\|\psi_k\| = 1$, since by construction there is a one-to-one correspondence between the QP states and the excited many-body states of the $N \pm 1$ particle states. This is equivalent to saying that the $N \pm 1$ can be represented by a single Slater determinant made of QP orbitals. For weakly correlated systems, we expect the single QP picture to be valid to a very good approximation and therefore we expect that here is one QP orbital with norm almost equal to 1.[34,138] In case the imaginary part of the self-energy is zero, the dual basis and the basis of QP states become equal since Σ becomes Hermitian and therefore (2.260) implies the existence of a QP state with norm exactly equal to 1. This observation is important for the approximations to Σ we will introduce below. Before we do so, we discuss the properties of the 2-particle Green's function.

2.3.2 The two-particle Green's function

The non-interacting 2-particle Green's function has been defined in (2.118) and is repeated here for completeness

$$G_2(1,2,1',2') = -\left\langle \Phi_0^{(N)} \middle| \mathcal{T}\left[\hat{\psi}(1)\hat{\psi}(2)\hat{\psi}^\dagger(2')\hat{\psi}^\dagger(1')\right] \middle| \Phi_0^{(N)} \right\rangle . \tag{2.264}$$

We are here only interested in the description of the process in which a hole below the chemical potential and an electron above the chemical potential are simultaneously created at $t = t_{1'} = t_1^+$ which are then both destroyed at $t = t_{2'} = t_2^+$. We can then define the electron-hole propagators,

$$G_{eh}^{>}(1,2,1',2') = \left\langle \Phi_0^{(N)} \middle| \mathcal{T}\left[\hat{\psi}^\dagger(1')\hat{\psi}(1)\hat{\psi}^\dagger(2')\hat{\psi}(2)\right] \middle| \Phi_0^{(N)} \right\rangle \Big|_{\substack{t_{1'}=t_1^+ \\ t_{2'}=t_2^+}} \tag{2.265}$$

and

$$G_{eh}^{<}(1,2,1',2') = \left\langle \Phi_0^{(N)} \middle| \mathcal{T}\left[\hat{\psi}^\dagger(2')\hat{\psi}(2)\hat{\psi}^\dagger(1')\hat{\psi}(1)\right] \middle| \Phi_0^{(N)} \right\rangle \Big|_{\substack{t_{1'}=t_1^+ \\ t_{2'}=t_2^+}} , \tag{2.266}$$

which are the building blocks of the time-ordered electron-hole Green's function. In particular, we have

$$G_{eh}^{>}(1,2,1',2') = G_{eh}^{<}(1',2',1,2) . \tag{2.267}$$

This object is similar to the single-particle Green's function with the only difference that electron-hole pairs are Bosons. Therefore, using (2.52) the time-ordered electron-hole Green's function is defined by

$$\begin{aligned} G_{eh}(1,2,1',2') =& \Theta(t_1 - t_2) G_{eh}^{>}(x_1, x_{1'}; x_2, x_{2'}, t_1 - t_2) \\ &+ \Theta(t_2 - t_1) G_{eh}^{<}(x_1, x_{1'}; x_2, x_{2'}, t_1 - t_2) . \end{aligned} \tag{2.268}$$

Using the same arguments leading to (2.209), we can now use (2.46) to obtain the Lehmann representation of (2.268). For instance, for the greater contribution we have

$$\begin{aligned} G^{>}_{eh}(1,1',2,2') =& -\sum_{S}^{\infty} \left\langle \Psi_0^{(N)} \middle| e^{-i\hat{H}t_1}\hat{\psi}^\dagger(x_{1'})\hat{\psi}(x_1)e^{i\hat{H}t_1} \middle| \Psi_S^{(N')} \right\rangle \\ & \times \left\langle \Psi_S^{(N')} \middle| e^{-i\hat{H}t_2}\hat{\psi}^\dagger(x_{2'})\hat{\psi}(x_2)e^{i\hat{H}t_2} \middle| \Psi_0^{(N)} \right\rangle \\ =& -\sum_{S} e^{-i(t_1-t_2)\left(E_S^{(N)}-E_0^{(N)}\right)} \left\langle \Psi_0^{(N)} \middle| \hat{\psi}^\dagger(x_{1'})\hat{\psi}(x_1) \middle| \Psi_S^{(N)} \right\rangle \\ & \times \left\langle \Psi_S^{(N)} \middle| \hat{\psi}(x_{2'})\hat{\psi}^\dagger(x_2) \middle| \Psi_0^{(N)} \right\rangle \ , \end{aligned} \tag{2.269}$$

where we have used for the last equation that the 2-particle Green's function only contain pairs of creation and anihilation operators in each factor so that only N-particle states remain. Therefore, the exponential in the last equation only contains the energy differences of the system in its ground and excited states. From now on, we abbreviate the 2-particle Lehman-amplitudes as

$$\chi_S(x_1,x_{1'}) = \left\langle \Psi_0^{(N)} \middle| \hat{\psi}^\dagger(x_{1'})\hat{\psi}(x_1) \middle| \Psi_S^{(N)} \right\rangle \ . \tag{2.270}$$

In practice, we will be interested in the time-ordered generalized susceptibilities, defined by (2.152). The time-ordered electron-hole generalized susceptibility becomes

$$\chi_{eh}(1,2,1',2') = iG_{eh}(1,2,1',2') - i \lim_{t_{1'}\to t_1^+} G(1,1') \lim_{t_{2'}\to t_2^+} G(2,2') \ . \tag{2.271}$$

Due to the equal-time limits in the single-particle Green's function, they reduce to 1-particle density matrices,

$$n(x_1,x_{1'}) = \left\langle \Psi_0^{(N)} \middle| \hat{\psi}(x_1)\hat{\psi}^\dagger(x_{1'}) \middle| \Psi_0^{(N)} \right\rangle \ .$$

Inserting this result together with (2.269) into (2.271) and using (2.270) and (2.267), we obtain

$$\begin{aligned} \chi_{eh}(1,2,1',2') =& i\Theta(t_1-t_2)G^{>}_{eh}(1,2,1',2') + i\Theta(t_2-t_1)G^{<}_{eh}(1,2,1',2') \\ & - i \lim_{t_{1'}\to t_1^+} G(1,1') \lim_{t_{2'}\to t_2^+} G(2,2') \\ =& i\Theta(t_1-t_2)G^{>}_{eh}(1,2,1',2') + i\Theta(t_2-t_1)G^{>}_{eh}(1',2',1,2) \\ & - i \lim_{t_{1'}\to t_1^+} G(1,1') \lim_{t_{2'}\to t_2^+} G(2,2') \\ =& -i\Theta(t_1-t_2) \sum_{S\neq 0} e^{-i(t_1-t_2)\left(E_S^{(N)}-E_0^{(N)}\right)} \chi_S(x_1,x_{1'})\chi_S^*(x_{2'},x_2) \\ & - i\Theta(t_2-t_1) \sum_{S\neq 0} e^{-i(t_2-t_1)\left(E_S^{(N)}-E_0^{(N)}\right)} \chi_S^*(x_2,x_{2'})\chi_S(x_{1'},x_1) \ , \end{aligned} \tag{2.272}$$

i.e. the contribution from $E_0^{(N)} - E_0^{(N)}$ drops out due to the static contribution in χ. Introducing the abbreviations

$$\Omega_S = E_n^{(N)} - E_0^{(N)} \ ,$$

and going to imaginary time ($it_1 - it_2 = \tau$) we can rewrite the last expression more compactly as

$$\begin{aligned} \chi_{eh}(1,2,1',2') = &- i\Theta(\tau) \sum_{S\neq 0} e^{-\Omega_S \tau} \chi_S(x_1, x_{1'}) \chi_S^*(x_{2'}, x_2) \\ &- i\Theta(-\tau) \sum_{S\neq 0} e^{-\Omega_S \tau} \chi_S^*(x_2, x_{2'}) \chi_S(x_{1'}, x_1) \ . \end{aligned} \tag{2.273}$$

The imaginary frequency representation is obtained from (2.231), where we use again (2.232),

$$\begin{aligned} &\chi_{eh}(x_1, x_2, x_{1'}, x_{2'}, i\omega) = -i \int d\tau \ \chi_{eh}(x_1, x_2, x_{1'}, x_{2'}, i\tau) e^{i\omega\tau} \\ &= -i \int_0^\infty d\tau \ \chi_{eh}(x_1, x_2, x_{1'}, x_{2'}, i\tau) e^{i\omega\tau} - i \int_0^\infty d\tau \ \chi_{eh}(x_1, x_2, x_{1'}, x_{2'}, -i\tau) e^{-i\omega\tau} \ . \end{aligned} \tag{2.274}$$

We thus obtain

$$\begin{aligned} \chi_{eh}(x_1, x_2, x_{1'}, x_{2'}, i\omega) = &- \int_0^\infty d\tau \ \sum_{S\neq 0} \chi_S(x_1, x_{1'}) \chi_S^*(x_{2'}, x_2) e^{-(\Omega_S - i\omega)\tau} \\ &- \int_0^\infty d\tau \ \sum_{S\neq 0} \chi_S(x_2, x_{2'}) \chi_S^*(x_{1'}, x_1) e^{-(i\omega - \Omega_S)\tau} \\ = &\sum_{S\neq 0} \frac{\chi_S(x_1, x_{1'}) \chi_S^*(x_{2'}, x_2)}{i\omega - \Omega_S} - \sum_{S\neq 0} \frac{\chi_S(x_2, x_{2'}) \chi_S^*(x_{1'}, x_1)}{i\omega + \Omega_S} \ . \end{aligned} \tag{2.275}$$

We also need a corresponding expression for the non-interacting generalized susceptibility (2.153).

$$\chi_{eh}^{(0)}(1,2,1',2') = \lim_{t_{1'}\to t_1^+} \lim_{t_{2'}\to t_2^+} \chi^{(0)}(1,2,1',2') = -i \lim_{t_{1'}\to t_1^+} \lim_{t_{2'}\to t_2^+} G(1,2') G(2,1') \ .$$

Here, the Lehmann amplitudes can be expressed analytically using the imaginary time representation of the single-particle Green's function (2.227),

$$\begin{aligned}
\chi^{(0)}_{eh}(x_1,x_2,x_{1'},x_{2'},i\tau) =& -iG(1,2')G(2,1') \\
=& -i\left[\Theta(\tau)G_>(x_1,x_{2'},\tau)-\Theta(-\tau)G_<(x_{2'},x_1,\tau)\right] \\
& \times\left[\Theta(-\tau)G_>(x_2,x_{1'},-\tau)-\Theta(\tau)G_<(x_{1'},x_2,-\tau)\right] \\
=& \, i\Theta(\tau)G_>(x_1,x_{2'},\tau)G_<(x_{1'},x_2,-\tau) \\
& + i\Theta(-\tau)G_<(x_{2'},x_1,\tau)G_>(x_2,x_{1'},-\tau) \\
=& -i\Theta(\tau)\sum_{kk'} e^{-(E^{(+)}_k-E^{(-)}_{k'})\tau}\psi_{+,k}(x_1)\psi^*_{+,k}(x_{2'})\psi^*_{-,k'}(x_{1'})\psi_{-,k'}(x_2) \\
& - i\Theta(-\tau)\sum_{kk'} e^{-(E^{(-)}_k-E^{(+)}_{k'})\tau}\psi^*_{-,k}(x_{2'})\psi_{-,k}(x_1)\psi_{+,k'}(x_2)\psi^*_{+,k'}(x_{1'}) \, .
\end{aligned} \tag{2.276}$$

The corresponding imaginary frequency representation can then again be obtained using (2.232). We will postpone this discussion to the next chapter where we will recast the BSE for the generalized susceptibility as an effective 2-particle Problem. Repeating the derivation (2.276) and using (2.229), we obtain

$$\begin{aligned}
& \chi^{(0)}_{eh}(x_1,x_2,x_{1'},x_{2'},i\tau) = -iG^{(0)}(1,2')G^{(0)}(2,1') \\
=& \, i\Theta(\tau)G^{(0)}_>(x_1,x_{2'},\tau)G^{(0)}_<(x_{1'},x_2,-\tau) + i\Theta(-\tau)G^{(0)}_<(x_{2'},x_1,\tau)G^{(0)}_>(x_2,x_{1'},-\tau) \\
=& -i\Theta(\tau)\sum_{kk'}\Theta(\epsilon_k-\mu)\Theta(\mu-\epsilon_{k'})e^{-(\epsilon_k-\epsilon_{k'})\tau}\phi_k(x_1)\phi^*_k(x_{2'})\phi^*_{k'}(x_{1'})\phi_{k'}(x_2) \\
& - i\Theta(-\tau)\sum_{kk'}\Theta(\epsilon_{k'}-\mu)\Theta(\mu-\epsilon_k)e^{-(\epsilon_{k'}-\epsilon_k)\tau}\phi^*_{k'}(x_{2'})\phi_{k'}(x_1)\phi_k(x_2)\phi^*_k(x_{1'}) \, ,
\end{aligned} \tag{2.277}$$

for the imaginary time representation of $\chi^{(0)}$. Using the definition of the polarizability

$$P^{(0)}(x_1,x_2,i\tau) = \chi^{(0)}_{eh}(x_1,x_2,x_{1'},x_{2'},i\tau)\delta(x_1,x_{1'})\delta(x_2,x_{2'}) \, , \tag{2.278}$$

we obtain

$$\begin{aligned}
P^{(0)}(x_1,x_2,i\tau) =& -i\Theta(\tau)\sum_{kk'}\Theta(\epsilon_k-\mu)\Theta(\mu-\epsilon_{k'})e^{-(\epsilon_k-\epsilon_{k'})\tau}\phi_k(x_1)\phi^*_k(x_2)\phi^*_{k'}(x_1)\phi_{k'}(x_2) \\
& - i\Theta(-\tau)\sum_{kk'}\Theta(\epsilon_{k'}-\mu)\Theta(\mu-\epsilon_k)e^{-(\epsilon_{k'}-\epsilon_k)\tau}\phi^*_{k'}(x_2)\phi_{k'}(x_1)\phi_k(x_2)\phi^*_k(x_1) \, .
\end{aligned} \tag{2.279}$$

For the numerical evaluation of the polarizability for closed-shell systems it is useful to integrate out spin from the beginning. Also for some of the following derivations it is convenient to work

with $P^{(0)}(\boldsymbol{r},\boldsymbol{r}',i\tau)$ instead of $P^{(0)}(x,x',i\tau)$. Using eqs. (2.9) and (2.10) we obtain

$$\begin{aligned}P^{(0)}(\boldsymbol{r}_1,\boldsymbol{r}_2,i\tau) =& -i\Theta(\tau)\sum_{kk'}\sum_{\sigma=\alpha,\beta}\sum_{\sigma'=\alpha,\beta}\Theta(\epsilon_k-\mu)\Theta(\mu-\epsilon_{k'})e^{-(\epsilon_k-\epsilon_{k'})\tau}\\ &\times\phi_k(\boldsymbol{r}_1)\phi_k^*(\boldsymbol{r}_2)\phi_{k'}^*(\boldsymbol{r}_1)\phi_{k'}(\boldsymbol{r}_2)\underbrace{s_k(\sigma_1)s_k^*(\sigma_2)}_{\delta_{\sigma,\sigma'}}\underbrace{s_{k'}^*(\sigma_1)s_{k'}(\sigma_2)}_{\delta_{\sigma,\sigma'}}\\ &-i\Theta(-\tau)\sum_{kk'}\sum_{\sigma=\alpha,\beta}\sum_{\sigma'=\alpha,\beta}\Theta(\epsilon_{k'}-\mu)\Theta(\mu-\epsilon_k)e^{-(\epsilon_{k'}-\epsilon_k)\tau}\\ &\times\phi_{k'}^*(\boldsymbol{r}_2)\phi_{k'}(\boldsymbol{r}_1)\phi_k(\boldsymbol{r}_2)\phi_k^*(\boldsymbol{r}_1)\underbrace{s_{k'}^*(\sigma_2)s_{k'}(\sigma_1)}_{\delta_{\sigma,\sigma'}}\underbrace{s_k(\sigma_2)s_k^*(\sigma_1)}_{\delta_{\sigma,\sigma'}},\end{aligned}\tag{2.280}$$

which shows that the polarizability is diagonal in spin

$$\begin{aligned}P^{(0)}(\boldsymbol{r}_1,\boldsymbol{r}_2,i\tau) =& \sum_{kk'}-i\Theta(\tau)\sum_{\sigma=\alpha,\beta}\Theta(\epsilon_k-\mu)\Theta(\mu-\epsilon_{k'})e^{-(\epsilon_k-\epsilon_{k'})\tau}\\ &\times\phi_k(\boldsymbol{r}_1,\sigma)\phi_k^*(\boldsymbol{r}_2,\sigma)\phi_{k'}^*(\boldsymbol{r}_1,\sigma)\phi_{k'}(\boldsymbol{r}_2,\sigma)\\ &-i\Theta(-\tau)\sum_{kk'}\sum_{\sigma=\alpha,\beta}\Theta(\epsilon_{k'}-\mu)\Theta(\mu-\epsilon_k)e^{-(\epsilon_{k'}-\epsilon_k)\tau}\\ &\times\phi_{k'}^*(\boldsymbol{r}_2,\sigma)\phi_{k'}(\boldsymbol{r}_1,\sigma)\phi_k(\boldsymbol{r}_2,\sigma)\phi_k^*(\boldsymbol{r}_1,\sigma).\end{aligned}\tag{2.281}$$

We will therefore often use the expression

$$P^{(0)}(\boldsymbol{r}_1,\boldsymbol{r}_2,i\tau)=\sum_{\sigma=\alpha,\beta}P^{(0)}(\boldsymbol{r}_1,\boldsymbol{r}_2,\sigma,i\tau)\tag{2.282}$$

2.3.3 One-Body expectation Values and Electron Interaction Energies

As seen before, one-body operators can be written as

$$\hat{A}=\int dx_1dx_2\hat{\psi}^\dagger(x_1)O(x_1,x_2)\hat{\psi}(x_2)\,,\tag{2.283}$$

where O trivially commutes with the fields. We can therefore write

$$\begin{aligned}\left\langle\Psi_0^{(N)}\middle|\hat{A}\middle|\Psi_0^{(N)}\right\rangle =& -i\int dxO(x_1,x_2)\lim_{t_1\to t_2^+}G(x_1,x_2,t_1-t_2)\\ =& -i\int dxO(x_1,x_2)G_<(x_1,x_2,0)\,.\end{aligned}\tag{2.284}$$

For the density matrix, $\rho(x_1,x_2)=\hat{\psi}^\dagger(x_1)\hat{\psi}(x_2)$, we therefore obtain

$$\rho(x_1,x_2)=-iG_<(x_1,x_2,0)\,.\tag{2.285}$$

Given a certain approximation to the self-energy, an expression for the electron-electron interaction energy (which we will often call the Hartree-exchange-correlation energy) follows from (2.174) and multiplication from the left with $\hat{\psi}^\dagger(x,t)$,

$$E_{Hxc}[G] = \left\langle \Psi_0^{(N)} \middle| \hat{V} \middle| \Psi_0^{(N)} \right\rangle = \frac{1}{2} \int dx' \lim_{x \to x', t \to t'} \left[\frac{\partial}{\partial t} + ih(x) \right] G(x, x, t - t') \, . \tag{2.286}$$

The total electronic ground state energy

$$E = E_0 + \left\langle \Psi_0^{(N)} \middle| \hat{V} \middle| \Psi_0^{(N)} \right\rangle$$

is then given by the Galitskii-Migal formula,[145]

$$E = \frac{1}{2} \int dx' \lim_{x \to x', t \to t'} \left[\frac{\partial}{\partial t} - ih(x) \right] G(x, x', t - t') \, . \tag{2.287}$$

2.4 Approximations

Solving eqs. (2.199)–(2.203) exactly is not desirable since this would correspond to an exact solution of the many-body problem which can be obtained much easier by diagonalization of (2.1). Equations (2.199)–(2.203) are useful in situations were they can be truncated at low order in W. The decisive quantity in these equations is the self-energy since it connects the single- and two-particle Green's functions. Approximations are therefore defined by the approximation made for (2.203), i.e. by certain ways to truncate its skeleton expansion. Such approximations are typically referred to as diagrammatic approximations. It turns out that already the evaluation of just a few terms of the skeleton expansion of the self-energy is computationally demanding.

In contrast, non-diagrammatic approximations can not be represented graphically in terms of diagrams. Non-diagrammatic approximations are often derived as certain approximations to diagrammatic approximations, as for instance common approximations to the GW equations which are central to this thesis. These approximations typically consist in combining the GW approximation (or diagrammatic approximations beyond) with KS-DFT, which we will introduce below.

2.4.1 The Hartree-Fock approximation

The HF approximation is one of the oldest approximations in quantum chemistry and its invention predates the outlined formalism by far.[79–82] It consists in approximating the self-energy by

$$\Sigma(1,1') \approx \Sigma^{HF}(1,1') = \Sigma_H(1,1') + \Sigma_x(1,1') \, . \tag{2.288}$$

This approximation to Σ depends neither on the 4-point vertex nor on the 2-particle Green's function. Therefore, it amounts to solving (2.199),

$$G^{HF}(1,1') = G^{(0)}(1,1') + G^{(0)}(1,2)\Sigma^{(0)}_{Hx}(2,3)G^{HF}(3,1') \, . \tag{2.289}$$

The solution of this equation gives access to single-particle excitations and electron-electron interaction energies. Optical absorption spectra are then obtained using the time-dependent (TD) HF approximation with

$$\Gamma^{(0)}_{Hx}(1,2,1',2') = i\frac{\delta\Sigma_{Hx}(1,1')}{\delta G(2',2)} \; . \tag{2.290}$$

The functional derivatives of (2.179) and (2.185) are respectively

$$i\frac{\delta\Sigma_H(1,1')}{\delta G(2',2)} = \delta(1,1')\delta(2',2)W^{(0)}(1,2) \tag{2.291}$$

and

$$i\frac{\delta\Sigma_x(1,1')}{\delta G(2',2)} = \delta(1,1')\delta(1',2)W^{(0)}(1,1') = -\delta(1,1')\delta(1',2)W^{(0)}(1,2) \; , \tag{2.292}$$

leading to

$$\begin{aligned}\chi(1,2,1'2') =& \chi^{(0)}(1,2,1'2') + \chi^{(0)}(1,4,1',3)W^{(0)}(3,5) \\ & \times \left[\delta(3,4)\delta(5,6) - \delta(3,6)\delta(4,5)\right]\chi(6,2,5,2')\end{aligned} \tag{2.293}$$

for (2.200). It can be easily verified that the kernel of this equation fulfills the crossing symmetry (2.172),

$$\begin{aligned}\Gamma^{(0)}_{Hx}(3,5,4,6) =& W^{(0)}(3,5)\left[\delta(3,4)\delta(5,6) - \delta(3,6)\delta(4,5)\right] \\ =& W^{(0)}(3,5)\left[\delta(3,6)\delta(5,4) - \delta(3,4)\delta(5,6)\right] \\ =& -\Gamma^{(0)}_{Hx}(3,5,6,4) \; .\end{aligned} \tag{2.294}$$

This property is important and we will come back to it in section. 2.4.5.

The HF approximation is not very useful by its own since the approximation (2.289) is rather crude. It is typically used as starting point for further approximations using (2.137). The HF self-energy is special since it contains all diagrams of the skeleton series figure 2.1c) which do not depend explicitly on time. In fact, it is also fully determined by the 1-particle reduced density matrix as the following calculation shows,

$$\begin{aligned}\Sigma_{Hx}(1,1') =& -i\delta(1,1')W^{(0)}(1,3)G(3,3^+) + iW^{(0)}(1,1')G(1,1') \\ =& -i\delta(1,1')v^{(0)}_c(\boldsymbol{r}_1,\boldsymbol{r}_3)\delta(t_1-t_3^+)G(3,3^+) + iv_c(\boldsymbol{r}_1,\boldsymbol{r}_{1'})\delta(t_1-t_{1'}^+)G(1,1') \Rightarrow \\ \Sigma_{Hx}(\boldsymbol{r}_1,\boldsymbol{r}_{1'}) =& -i\delta(\boldsymbol{r}_1,\boldsymbol{r}_{1'})\int d\boldsymbol{r}_3 v^{(0)}_c(\boldsymbol{r}_1,\boldsymbol{r}_3)n(\boldsymbol{r}_3) - v_c(\boldsymbol{r}_1,\boldsymbol{r}_{1'})n(\boldsymbol{r}_1,\boldsymbol{r}_{1'}) \; .\end{aligned} \tag{2.295}$$

This calculation also shows that Σ_{Hx} only depends on occupied single-particle states due to the time-ordering in the δ-functions involving t (specified by the plus).

It can be shown that any self-energy approximation which does not depend on time is Hermitian: To see this one first decomposes the self-energy into it skew-Hermtian and Hermitian parts and realizes that the skew-Hermitian part of $\Sigma(\omega)$ changes sign when $\omega = \mu$ (for the rather

complicated details of the proof see ref. [146]). The skew-Hermitian part therefore vanishes for the HF self-energy which has important consequences. In the HF approximation both equations in (2.259) are equivalent (since the self-energy is Hermitian) and the amplitudes become frequency-independent. Therefore, the HF approximation can be formulated as

$$h_1(\boldsymbol{r}_1)\phi_k(\boldsymbol{r}_1) + \int d\boldsymbol{r}_2 \Sigma(x_1, x_2)\phi_k(\boldsymbol{r}_2) = \epsilon_k \phi_k(\boldsymbol{r}_1) \;, \tag{2.296}$$

which is a single-particle problem with exactly the same properties as (2.7) and the associated single-particle Green's function has the same structure as $G^{(0)}$. In fact, the HF approximation is the most complete diagrammatic expansion of the self-energy which retains the picture of non-interacting electrons. This is seen from the most common derivation of the HF equations: the HF equations are often derived by imposing that the many-body wave function can be written as a single Slater determinant and by minimizing the expectation value of the Hamiltonian with respect to the single-particle states under the constraint that they remain orthonormal.

Instead of non-interacting particles, however, the HF equations describes non-interacting QPs whose external potential already contains the most important aspects of electron-electron interaction: The interaction of the electron with the average charge density produced by the other electrons (described by the Hartree term) as well as the exchange interaction which accounts for the antisymmetry of the Fermionic wave function. Therefore, the HF Green's function is a suitable starting point for (2.137). As already indicated in (2.187), the electron-electron interactions which are not described in the HF approximation are typically referred to as electron correlation effects.

Similarly, the part of the electron-electron interaction energy beyond the energy resulting from the HF self-energy is typically referred to as correlation energy. This distinction is somehow arbitrary but makes sense if one uses perturbation theory based on the HF wavefunction. On the other hand, in the self-consistent solution of Dyson's equation beyond the HF approximation to the self-energy, inclusion the higher-order terms will alter the HF density matrix and therefore the Hartree-exchange contribution to the total electron-electron interaction energy will be different than in the HF approximation.

It is instructive to also consider the Hartree-approximation. In this case, (2.296) becomes

$$\left[h_1(\boldsymbol{r}) + \Sigma^H[n(\boldsymbol{r})]\right] \psi_k(\boldsymbol{r}) = \epsilon_k^H \psi_k(\boldsymbol{r}) \;,. \tag{2.297}$$

The Hartree self-energy only depends on the elecron density and therefore (2.297) is even easier to solve than (2.296).

2.4.2 The GW approximation

The GW approximation (GWA) extends the HF approximations by replacing the bare electron-electron interaction v_c by the dynamically screened interaction W. In the GWA, one first calculates the Hartree Green's function

$$G^{\mathrm{H}}(1,2) = G^{(1,2)} + G^{(0)}(1,3)\Sigma_H^{(0)}(3,4)G^{\mathrm{H}}(4,2) \;, \tag{2.298}$$

One then obtains $\Gamma^{(0)}_{xc} = 0$ and $\Gamma^{(0)} = W^{(0)}$. Using these expressions for Γ in eqs. (2.199)–(2.203) one obtains the reduced set of equations

$$G(1,2) = G^{\mathrm{H}}(1,2) + G^{\mathrm{H}}(1,3)\Sigma^{(0)}(3,4)G(4,2) \tag{2.299}$$

$$\chi(1,2,1',2') = \chi^{(0)}(1,2,1',2') + \chi^{(0)}(1,4,1',3)\Gamma^{(0)}_{H}(3,5,4,6)\chi(6,2,5,2') \tag{2.300}$$

$$W(1,2) = W^{(0)}(1,2) + W^{(0)}(1,3)P(3,4)W^{(0)}(3,2) \tag{2.301}$$

$$\Sigma(1,2) = \Sigma_H(1,2) + iG(1,2)W(1^+,2)\ , \tag{2.302}$$

which is typically referred to as the GW approximations since the series expansion of the self-energy in terms of the screened electron-electron interaction[52,67,68] beyond the Hartree terms is truncated after first order in W. From a different point of view, the hierarchy of equations eqs. (2.299)–(2.302) actually comprises two distinct approximations: the truncation of the 4-point vertex in the self-energy (leading to the GW approximation) and of the 4-point vertex in the BSE for χ. The approximation to χ (2.300) is known under several names depending on the context: It is often referred to as time-dependent Hartree approximation since $\Gamma^{(0)}$ is approximated by the functional derivative of the Hartee kernel. It is also termed bubble approximation (Due to the diagrammatic form of the particle-hole bubble in figure 2.5a) which looks like a bubble) or random phase approximation (RPA). The latter approximation is the most common name, even though it is actually a misnomer (see discussion on page 252 of ref. [15]). A common approximation to the correlation energy is also called RPA. To avoid confusion with the expression for the screened electron-electron interaction, we will therefore sometimes refer to the latter one as bubble approximation.

Figure 2.5a) shows how the screened interaction within the RPA is obtained from (2.200) as an expansion in terms of the bare electron-electron interaction,

$$W = v_c + v_c\chi^{(0)}v_c + v_c\chi^{(0)}v_c\chi^{(0)}v_c + \dots\ . \tag{2.303}$$

Physically, (2.202) describes the screening of the electron-electron interaction due to the presence of other electrons. The kernel P, which relates the bare to the screened interaction in (2.202) is completely determined by the generalized susceptibility which describes all scattering processes which can take place between 2 particles. The RPA transforms eq. (2.200) into eq. (2.300) which describes non-interacting particle-hole pairs, interacting though the bare Coulomb interaction.

The self-energy in the GW approximation is shown diagrammatically in figure 2.5. Inserting eq. (2.303) into the expression for the GW self-energy (2.302), one sees that it contains an infinite amount of terms,

$$\Sigma^{GW} = iGW = iGv_c + iGv_c\chi^{(0)}v_c + iGv_c\chi^{(0)}v_c\chi^{(0)}v_c\ , \tag{2.304}$$

with the first term in this expansion being the HF approximation to the self-energy. From the perspective of quantum electrodynamics the HF self-energy describes a QP emitting a bare photon and absorbing it again. In contrast, the GW self-energy describes a QP emitting a renormalized photon and absorbing it again.

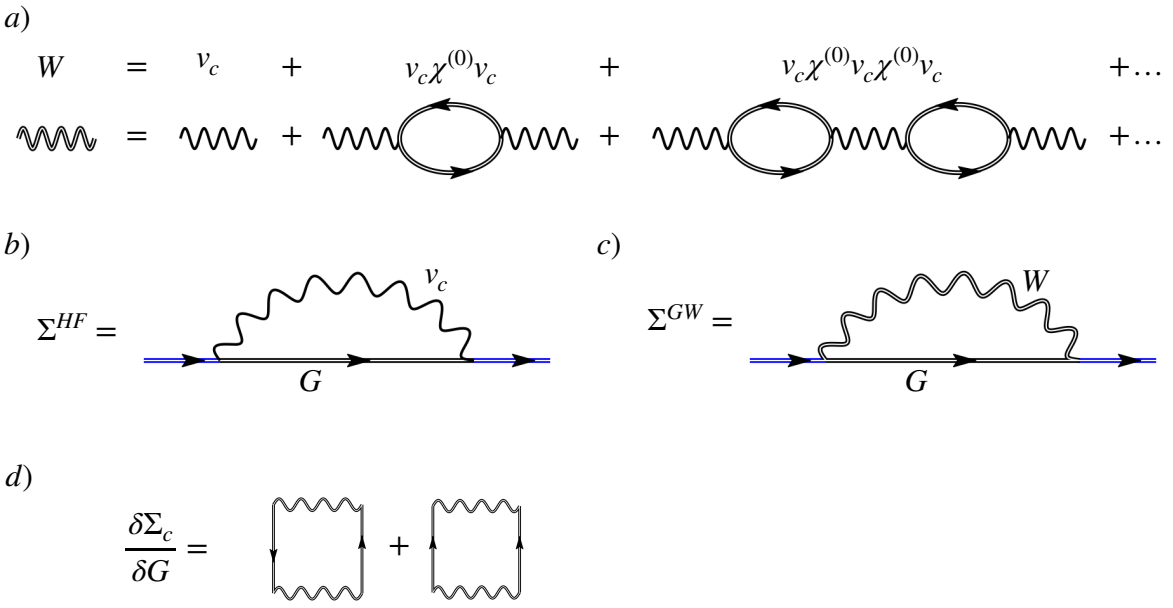

Figure 2.5: a) Diagrammatic representation of the screened electron-electron interaction in the RPA. b) and c): Diagrammatic representations of different approximations to the self-energy beyond the Hartree term. Black parts denote the self-energy contributions which, combined with the blue parts give the single-particle Green's function. b) HF self-energy, c) *GW* self-energy. The HF self-energy is the first term in the expansion of the *GW* self-energy in terms of the *bare* Coulomb interaction d) functional derivative of the self-energy with respect to G, leading to one term in the particle-hole channel and another one in the particle-particle channel.

Generally speaking, already in the static limit, screening dampens the electron-electron interactions at at large distances. We follow Mattuck[112] and show this analytically by considering the homogeneous electron gas. On the reciprocal lattice, the RPA gives the Lindhard formula for the polarizability

$$P(\boldsymbol{q},\omega) = \frac{2i}{(4\pi)^2}\int d\boldsymbol{k}d\omega' \frac{1}{(\omega+\omega'-\epsilon_{k+q}+i\delta_{k+q})(\omega'-\epsilon_k+i\delta_k)} \,. \tag{2.305}$$

In the static limit ($\omega \to 0$) and for large electron-electron separation ($\boldsymbol{r} \to \infty$, i.e. $q \to 0$), one obtains

$$P(\boldsymbol{q}\to 0,\omega=0) = \frac{\lambda^2}{4\pi} \,, \tag{2.306}$$

with

$$\lambda^2 = \frac{6\pi n}{\epsilon_F} \,,$$

with ϵ_F being the Fermi energy and n being the (homogeneous) electron density. Rewriting the Dyson equation for the screened interaction in the RPA (2.202),

$$W(\boldsymbol{q},\omega) = v_c(\boldsymbol{q})\left[1 + v_c(\boldsymbol{q})P^{(0)}(\boldsymbol{q},\omega)\right]^{-1} ,$$

and using the explicit form of the Coulomb interaction in reciprocal space,

$$v_c(\boldsymbol{q}) = \frac{4\pi}{\boldsymbol{q}^2} ,$$

we obtain

$$W(\boldsymbol{q}\to 0,\omega = 0) = \frac{4\pi}{\boldsymbol{q}^2 + \lambda^2} . \tag{2.307}$$

Assuming that (2.307) holds for all $\boldsymbol{q}$, Fourier transformation to real space yields the Yukawa potential (we note again that the potential is isotropic due to the symmetry of the HEG),

$$W(\boldsymbol{r}\to\infty,\omega = 0) = \frac{1}{r}e^{-\lambda r} , \tag{2.308}$$

which is a shielded Coulomb interaction. We have hereby recovered the theory of screening due to Thomas and Fermi, which is indeed the limiting case of the Lindhard screening for large $\boldsymbol{r}$.[147]

We see, that the strength of the screening is proportional to the width of the band gap. The Fermi level can be considered to be a hypothetical energy level, such that at equilibrium this energy level would be occupied at any given time with 50 % probability. When the band gap is large, ϵ_F will be large as well and λ will be small, i.e. the screening is weak. On the other hand, when the band gap is small, ϵ_F will be small as well and λ will be large. In that case, screening of the electron-electron interaction will be strong.

The *GW* Kernel in the BSE

Solving Dyson's equation within the *GW* approximation alone does not give access to excitonic states, since these require the solution of the BSE. In a canonical approach denoted as *GW*-BSE or BSE@*GW*, the *GW* equations with RPA screening eqs. (2.299)–(2.302) are solved and only afterwards one solves the BSE for the generalized susceptibility. As pointed out by Hanke, Strinati and coworkers[148], "No criterion, however, has been supplied to justify this specific decoupling of the set of equations".

Interestingly, the BSE methods for the description of excitonic effects has been pioneered by Hanke and Sham[149–152] (the general prcedure has already been outlined by Sham and Rice in 1966[153]) and a few years later by Strinati and coworkers[148,154–156] prior to the first *GW* calculations by Hybertsen and Louie. Hanke, Sham and Strinati did not use *GW* QP energies as input for their BSE calculations but rather used empirical parameters or a simplified HF scheme.[148] The first BSE@*GW* calculations in which *GW* QP were used were only carried out much later by Onida *et. al.* for the sodium tetramer[157] and by Rohlfing and Louie for silicon clusters.[158]

The 4-point vertex function within the GW approximation is given as

$$\Gamma^{(0)^{GW}}_{Hxc}(1,2,1',2') = i\frac{\delta\Sigma^{GW}(1,1')}{\delta G(2',2)} \, . \tag{2.309}$$

The first term in this kernel describes the particle-hole exchange and the second-one the Coulombic particle-hole attraction. Thus, in contrast to the TD-HF approximation, the GW kernel contains the information that the attraction between electrons and holes is screened and therefore weaker than without screening. Fore this reason, the excitonic binding energies calculated within BSE@GW will be lower than within TD-HF. Working out the functional derivative, we obtain

$$\begin{aligned}\Gamma^{(0)^{GW}}_{Hxc}(1,2,1',2') =& i\frac{\delta\Sigma^{GW}(1,1')}{\delta G(2',2)} = i\frac{\delta\left[iG(1,1')W(1^+,1')\right]}{\delta G(2',2)} \\ =& -\frac{\delta G(1,1')}{\delta G(2',2)}W(1^+,1') - G(1,1')\frac{\delta W(1^+,1')}{\delta G(2',2)}\end{aligned} \tag{2.310}$$

Using

$$\frac{\delta G(1,1')}{\delta G(2',2)} = \delta(1,2')\delta(1',2) \, , \tag{2.311}$$

the first term is

$$-\frac{\delta G(1,1')}{\delta G(2',2)}W(1^+,1') = -\delta(1,2')\delta(1',2)W(1,1') \tag{2.312}$$

For the second term, we use the definition of W (2.198) with W calculated in the RPA and obtain

$$\begin{aligned}\frac{\delta W(1,1')}{\delta G(2',2)} =& W^{(0)}(1,3)\frac{\delta P(3,3')}{\delta G(2',2)}W(3',1') + W^{(0)}(1,3)P(3,3')\frac{\delta W(3',1')}{\delta G(2',2)} \\ =& W^{(0)}(1,3)\frac{\delta P(3,3')}{\delta G(2',2)}W(3',1') \\ &+ W^{(0)}(1,3)P(3,3')W^{(0)}(3',4)\frac{\delta P(4,4')}{\delta G(2',2)}W(4',1') \\ &+ W^{(0)}(1,3)P(3,3')W^{(0)}(3',4)P(4,4')\frac{\delta W(4',1')}{\delta G(2',2)} \\ =& \left[W^{(0)}(1,3) + W^{(0)}(1,3)P(3,3')W^{(0)}(3',4)\dots\right] \\ &\times\left[\frac{\delta P(4,4')}{\delta G(2',2)}W(4',1') + P(4,4')\frac{\delta W(4',1')}{\delta G(2',2)}\right] \\ =& W(1,3)\frac{\delta P(3,3')}{\delta G(2',2)}W(3',1') \\ =& -i\delta(3,2')\delta(3',2)W(1,3)G(3',3)W(3',1') \\ &- i\delta(3',2')\delta(3,2)W(1,3)G(3,3')W(3',1') \, .\end{aligned} \tag{2.313}$$

Using this result as well as (2.312), we obtain the GW kernel of the form

$$\begin{aligned}\Gamma_{Hxc}^{(0)^{GW}}(1,2,1',2') =& \delta(1,1')\delta(2,2')W^{(0)}(1,2) - \delta(1,2')\delta(1',2)W(1,1') \\ &+ i\delta(3,2')\delta(3',2)G(1,1')W(1,3)G(3',3)W(3',1') \\ &+ i\delta(3',2')\delta(3,2)G(1,1')W(1,3)G(3,3')W(3',1') \ .\end{aligned} \tag{2.314}$$

This shows that the variation of the screened interaction with respect to the single-particle Green's function generated two diagrams of second order in W, one in the particle-particle and the other in the particle-hole channel as can be seen from their diagrammatic representation in figure 2.5d). In applications of the BSE@GW method to optical excitations they are always neglected. We will come back to these terms in section 2.4.5.

To first order in the screened Coulomb interaction, the 4-point vertex assumes the same form as in the time-dependent HF equations (2.293). If we only keep the first-order term in (2.314), we obtain an expression similar to (2.293),

$$\begin{aligned}\chi(1,2,1'2') =& \chi^{(0)}(1,2,1'2') + \chi^{(0)}(1,4,1',3) \\ &\times \Big[W^{(0)}(3,5)\delta(3,4)\delta(5,6) - W(3,5)\delta(3,6)\delta(4,5)\Big]\,\chi(6,2,5,2') \ .\end{aligned} \tag{2.315}$$

This vertex does not fulfill (2.172), however, inserting (2.303) into (2.315) one sees that (2.172) is fulfilled to first order in $W^{(0)}$. To first order in $W^{(0)}$, the first-order GW vertex is of course the HF vertex. When only the static limit of W is considered, (2.315) is considerably simplified and becomes technically equivalent to (2.293),

$$\begin{aligned}\chi(1,2,1'2') =& \chi^{(0)}(1,2,1'2') + \chi^{(0)}(1,4,1',3) \\ &\times \Big[W^{(0)}(3,5)\delta(3,4)\delta(5,6) - W(3,5)\delta(3,6)\delta(4,5)\delta(t_3-t_5)\Big] \\ &\times \chi(6,2,5,2') \ .\end{aligned} \tag{2.316}$$

Practical applications are almost exclusively based on eq. (2.316) and for real materials or molecules, only few calculations beyond the static approximation have been performed.[159–161] Typically, these dynamical effects have then been included perturbatively.[162,163] The few studies which scrutinized the role of the dynamical contributions on optical excitation energies[128,164,165] revealed that retaining the dynamical screening effects creates poles in the generalized susceptibility beyond the ones obtained from (2.316) which describe for instance excited states with multiple-excitation character[128] or QP damping.[164]

2.4.3 Kohn–Sham Density Functional Theory

KS-DFT allows to formally replace the exact self-energy (2.203) by a local, Hermitian and time-dependent potential which only depends on the electron density alone,

$$\Sigma(1,1') \to v_{Hxc}(\boldsymbol{r})\,[n(\boldsymbol{r})] \ .$$

The foundations of KS-DFT are due to Kohn and coworkers.[77,78,136] Hohenberg and Kohn could prove, that the ground state of the interacting N-electron system is uniquely determined by the density $n(\boldsymbol{r})$. In a next step, they showed that the density of the interacting system can be obtained by solving a non-interacting single-particle problem. The decisive quantity is v_{Hxc} which takes the role of the self-energy and maps the density of the non-interacting system (the one described by h_1) to the one of the KS-system,

$$v_{Hxc} : n_0(\boldsymbol{r}) \mapsto n(\boldsymbol{r}) \ , \tag{2.317}$$

in the same way as the self-energy maps the non-interacting single-particle Green's function to the interacting one,

$$\Sigma(\boldsymbol{r}, \boldsymbol{r}', \omega) : G_0(\boldsymbol{r}, \boldsymbol{r}', \omega) \mapsto G(\boldsymbol{r}, \boldsymbol{r}', \omega) \ . \tag{2.318}$$

Using the representation of the density in terms of the single-particle states,

$$n(\boldsymbol{r}) = \sum_k \Theta(\mu - \epsilon_k)\phi_k(\boldsymbol{r})\phi_k^*(\boldsymbol{r}) \ ,$$

one can easily see that the KS equations can be written as a Dyson-type equations of the form (2.297) since the potential is local.

The KS potential can be found formally by taking the limits $\boldsymbol{r}_1 \to \boldsymbol{r}_2$ and $t \to 0$ in (2.199) and summing over spin. The resulting equations are the Sham-Schlüter equations (SSE).[110,166] In frequency space,

$$\begin{aligned} n(\boldsymbol{r}) - n_0(\boldsymbol{r}) =& 2\int d\boldsymbol{r}_3 d\boldsymbol{r}_4 \int d\omega G^{(0)}(\boldsymbol{r}, \boldsymbol{r}_3, \omega)\Sigma(\boldsymbol{r}_3, \boldsymbol{r}_4, \omega)G(\boldsymbol{r}_4, \boldsymbol{r}, \omega) \\ \stackrel{!}{=}& 2\int d\boldsymbol{r}_3 d\boldsymbol{r}_4 \int d\omega G^{(0)}(\boldsymbol{r}, \boldsymbol{r}_3, \omega)v_{Hxc}(\boldsymbol{r}_3)\delta(\boldsymbol{r}_3 - \boldsymbol{r}_4)G(\boldsymbol{r}_4, \boldsymbol{r}, \omega) \\ =& 2\int d\boldsymbol{r} \int d\omega G^{(0)}(\boldsymbol{r}, \boldsymbol{r}', \omega)v_{Hxc}(\boldsymbol{r}')G(\boldsymbol{r}', \boldsymbol{r}, \omega) \ . \end{aligned} \tag{2.319}$$

$n(\boldsymbol{r}) - n_0(\boldsymbol{r})$ is the difference in the electron density of the interacting and the non-interacting system. In principle, we can therefore find the exact v_{Hxc} by inversion. When Σ is replaced by v_{Hxc}, the Dyson equation (2.131) assumes the same form as (2.297).

The linearised Dyson-equation (2.138) leads to the linearized SSE (LSSE)[110],

$$\begin{aligned} n(\boldsymbol{r}) - n_0(\boldsymbol{r}) &\approx \int d\boldsymbol{r} \int d\omega G^{(0)}(\boldsymbol{r}, \boldsymbol{r}', \omega)v_{Hxc}(\boldsymbol{r}')G^{(0)}(\boldsymbol{r}', \boldsymbol{r}, \omega) \\ &= 2i \int d\boldsymbol{r}' \int d\omega P^{(0)}(\boldsymbol{r}, \boldsymbol{r}', \omega)v_{Hxc}(\boldsymbol{r}') \ , \end{aligned} \tag{2.320}$$

which is often used to construct approximations to v_{Hxc}[167–169]. Whenever the *l.h.s.* of (2.320) is known, the corresponding v_{Hxc} can be obtained by inversion of the non-interacting polarizability $P^{(0)}$ (this is not straightforward in practice since strictly speaking the inverse of density-density

response is ill-defined, see ref. [170] for details). Furthermore, in case of a static approximation to the self-energy, the frequency integral can be solved analytically. When the HF approximation to the self-energy is used, one obtains a potential which is typically referred to as the optimized effective potential (OEP).[136,170,171] Sometimes, the resulting local potential is referred to as exact exchange (exx), but this needs to be carefully distinguished from the non-local Hartree-Fock self-energy which is also sometimes referred to as exx. We also briefly note that within a static approximation to the GW self-energy, (2.320) leads to the so-called RPA-OEP method. This approach has been pioneered by Casida[172] and is closely related (see for instance ref. [173] or ref. [168]) to the quasi-particle self-consistent GW (qsGW) method[142,174–177] which we will introduce in section 2.4.4.

KS-DFT gives access to all properties which directly depend on the density. However, it does not allow to obtain an interacting Green's function (There is no v_{Hxc} which maps G_0 to G) and therefore it does not allow for the description of single-particle excitations. However, there is one important exception: The negative of the highest occupied molecular orbital energy (HOMO) of a finite system equals its ionization potential.[178,179]

Furthermore, there exists an extension of DFT to time-dependent densities, the so-called time-dependent (TD) DFT.[180] In frequency-space, TD-DFT allows to formulate a Dyson equation for the density-density response,[136] and the poles of the interacting density-density response can be identified with the excitonic states of the $N-$electron system, in exactly the same way as the poles of (2.275). In contrast to the 4-point vertex in the BSE, the kernel of this Dyson equation f_{Hxc} is local and is obtained by variation of v_{Hxc} with respect to the density,

$$f_{Hxc}(1,2) = \frac{\delta v_{Hxc}(1)}{\delta n(2)} \ ,$$

which is split in Hartree, exchange, and correlation contributions $f_{Hxc} = f_H + f_x + f_c$. In practice, DFT comes with the major shortcoming that the construction of v_{Hxc} via (2.319) is very demanding and also not always useful in practice since it requires knowledge of Σ. Therefore, one is forced to use approximate potentials. The search for an appropriate mappings $\Sigma \mapsto v_{Hxc}$ is a very active field of research and countless approximations have been developed in the last decades[181] Despite the many available approximations, they can be put on certain rungs of increasing complexity according to their basic ingredients. We give a brief overview in the following.

Local density approximation Possibly the oldest approximation to v_{xc} is the family of local density approximations (LDA)[78] in which the xc potential only depends on the value of the electron density at each point in space.[136] While the exchange-component of the LDA is known exactly,[136] different approximate expressions are available for the correlation part. The most popular ones have been developed by Vosko, Wilk, and Nusair.[182]

(Meta-)Generalized Gradient Approximation Another popular approximation is the so-called generalized gradient approximations which have already been developed in the 1960s

shortly after the work of Kohn and Sham.[183,184] The approximations used today have mostly been developed by Becke[185–187] and Perdew and coworkers.[188–190] The functionals developed by Perdew in 1986 (P86) and by Perdew, Burke and Ernzerhof (PBE)[189,190] are also used in this thesis. The resulting equations are equivalent to (2.297). Additionally, such functionals can depend on the Laplacian of the density. These functionals are then called meta-GGAs, a popular example being the functional developed by Tao, Perdew, Staroverov and Scuseria (TPSS).[191]

Hybrid functionals One often mixes such a v_{Hxc} with a portion of Σ_x. Such functionals are typically referred to as hybrid functionals,

$$v^{hyb}_{Hxc}(\boldsymbol{r},\boldsymbol{r}') = \Sigma_H(\boldsymbol{r})\delta(\boldsymbol{r}-\boldsymbol{r}') + \alpha\Sigma_x(\boldsymbol{r},\boldsymbol{r}') + (1-\alpha)v_x(\boldsymbol{r})\delta(\boldsymbol{r}-\boldsymbol{r}') + v_c(\boldsymbol{r})\delta(\boldsymbol{r}-\boldsymbol{r}') \tag{2.321}$$

The resulting equations are equivalent to (2.296). For many purposes the resulting Green's function, typically called Kohn–Sham Green's function serves as a better starting point in (2.137) than the HF one. For instance, the combination of the PBE functional with exact exchange is called PBE0, which is used in this work as well.[192,193] Another popular example denoted as M06-2X has been developed by Truhlar and coworkers.[194] Hybrid functionals can also be constructed starting from meta-GGAs. For example, combining TPSS with exact exchange leads to TPSSh.[195] Such hybrid functionals are typically referred to as meta-hybrids.

In the extension of such functionals to TD-DFT, one then uses an xc contribution to the 4-point vertex of the form

$$\begin{aligned}\Gamma^h_{xc}(1,2,1',2') = &\left[(1-\alpha)f_x(1,1') + f_c(1,1')\right]\delta(1,2)\delta(1',2') \\ &+ \alpha\Sigma_x(1,2,1',2')\ ,\end{aligned}$$

so that one needs to solve the BSE for the generalized susceptibility instead of the Dyson equation for the density-density response in case of a (meta-)GGA calculation.

range-separated hybrid functionals For many purposes, for instance for the purpose of calculating single-particle excitation energies, it is useful to combine the GGA and the hybrid concept into a single functional through the concept of range-separation.[196,197] One uses the identity

$$\frac{1}{r} = \frac{1-f(\mu r)}{r} + \frac{f(\mu r)}{r}\ , \tag{2.322}$$

to decompose the Coulomb interaction into a short-range (first term) and a long-range part (second term). Any function f which satisfies the boundary conditions

$$f(0) = 0 \quad \lim_{|r|\to\infty} f(r) = 1 \tag{2.323}$$

can be used in principle. The error function (erf) is typically used for range-separated hybrid functionals (RSHs). One then typically uses the HF self-energy for the latter but a GGA potential for the former term in (2.322). Examples for range-separated hybrid functionals which

are also used in this thesis are CAM(Y)-B3LYP[198] (in the CAMY variant a Yukawa function is used for range-separation instead of the error function. Also the parameter α in (2.322) is chosen differently), ω-B97-X[199] or LRC-ωPBEh[200]. In addition to the parameter α, RSHs also require the determination of the parameter μ. Systematic procedures to find this parameter have been suggested,[201–205] but these are rather cumbersome since they require to perform multiple exploratory calculations for each system at hand. Furthermore, in a heterogeneous system different moieties may require different range-separation parameters which makes such a procedure even more difficult to implement.[206]

rungs	ingredients	examples
LDA	$n(\boldsymbol{r})$	VWN5[182]
GGA	$n(\boldsymbol{r})$, $\nabla n(\boldsymbol{r})$	PBE[189,190]
meta-GGA	$n(\boldsymbol{r})$, $\nabla n(\boldsymbol{r})$, $\nabla^2 n(\boldsymbol{r})$	TPSS[191]
hybrid	$n(\boldsymbol{r})$, $\nabla n(\boldsymbol{r})$, $\{\phi_i\}_{i\in occ}$	PBE0[192] M06-2X[194]
meta-hybrid	$n(\boldsymbol{r})$, $\nabla n(\boldsymbol{r})$, $\nabla^2 n(\boldsymbol{r})$, $\{\phi_i\}_{i\in occ}$	TPSSh[195]
hybrid + D	$n(\boldsymbol{r})$, $\nabla n(\boldsymbol{r})$, $\{\phi_i\}_{i\in occ}$	PBE0 + D3(BJ)[192,207] ω-B97-X[199]
RSH	$n(\boldsymbol{r})$, $\nabla n(\boldsymbol{r})$, Σ_x	LRC-ωPBEh[200] CAMY-B3LYP[198]
OEP	$n(\boldsymbol{r})$, $\nabla n(\boldsymbol{r})$, $\{\phi_i\}_{i\in occ}$	OEP[171]
DH + D	$n(\boldsymbol{r})$, $\nabla n(\boldsymbol{r})$, $\{\phi_k\}_{k\in all}$, E_D	DSD-PBE-P86-D3(BJ)[208]

Table 2.1: Overview of different approximations to the Hxc potential v_{Hxc} used in this work. The second column lists all parameters on which a functional of a ceratin rung depends. D stands for dispersion and E_D for the energy contribtution due to empirical dispersion corrections.

Empirical dispersion corrections One of the major short-comings of the common approximations to v_{Hxc} is their inability to accurately describe van-der-Waals (vdW) interactions,[209] the main component of the long-range contribution to the electron-electron correlation energy. In the following, we outline the main ideas behind empirical approaches to describe these interactions within a DFT framework. For more detailed derivations see for instance ref. [210] or ref. [209]. Most empirical dispersion corrections can be derived from the Casimir-Polder integral[211]

$$E_{corr}^{(2)} = -\frac{1}{2}\sum_{AB}\frac{3}{\pi}\int_0^\infty d\omega \alpha_A \alpha_B \mathrm{Tr}\left[T_{AB}^{(lr)} T_{BA}^{(lr)}\ .\right] \tag{2.324}$$

Here, α denotes the isotropic polarizability tensor[209] and T is the dipole-coupling tensor

$$T(\boldsymbol{r},\boldsymbol{r}') = \nabla_{\boldsymbol{r}} \otimes \nabla_{\boldsymbol{r}'} v_c(\boldsymbol{r},\boldsymbol{r}')\ , \quad T^{(lr)}(\boldsymbol{r},\boldsymbol{r}') = f(|\boldsymbol{r}-\boldsymbol{r}'|)T(\boldsymbol{r},\boldsymbol{r}')\ , \tag{2.325}$$

where f is the range-separation function defined in (2.322). The sum runs over all polarizability centers A and B. Noting that

$$\mathrm{Tr}\left[T_{AB}^{(lr)}T_{BA}^{(lr)}\right] = \frac{6}{|\boldsymbol{R}_A - \boldsymbol{R}_B|^6} \tag{2.326}$$

and $T_{AA} = 0$ ($\boldsymbol{R}_A$ denotes the position of center A), one obtains

$$\begin{aligned} E_{corr}^{(2)} &= -\frac{1}{2}\sum_{A\neq B}\frac{3}{\pi}\int_0^\infty d\omega \alpha_A\alpha_B \frac{\left[f(|\boldsymbol{R}_A - \boldsymbol{R}_B|)\right]^2}{\left|\boldsymbol{R}_A - \boldsymbol{R}_B\right|^6} \\ &= -\frac{1}{2}\sum_{A\neq B} C_{6,AB}\frac{f_{\mathrm{damp}}(|\boldsymbol{R}_A - \boldsymbol{R}_B|)}{\left|\boldsymbol{R}_A - \boldsymbol{R}_B\right|^6}\,, \end{aligned} \tag{2.327}$$

the formula for the vdW interaction between two bodies within the dipole approximation. Empirical dispersion correction schemes differ by the choice of the damping function f_{damp} and the parametrization of the C_6 coefficients. A and B are typically chosen as atomic centers so that α_A and α_B are the atomic polarizability tensors. The form of empirical correction we use in this work is due to Grimme and coworkers[207,212,213] and is referred to as D3(BJ), where BJ denotes the damping function due to Becke and Johnson.[214,215]

Double Hybrid Functionals For the purpose of calculating total energies one often combines hybrid functionals with a fraction of the MP2 or RPA correlation energy and also empirical dispersion corrections. The first modern functional of this kind has been proposed by Grimme.[216] A plethora of such functionals have been suggested over the last years (for an overview and benchmarks see for instance[208,217,218]). They can also be implemented with range-separated electron-electron interaction where (2.322) is either only used in the hybrid part of the functional,[199,219,220] or also for the calculation of the MP2/RPA part[221–223] In this thesis they are only used to put the results of total energy calculations of more rigorous MBPT based energy expressions into context.

Table 2.1 summarizes the functionals introduced in this section. The examples given are all used in this work.

2.4.4 Approximations to *GW*

Static approximations

The HF approximation can be regarded as a first-order approximation to the GW self-energy. As an alternative approximation, one introduces the statically screened exchange (SEX)

$$W(\boldsymbol{r},\boldsymbol{r}',0) = \lim_{\eta\to 0} W(\boldsymbol{r},\boldsymbol{r}',t-t')\delta(t-t'+\eta)\,,$$

where η is an infinitesimal shift. Inserting this into (2.302) gives

$$\begin{aligned}\Sigma^{SEX}(\boldsymbol{r},\boldsymbol{r}') =& i\lim_{\eta\to 0^+} G(\boldsymbol{r},\boldsymbol{r}',t-t'+\eta)W(\boldsymbol{r},\boldsymbol{r}',0)\delta(t-t') \\ =& -W(\boldsymbol{r},\boldsymbol{r}',\omega=0)n(\boldsymbol{r},\boldsymbol{r}')\ ,\end{aligned} \tag{2.328}$$

where the parameter η selects only the lesser component of the Green's function. As in the HF approximation, the Green's function in the resulting expression for the self-energy reduces to the 1-particle reduced density matrix. This shows that the dynamical screening effects distinguish the GW approximation qualitatively from the HF approximation. For solids, it has been shown that static screening already improves the band gaps compared to HF.[15] This is dues to the fact that the statically screened interaction already contains the information that the many-electron system relaxes in response to the addition of an additional hole or electron while in the HF approximation the many-body states remain 'frozen'.

One might improve over SEX by placing the δ function symmetrically and assuming $\Theta(0)=\frac{1}{2}$, after some manipulations[224] one obtains a self-energy of the form

$$\begin{aligned}\Sigma_{xc}^{COHSEX} =& -n(\boldsymbol{r},\boldsymbol{r}')W(\boldsymbol{r},\boldsymbol{r}',\omega=0) \\ &+\frac{1}{2}\delta(\boldsymbol{r}-\boldsymbol{r}')\left[W(\boldsymbol{r},\boldsymbol{r}',\omega=0)-W^{(0)}(\boldsymbol{r},\boldsymbol{r}')\right]\ .\end{aligned} \tag{2.329}$$

The second term on the *r.h.s.* of (2.329) is called Coulomb hole (COH) and the first term is the SEX term (2.328). This form of the self-energy is typically referred to as Coulomb hole + screened exchange (COHSEX) approximation and is already been introduced by Hedin.[67] In contrast to SEX, the evaluation of the COHSEX approximation requires a summation over all unoccupied states.[167]

G_0W_0

The calculation of the band structure of a few selected metals and insulators by Hybertsen and Louie in 1986[225] is typically considered as the first application of the GW method to a real material. To make these calculations feasible, Hybertsen and Louie introduced a large number of approximations. Besides numerical approximations like an approximate treatment of the frequency dependence of the Green's function with a generalized plasmon-pole model,[225] (for a comparison of the accuracy of different plasmon-pole models see ref. [226]) they also introduced a perturbative approach to the GW approximations where the self-consistent solution of eqs. (2.299)–(2.302) is bypassed. This so-called G_0W_0 approximation has the advantage that it only requires a single evaluation of the GW self-energy, i.e. is non-iterative. Another advantage is, that only the diagonal element of the GW self-energy need to be evaluated while for the off-diagonal elements only a (hybrid) KS potential is needed which is much cheaper to obtain. The fact that the solutions of (2.334) or (2.335) heavily depend on the choice of v_{Hxc} is a major downside of G_0W_0. Furthermore, properties beyond single-particle excitations which depend on

the Green's function like densities, density matrices or electron-electron interaction energies can not be obtained in this way.

The G_0W_0 approach is derived by using the identity

$$\Sigma^{GW} = \Sigma^{GW} + v_{Hxc} - v_{Hxc} \tag{2.330}$$

and uses (2.137) to rewrite the GW approximation as a coupled set of Dyson equations,

$$\begin{aligned} G^{(s)}(1,1') =& G^{(0)}(1,1') + G^{(0)}(1,2)v_{Hxc}(2)G^{(s)}(2,1') \\ G^{GW}(1,1') =& G^{(s)}(1,1') + G^{(s)}(1,2)\left[\Sigma^{GW}(2,3) - v_{Hxc}(2)\delta(2,3)\right] G^{GW}(3,1') \ . \end{aligned} \tag{2.331}$$

Following the arguments leading to (2.296) we can then rewrite this as

$$\begin{aligned} &\left[h(\boldsymbol{r}_1) + v_{Hxc}(\boldsymbol{r}_1) - \epsilon_k^{GW}\right] \phi_k^{GW}(\boldsymbol{r}_1, \epsilon_k^{GW}) \\ &+ \int dx_2 \left[\Sigma(x_1, x_2, \epsilon_k^{GW}) - v_{Hxc}(\boldsymbol{r}_1)\delta(\boldsymbol{r}_1 - \boldsymbol{r}_2)\right] \phi_k^{GW}(\boldsymbol{r}_2, \epsilon_k^{GW}) = 0 \ , \end{aligned} \tag{2.332}$$

and the same for the associated equation for the $\phi_k^{GW^*}$. Not we can express the Hamiltonian in this equation in the basis in which the KS Hamiltonian $h + v_{Hxc}$ is diagonal,

$$\sum_r \left[\Sigma(\omega) - v_{Hxc}\right]_{kr} \phi_r^{GW}(\boldsymbol{r}_1, \omega) = \left(\epsilon_k^{GW}(\omega) - \epsilon_k^{KS}\right) \phi_k^{GW}(\boldsymbol{r}_1, \omega) \ , \tag{2.333}$$

which is a eigenproblem whose solution gives the difference between the KS and the GW QP energies. Now, we can make the approximation that all the off-diagonal elements of the operator on the *l.h.s.* of (2.333) are zero. Using that we can write $\epsilon_k^{GW}(\omega) = \omega$, this leads to the approximation,

$$\Sigma_k(\omega) - \left[v_{Hxc}\right]_k + \epsilon_k^{KS} = \omega \ . \tag{2.334}$$

For each k, the ω for which (2.334) has a solution can in principle be identified with a QP energy, $\epsilon_k^{GW}(\omega) = \omega$. Since the equations are non-linear, there might multiple solutions. One then typically associates the solution for which the absolute value of the derivative of the real part of the self-energy with respect to ω is largest with the QP solution. The G_0W_0 approximation is still the most used approach to perform GW calculations in practice.

Solution of (2.334) requires the knowledge of the diagonal elements of the GW self-energy at many frequency points (or at least that it can be calculated without much effort), depending on the used solver. If the frequency dependence of Σ is unknown, one can use (2.244). To zeroth order, one has

$$\Sigma_k(\epsilon_k^{KS}) - \left[v_{Hxc}\right]_k + \epsilon_k^{KS} = \epsilon_k^{GW} \ , \tag{2.335}$$

which is now linear. The self-energy is often treated to first order, which results in multiplication with the renormalization factor Z, (2.245). This is typically referred to as linearized G_0W_0 (lin-G_0W_0) and is commonly implemented in solid state codes which evaluate ω on the real frequency

axis. Note, that it has been argued that the zeroth-order treatment is to be preferred on the GW level.[227]

In practice, most GW calculations are performed using G_0W_0 or its self-consistent evGW extension. In contrast, GW calculations are rarely performed fully self-consistently (scGW). The first (partially[228]) self-consistent GW calculations have been performed in the late 1990s and early 2000s for the homogeneous electron gas,[229,230] jellium,[231] and simple semiconductors (Silicon) and metals (Potassium).[232] While the total energies for the homogeneous electron gas were found to be in excellent agreement with quantum monte carlo data[10], it turned out that the calculated band structures were worse than the ones from G_0W_0. Later results were more ambiguous: For instance, for single atoms and diatomic molecules, Stan, Dahlen and van Leeuwen confirmed the good quality of total energies found for the HEG and also found the self-consistently calculated ionization potentials to be better than the ones from G_0W_0.[235,236] Also Ku and Eguiluz reported improvements over the G_0W_0 band gaps for the semiconductor Germanium with scGW,[237] while in a more recent study Koval et al. could not find clear improvements over G_0W_0 with scGW.[238]

All of these studies have in common that not much attention has been paid to the choice of $G^{(s)}$. However, the proper choice of $G^{(s)}$ is crucial for accurate G_0W_0 calculations. Following Hybertsen and Louie and in the tradition of most band structure calculations for the solid state, in most of these studies LDA Green's functions were used. Koval et al. also employed HF Green's functions which is a common choice for perturbation theory in quantum chemistry. By now, systematic investigations of the starting point dependence of G_0W_0 calculations[40,224,239–242] have established that LDA is a terrible and HF at best a mediocre choice for $G^{(s)}$ for the calculation of single-particle excitations.

Caruso et al. have presented a few years ago an implementation of scGW in the FHI-AIMS code, which, in contrast to earlier implementations allowed applications to molecules with tens of atoms.[243,244] It turned out that G_0W_0 ionization potentials evaluated with a PBE0 Green's function (G_0W_0@PBE0 in short) where superior to scGW results for azabenzenes. On the other hand, the accuracy of G_0W_0@PBE was comparable to scGW while G_0W_0@HF performed worse.[245] More recent comparisons of G_0W_0 for different starting points to scGW have clearly shown that G_0W_0 is superior to scGW for the calculation of ionization potentials and also electron affinities for a set of organic acceptor molecules[246] if a good starting point is chosen.[242,247]

Selection of the starting point for G_0W_0

The choice of the starting point is crucial for a successful outcome of a G_0W_0 calculation. Therefore, especially for molecular systems,[40,240–242,245,248] but also for solids,[224,239] many researchers have investigated the influence of the choice on $G^{(s)}$ on the single-particle excitation energies. The outcome of these investigations can be summarized as follows: If the eigenvalues of the KS Hamiltonian are too bad of an approximation to the true QP energies, the G_0W_0 approach will

[10] The performance of scGW for electron-electron interaction energies of small molecules was also investigated. In contrast to the HEG, the results were generally found to be of pour quality.[233,234]

fail.[241] Therefore, it is mandatory to calculate the G_0W_0 correction starting from $G^{(s)}$ which is already close to the GW Green's function.[167,249]

The following paragraphs summarize the different strategies which can be pursued and the accuracies which can be achieved for molecules. It should be emphasized that many investigations on the starting point dependence carried out for solids are not necessarily transferable to molecular systems. This is due to the fact the screening of the electron-electron interaction in the latter ones is typically much weaker[141,250] (we also refer here to studies comparing screening in 2D and 3D[251–254] where qualitative differences are observed). We will come back to this point later in this chapters. We mostly comment here on the accuracy of the different strategies for the description of single-particle excitations. However, approaches which work well for single-particle excitations typically also give good optical excitation energies, since the latter ones are mostly determined by the differences in the QP energies.

General considerations G_0W_0 is a perturbation method. Generally, perturbation theory works best when the reference Hamiltonian is as close to the full Hamiltonian as possible, i.e. when the perturbation is small. There are many possible ways to measure' closeness. The G_0W_0 QP energies will generally be very close to the scGW quasi-particle energies when the zeroth-order Hamiltonian used to calculate $G^{(s)}$ is chosen in a way that it produces the same density as scGW. A second possibility is to directly require that the QPs produced by the zeroth-order Hamiltonian correspond as closely as possible to the true QP energies.

For instance, GGA or LDA calculations typically underestimate single-particle excitations energies and fundamental gaps (the difference between HOMO and LUMO QP energies) by a few eV.[255] In the other hand, the HF approximation overestimates single-particle excitations and fundamental gaps. Hybrid- and range-separated hybrid functionals can be regarded as attempts to interpolate between a GGA/LDA potential and indeed the resulting eigenvalues are often good approximations to the true QP energies. Therefore, G_0W_0 calculations based hybrid and RSH functional give typically the best results. This can be rationalized by the close connection of the HF and the GW self-energy expressions we have discussed in paragraph 2.4.4.

Hybrid and range-separated Hybrid Functionals While being much cheaper than a scGW calculation, the self-consistent evaluation of SEX and COHSEX is still much more demanding than the evaluation of a HF or a hybrid Green's function. It turns out, that the COHSEX self-energy can be very well approximated by retaining the HF self-energy and to account for screening effects by scaling it down using a constant parameter α. If one adds a local (GGA) correlation potential and a compensating fraction (1- α) of local (GGA) exchange, one recovers exactly (2.321). Therefore in the context of GW calculations hybrid functionals can be interpreted as computationally very efficient approximations to scGW which offers a qualitative justification to base a G_0W_0 calculation on a hybrid Green's function.[167] Similar arguments can be used to justify the use of range-separated hybrid functionals.

Optimization of free parameters in hybrid functionals The downside of using hybrid functionals is the appearance of the free parameter α. Since screening effects will be different from system to system it is clear that the optimal α will vary for different systems as well. The same considerations apply to the range-separation parameter in RSHs. Strategies to find the optimal α in a system specific way has been suggested[249,256] based on the observation that within (exact) KS-DFT the negative of the HOMO of a finite system equals the ionization potential. One can then find an optimal α^* by minimizing the QP correction to the HOMO eigenvalue in (2.334),[249]

$$\alpha^* = \arg\min_{\alpha} \left| \Sigma_{\text{HOMO}}(\omega) - [v_{Hxc}]_{\text{HOMO}} \right| . \tag{2.336}$$

In practice, such a minimization can be achieved by performing a few G_0W_0 calculations for different values of α and to find α^* by interpolation. A similar strategy has been suggested in ref. [256] where α^* is obtained instead by linear regression over the full occupied spectrum. The resulting values of α^* turned out to lie typically in the range of 0.7-1.0 for a wide range of small molecules. However, the results were worse than the ones for G_0W_0@PBE0 where $\alpha = 0.25$.[249] A related strategy, combining such approaches with the RPA-OEP method has recently been introduced by Hellgren *et al.*[167].

Other investigations have established that hybrid functionals with 40 to 50 % exact exchange generally give the best QP energies,[240,248] (a recent investigation of G_0W_0 IPs with more than 60 functionals confirmed this[257]) with mean absolute deviations (MAD) to more accurate *ab initio* calculations of around 0.2 eV for organic molecules. The same accuracy can be achieved with RSHs, independently of whether the range-separation parameter is empirically optimized or not.[40,242]

Static approximations to the GW self-energy Both the SEX and the COHSEX approximations can be solved self-consistently. While both approximations by themselves are typically not very accurate (albeit more accurate than the HF approximation), the resulting $G^{(s)}$ can be also used as starting points for a G_0W_0 (or evGW) calculations. G_0W_0@COHSEX has been found to give good results for many materials.[224]

eigenvalue-only self-consistent GW

A computationally more involved alternative to G_0W_0 is eigenvalues-only self-consistent GW (evGW). In contrast to G_0W_0, evGW is a self-consistent perturbation method which aims to optimize the starting point for a G_0W_0 calculation by optimizing the input QP energies. In evGW, a series of G_0W_0 calculations is performed until self-consistency in the QP energies is reached. Although the density remains unaltered with respect to the KS reference, evGW largely overcomes the starting point dependence of G_0W_0. Even in the evGW_0 variant, where the screened interaction of the first G_0W_0 calculation is used, the starting point dependence is reduced drastically.

Despite its higher computational cost, evGW is therefore a popular alternative to G_0W_0[258–269] and its improved accuracy compared to G_0W_0@LDA or G_0W_0@PBE have been highlighted.[265]

On the other hand, when a good starting point is chosen, evGW does not give any improvements over G_0W_0.[248] We will present additional data supporting this claim in appendix A.3.

Quasi-particle self-consistent *GW*

As evGW, the quasi-particle self-consistent GW (qsGW) method is a self-consistent perturbation method. However, qsGW goes beyond evGW and self-consistently determines the optimum division of the GW Hamiltonian into the zeroth-order reference h_1 and the perturbing part. To derive the quasi-particle self-consistent form of Dyson's equations, one starts from (2.259) and writes the self-energy as

$$\Sigma(\omega) = \frac{1}{2}\left[\Sigma(\omega) + \Sigma^\dagger(\omega)\right] + \frac{1}{2}\left[\Sigma(\omega) - \Sigma^\dagger(\omega)\right] \ , \tag{2.337}$$

where the first term on the *r.h.s.* of this equation is Hermitian and the second one is skew-Hermitian. The Hermitian part in (2.337) is related to the QP part of the single-particle Green's function while the skew-Hermitian part is responsible for the finite lifetime effects of the QPs and together with the frequency dependence of the self-energy desrcibes satellites in the single-particle spectrum. Retaining only the Hermitian part in (2.259) gives

$$\left\{h_1(\boldsymbol{r}_1) + \frac{1}{2}\int d\boldsymbol{r}_2 \left[\Sigma(\boldsymbol{r}_1,\boldsymbol{r}_2,\omega) + \Sigma^\dagger(\boldsymbol{r}_1,\boldsymbol{r}_2,\omega)\right]\right\}\psi_k(\boldsymbol{r}_2,\omega) = \epsilon_p^{QP}\psi_k(\boldsymbol{r}_1,\omega) \ , \tag{2.338}$$

and in an orthonormal basis of single-particle states, (2.338) becomes

$$\sum_p \left[\Sigma(\omega) + \Sigma^\dagger(\omega)\right]_{pk}\psi_p(\boldsymbol{r}_1,\omega) = \left[\epsilon_k^{QP}(\omega) - \epsilon_k\right]\psi_k(\boldsymbol{r}_1,\omega) \ . \tag{2.339}$$

The real part of the full self-energy is a real quantity and so is the imaginary part. Therefore, the real and the imaginary part of the self-energy are Hermitian by themselves, even though the full self-energy is not. Therefore,

$$\text{Re}\ (\Sigma(\omega)) = \frac{1}{2}\left[\Sigma(\omega) + \Sigma^\dagger(\omega)\right] \ . \tag{2.340}$$

Equations (2.338) and (2.339) are a series of Hermitian eigenproblems, one for each value of ω. This form of Dyson's equation is general and independent of any approximation to the self-energy. If the GW approximation to the self-energy is made, (2.338) is the closest approximation to fully self-consistent GW which only retains the QP features of the theory. In the quasi-particle self-consistent GW approach[142,174,175] introduced by Kotani, Faleev, and van Schilfgaarde the frequency dependent self-energy in (2.339) is mapped to an effective static and Hermitian non-local potential which is a functional of the non-interacting single-particle Green's function. The choice of this potential is not unique. Kotani, Faleev, and van Schilfgaarde suggested to use one of the real symmetric definitions

$$v_{pq}^{QP}(\epsilon_p) = \frac{1}{2}\left[\text{Re}\ \left[\Sigma_c^{GW}\right]_{pq}(\epsilon_p) + \text{Re}\ \left[\Sigma_c^{GW}\right]_{pq}(\epsilon_q)\right] \ , \tag{2.341}$$

or

$$v_{pq}^{QP}(\epsilon_p) = \delta_{pq}\mathrm{Re}\ \left[\Sigma_c^{GW}\right]_{pq}(\epsilon_p) + (1-\delta_{pq})\mathrm{Re}\ \left[\Sigma_c^{GW}\right]_{pq}(\omega=0)\ . \tag{2.342}$$

Inserting these definitions into (2.339)

$$\sum_p v_{kp}^{QP}(\epsilon_p)\psi_p(\boldsymbol{r}) = \left[\epsilon_k^{QP} - \epsilon_k\right]\psi_k(\boldsymbol{r})\ . \tag{2.343}$$

Kotani, Faleev, and van Schilfgaarde used (2.341) since they found that this form corresponded to experiment most systematically.[142] There are also formal reasons why (2.341) should be preferred over (2.342).[270] Constructing the *qsGW* Hamiltonian via (2.341) minimizes the length of the gradient of the Klein functional[57] with respect to G_0[270] On the other hand, (2.342) is to be preferred from a computational perspective as we will discuss in the next chapter. We will also see that the differences in the QP energies between both variants are negligible for practical purposes. As in the lin-G_0W_0 method, both variants eqs. eqs. (2.341) and (2.342) can be seen as Taylor expansion of the self-energy around the input QP energies where only the zeroth-order term is retained (compare to (2.244)). Shishkin and Kresse suggested to also retain the first-order term in (2.244)[177] which has also been done by Kutepov et al.[271,272]

While such modifications of the potentials eqs. (2.341) and (2.342) are easily implemented, a zeroth-order expansion is appropriate under the assumption that the input QP energies are close to the final QP energies. At self-consistency, this requirement will be fulfilled by definition. Furthermore, in situations where the single QP picture is valid, the self-energy will be varying slowly around the QP position[273] and the effect of the first-order term in (2.244) will vanish. It has also been suggested to perform a G_0W_0 calculation on top of a qsGW calculation (G_0W_0@qsGW).[274] One can use the same arguments to see that the effect of the G_0W_0 correction will vanish when the single QP picture is valid.[275] The definitions of the qsGW Hamiltonians by Kutepov and coworkers and Kresse and coworkers might still be useful since they could accelerate the convergence of the self-consistency scheme needed to solve the qsGW equations.

Using one of the definitions eqs. (2.341) and (2.342) turns (2.339) into an effective single-particle problem,

$$\sum_p v_{pk}^{QP}(\epsilon_p)\phi_p(\boldsymbol{r}_1) = \left[\epsilon_k^{QP} - \epsilon_k\right]\phi_k(\boldsymbol{r}_1)\ . \tag{2.344}$$

reminiscent of HF or KS-DFT. Diagonalization of the effective Hamiltonian in (2.344) yields eigenvectors and eigenvalues from which a new non-interacting Green's function is obtained. However, the xc potential defined by eqs. (2.341) and (2.342) is not a functional of the 1-particle reduced density matrix or the density but rather of the non-interacting single-particle Green's function itself.

qsGW calculations combine the advantages of G_0W_0 and scGW. It is at least as accurate than G_0W_0 for molecules[39,40,276,277] Moreover, it is strictly starting-point independent since in contrast to evGW, not only the QP energies but also the density is updated in each iteration. Therefore, at self-consistency the qsGW Green's function is independent of the initial $G^{(s)}$. Issues

with diagonal QP approximations arise when a re-ordering of the GW orbitals with respect to the DFT orbitals occurs. This is an indication that DFT orbitals are a qualitatively wrong reference for a G_0W_0 calculation. This has been found problematic in in the study of energy level-alignment in photocatalytic interfaces.[278–281] The discussion on this subject found in ref. [278] is especially insightful.

Generally, compared to G_0W_0 based on a semi-local or hybrid starting point, self-consistency weakens the screening of the electron-electron interaction which widens the band gap. For solids this is problematic and vertex corrections are needed to restore agreement with experiment.[282] The overestimation of the band gap is rather systematic and therefore another approach to restore agreement with experiment is to combine 80 % of the qsGW with 20 % of the LDA self-energy.[283,284] For molecules, we will discuss qsGW fundamental gaps in section 5.2. When qsGW QP energies are used in the BSE, weaker screening results in a stronger electron-hole interaction which should localize the excitons. On the other hand, since the QP energy differences will be larger than with G_0W_0, optical exciation energies will be higher as well.

In contrast to diagonal approximations, qsGW provides access to properties which directly depend on the 1-particle reduced density matrix. Only recently, qsGW densities of molecular systems have been investigated by Bruneval.[285] The quality of these densities is a subject of on-going research.

Further approximations

Approximation	update of		dependency	approximation to Σ		
	ϵ^{QP}	ϕ^{QP}	on $G^{(s)}$	Diag.	Hermitian	static
lin-G_0W_0	no	no	strong	yes	yes	Σ
G_0W_0	no	no	strong	yes	yes	no
COHSEX	yes	yes	non	no	yes	W
evGW	yes	no	weak	yes	yes	no
qsGW	yes	yes	non	no	yes	Σ
scGW	yes	yes	non	no	no	no
qsGW(Hx)	yes	yes	strong	no	yes	Σ
scGW(Hx)	yes	yes	strong	no	no	no
evGW_0	yes	no	strong	yes	yes	no
qsGW_0	yes	yes	strong	no	yes	Σ
scGW_0	yes	yes	strong	no	no	no

Table 2.2: Overview of the common variants to perform GW calculations and the main features of the approximations to Σ which are made.

Besides the commonly used strategies outlined above, there is a plethora of conceivable ways to perform GW calculations (one could even say, that the possibilities are almost endless).

van Leeuwen and coworkers suggested to perform fully self-consistent GW calculations but to keep the dynamical part of the self-energy fixed in all iterations but the first one.[236] We have implemented the same strategy using qsGW instead of scGW. Since the calculation of the dynamical self-energy part is computationally much more demanding than the calculation of the static part, this strategy is efficient from a computational point of view. On the other hand, the results are not starting-point independent anymore. A similar partially self-consistent scheme in which only one full update of the full self-energy is performed has been suggested by Rubio and coworkers.[279,280] Also in the linearized density-matrix method by Bruneval and coworkers[285–287] only a single scGW iteration is performed.

evGW calculations have also be performed starting from a self-consistent COHSEX calculation (evGW@COHSEX).[263,288] evGW@COHSEX comes with the advantage that the results are completely independent of the initial choice of $G^{(s)}$.

In all self-consistency schemes (evGW, qsGW, scGW), it is always possible to keep the screened interaction fixed, i.e. to only evaluate it on the $G^{(s)}$ level (evGW_0, qsGW_0, scGW_0). scGW_0 have been performed by Holm and von Bart even before the first fully self-consistent GW calculations[228] for the homogeneous electron gas. While this approach was rather motivated by the numerical difficulties to perform scGW calculations, it was noticed later on that evGW and qsGW significantly overestimate band gaps in solids[176,177,282] since in these approaches the Coulomb interaction is underscreened.[280] It was then suggested to replace the self-consistently obtained W by a $W^{(0)}$ from a (semi-)local DFT calculation to fix the systematic underscreening, which improved the investigated band gaps[177] As we will discuss later on, screening effects are much weaker in molecules than in solids and in fact qsGW does not overestimate fundamental gaps (the equivalent to band gaps in molecules). Indeed, there is some indication from our own work that qsGW_0 does not necessarily seem to be a good method for molecular systems.[248] Also evGW_0 has been shown to be mostly inadequate for many systems.[265,266]

All different ways to perform GW calculations we have just discussed are summarized in table 2.2.

Ward Identity

The Ward identity expresses important constraints between the single- and two-particle Green's functions.[289] Alternatively, these constraints can be formulated as identities involving the derivatives of the 2-point and the 4-point vertices in the limit of large electron-electron separation and small frequencies.[127] In the context of MBPT, the most thorough discussion of these identities is most likely the one given by Strinati in ref. [127]. In combination with (2.251), the Ward identity has been used by Kotani, van Schilfgaarde and Faleev to explain the success of QP approximations to GW.[142]

To introduce the Ward identity, we first define the 3-point vertex as the quantity which relates the interacting and non-interacting generalized susceptibilities via[127]

$$\chi(1,3,2,3^+) = \int d4d5\chi^{(0)}(1,5,2,4)\Xi(4,5,3^+) \; . \tag{2.345}$$

It can then be shown[127], that close to the chemical potential the irreducible vertex goes as

$$\Gamma^{(0)} \to \frac{\partial \Sigma}{\partial \omega} \mid_{\omega \to \mu} = Z^{-1} \tag{2.346}$$

where we have used (2.245). It can then be shown that using the vertex Ξ, the xc-contribution to the self-energy can be written as[15,67,127]

$$\Sigma(1,2) = iG(1,4)W(1^+,3)\Xi(4,2,3) \; , \tag{2.347}$$

with W defined in the usual way and

$$P(1,2) = \chi^{(0)}(1,4,1^+,3)\Xi(3,4,2) \; . \tag{2.348}$$

This is the standard form of Hedin's equations. Inserting (2.251) and using (2.346), we obtain

$$\Sigma(1,2) \xrightarrow{\boldsymbol{r}\to 0,\omega\to 0} = iG^{(0)}(1,2)W(1^+,2) + i\frac{1}{Z}G^{inc}(1,2)W(1^+,2) \; . \tag{2.349}$$

This only holds close to the chemical potential. If we now assume that the incoherent part of the self-energy is unimportant for the description of QPs (which we assume to be the case close to the chemical potential), we can then write

$$\Sigma(1,2) = iG^{(0)}(1,2)W(1^+,2) \; . \tag{2.350}$$

Equation (2.350) suggests that the best way to perform a GW calculation would be to use the QP $G^{(0)}$ but to construct W from the interacting G. This result is physically intuitive. The 4-point vertex function couples the QPs. When the distance between the QPs becomes large, their mutual interactions will vanish at small energy scales.

Correlation Energies from the GW Approximation

We now derive an expression for the electron correlation energy from the GW approximation. In this work, we are not interested in evaluating this quantity with G and we focus on $G^{(s)}$. The resulting expression for the correlation energy is known as RPA and has first been introduced by Macke[111] many years prior to Hedin's work. Within MBPT, the electron-electron interaction energy can be obtained as[56]

$$\begin{aligned} E_{Hxc}[G^s] =& E_{Hx}[G^s] + E_c[G^s] \\ E_{Hx}[G^s] =& \frac{1}{2}\int d1d2G^s(1,2)\Sigma^{(1)}(2,1)[G^s] \\ E_c[G^s] =& \frac{1}{2}\sum_{n=2}\frac{1}{n}\int d1d2G^s(1,2)\Sigma^{(n)}(2,1)[G^s] \end{aligned} \tag{2.351}$$

from a non-interacting Green' function,[290] where we use the decomposition of the self-energy in orders in $W^{(0)}$ eq. (2.134). With the GW approximation for Σ and using eqs. (2.300) and (2.301) the expression

$$\begin{aligned} E_{xc}^{RPA} =& i\frac{1}{2}\int d1d2 G^{(s)}(1,2)G^{(s)}(2,1)W(2,1) \\ =& -\frac{1}{2}\int d1d2 P^{(0)}(1,2)\left\{ W^{(0)}(1,2) + \frac{1}{2}W^{(0)}(1,3)P^{(0)}(3,4)W^{(0)}(4,2) + \dots \right\} \end{aligned} \tag{2.352}$$

for the xc-energy is obtained. Isolating the exchange contribution to the Hartree-exchange energy,

$$E_x = \int d1d2\ \delta(\tau_{12})G(1,2)W^{(0)}(2,1)G^{(s)}(2,1)\ , \tag{2.353}$$

we obtain what is typically called RPA correlation energy

$$\begin{aligned} E_c^{RPA} =& -\frac{1}{2}\sum_n \frac{1}{n}\int d1d2\delta(1,2)\left\{ \left[\int d3 P^{(0)}(1,3)W^{(0)}(3,2)\right]^n + \int d3 P^{(0)}(1,3)W^{(0)}(3,2)\right\} \\ =& \frac{1}{2}\int d1d2 \left\{ \ln\left[\delta(1,2) - \int d3 P^{(0)}(1,3)W^{(0)}(3,2)\right] + \int d3 P^{(0)}(1,3)W^{(0)}(3,2)\right\}\ , \end{aligned} \tag{2.354}$$

and using (2.230) as well as the symmetry of the polarizability on the imaginary frequency axis (which cancels the prefactor of 1/2), its representation due to Langreth and Perdew[291] on the imaginary axis is obtained,

$$\begin{aligned} E_c^{RPA} =& \frac{1}{2\pi}\int d\boldsymbol{r}_1 d\boldsymbol{r}_2 \delta(\boldsymbol{r}_1 - \boldsymbol{r}_2)\int_0^\infty d\omega \left\{ \ln\left[\delta(1,2) - \int d\boldsymbol{r}' P^{(0)}(\boldsymbol{r}_1,\boldsymbol{r}',i\omega)v_c(\boldsymbol{r}',\boldsymbol{r}_2)\right] \right. \\ & \left. + \int d\boldsymbol{r}' P^{(0)}(\boldsymbol{r}_1,\boldsymbol{r}',i\omega)v_c(\boldsymbol{r}',\boldsymbol{r}_2)\right\}\ . \end{aligned} \tag{2.355}$$

Expanding the correlation energy as a series in v_c, we obtain

$$E_c^{RPA} = E_c^{(2)} + E_c^{(3)} + E_c^{(4)}\ ,$$

where the first term is given as

$$E_c^{(2)} = -\frac{1}{4\pi}\int d\boldsymbol{r}_1 \dots \boldsymbol{r}_4 \int_0^\infty P^{(0)}(\boldsymbol{r}_1,\boldsymbol{r}_2,i\omega)v_c(\boldsymbol{r}_2,\boldsymbol{r}_3)P^{(0)}(\boldsymbol{r}_3,\boldsymbol{r}_4,i\omega)v_c(\boldsymbol{r}_4,\boldsymbol{r}_1)\ .$$

We will now show that this gives a first principle parametrization of the vdW interaction energy we have written down in (2.327). Let us now consider two neutral fragments A and B which are separated by a large enough distance

$$R = |\boldsymbol{R}| = |\boldsymbol{R}_A - \boldsymbol{R}_B|$$

so that their electron densities approximately do not overlap. The single-particle states from which the $P^{(0)}$ are build are then localized on these fragments (in case of degeneracies, we can always apply a unitary transformation which localizes the single-particle states). Under this assumption, we can rewrite the previous expression[210] as

$$E_c^{(2)} = -\frac{1}{4\pi}\int d\boldsymbol{r}_1 \dots \boldsymbol{r}_4 \int_0^\infty P_A^{(0)}(\boldsymbol{r}_1, \boldsymbol{r}_2, i\omega) v_c(\boldsymbol{r}_2, \boldsymbol{r}_3) P_B^{(0)}(\boldsymbol{r}_3, \boldsymbol{r}_4, i\omega) v_c(\boldsymbol{r}_4, \boldsymbol{r}_1) \ ,$$

and choose the center of A as the origin of the $\boldsymbol{r}_1$ and $\boldsymbol{r}_2$ integration and B as the origin of the $\boldsymbol{r}_4$ and $\boldsymbol{r}_4$ integration. We can then write $v_c(\boldsymbol{r}_2, \boldsymbol{r}_3)$ as

$$v_c(\boldsymbol{r}_2, \boldsymbol{r}_3) = \frac{1}{|\boldsymbol{R} + \boldsymbol{r}_2 - \boldsymbol{r}_3|}$$

and Taylor expand it around R. We will then find that v_c^2 goes as

$$v_c^2(R) = \frac{1}{R}\left[\alpha(R)\frac{1}{R} - \beta(R)\frac{1}{R^3} + \gamma(R)\frac{1}{R^5}\dots\right] \ ,$$

where the first two terms do not contribute due to charge conservation. We therefore obtain an espression of the form

$$E_c^{(2)} = -\int_0^\infty d\omega \frac{1}{4\pi}\int d\boldsymbol{r}_1 \dots \boldsymbol{r}_4 \frac{\gamma(R)}{R^6} P_A^{(0)}(\boldsymbol{r}_1, \boldsymbol{r}_2, i\omega) P_B^{(0)}(\boldsymbol{r}_3, \boldsymbol{r}_4, i\omega) \ , \tag{2.356}$$

which is of the same form as (2.327).

2.4.5 Vertex corrections

Shortcomings of the GW Approximation

It is commonly accepted that the GW term in the electronic self-energy is the major source of of electron correlation and successfully describes weakly to moderately correlated systems where the major source of electron interactions is the classical electrodynamic screening.[292–294] This is indeed the most important physics for the description of electron addition and removal energies since it accounts for correlation effects stemming from the rearrangement of charge responding to the addition or removal to a system.[292,295,296] The Ward identity explains this from a different perspective: in the static long-range limit, the errors introduced by the neglect of self-consistency and the absence of vertex corrections in the self-energy cancel to a large extent.[142]

There are, however, major shortcomings in the GW formalism. First, the cancellation of vertex corrections in the self-energy (i.e. higher order terms in the expansion of Σ in terms of W) and self-consistency only takes place in the static long-range limit. For systems in which short-ranged interactions become important, the Fermi liquid hypothesis does not hold any more and interactions between the QPs need to be taken into account.[294,297] The contributions to the

self-energy due to the vertex function indeed describes these coupling between the QPs. These terms are fundamentally short-ranged and become less and less important for large electron-electron distances.[298,299] However, in the short-range limit they might even become the dominant source of electron correlation.[300]

Second, the Ward identity only explains the cancellation of the vertex in the self-energy but not in the polarizability which screens the interaction. The need to go beyond the RPA is recognized immediately since the xc contribution to the 4-point vertex is completely absent and the crossing symmetry eq. (2.172) is already violated to first order in the bare electron-electron interaction. This gives rise to a problem which is sometimes referred to as self-screening error,[292,301] an effect which has been thoroughly studied for one-electron systems[302,303] and simple model systems:[301] For a one-electron system, the screening of the electron-electron interaction needs to vanish since an electron can not screen itself. Therefore, the density-density response of any 1-electron system needs to be zero which is not the case within the RPA. This is a fundamental flaw of this approximation and a direct consequence of the violation of the crossing symmetry.[292]

The RPA describes screening by non-interacting (renormalized) electron-hole pairs and in the same way as the vertex in the self-energy describes interactions between the QPs, the vertex in the BSE describes the interactions between the electron-hole pairs. For many-electron systems, ignoring these interactions underestimates the screening. The violation of the crossing symmetry also results in overestimated correlation energies[298,304] due to the appearence of Pauli exclusion principle violating contributions terms.[305] Notice, that theories like Møller–Plesset (MP)perturbation theory[306] or CC do no include such contributions since only properly antisymmetrized terms are included in the equations. The same is also true for the Parquet approximation.[307,308]

Overview over earlier Work

By now, there is a vast literature on vertex corrected GW calculations which is in our opinion difficult to read and often confusing. We herein try to give a brief overview: A large number of such calculations have been carried out early on for the homogeneous electron gas,[309] Hubbard clusters[310–312] and other model systems[141,313,314] as well as simple semiconductors like Silicon and Diamond.[315–318] One of the overarching conclusions was indeed that vertex corrections in the self-energy often cancel to a large extent with the effect of self-consistency. This is the result which we have introduced before and been rationalized later on in ref. [142]. Also, Bechstedt *et al.*[318] could demonstrate the cancellation of the effect of self-consistency and the vertex corrections in the polarizability. It has also been concluded that vertex corrections in the polarizability alone do not improve[310,311] the accuracy of charged excitations compared to GW and rather recently it has been argued that such corrections might even deteriorate the description of single-particle excitations in molecules.[319] Consequently, it has indeed been argued, that the Vertex should always be included at the same level in χ and Σ.[67,317] Furthermore it has been shown by Minnhagen, that the straightforward inclusion of vertex corrections beyond the GW level

yields to the loss of the positive definiteness of the spectral funtion[309], an issue which has been rationalized and corrected by Stefanucci and coworkers.[137]

The results of these early studies are generally difficult to interpret due to the different approximations involved (for instance, use of Plasmon-pole models to model the frequency dependence of the self-energy[320] or static approximations, LDA Green's functions etc.) and the results are often contradicting. Furthermore, these studies give little indication about the transferability of these results to molecular systems.

Vertex Corrections in χ only

Over the last years, there has been a surge of articles exploring vertex corrections to GW including studies dedicated to realistic molecules. Typically, these studies either aim at improving RPA correlation energies or GW QP energies. Corrections to the RPA are often derived by including vertex corrections in χ. [11] This strategy has also been pursued frequently for QP calculations in the solid state, motivated by the observation that qsGW and scGW with RPA screening lead to overestimated band gaps.

Via MBPT, the RPA can generally be improved upon inclusion of the 4-point vertex in the electronic self-energy, either directly, or indirectly through the kernel of the Bethe-Salpeter equation (BSE) for the generalized susceptibility. As opposed to the derivation from the GW approximation within the bubble approximation to W, RPA correlation energies are often derived from the adiabatic connection fluctuation dissipation (ACFD) theorem in which the correlation energy is determined by the difference between the non-interacting and the interacting density-density response functions,[335]

$$E_c = \int_0^1 d\lambda \int_0^\infty d\omega \int d\boldsymbol{r} d\boldsymbol{r}' v_c(\boldsymbol{r},\boldsymbol{r}') \left[P_\lambda(\boldsymbol{r},\boldsymbol{r}',i\omega) - P^{(0)}(\boldsymbol{r},\boldsymbol{r}',i\omega) \right] . \tag{2.357}$$

In this expression, P_λ is calculated from a modified Dyson equation for the density-density response,

$$P_\lambda(\boldsymbol{r},\boldsymbol{r}',i\omega) = P^{(0)}(\boldsymbol{r},\boldsymbol{r}',i\omega) + P^{(0)}(\boldsymbol{r},\boldsymbol{r}_2,i\omega) \left[\lambda v_c(\boldsymbol{r}_2,\boldsymbol{r}_3) + f_{xc}(\boldsymbol{r}_2,\boldsymbol{r}_3) \right] P_\lambda(\boldsymbol{r}_3,\boldsymbol{r}',i\omega) , \tag{2.358}$$

which differs from the ordinary one only by the factor λ in front of the electron-electron interaction. Apart from this factor, this is the Dyson equation which is also solved in TD-DFT.[336] The f_{xc} kernel can then be derived from the 4-point vertex of the BSE or the BSE can be solved directly and the resulting χ is contracted to obtain P. Modifications of the bare Coulomb kernel include exact exchange (exx) (often denoted as exx-RPA)[337–343] and higher order contributions,[344–346] or the statically screened GW kernel,[347–349] but also empirically tuned functions of the eigenvalues of the KS density-density response.[350,351]

[11] There have also been many attempts to correct the RPA correlation energy expression by adding additional terms to improve the description of short-range correlation. This modifications are often not diagrammatic and especially range-separation based approaches,[321–331] have been very popular but also the inclusion of excitations to singles.[332–334]

Vertex corrections in χ have frequently been explored in the solid state where scGW but also qsGW underestimate the strength of the screening and consequently also band gaps of many materials. These include for instance the so-called nanoquanta kernel[176,352–354] or the bootstrap kernel[355,356] (see ref. [356] for an overview) or long-range corrections of the form $f_{xc} = -(a+b\omega^2)/q^2$ (q is a reciprocal lattice vector) where a and b need to be fitted to experimental data.[357,358] For reviews see ref. [292, 345]. Recently, an approach in which the f_{xc} kernel is only included on the short-range part has been proposed.[282] Finally, we also mention that adiabatic LDA kernels have been tested for molecules as well.[359] The most common diagrammatic modification is to solve the BSE with the static GW kernel (2.316),[360–364] typically adopting the Tamm-Dancoff approximation (TDA)[365] and within the qsGW approximation to Dyson's equation.[361–364,366]

The $G3W2$ Contribution to the Self-Energy

The most systematic investigations of vertex corrections to GW for realistic systems have possibly been conducted by Kutepov in a series of articles[367–372] and also very recently by Vlček and coworkers for Hubbard systems.[294] We have already given the explicit expression of the vertex function which is obtained as the functional derivative of the GW self-energy in (2.314). It consists of one first order term and two second-order terms. Inserting this vertex into the self-energy results in a single term of second order in W and two terms of third order in W. As shown by Hedin, the expansion of the self-energy in terms of the screened electron-electron interaction contains six third-order terms. Including only 2 out of 6 terms is not a systematic approximation, as has already pointed out by Hedin[67] and we are not aware of any justification as to why these two terms should be more important than the remaining four. We note, that Vlcček and coworkers have recently investigated the role of all of the third-order contributions, the remaining ones of which are obtained when the functional derivatives of the first-order and second-order contributions Vertex with respect to the single-particle Green's function are taken as well. They found, that the third-order terms give a good description of multi-QP coupling[294] and they concluded that their inclusion extends the applicability of MBPT based expressions to the strongly correlated regime.

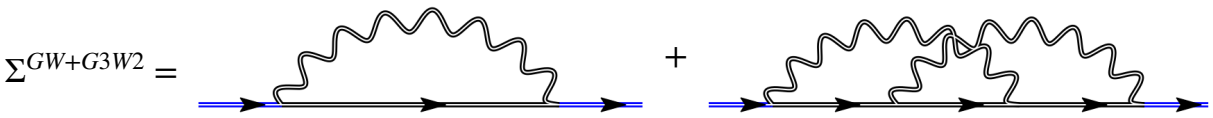

Figure 2.6: Diagrammatic representation of the $GW + G3W2$ contribution to the self-energy, the complete self-energy up to second order in the screened electron-electron interaction. Again, the black part of the diagrams are the contributions to the self-energy only which, combined with the blue lines yield the corresponding single-particle propagator.

In this thesis, we are exclusively concerned with the properties of the second order term. To obtain the second-order term one first calculates χ within the RPA. In this case, χ is related to its

non-interacting counterpart $\chi^{(0)}$ by a Dyson equation with the bare electron-electron interaction as its kernel,

$$\chi(1,2,3,4) = \chi^{(0)}(1,2,3,4)\chi^{(0)}(1,5,3,6)W^{(0)}(5,7,6,8)\delta(5,6)\delta(7,8)\chi(8,2,7,4) \; . \tag{2.359}$$

Then, one can see that

$$\begin{aligned} W^{(0)}\chi =& W^{(0)}\left[\chi^{(0)} + \chi^{(0)}W^{(0)}\chi^{(0)} + \chi^{(0)}W^{(0)}\chi^{(0)}W^{(0)}\chi^{(0)} + \dots\right] \\ =& \left[W^{(0)} + W^{(0)}\chi^{(0)}W^{(0)} + W^{(0)}\chi^{(0)}W^{(0)}\chi^{(0)}W^{(0)} + \dots\right]\chi^{(0)} \\ =& W\chi^{(0)} \; . \end{aligned} \tag{2.360}$$

Equation (2.203) can now be rewritten as

$$\Sigma^{RPA}(1,2) = \Sigma_H(1,2) + iG(1,2)W(1,2) + iG(1,3)W^{RPA}(1,4)\chi^{(0)}(6,4,5,4^+)\Gamma^{(0)}_{xc}(3,5,2,6) \; , \tag{2.361}$$

where the unscreened electron-electron interaction $W^{(0)}$ does not appear any more, and where the superscript indicates that this expression is only valid when W has been calculated within the RPA.

Now, one inserts the second first-order contribution to the vertex (2.314) into (2.361). We see that the resulting self-energy contribution consists of three single-particle Green's functions which are connected by two screened electron-electron interaction lines,

$$\Sigma^{G3W2}(1,2) = -G(1,3)W(1,4)G(3,4)G(4,2)W(3,2) \; . \tag{2.362}$$

Therefore, following Kutepov[272,367,368] we call this term the $G3W2$ term. The complete self-energy up to third order in W is called $GW + G3W2$ self-energy,

$$\Sigma^{GW+G3W2}(1,2) = \Sigma_H(1,2) + iG(1,2)W(1^+,2) - G(1,3)W(1,4)G(3,4)G(4,2)W(3,2) \tag{2.363}$$

and is shown diagrammatically in figure 2.6.

The structure of the $G3W2$ self-energy terms has been scrutinized by Stefanucci, Pavlyukh, van Leeuwen and coworkers.[137,293] We follow their work and use the framework of the Keldysh formalism to discuss the $G3W2$ self-energy.[137,373,374] In the Keldysh formalism, we work on the contour $\mathcal{C} = \mathcal{C}^+ \cup \mathcal{C}^-$, with $\mathcal{C}^+$ being the backward branch and $\mathcal{C}^-$ being the forward branch. The time-ordered (anti-time-ordered) Green's function G^{--} (G^{++}) is built from field-operators evolving on $\mathcal{C}^-$ ($\mathcal{C}^+$) while lesser ($G^{-+} = G^<$) and greater $G^{+-} = G^>$ Green's function involve both branches and describe propagation of holes and particles, respectively. In the same way, the dynamically screened interaction can either connect both different branches on the Keldysh contour ($W^{+-} = W^>$ and $W^{-+} = W^<$) or not (W^{--} and W^{++}). However, a static interaction line can only connect points on the same branch of the Keldysh contour.[374]

As shown in figure 2.7a), greater and lesser component of the second-order contribution consist of four terms each, since both intermediate vertices can connect both branches of the Keldysh

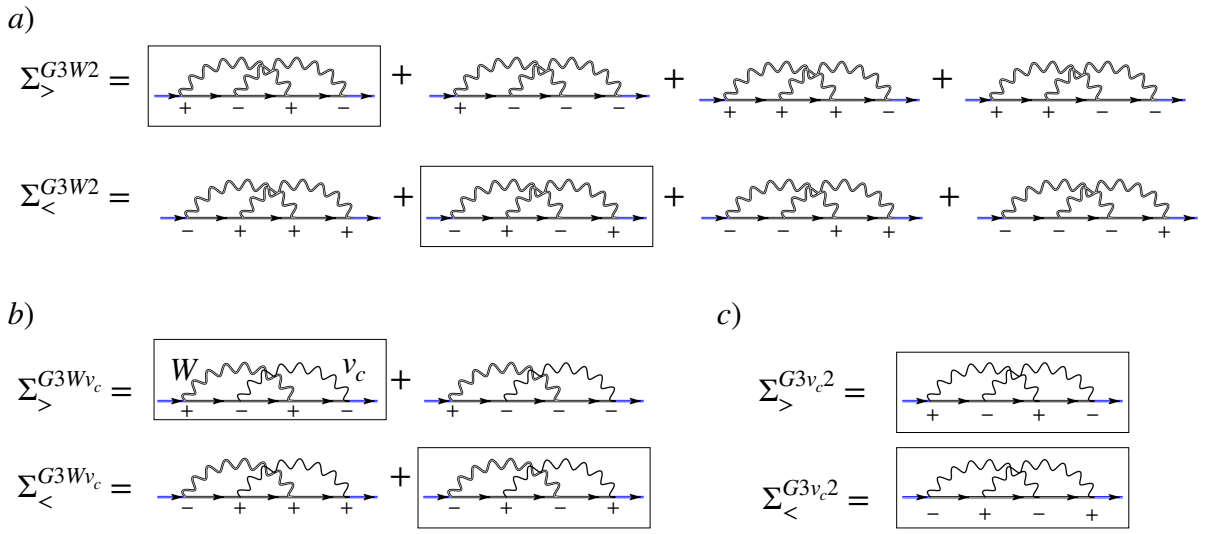

Figure 2.7: Diagrammatic representation of the different contributions to the second order exchange (SOX) term on the Keldysh contour with different Coulomb interaction types. The terms in the black boxes are the ones in which the vertices with pluses and minuses alternate. a) Greater and lesser contributions to the full $G3W2$ the self-energy term. b) Greater and lesser components of the SOX term in the SOSEX self-energy c) Greater and lesser components of the SOX term of the MP2 self-energy. The static approximation to the $G3W2$ self-energy looks the same, with the bare electron-electron interaction lines replaced by the statically screened ones. Again, the black part of the diagrams are the contributions to the self-energy only which, combined with the blue lines yield the corresponding single-particle propagator.

contour. Together, the four diagrams describe three distinct scattering processes.[293,375] Among others, they are responsible for spectral features which do not appear in fully self-consistent GW, like the excitation of two plasmons and two particle hole pairs. In this work, these terms should be of minor relevance only since we are interested in improving QP energies and correlation energies. The diagrams in the boxes in fig. 2.7a), however, only contribute to the $2h1p$ ($1h2p$) space and describes the exchange of two final particles/holes.[293] It ensures the antisymmetry of the 4-point vertex to first order in the electron-electron interaction. This can be verified by inspecting the kernel which is used to generate these diagrams and applying (2.294).

We have already shown that the inclusion of the first-order contribution to the vertex in the BSE for χ (2.200) gives (2.315). Kutepov has solved Hedin's equations in a fully self-consistent fashion using (2.315) for χ and (2.363) for Σ without any static approximations. He has applied the second-order self-energy variant (coined $GW + G3W2$) to a wide range of metals, semiconductors, and insulators,[367–372] and observed major improvements over fully

self-consistent GW for spectral properties using the $GW + G3W2$ approximation to the self-energy. According to his work, the vertex corrected calculations should be performed without any constraining approximations. This means, Hedin's equations should be solved fully self-consistently and the frequency dependence of all quantities should be properly accounted for. As many other authors,[176,282,292,345,353–356,360–364,376–378] he also emphasized the importance of vertex corrections in the BSE for χ to correctly describe the screening in periodic systems.

In a recent study, the $GW + G3W2$ self-energy has also been employed by Rinke, Ren and coworkers[379] to ionization potentials and electron affinities of molecules. Rinke, Ren and coworkers used the dynamically (RPA) screened interaction and did not consider any self-consistency in solving Dyson's equation. Improvements over GW were found to be substantial, especially for electron affinities and the dependence on the starting point was reduced.[379]

Static Approximations The evaluation of the $G3W2$ term with the full frequency dependence is computationally already very involved. It is therefore tempting to reduce the computational effort of this diagram by invoking statical approximations to W. This can either be done by replacing W with $W^{(0)}$. It can be seen that this reduces the complexity of the calculations since each electron-electron interaction line which is approximated as static reduces the number of self-energy diagrams on the Keldysh contour by a factor of two. This can also be shown quite easily by performing the integrals over time analytically but we postpone this discussion to the next chapter.

The procedure is also illustrated in figure 2.7. With the replacement $W \to W^{(0)}$ for one of the electron-electron interaction lines in the complete $G3W2$ term, the $G3Wv_c$ self-energy is obtained in which greater and lesser contributions to the self-energy only consist of two term each instead of four. This self-energy approximation is commonly known as second-order screened exchange (SOSEX),

$$\Sigma^{\mathrm{SOSEX}(W,v_c)}(1,2) = -\int d3d4 G(1,3)W(1,4)G(3,4)G(4,2)W^{(0)}(3,2)\ . \tag{2.364}$$

SOSEX has already been introduced in the context of CC theory by Freeman.[380] By now, the merits of the SOSEX self-energy for the calculation of single-particle excitations have been assessed in many articles.[242,381–383] The SOSEX self-energy is also obtained by taking the functional derivative of the HF self-energy with respect to the single-particle Green's function instead of the GW one. Maggio and Kresse[131] and Vlček and coworkers[297] have also assessed the combination of the SOSEX self-energy with screening in the TD-HF approximation eq. (2.293). This approach can be understood as a full iteration of Hedin's equations beyond HF: The functional derivative of the HF self-energy with respect to G results in the TD-HF approximation for χ and the SOSX self-energy for Σ. However, in non of these studies the GW equations have been solved self-consistently and the results did not show any improvements over G_0W_0 with a judiciously chosen starting point. For correlation energies, SOSEX has been shown to give major improvements over plain RPA.[305,333,334,384–386]

MP2 If one also replaces the second dynamically screened electron-electron interaction line by the bare electron-electron interaction, the $G3v_c2$ self-energy shown in figure 2.7c) is obtained. Since the electron-electron interaction in this term is completely unscreened, combination of this self-energy contribution with the GW self-energy does not seem to be reasonable and has not been pursued to the best of our knowledge. However, this term is identified as one of the two second-order diagrams in the skeleton expansion of the irreducible self-energy in figure 2.1c). This term is typically referred to as the second-order exchange (SOX) term. We have already seen that the other second-order term in figure 2.1c) is contained in the GW self-energy (see figure 2.5a) and figure 2.5b)) Combining these terms with the HF self-energy one has all contributions to the self-energy up to second order in $W^{(0)}$.

The Green's function resulting from the self-consistent solution of Dyson's equation within this approximation to Σ is sometimes called second-order Green's function (GF2).[387,388] If the correlation energy within this approximation is evaluated perturbatively using a HF Green's function, this approximation is known as second-order MP perturbation theory.[306] Screening effects are entirely absent in MP perturbation theory and electron correlation is described by HF QPs interacting via the bare Coulomb interaction instead, neglecting the fact that the interactions between the HF QPs are generally much weaker than the ones between the undressed electrons. This issue is also present in orbital optimized MP2 in which the HF QPs are replaced by MP2 QPs.[389–391] Therefore, MP2 is a suitable method only for (typically small) systems in which screening effects are negligible. The divergence of MPPT for the uniform electron gas (see for instance chapter 10 in ref. [112] for a thorough discussion) is known at least since early work by Macke[111] and has been demonstrated later on for metals[392] and recently also for large, non-covalently bound organic complexes.[393] The divergence of the MP series for small-gap systems is directly related to this issue since the magnitude of the screening is proportional to the width of the fundamental gap.[175,282] Due to its relatively low computational cost and its widespread availability in quantum chemistry codes, here have been various approaches to regularize MP2 by an approximate treatment of screening effects, either using empirical[394–404] or diagrammatically motivated modifications[405–408] or attacking the problem from a DFT perspective.[409,410] Therefore, for the calculation of correlation energies MP2 is mostly relevant as ingredient in DH density functionals,[208,217,218,411–413] as a stepping stone in the implementation of more advanced methods and it is a key ingredient in (local) CC codes.[414–417] MP2 and its third-order extension MP3 have also been investigated for the description of single-particle excitations in finite systems for which is seems to be generally applicable[383,387,418–421] but not necessarily accurate[383]

Statically screened $G3W2$ Instead of replacing W with $W^{(0)}$ in the $G3W2$ term, one can also take the static limit by taking the static limit in both W ($W \to W(0)$) which leads to the statically screened second-order exchange contribution to the self-energy,

$$\Sigma^{\mathrm{SOSEX}(W(0),W(0))}(1,2) = -\int d3d4 G(1,3)W(1,4)G(3,4)G(4,2)W(3,2)\delta(\tau_{32})\delta(\tau_{14}) \; . \quad (2.365)$$

To distinguish this self-energy approximation from the SOSEX self-energy described before, we will refer to the former one as SOSEX(W,v_c) and to the statically screened version as SOSEX($W(0)$,$W(0)$). The computation of this version of SOSEX is computationally more efficient than SOSEX(W,v_c) since no expensive numerical frequency integration is required.

Following Jansen *et al.*[384] we will also use the term AC-SOSEX, where AC stands for adiabatic connection and should not be confused with analytical continuation, a numerical technique wich will be introduced in the following chapter and which we will abbreviate with AC as well. One can derive an energy expression similar do SOSEX as a subset of the CCD equations by only taking into account ring diagrams but with antisymmetrized electron repulsion integrals, $(pq||rs) = v_{pqrs} - v_{psrq}$ in the spin-orbital basis. This is typically termed ring-CCD (rCCD)[384,422,423] and has been introduced by Freeman.[380] If one evaluates the rCCD equations with non-antisymmetrized electron repulsion integrals only, one obtains direct rCCD (drCCD) which is completely equivalent to the RPA correlation energy expression.[422] The SOSEX correlation energy which can be derived from (2.364) is formally not completely equivalent to the one from rCCD[384] even though the numerical differences are too small to be relevant in practice.[334] To distinguish between both variants, Jansen *et al.* termed rCCD SOSEX and referred to the energy expression derived from (2.364) as AC-SOSEX.

Equation (2.365) can be written as

$$\Sigma^{\text{SOSEX}(W(0),W(0))}(1,2) = \Sigma^{\text{MP2-SOX}}(1,2) + \Sigma^{\delta\text{MP2-SOX}}(1,2) \; , \tag{2.366}$$

with the first term being the SOX term in MP2 and with the remainder accounting for the screening of the electron-electron interaction. Defining

$$\delta W(1,2) = \int d3d4 W^{(0)}(1,3) P(3,4) W^{(0)}(4,2) \; , \tag{2.367}$$

it can be written as

$$\Sigma^{\delta\text{MP2-SOX}}(1,2) = -\int d3d4 G(1,3)\delta W(1,4)\delta(\tau_{14}) G(3,4) G(4,2)\delta W(3,2)\delta(\tau_{32}) \; . \tag{2.368}$$

One can make a similar decomposition for SOSEX(W,v_c). The MP2 self-energy only contains all skeleton diagrams to first and second order and therefore strictly fulfills the crossing symmetry. Therefore, all of the corrections we have derived here from the $G3W2$ fulfill the crossing symmetry to first order in $W^{(0)}$. Therefore, we can expect that all of these approximations compensate the overestimation of the electron correlation energy in the RPA.

For QP energies in solids, the statically screened $G3W2$ correction to the self-energy has first been introduced by Grüneis et al.[360] who used this term to calculate perturbative corrections to qsGW[142,175] QP energies. They also combined this method with a beyond RPA screening of the Coulomb interaction using a static exchange-correlation kernel. As Kutepov, they reported major improvements over the GW method for the band structures of solids. Comparing their results to Kutepov's, the logical conclusion would be, that the errors introduced by the static

approximation, the use of a non-interacting Green's function, and the perturbative treatment of the $G3W2$ cancel to a large extent. A recent study by Kutepov has confirmed this conjecture.[372] From a pragmatic point of view this is of course convenient, since all of these approximations come with drastically reduced computational cost compared to the rigorous, self-consistent formalism[424].

To a large part, chapter 5 will focus on assessing the accuracy of the SOSEX($W(0)$,$W(0)$) correction to GW for total correlation energies of atoms, interaction energies of non-covalently bound complexes, as well as charged excitations of a wide range of molecular systems.

Chapter 3

Numerical Implementation

In chapter 2 we have used MBPT to rewrite N-electron problem as the problem of calculating the skeleton expansion of the electronic self-energy. Even in terms of the screened electron-electron interaction, the skeleton series contains an infinite number of terms and in section 2.4 we have introduced different approximations to it. In a next step, we have introduced QP and diagonal approximations to the self-energy as well as static approximations to the screened interaction. These approximations are of course motivated by numerical constraints but they are of physical nature: we have selected certain patterns of electron-electron interactions which we believe (or know) to dominate the physics of the problems we would like to solve.

In this chapter, we turn to the numerical implementation of these equations with low scaling with system size and with a low prefactor. Achieving Low-order scaling implementations of the GW approximation for periodic and finite systems has been a very active area of research over the past decades[6,36,134,269,272,425–439] and also efficient implementations of the BSE@GW approximation[39,440–444] and even vertex corrections[382] have been achieved. In a series of articles[36–39] we have also contributed to these efforts.

In section 3.1 we will introduce a real space discretization by transforming our equations to the spin-orbital basis and by expanding the spatial orbitals in terms of localized atomic orbitals (AO). The choice of this basis of AOs is crucial for the efficient implementation of the equations. All 4-point correlation functions can be represented as 4-leg tensors in this basis even though the polarizability $P^{(0)}$, the electron-electron interaction v_c as well as their reducible counterparts only depend on two spatial coordinates. We have already seen this for the Coulomb potential eq. (2.74). For these quantities the AO-based representation is inefficient and we will introduce a more suitable auxiliary basis in which the 4-point correlation functions transform as 2-leg tensors. The efficient implementation of the transformation between both bases, known as density fitting (DF),[445–452] is thereby decisive. To calculate this transformation we will use the pair-atomic density fitting (PADF) approximation,[453–462] sometimes also referred to as concentric density fitting or pair-atomic resolution of the identity (PARI) which allows for transformations from the primary basis to the auxiliary basis and back with quadratic scaling with system size.

Next, we will describe our strategy for the discretization of time or frequency. The poles of the single-particle Green's function correspond to single-particle excitation energies which can be probed in (inverse) photoemission experiments and the poles of the generalized susceptibility correspond to the energies of bound electron-hole pairs, so called excitons, which can be identified with the positions of the peaks in optical spectra. These poles are located on the real frequency axis. For this reason, it is numerically inefficient to work in real frequency space since often a rather large number of integration points will be required to obtain accurate results.[463] Following Godby and coworkers[132,133] we will work mostly on the imaginary time and imaginary frequency axes instead. This necessitates efficient ways to discretize these domains and to transform quantities from imaginary time to imaginary frequency and back. Finally, we need to model the behavior of the self-energy in the whole complex plain using information from the imaginary frequency dependence only. This so-called analytical continuation (AC) of the self-energy is exact in principle if the self-energy is known at an infinite number of points including the points at infinity,[464,465] but extremely ill-conditioned from a numerical perspective.[466,467]

We have already mentioned that some of the methods introduced in section 2.4 need to be solved self-consistently. This is always necessary when solving an equation of the type (2.131): We wish to calculate G, but the kernel Σ which maps $G^{(s)}$ to G depends on G. We will outline our strategy to solve such problems using iterative subspace algorithms.[468,469] After introducing these approximations, we can combine them with the results of section 2.4 and write down the working equations we have implemented in ADF. The careful analysis of the errors which are introduced by these approximations are the subject of chapter 4.

To keep the notation of this chapter light we give all single-particle energies with respect to the chemical potential μ. Also, we will frequently use the abbreviations

$$\sum_i = \sum_k \Theta(\mu - \epsilon_k)$$

and

$$\sum_a = \sum_k \Theta(\epsilon_k - \mu) \ ,$$

with the understanding that summations over $i, j \ldots$ $(a, b, \ldots)$ run over occupied (unoccupied) states only. The labels $k, l, m \ldots$ are reserved for general single-particle orbitals. $\mu, \nu, \kappa, \lambda$ will denote atomic orbitals, $\alpha, \beta, \gamma, \delta$ will label auxiliary functions, and $A, B, C, D \ldots$ will label atomic centers. We will often perform summations over indices corresponding to functions centered on a particular atomic center. For instance, $\sum_{\alpha \in A}$ means that α runs over all auxiliary basis functions centered on atom A.

3.1 Discretization

3.1.1 Basis Sets

A discrete representation of our working equations starts with the expansion of the single-particle states in terms of a second set of functions,

$$\phi_k(\boldsymbol{r}) = \sum_{\mu}^{N_{\text{bas}}} b_{\mu k}\chi_\mu(\boldsymbol{r}) \ . \tag{3.1}$$

We call χ a basis function, and the set of N_{bas} functions which we use to represent ϕ_k is called a primary basis set. Unless the primary basis set spans the entire single-particle Hilbert space, eq. (3.1) is an approximation. In practice, we assume that we can find a sufficiently large N_{bas} so that

$$\phi_k(\boldsymbol{r}) \approx \sum_{\mu}^{N_{\text{bas}}} b_{\mu k}\chi_\mu(\boldsymbol{r}) \ , \tag{3.2}$$

i.e. that the error introduced by this expansion is small. Using the expansion (3.1) then restricts the number of single-particle states to N_{MO} where $N_{\text{MO}} \leq N_{\text{bas}}$ for a closed-shell, and $N_{\text{MO}} \leq 2N_{\text{bas}}$ for an open shell system.

The complete Basis Set Limit

Since the MOs depend on $\boldsymbol{r}$ One could choose dirac delta functions or different flavours of splines as basis functions in (3.1). This is often done for spherical systems where one can work in polar coordinates[169,298,470–472] but also sometimes for molecules as for instance in refs. [473, 474]. The straightforward sampling of the whole $\mathbb{R}^3$ with equidistant grid points is easy to implement and allows for a uniform convergence to the complete basis set (CBS) limit, i.e. the limit in which the error introduced by the expansion eq. (3.1) vanishes,

$$\phi_k(\boldsymbol{r}) \simeq \sum_{\mu}^{N_{\text{bas}}} b_{\mu k}\chi_\mu(\boldsymbol{r}) \ . \tag{3.3}$$

With uniform convergence (on $\mathcal{R}^3$), we mean that there is an integer N'_{bas}, so that $\forall\epsilon > 0$

$$\left|\phi_k(\boldsymbol{r}) - \sum_{\mu}^{N_{\text{bas}}} b_{\mu k}\chi_\mu(\boldsymbol{r})\right| < \epsilon \ , \quad \forall N_{\text{bas}} > N'_{bas} \forall \boldsymbol{r}, k \ , \tag{3.4}$$

when the set of all ϕ_k is restricted to a finite subset. For delta functions or their equivalent in reciprocal space, plane waves (PW), one can show that they indeed fulfill (3.4). This is due to the fact that PWs are eigenfunctions of the kinetic energy operator.

$$-\frac{1}{2}\nabla^2 e^{i\boldsymbol{G}\boldsymbol{r}} = \frac{1}{2}\left|\boldsymbol{G}\right|^2 e^{i\boldsymbol{G}\boldsymbol{r}} \ . \tag{3.5}$$

The kinetic energy operator is a Sturm-Liouville operator and therefore the property (3.4) follows as a corollary form the Sturm-Liouville expansion theorem.[475] This also implies the validity of (3.4) for the χ_μ being dirac deltas (with appropriate boundary conditions[475]) since the uniform convergence property also holds in Fourier space. One can then increase N_{bas} by decreasing the centers of the dirac deltas and evaluate the error of the expansion using (3.4) until the error vanishes.

Atomic Orbital Basis sets

While uniform convergence is a strong argument for using dirac delta basis sets, the downside of this approach is that a very large N_{bas} will be needed to converge the expansion. However, the aim of the expansion (3.1) is to provide the best representation of the ϕ_k with as small a N_{bas} as possible.

The solutions of the Schrödinger equation describing the hydrogen atom decay exponentially from the atomic center and have a cusp at the position of the nucleus due to the singularity of the external potential. Furthermore, each of these states can be characterized by three quantum numbers describing the electron's energy, angular momentum, and an angular momentum vector component. The situation is qualitatively similar for atoms with more than one electron. Since a molecule is composed of atoms one might therefore make the assumption that much of the information which is needed to describe the behavior of the molecular orbitals is already contained in the atomic orbitals. For this reason one typically uses atomic orbitals in the expansion (3.1). The expansion (3.1) is then typically referred to as the linear combination of atomic orbitals (LCAO) method. It is important to notice here that it is inefficient to use directly the solutions of the Schrödinger equation for the Hydrogen atoms. When we refer to atomic orbitals in the following we mean basis functions which resemble, loosely speaking, the hydrogenic orbitals: More precisely, we denote all basis functions as AOs which are exponentially decaying for $|\boldsymbol{r}| \to \infty$ and atom-centered.

There are many possible realizations of this type of basis functions: Sturmians[476–480], reduced Bessel functions,[481–483] Slater type orbitals (STO)[446,484–487], Gaussian type orbitals (GTO)[488,489] or any other type of atomic orbitals which do not have an analytical expression, typically referred to as numerical atomic orbitals (NAO).[490–493] The algorithms we will outline in this chapter can be implemented with any of these types of basis functions.

Compared to the other types of AOs, GTOs have favorable analytical properties which allow the efficient semi-analytical evaluation of integrals of the type (2.74). Therefore, they became very popular in the early days of quantum chemistry and are still the most popular type of basis functions. For an overview over the different types of GTO-type basis sets for non-relativistic calculations, see ref. [489]. Bessel functions and Sturmians are essentially not used in practical applications.[1] STOs are used in the Amsterdam density functional (ADF) code[446,496] in which

[1] Interestingly, reduced Bessel functions combine a variety of interesting properties which could make them a suitable choice as basis functions for molecules: An integral involving the Coulomb potential and three atomic centers which arise in DF can be solved analytically except for a semi-infinite 1-center integral. Furthermore, any

all the algorithms introduced in this thesis have been implemented. One typically hopes, that one approaches the CBS limit faster with STOs than with GTOs. Therefore, they are sometimes used in calculations where the evaluation of molecular integrals is relatively inexpensive compared to tensor contractions of matrices in the AO or MO basis.[497] This also the motivation for using NAOs. Popular NAO-based codes are FHI-AIMS[492,498,499] and BAND.[491]

Extrapolation to the Complete Basis set Limit

The uniform convergence of a basis set expansion allows for the extrapolation to the CBS limit. This is only helpful if the convergence rate of the expansion is known and it is typically impossible to determine this property analytically. However, to obtain converged MBPT results it is in most cases decisive to perform extrapolations to the CBS limit. One then typically resorts to numerical experiments and fits the empirical results to analytical formulas which describe the error introduced by (3.1) as a function of N_{bas}. For GW calculations with PW basis sets, there is for instance numerical evidence that the QP energies converge like $\frac{1}{N_{\text{bas}}}$.[500] Interestingly, the same behavior has been observed in GW calculations for molecules.[501] For correlation energies, different extrapolation schemes are in use.[502] The most popular techniques is possibly the one introduced by Helgaker and coworkers in ref. [503]

3.1.2 Slater Type Orbital Basis Sets

In this section, we will describe the design of STO-type basis sets which are suitable for MBPT calculations. In this context, the index μ in eq. 3.1 becomes a composite index, collecting the five defining parameters of a Slater type function

$$\chi_\mu(r,\theta,\phi) = \chi_{A,\alpha,n,l,m}(r,\theta,\phi) = C(\alpha,n) r^{n-1} e^{-\alpha r} Z_{lm}(\theta,\phi) \;, \quad r = |\boldsymbol{r} - \boldsymbol{R}_A| \;, \tag{3.6}$$

the exponent α and the quantum numbers (n,l,m), as well as the nucleus A on which the function is centred. In (3.6), $C(\alpha,n)$ is a normalization constant and Z_{lm} denotes a real spherical harmonic. The main difference to Gaussian type functions is in the dependence of the exponential on r instead of r^2 which mainly results in a different behavior close to the atomic nuclei and a slower decay for large r. While STO-type basis sets are well developed for independent-electron methods[487,504–507] we are not aware of any attempt to construct general Slater type basis sets which are consistent with the requirements of correlated electrons methods. Here, we make a first attempt to present such basis sets for the whole periodic table. Notice, that the concept of correlation consistency has also been applied to NAO basis sets for RPA total energy calculations.[493]

STO can be exactly expanded in terms of spherical Bessel functions.[482,494] The resulting 1-centers integrals are difficult to evaluate numerically but it has recently been shown that a more favorable expression can be obtained by applying an S transformation which converts them to sine integral.[495]

Correlation Consistent Atomic Basis Sets

In the construction of our basis sets we make two assumptions: First, we assume that the principles guiding the construction of GTO-type basis sets for correlated-electron methods which have been developed over the last decades should be applicable to STO-type basis sets as well. This can be justified as follows: Based on numerical experiments on correlation consistent GTO-type basis sets, Helgaker et al.[503] established the relation

$$E_{\infty}^{corr} - E_{X}^{corr} = aX^{-3} \tag{3.7}$$

between the correlation energy E_{∞}^{corr} at the CBS limit and the correlation energy E_{X}^{corr} calculated with a given correlation consistent basis set with cardinal number $X = l_{max} + 1$. Conceptually, their formula is based on earlier work by Schwartz[508] and the mathematical more rigorous work by Hill[509] on the convergence of the ground state of the Helium atom in a full configuration interaction calculation with respect to the single-particle basis. Later on, Kutzelnigg and Morgan[510] generalized that result to arbitrary n-electron systems for MP2 calculations.

In principle, (3.7) is only valid in the limit of large X, however, there is numerical evidence that it is already a good approximation for $X = 3$ and $X = 4$.[503,511] Since (3.7) is independent of the type of localized basis functions[508–510], this should also be the case for STO-type basis sets provided that they are also constructed in a correlation consistent fashion as first defined by Dunning;[512] such that the total basis set incompleteness error is distributed equally between the different angular momenta functions. This requires that polarization functions are added in well-defined sequences.[489] There is numerical evidence that the consistent polarization for correlated methods is $1p$ on the double-ζ (DZ), $2p1d$ on the TZ and $3p2d1f$ on the QZ level for first-row, and $1d$ on the double-ζ (DZ), $2d1f$ on the TZ and $3d2f1g$ on the QZ level for second- and third row elements[489] and analogously for first-row atoms. The design of correlation consistent basis sets for heavier elements might follow different principles.[513–517]

Construction of Correlation Consistent Slater-Type Basis sets

Based on the considerations above, we construct correlation consistent basis sets of TZ and QZ quality. We name these basis sets TZ3P and QZ6P, respectively. We also add additional diffuse functinos to these basis sets. The sets containing those functionas are named aug-TZ3P and aug-QZ6P. The acronym xP refers to the number of polarization functions we use for the elements of the first three rows of the periodic table. This choice is consistent with the requirements for correlation consistent basis sets stated above.

At this point, we introduce our second assumption: Since the ADF code only supports basis functions up to $l = 3$, for second- and third-row elements we chose the polarization $2d1f$ and $3d3f$ for TZ and QZ respectively, and for consistency also $2p1d$ and $3p3d$ for Hydrogen and Helium. A good justification for the validity of this approximation can not be given and as we will see later, our results indeed suggest that the replacement of a g with another f function negatively affects the QP energies for small molecules. Generalization of ADF to accommodate

use of higher angular momenta functions is therefore desirable. Therefore, we emphasize that the basis sets we are constructing here are not correlation consistent in a strict sense but rather as correlation consistent as possible in our current implementation.

The TZ2P and QZ4P basis sets which have been described in detail in ref. [487] serve as starting points for our new basis sets. TZ2P (QZ4P) is of DZ (TZ) quality in the core region and of TZ (QZ) quality in the valence region. For the TZ3P and QZ6P basis sets, we chose not to optimize exponents but rather to add additional polarization functions in an ad-hoc manner. This approach can be justified by the observation that precise values of exponents become less important as a basis set approaches completeness.[489,504] This is especially true for molecules as opposed to isolated atoms. The latter case generally requires larger and more optimized basis sets than the molecular case. Instead, we rather focus on choosing the exponents in a way that their overlap is small and linear dependency problems are more likely to be avoided.

TZ3P is simply obtained by augmenting the TZ2P basis set by another $l_{occ}+1$-function for all elements. The exponent is chosen so that it is twice as large as the exponent of the $l_{occ}+1$-function in the TZ2P basis set. This is due to the fact that the exponents of the polarization functions in the TZ2P and QZ4P basis sets are chosen in a way that the basis sets become more accurate in the valence region, which is favorable for the calculation of bonding energies. The calculation of IPs also requires the accurate representation of the electron density closer to the core, and TZ3P should yield a major improvement over TZ2P in that respect. The same reasoning has also been followed in ref. [518]. In complete analogy, the QZ6P basis set is obtained by adding an additional tight $l_{occ}+1$-function and an $l_{occ}+2$-function for all elements.

The exponents α_1, α_2 of the polarization functions in the QZ4P basis set fulfill $\frac{\alpha_1}{\alpha_2} \approx 2$ for each l. Thus, the polarization functions in the TZ3P and QZ6P basis sets loosely follow an even-tempering scheme[519],

$$\alpha_i = \alpha_1 \beta^{i-1} , \quad i = 2, \ldots, M , \quad \beta = 2 , \tag{3.8}$$

with M being equal to two (three) for $l_{occ}+1$ in TZ3P (QZ6P) and one (three) for $l_{occ}+2$. The value of β is rather large to avoid linear dependency problems, and in conjunction with a rather small α_1 ensures that the exponents span a rather wide range of values in the QZ6P case.[520] Ren et al. recently used a similar reasoning to chose the exponents of Slater type functions for G_0W_0 calculations for periodic systems.[521]

Adding Diffuse Functions

It is known from electron scattering experiments that molecular electron affinities are sometimes negative, i.e. their anion state at the geometry of the neutral molecule is unstable.[522–524] This corresponds to a positive LUMO QP energy which formally corresponds to a non-normalizable continuum orbital. However, as an artefact of working with a finite basis, the orbital will always be constrained to be normalizable.[525] Very diffuse functions are then needed to mimic the continuum state, and for this reason we augment our basis sets with additional diffuse functions (See also ref. [526] and ref. [527]). The resulting basis sets are denoted as aug-TZ3P and aug-QZ6P

and are obtained from TZ3P and QZ6P, respectively by adding diffuse s, p and d-functions for all element types, with the important exceptions of first row atoms where we only add diffuse s and p functions.[2] We decided to chose the exponents of the diffuse functions in line with (3.8), except for a small shift. More precisely, the exponent of the most diffuse function for a given angular momentum is $\alpha_{l,min}$, the exponents of the diffuse function is chosen to be

$$\alpha_{l,diffuse} = \alpha_{l,min}/2 + 0.05\alpha_{l,min} \tag{3.9}$$

The exceptions are the elements Hydrogen to Beryllium for which we chose the already optimized exponents by Chong et al.[528] These exponents are very close to fulfilling (3.9). Our choice of exponents is a compromise between two requirements: We would like the additional functions to be as diffuse as possible but we still want to be able to fit them accurately with a large auxiliary basis set, which, as we will discuss in chapter 3.1.3, is already challenging. In practice, this means that $2\alpha_{l,diffuse}$ should be at least equal or preferably slightly larger (for this reason we added the shift in (3.9)) than the exponent of the most diffuse function in the auxiliary basis set.

3.1.3 Auxiliary Basis Sets and Basis Transformations

We have already seen that the electron-electron interaction in the MO basis eq. (2.74) becomes a 4-index tensor. This obviously does not change when we transform to the AO basis. Using

$$\begin{aligned} v_{klmn} &= \sum_{\mu\nu\kappa\lambda} \int d\boldsymbol{r} \int d\boldsymbol{r}' b^*_{\mu k} \chi_\mu(\boldsymbol{r}) b_{\lambda n} \chi_\lambda(\boldsymbol{r}) v_c(\boldsymbol{r},\boldsymbol{r}') b^*_{\nu l} \chi_\nu(\boldsymbol{r}') b_{\kappa m} \chi_\kappa(\boldsymbol{r}') \\ &= \sum_{\mu\nu\kappa\lambda} b^*_{\mu k} b_{\lambda n} v_{\mu\lambda\nu\kappa} b^*_{\nu l} b_{\kappa m} \ , \end{aligned} \tag{3.10}$$

the Coulomb potential in the AO basis is

$$v_{\mu\nu\kappa\lambda} = \int d\boldsymbol{r} \int d\boldsymbol{r}' \chi_\mu(\boldsymbol{r}) \chi_\nu(\boldsymbol{r}) v_c(\boldsymbol{r},\boldsymbol{r}') \chi_\kappa(\boldsymbol{r}') \chi_\lambda(\boldsymbol{r}') \ . \tag{3.11}$$

This implies that all operations involving a contraction of the form (2.144) (or inversions, diagonalizations and related operations which can be formulated in terms of matrix multiplications) will scale as N^6 in the basis of AOs or MOs. While this scaling is difficult to circumvent for quantities which depend on 4 coordinates in real space like the 2-particle Green's function, the scaling of N^6 is simply an artefact of the chosen representation for all 4-point quantities which only depend on 2 spatial coordinates.

[2] This is slightly different from usual augmentation approaches encountered for Gaussian type basis sets. Dunning and coworkers defined the prefix "-aug" to mean adding an additional diffuse functions for all angular momenta already present in a basis set for every atom type.[526] On the contrary, in a process which they denoted as minimal augmentation, Truhlar and coworkers only added diffuse s and p functions to all elements heavier than Hydrogen.[527] Our approach is can be seen as a compromise between both.

While this might be clear from physical considerations, it can also demonstrated by numerical experiments that the rank of such quantities grows slower than their dimension with system size: The Eckard–Young theorem[529–531] guarantees the optimal rank-r approximation $M^{(r)}$ to some matrix M to be given by the first r terms in the sum on the *r.h.s.* of

$$M^{(r)} = \sum_{i}^{r} \sigma_i v_i \otimes u_i, \quad \sigma_i \geq \sigma_{i+1} \ , \tag{3.12}$$

where σ is a singular value and v_i and u_i are vectors of the matrices v_c and U from the singular value decomposition (SVD) of M. In this way one can indeed show that the ranks of $P^{(0)}$, v_c and W should only grow linearly with system size[532] and using (3.12) one might decompose $P^{(0)}$ and v_c and therefore also their reducible counterparts as

$$M_{\mu\nu\kappa\lambda} = \sum_{\alpha\beta} C_{\mu\nu\alpha} Z_{\alpha\beta} [C^T]_{\beta\kappa\lambda}, \quad M = P^{(0)}, v_c \ , \tag{3.13}$$

where Z is the diagonal matrix of singular values and C collects the left singular vectors of M. An explicit SVD would scale as $N_{\text{bas}}^4 r$ and is prohibitive in practice.[532] Instead, it is common to represent v_c and W in a predefined auxiliary basis $\mathcal{A} = \{f\}$, growing linearly with system size. Expanding all products of AO pairs in terms of $\mathcal{A}$,

$$\chi_\mu(\boldsymbol{r})\chi_\nu(\boldsymbol{r}) = \sum_{\alpha} C_{\mu\nu\alpha} f_\alpha(\boldsymbol{r}) \ , \tag{3.14}$$

v_c and W can be expressed as

$$v_{\alpha\beta} = \int d\boldsymbol{r} d\boldsymbol{r}' f_\alpha(\boldsymbol{r}) v_c(\boldsymbol{r}, \boldsymbol{r}') f_\beta(\boldsymbol{r}') \tag{3.15}$$

$$W_{\alpha\beta} = \int d\boldsymbol{r} d\boldsymbol{r}' f_\alpha(\boldsymbol{r}) W(\boldsymbol{r}, \boldsymbol{r}') f_\beta(\boldsymbol{r}') \ . \tag{3.16}$$

For historical reasons, this is known as density fitting (DF), sometimes also denoted as resolution of the identity (RI).[533,534] The same goal can be achieved by using Cholesky decomposition (CD) methods[535–539] which can be seen as on-the-fly generations of auxiliary basis sets.

We see that eq. (3.15) is related to (3.11) by a basis transformation which can generally be written as

$$C : v^{\mathcal{P}} \mapsto v^{\mathcal{A}} \tag{3.17}$$

and in the special case of v_c, we have through (3.14)

$$v_{\mu\nu\kappa\lambda} = \sum_{\alpha\beta} C_{\mu\nu\alpha} v_{\alpha\beta} C_{\kappa\lambda\beta} \ . \tag{3.18}$$

For the implementation of the SOX term and for the solution of the BSE@GW equations we will also need to transform the bare and screened electron-electron interactions from the auxiliary basis to the MO basis. This is achieved by combining (3.1) and (3.14),

$$\phi_k(\boldsymbol{r})\phi_l(\boldsymbol{r}) = \sum_{\mu\nu}\sum_{\alpha} b_{\mu k} b_{\nu k'} C_{\mu\nu,\alpha} f_\alpha(\boldsymbol{r}) = \sum_{\alpha} C_{kl\alpha} f_\alpha(\boldsymbol{r}) \ , \tag{3.19}$$

in which we have defined

$$C_{kl,\alpha} = \sum_{\mu,\nu} b_{\mu k} C_{\mu\nu,\alpha} b_{\nu l} \ , \tag{3.20}$$

and therefore

$$M_{pqrs} = \sum_{\alpha\beta} C_{pq\alpha} Z_{\alpha\beta} [C^T]_{\beta rs}, \quad M = P^{(0)}, v_c \ , \tag{3.21}$$

Using transformations of this type, the asymptotic scaling for the implementation of the GW approximation reduces to N^4. For instance, the G_0W_0 self-energy becomes

$$\begin{aligned}
\Sigma_{\mu\nu,i\tau} =& i \sum_{\kappa\lambda} G^{(s)}_{\kappa\lambda} W_{\mu\kappa\nu\lambda} \\
=& i \sum_{\kappa\lambda} G^{(s)}_{\kappa\lambda} \sum_{\alpha\beta} C_{\mu\kappa\alpha} W_{\alpha\beta,i\tau} [C^T]_{\beta\nu\lambda} \\
=& i \sum_{\kappa} \sum_{\beta} \underbrace{\left[\sum_{\alpha} C_{\mu\kappa\alpha} W_{\alpha\beta,i\tau} \right]}_{\mathcal{O}(N^4)} \underbrace{\left[\sum_{\lambda} [C^T]_{\beta\nu\lambda} G_{\kappa\lambda} \right]}_{\mathcal{O}(N^4)} \ ,
\end{aligned} \tag{3.22}$$

and the ordering of the terms clearly shows that this scales as N^4. Such a procedure, often called global density fitting, is often encountered in implementations of GW and RPA in quantum chemistry codes.[244,499,501,540–544]

Given some target precision ϵ, the two main goals of DF are first, to find a matrix M' with dimension N_{aux} for which

$$\|M - M'\| < \epsilon \tag{3.23}$$

with N_{aux} as small as possible and M defined by (3.13) and second, to improve over the N^4 scaling of (3.17) by constructing C in a way that it becomes sparse. In fact, (3.17) can be constructed in a way that the number of non-zero elements in C increases asymptotically linearly with system size, which then allows us to implement transformations eqs. (3.13) and (3.21) with quadratic scaling with system size. Both goals are in principle in conflict with each other. In DF, one minimizes the residual function

$$r_{\mu\nu}(\boldsymbol{r}) = \chi_\mu(\boldsymbol{r})\chi_\nu(\boldsymbol{r}) - \sum_p C_{\mu\nu p} f_p(\boldsymbol{r}) \quad \forall \mu, \nu \ , \tag{3.24}$$

with respect to some appropriate norm. In the RI-V approach, the Coulomb repulsion of r is minimized,

$$\frac{\partial}{\partial C_{\kappa\lambda q}} \int d\boldsymbol{r} d\boldsymbol{r}' \; r_{\kappa\lambda}(\boldsymbol{r}) v_c(\boldsymbol{r}, \boldsymbol{r}') r_{\mu\nu}(\boldsymbol{r}') = 0 \; , \tag{3.25}$$

and it follows that

$$\sum_p C_{\mu\nu p} V_{pq} = \int d\boldsymbol{r} d\boldsymbol{r}' \; \chi_\mu(\boldsymbol{r}) \chi_\nu(\boldsymbol{r}) v_c(\boldsymbol{r}, \boldsymbol{r}') f_q(\boldsymbol{r}') \; , \tag{3.26}$$

i.e. the error in the low-rank approximation of v_c is quadratic in r since the terms linear in C vanish. Of course, a similar conclusion can not be drawn for $P^{(0)}$ and consequently also not for W. Still, it seems that this metric is an excellent choice if the goal is to fulfil (3.23) with N_{aux} as small as possible and using auxiliary fit sets from standard libraries. As shown by van Setten et al, QP HOMOs and LUMOs only deviate by a few meV from the ones obtained from calculations without any low-rank approximation[501,545] when appropriate auxiliary fit sets[546,547] are used.

On the other hand, RI-V is a very bad choice in the sense that the slow decay of the kernel of the Coulomb operator ensures that C will be dense. In the RI-SVS approach,[449,452] (3.24) is minimized with respect to the L_2 norm which requires larger N_{aux} to fulfil (3.23) but results in a C with the number of non-zero elements increasing only linearly with system size for exponentially decaying basis functions. It has been shown by Wilhelm et al. that this approach results in tremendous speed-ups in the evaluation of eqs. (3.79), (3.81) and (3.82) without requiring to large N_{aux} to make the evaluation of (3.80) problematic for systems of more than 1000 atoms.[6] However, for rather small systems in which many basis functions are centered very closely to each other, the number of non-zero elements in C will not be much different from $N_{\text{bas}}^2 \times N_{\text{aux}}$. Thus, due to the usually larger N_{aux} compared to RI-V, the method will only be advantageous for sufficiently large systems.[6]

Local density fitting approximations

In local density fitting (LDF) approximations, this shortcoming is addressed by building in sparsity into the fitting procedure *a priori*. In pair atomic density fitting (PADF), an expansion of products of AOs $\chi_\mu(\boldsymbol{r})\chi_\nu(\boldsymbol{r})$ of the form

$$\chi_\mu(\boldsymbol{r})\chi_\nu(\boldsymbol{r}) = \sum_{p \in A \cup B} C_{\mu\nu p} f_p(\boldsymbol{r}) \quad \forall \mu \in A, \nu \in B \tag{3.27}$$

is used so that the number of non-zero elements in C scales at most quadratic with system size. Eq. (3.24) then becomes

$$r_{\mu\nu}^{PADF}(\boldsymbol{r}) = \chi_\mu(\boldsymbol{r})\chi_\nu(\boldsymbol{r}) - \sum_{\alpha \in A \cup B} C_{\mu\nu p} f_\alpha(\boldsymbol{r}) \quad \forall \mu \in A, \nu \in B \; , \tag{3.28}$$

and the self-repulsion of the residual

$$r_{\mu\nu}^{PADF}(\boldsymbol{r}) v_c(\boldsymbol{r}, \boldsymbol{r}') r_{\mu\nu}^{PADF}(\boldsymbol{r}') \quad \forall \mu \in A, \nu \in B$$

is minimized. This leads to an expression of the form

$$C_{\nu\mu\alpha} = \sum_{\beta\in B} O_{\mu\nu\beta} \left[v_c^{-1}\right]_{\beta\alpha} \quad \forall\mu,\alpha\in A,\nu\in B \tag{3.29}$$

for the fit coefficients where

$$O_{\mu\nu\beta} = \int d\boldsymbol{r}\chi_\mu(\boldsymbol{r})\chi_\nu(\boldsymbol{r}) \int d\boldsymbol{r}' v_c(\boldsymbol{r},\boldsymbol{r}') f_\beta(\boldsymbol{r}') \;, \tag{3.30}$$

and $v_{\alpha,\beta}$ is given by (3.15). Also, in the fit coefficients, the fit function is always assumed to be centered on the second atom. The PADF expansion of the products of AOs can then be written as

$$\chi_\mu(\boldsymbol{r})\chi_\nu(\boldsymbol{r}) = \begin{cases} \sum_{\beta\in B} b_{\mu\nu,\beta} f_\beta(\boldsymbol{r}) + \sum_{\alpha\in A} b_{\nu\mu,\alpha} f_\alpha(\boldsymbol{r}) & A\neq B \\ \sum_{\alpha\in A} \frac{1}{2}\left(b_{\nu\mu,\alpha} + b_{\mu\nu,\alpha}\right) f_\alpha(\boldsymbol{r}) & A = B \;, \end{cases} \tag{3.31}$$

where the factor of $1/2$ in case $A = B$ is introduced to facilitate evaluation with the same algorithm while avoiding double counting. Therefore, the basis transformation (3.13) then becomes

$$\begin{aligned} M_{\mu\nu\kappa\lambda} = &\sum_{\beta\in B}\sum_{\delta\in D} C_{\mu\nu\beta} Z_{\beta\delta} C_{\kappa\lambda\delta} + \sum_{\alpha\in A}\sum_{\delta\in D} C_{\nu\mu\alpha} Z_{\alpha\delta} C_{\kappa\lambda\delta} \\ &+ \sum_{\beta\in B}\sum_{\gamma\in C} C_{\mu\nu\beta} Z_{\beta\gamma} C_{\lambda\kappa\gamma} + \sum_{\alpha\in A}\sum_{\gamma\in C} C_{\nu\mu\alpha} Z_{\alpha\gamma} C_{\lambda\kappa\gamma} \quad M = P^{(0)}, v_c \;, \end{aligned} \tag{3.32}$$

One can imagine that the AOs which are decaying the fastest (i.e. the ones with the largest exponents) will only overlap with a limited amount of basis functions in the molecule. If μ denotes one of those functions, $\chi_\mu(\boldsymbol{r})\chi_\nu(\boldsymbol{r})$ will therefore be almost zero for many pairs of μ,ν. If

$$\chi_\mu(\boldsymbol{r})\chi_\nu(\boldsymbol{r}) \approx 0 \quad \forall\boldsymbol{r} \tag{3.33}$$

we also have

$$\sum_\alpha C_{\mu\nu\alpha} f_\alpha(\boldsymbol{r}) \approx 0 \tag{3.34}$$

by (3.14). In practice, this means that all of these coefficients are assumed to be zero and are therefore not calculated. In case two atoms A and B are very far apart, none of the pair products which can be built from the AOs centered on these atoms will be different from zero and therefore

$$C_{\mu\nu\alpha} = 0 \quad \forall\mu\in A,\nu\in B \;. \tag{3.35}$$

Therefore, the number of so that the number of non-zero elements in C will asymptotically increase linearly with the system size. How fast this asymptotic limit can be reached will depend on the geometry of the system as well as one the cut-offs which are used to define an overlap

	Basic	*Normal*	*Good*	*VeryGood*
Potential	0.01	0.005	0.001	0.0005
Basis	0.002	0.001	0.0005	0.0001
Fit	0.02	0.01	0.005	0.0001

Table 3.1: Thresholds for the linear scaling of the fit coefficient tensor C. All values are in atomic units.

to be zero. For many atoms pairs, some of the pair-products will be zero, but not all of them. Therefore, for each atom, we reorder all AOs from the most diffuse to the least diffuse one so that all non-zero elements in C are grouped in dense blocks. This allows us to only work with basic BLAS routines for dense matrices, even though C is sparse.

To determine when a pair-product is negligible, we define a threshold $\varepsilon > 0$ and consider a basis functions as negligible for $|\boldsymbol{r}| > d_\mu$ if

$$|\chi_\mu(\boldsymbol{r})| < \varepsilon \quad \forall |\boldsymbol{r}| > d_\mu \; .$$

d_μ is a basis function dependent distance which is determined at run-time and depends on ε. The fit-coefficient $C_{\nu\nu\alpha}$ is then only calculated if

$$|\boldsymbol{R}_A - \boldsymbol{R}_B| < d_\mu + d_\nu \; .$$

We define a similar threshold for the overlap of two auxiliary basis functions: If two atoms are further apart than the sum of the ranges of the most diffuse fit functions, then we can use the multipole approximation to the Coulomb potential.[548] Furthermore, if the range of the Coulomb potential on atom A does not overlap with any AO on atom B (and vice versa) the two atoms are defined as not interacting. Therefore, we end up with three different thresholds in total, which we call *Basis*, *Fit* and *Potential*, respectively. We group the thresholds into different tiers, ranging from *Basic* to *VeryGood*. The values in the currently used implementation of MBPT in ADF are given in table 3.1. Notice, that these values are not the same as the ones we have used in ref. [35, 36] and they are also different from the ones used in HF where looser thresholds can be used to obtain the same level of accuracy.

Numerical Issues with PADF

Issues with PADF frequently arise from the presence of diffuse functions in the AO-basis set. To understand the source of the problem, we recall that very large AO basis sets with many diffuse functions might be locally overcomplete which causes almost linear dependence of a subset of basis functions. These lead to numerical instabilities in the SCF[549] during canonical orthonormalization when the condition number of the AO-overlap matrix approaches infinity.[550] To restore numerical stability, one projects out the almost linearly dependent part from the

basis by removing eigenvectors from the transformation matrix corresponding to eigenvalues of the AO-overlap matrix smaller than some threshold ϵ_D,[551] effectively diminishing the basis set size. This is not a severe restriction in practice since numerical instabilities usually do not occur when all eigenvalues are larger than $\epsilon_D = 10^{-6}$ - 10^{-7}.[552–554]

Using PADF, numerical instabilities can already occur when all eigenvalues are considerably larger as has e.g. been observed for linear-response TDDFT with augmented basis sets[555] and MP2/QZ calculations[35]. The reason for this behavior is that individual fitting coefficients can become quite large for diffuse products from AOs centered on distant atoms. Note, that this is a fundamental difference to global DF. As a qualitative example, consider a linear alkane chain C_nH_{2n+2} and the pair product of a diffuse AOs on C_1 and C_n, respectively. The AOs will only have some (small) overlap in the middle of the chain. In global DF, this pair product could possibly be described very well with only a small set of ABFs centered on atoms in this region. In PADF, this overlap needs to be described with the asymptotic tails of diffuse ABFs on C_1 and C_n. When there is no appropriate ABF in the auxiliary basis, this will lead to very large fitting coefficients for some (diffuse) ABFs. In the transformation of the Coulomb potential from auxiliary basis to AO-product basis, these large fitting coefficients must cancel with contributions with opposite sign which is numerically unstable.[556] Thus, relatively small errors might accumulate during the SCF and lead to an erroneous (hole) density matrix and potentially wrong eigenvalues.

To summarise, projecting out parts of the basis during canonical orthonormalization plays a dual role when PADF is used in the SCF. First, it ensures numerical stability of the SCF and second, as a side-effect, it removes the part of the basis which potentially results in diffuse AO-products which are potentially difficult to fit. This nicely illustrates that the appropriate choice of auxiliary basis and the problem of linear dependencies are intertwined. Adding more diffuse functions to the auxiliary basis the pair product in our example can be better approximated, the fitting coefficient become smaller, and the linear dependency problem is extenuated. This means, the number of AOs which needs to be removed becomes smaller and larger basis sets can be used in practice.

For correlated methods we observed, that a value of $\epsilon_D = 10^{-3}$, corresponding to a drastic truncation of the basis, seems to provide a good trade-off between accuracy and numerical stability for all basis sets beyond TZ quality and also augmented basis sets. However, while this truncation prevents collapse to artificially low QP energies, it also leads to deteriorated results compared to the default of $\epsilon = 10^{-4}$. Increasing the basis set more and more, larger and larger parts of the virtual space need to be projected out which ultimately prevents us from reaching the complete basis set (CBS) limit for correlated methods. We expect, however, that carefully optimized auxiliary fit sets will enable the numerically stable application of PADF to these methods with larger basis sets.

In addition to the usual canonical orthonormalization[550] during the SCF we also project out too diffuse functions from the primary basis from all quantities in the primary basis, i.e. Green's functions and self-energy like objects. To do so, we first diagonalize the overlap matrix

of primary basis functions $\mathbf{S}$,

$$\mathbf{S} = \mathbf{U}^T \Lambda \mathbf{U} \; . \tag{3.36}$$

We then remove a column u_i from the transformation matrix if the corresponding eigenvalue λ_i is smaller than some predefined threshold ϵ_s. We then define

$$\mathbf{V} = \mathbf{U}\mathbf{U}^T \; , \tag{3.37}$$

and use this projector to transform all matrices in the primary basis, the Green's functions, the self-energy contributions as well as the matrices defined in (3.215) according to

$$\mathbf{K} = \mathbf{V}^T \mathbf{K}' \mathbf{V} \; , \tag{3.38}$$

where $\mathbf{K}'$ would be the original exchange-like matrix in the primary basis including the diffuse part. This transformation is not necessary if a very large auxiliary basis set is used and is switched off in that case.

3.1.4 Imaginary time and Frequency discretization

Our implementation of the *GW* approximation is based on the so-called space-time method by Godby and coworkers.[132,133] They observed that it is much simpler to solve the Dyson equations in the GWA in reciprocal space and frequency while the kernels of these Dyson equations are most easily evaluated in real space and time. This is due to the fact that the kernels are direct products in time while they are convolutions in frequency space. On the other hand, the Dyson equations can be solved by inversion in frequency space while this is not possible in time. We can switch between both representations using Fourier transforms (FT).

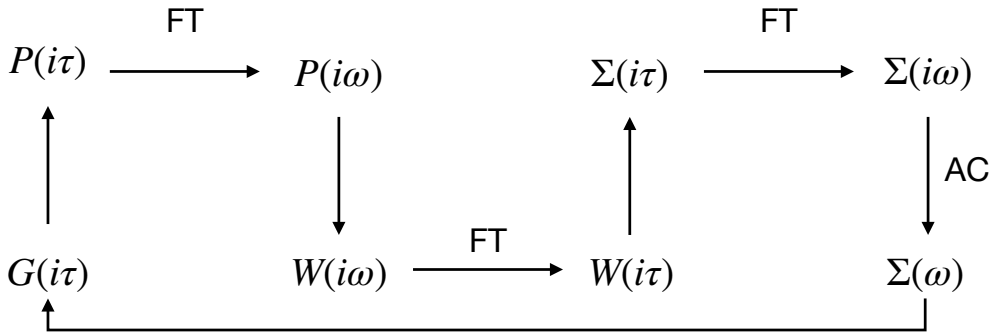

Figure 3.1: Schematic work flow for the calculation of the self-energy in the whole complex plane in ADF. FT denotes Fourier transform and AC denotes analytical continuation.

Moreover, it is beneficial to work on the imaginary axes. In section 2.3.1 we have already seen why this is the case. On the real time axis, the single-particle Green's function oscillates,

while it is exponentially decaying on the imaginary time axis. On the real frequency axis the Green's function has poles (in which we are interested, but only at the end of the calculation), while it has none on the imaginary time axis. Only in the end, we need to transform to the real frequency axis from where we extract the physically relevant properties (the positions of the poles). The procedure is illustrated in figure 3.1.

To achieve an efficient implementation of this method we therefore need to discretize imaginary time and imaginary frequency with as little grid points as possible while still retaining the necessary accuracy. In their original work, Godby and coworkers could not find small enough grids in order to implement the space-time method efficiently and only recently, building on earlier work by Almlöf[557], Kresse, Kaltak and coworkers could solve this issue by using non-uniform spaced grids in imaginary time and imaginary frequency and an efficient way to switch between both domains[134,558]. Following this development, there has been a surge of new *GW* implementations based on the space-time method for periodic[134,272,425–430] and finite[6,36,269,431,433] systems. The algorithms for finding the imaginary time and frequency points are rather sophisticated. In the following, we will outline our algorithm which closely follows the work by Kresse, Kaltak and coworkers.[558]

Definition of the Optimization Problem

The algorithm for the determination of imaginary time and frequency grids and corresponding weights for the numerical integration over these variables start from the RPA correlation energy expression, (2.355). Using the expansion

$$\ln(1-x) = -\sum_{n=1}^{\infty} \frac{1}{n} x^n \ ,$$

eq. (2.355) becomes

$$E_c^{RPA} = E_c^{(2)} + E_c^{(3)} + \dots \ , \tag{3.39}$$

where

$$E_c^{(2)} = -\frac{1}{8\pi} \int d\boldsymbol{r} \int d\omega \left[\int d\boldsymbol{r}' P^{(0)}(\boldsymbol{r}, \boldsymbol{r}', i\omega) v_c(\boldsymbol{r}', \boldsymbol{r}) \right]^2 \ . \tag{3.40}$$

We now use (2.231) to make the substitution

$$P^{(0)}(\boldsymbol{r}, \boldsymbol{r}', i\omega) = -i \int d\tau e^{i\omega\tau} P^{(0)}(\boldsymbol{r}, \boldsymbol{r}', i\tau) \ , \tag{3.41}$$

and use

$$\int d\omega e^{i\omega(\tau+\tau')} = 2\pi\delta(\tau+\tau')$$

to obtain the corresponding expression in imaginary time,

$$\begin{aligned} E_c^{(2)} =& \frac{1}{8\pi}\int d\tau \int d\tau' \int d\omega e^{i\omega(\tau+\tau')} \\ & \times \int d\boldsymbol{r}d\boldsymbol{r}_2 d\boldsymbol{r}_3 d\boldsymbol{r}_4 P^{(0)}(\boldsymbol{r},\boldsymbol{r}_2,i\tau)v_c(\boldsymbol{r}_2,\boldsymbol{r}_3)P^{(0)}(\boldsymbol{r}_3,\boldsymbol{r}_4,i\tau')v_c(\boldsymbol{r}_4,\boldsymbol{r}) \\ =& \frac{1}{2}\int_0^\infty d\tau \int d\boldsymbol{r}d\boldsymbol{r}_2 d\boldsymbol{r}_3 d\boldsymbol{r}_4 P^{(0)}(\boldsymbol{r},\boldsymbol{r}_2,i\tau)v_c(\boldsymbol{r}_2,\boldsymbol{r}_3)P^{(0)}(\boldsymbol{r}_3,\boldsymbol{r}_4,i\tau)v_c(\boldsymbol{r}_4,\boldsymbol{r}) \ . \end{aligned} \tag{3.42}$$

This term is called the direct second-order term and is the counterpart of the SOX term introduced in section 2.4.5. Using (2.277) as well as the definition of $P^{(0)}$ (2.194) in terms of $\chi^{(0)}$,

$$P^{(0)} = \chi^{(0)}(1,2,3,4)\delta(1^+,3)\delta(2,4) \ ,$$

$P^{(0)}$ assumes the form

$$P^{(0)}(\boldsymbol{r}_1,\boldsymbol{r}_2,i\tau>0) = -i\sum_{ia} e^{-(\epsilon_a-\epsilon_i)\tau}\phi_i(\boldsymbol{r}_1)\phi_i^*(\boldsymbol{r}_2)\phi_a(\boldsymbol{r}_2)\phi_a^*(\boldsymbol{r}_1) \tag{3.43}$$

and therefore we obtain for the last expression in (3.42)

$$\begin{aligned} E_c^{(2)} =& \frac{1}{2}\int_0^\infty d\tau \int d\boldsymbol{r}_1 d\boldsymbol{r}_2 d\boldsymbol{r}_3 d\boldsymbol{r}_4 e^{-(\epsilon_a+\epsilon_b-\epsilon_i-\epsilon_j)\tau}\phi_i(\boldsymbol{r}_1)\phi_i^*(\boldsymbol{r}_2)v_c(\boldsymbol{r}_1,\boldsymbol{r}_2) \\ & \times \phi_a(\boldsymbol{r}_2)\phi_a^*(\boldsymbol{r}_1)\phi_j(\boldsymbol{r}_3)\phi_j^*(\boldsymbol{r}_4)v_c(\boldsymbol{r}_3,\boldsymbol{r}_4)\phi_b(\boldsymbol{r}_4)\phi_b^*(\boldsymbol{r}_3) \\ =& -\frac{1}{2}\int_0^\infty d\tau \sum_{iajb} v_{iajb}^2 e^{-(\epsilon_a+\epsilon_b-\epsilon_i-\epsilon_j)\tau} \ , \end{aligned} \tag{3.44}$$

where we have used (2.74) to arrive at the last equation. Solving the integral over imaginary time analytically,

$$\int_0^\infty d\tau e^{-(\epsilon_a+\epsilon_b-\epsilon_i-\epsilon_j)\tau} = \frac{1}{\epsilon_a+\epsilon_b-\epsilon_i-\epsilon_j} \tag{3.45}$$

eq. (3.44) becomes

$$E_c^{(2)} = -\frac{1}{2}\sum_{iajb}\frac{v_{iajb}^2}{\epsilon_a+\epsilon_b-\epsilon_i-\epsilon_j} \ . \tag{3.46}$$

Since $P^{(0)}$ is even in time, its Fourier transform to imaginary frequency reduces to a cosine transform. Using (A.11), eq. (3.43) becomes

$$\begin{aligned} P(x_1,x_2,i\omega) =& -2i\sum_{ia}\int_0^\infty d\tau e^{-(\epsilon_a-\epsilon_i)\tau}\phi_i(\boldsymbol{r}_1)\phi_i^*(\boldsymbol{r}_2)\phi_a(\boldsymbol{r}_2)\phi_a^*(\boldsymbol{r}_1)\cos(\tau\omega) \\ =& -2i\sum_{ia}\frac{\epsilon_a-\epsilon_i}{(\epsilon_a-\epsilon_i)-\omega^2}\phi_i(\boldsymbol{r}_1)\phi_i^*(\boldsymbol{r}_2)\phi_a(\boldsymbol{r}_2)\phi_a^*(\boldsymbol{r}_1) \ , \end{aligned} \tag{3.47}$$

which allows us to evaluate $E_c^{(2)}$ by integration over imaginary frequency,

$$E_c^{(2)} = -\frac{1}{4\pi}\sum_{iajb} v_{iajb}^2 \int_0^\infty d\omega \frac{\epsilon_a - \epsilon_i}{(\epsilon_a - \epsilon_i)^2 - \omega^2}\frac{\epsilon_b - \epsilon_j}{(\epsilon_b - \epsilon_j)^2 - \omega^2} \ . \tag{3.48}$$

We can now approximate the integrals eqs. (3.44) and (3.48) by numerical quadrature,

$$\int_0^\infty d\tau e^{-(\epsilon_a+\epsilon_b-\epsilon_i-\epsilon_j)\tau} \approx \sum_{k=1}^{N_\tau} \alpha_j e^{-(\epsilon_a+\epsilon_b-\epsilon_i-\epsilon_j)\tau_j} \ , \tag{3.49}$$

and

$$\int_0^\infty d\omega \frac{\epsilon_a - \epsilon_i}{(\epsilon_a - \epsilon_i)^2 - \omega^2}\frac{\epsilon_b - \epsilon_j}{(\epsilon_b - \epsilon_j)^2 - \omega^2} \approx \sum_{k=1}^{N_\omega} \sigma_k \frac{\epsilon_a - \epsilon_i}{(\epsilon_a - \epsilon_i)^2 - \omega_k^2}\frac{\epsilon_b - \epsilon_j}{(\epsilon_b - \epsilon_j)^2 - \omega_k^2} \ . \tag{3.50}$$

Since we know the exact expression for $E_c^{(2)}$, (3.46), comparison of eqs. (3.49) and (3.50) with (3.46) provides us with a measure for the error introduced by the numerical quadratures eqs. (3.49) and (3.50). We now introduce the abbreviations $x = \epsilon_a - \epsilon_i$ and $x' = \epsilon_b - \epsilon_j$ and subtract eqs. (3.49) and (3.50) from (3.46). This yields the minimization problems

$$\frac{1}{x + x'} - \sum_k^{N_\tau} \alpha_k e^{-(x+x')\tau_k} \stackrel{!}{=} 0 \tag{3.51}$$

in imaginary time and

$$\frac{1}{x + x'} - \frac{1}{2\pi}\sum_k^{N_\tau} \sigma_k \frac{x}{x^2 - \omega_k^2}\frac{x'}{x'^2 - \omega_k^2} \stackrel{!}{=} 0 \tag{3.52}$$

in imaginary frequency over all pairs

$$(x, x') \in [\epsilon_{min}, \epsilon_{max}] \times [\epsilon_{min}, \epsilon_{max}] \ .$$

We now use the approximation that the error can be sufficiently minimized by restricting ourselves to $x = x'$.[558] We then obtain

$$\frac{1}{2x} - \sum_k^{N_\tau} \alpha_k e^{-2x\tau_j} \stackrel{!}{=} 0 \tag{3.53}$$

in imaginary time and

$$\frac{1}{x} - \frac{1}{\pi}\sum_k^{N_\omega} \sigma_k \left(\frac{2x}{x^2 - \omega_k^2}\right)^2 \stackrel{!}{=} 0 \tag{3.54}$$

in imaginary frequency which are well defined one-dimensional optimization problems. We can now minimize the errors described by these expressions for predefined grid sizes N_τ and N_ω

with respect to a suitable norm to find optimal sets of imaginary frequency $\{\omega_k)\}_{k=1,\dots N_\omega}$ and imaginary time points $\{\tau_k)\}_{k=1,\dots N_\tau}$. For imaginary time, we use the algorithm described in ref. [559] to minimize

$$\left\|\eta^{(\tau)}(x;\alpha,\tau)\right\|_\infty \ , \quad \eta^{(\tau)}(x;\alpha,\tau) = \frac{1}{2x} - \sum_j^{N_\tau} \alpha_j e^{-2x\tau_j}. \ , \tag{3.55}$$

i.e., we try to minimize the maximum (Chebyshev) norm. Therefore, this algorithm is sometimes called minimax algorithm. This norm is in principle to be preferred over the L_2 norm since it will keep the error introduced by the numerical quadrature well balanced for all x. However, it is difficult to converge and requires points and weights as input which are already very close to the final grid points. In the absence of knowledge of such grid points and weights for the imaginary frequency domain, we perform a least-squares (LS) optimization for the imaginary frequency grid instead

$$\left\|\eta^{(\omega)}(x;\sigma,\omega)\right\|_2 \ , \quad \eta^{(\omega)}(x;\sigma,\omega) = \frac{1}{x} - \frac{1}{\pi}\sum_k^{N_\omega} \sigma_k \left(\frac{2x}{x^2+\omega_k^2}\right)^2 \ . \tag{3.56}$$

For a discussion of the pros and cons of minimizing the L_2 instead of the Chebyshev norm we refer to the appendix of ref. [560].

The Levenberg-Marquardt algorithm We solve both optimization problems eqs. (3.55) and (3.56) using a Levenberg–Marquardt algorithm (LMA),[561] an extension of the Newton-method to solve non-linear systems of equations.[562] Since the minimax algorithm for the determination of the imaginary time grid is well documented[559,563,564] we focus here on the imaginary frequency domain. In the LMA for the determination of frequency points and corresponding weights, we follow the gradient of the residual function η with respect to the parameters $\{\sigma\}$ and $\{\omega\}$ until the LS error is converged. The necessary derivatives on the imaginary frequency axis are

$$\begin{aligned} \frac{\partial\eta}{\partial\sigma_k} &= -\frac{4}{\pi}\frac{x^2}{(x^2+\omega_k^2)^2} \\ \frac{\partial\eta}{\partial\omega_k} &= = \frac{16\sigma_k}{\pi}\frac{x^2\omega_k}{(x^2+\omega_k^2)^3} \ . \end{aligned} \tag{3.57}$$

The error function $\eta^{(\omega)}$ is minimized on a logarithmic grid (which places the majority of the sampling points at small values of x) of size $40\times N_\omega$, $\{x_i\}_{i=1,\dots,40\times N_\omega}$ in the interval $[1, x_{min}/x_{max}]$, with x_{min} (x_{max}) being the smallest (largest) considered electron-hole transition energy. Using such a logarithmic grid emphasizes the dominance of particle-hole transitions with small energies in the screening of the electron-electron interaction. Smaller sized grids than ours would most likely suffice as well. However, the computational effort for the determination of the frequency grids is negligible.

Writing $\eta_i = \eta\left(x_i; \{\sigma\}, \{\omega\}\right)$, we can define the Jacobian (the matrix of all partial first-order derivatives)

$$J_{ik} = \begin{cases} -\frac{4}{\pi} \frac{x_i^2}{(x_i^2+\omega_k^2)^2} & k \leq N_\omega \\ \frac{16\sigma_k}{\pi} \frac{x_i^2 \omega_k}{(x_i^2+\omega_k^2)^3} & k > N_\omega \end{cases} \tag{3.58}$$

which is a concatenation of the derivatives defined in (3.57) evaluated at the positions of all grid points $x_{ii=1,\ldots,40\times N_\omega}$. In the Newton procedure, we will find an update vector $\vec{\delta}$ by solving

$$\boldsymbol{J}\vec{\delta} = \vec{\eta} \tag{3.59}$$

using the pseudo-inverse of $\boldsymbol{J}$,

$$\delta\gamma = \left(\boldsymbol{J}^T\boldsymbol{J}\right)^{-1}\boldsymbol{J}^T\vec{\eta}\,. \tag{3.60}$$

In the variant of Levenberg and Marquardt, we solve instead

$$\left(\boldsymbol{J}^T\boldsymbol{J} - \lambda \mathrm{diag}\left(\boldsymbol{J}^T\boldsymbol{J}\right)\right)\vec{\delta} = \boldsymbol{J}^T\vec{\eta}\,, \tag{3.61}$$

for δ in a LS sense. We start by setting $\lambda = 0.001$. When the LS error is smaller than the one of the previous iteration, λ is divided by 10, i.e. damping is reduced. If the LS error increases. λ is multiplied by 10, i.e. damping is increased. The procedure is repeated until variation of the LS error between 2 consecutive iterations is smaller than some predefined threshold. This procedure is also known as Tikhonov regularization or kernel ridge regression in the literature.

For the imaginary frequency domain we first minimize the L_2 norm on the logarithmic grid which provides us with a preliminary error distribution function η^ω. We then find the extrema of this error distribution function and minimize the L_2 norm for the positions of these extrema x_k. This gives an improved error distribution function η^ω with smaller maximum error. We then go back to minimizing the L_2 norm on the logarithmic grid and continue this procedure until the error function is stationary. The effect of this combined optimization is demonstrated for the Ne atom in figure 3.2 which shows that the combined optimization scheme leads to a much smaller numerical integration error than a simple LS scheme.

preconditioning for the ω-Optimization $\eta^{(\omega)}$ might have multiple minima and especially for larger N_ω the LMA only converges to a useful minimum when it is initialized with σ and ω which are already sufficiently close to the parameters which minimize $\eta^{(\omega)}$. In practice, we found that at a useful (but not necessarily global) minimum of $\left\|\eta^{(\omega)}(x;\sigma,\omega)\right\|_2$ $\eta^{(\omega)}$ has $2N_\omega$ or $2N_\omega - 1$ extrema. This behavior can be exploited to find good starting points for the LMA for different ratios x_{min}/x_{max} and N_ω. We always start the LMA from pretabulated values.[3] These values have been obtained by a simple metropolis algorithm for several x_{min}/x_{max} and for N_ω between 1 and 40 and are chosen so that $\eta^{(\omega)}$ has $2N_\omega$ or $2N_\omega - 1$ extrema for a given N_ω. In a GWA

[3]The pretabulated values are available on Github (https://github.com/ArnoFoerster/Imaginary-Frequency-Grids-GW-and-RPA)

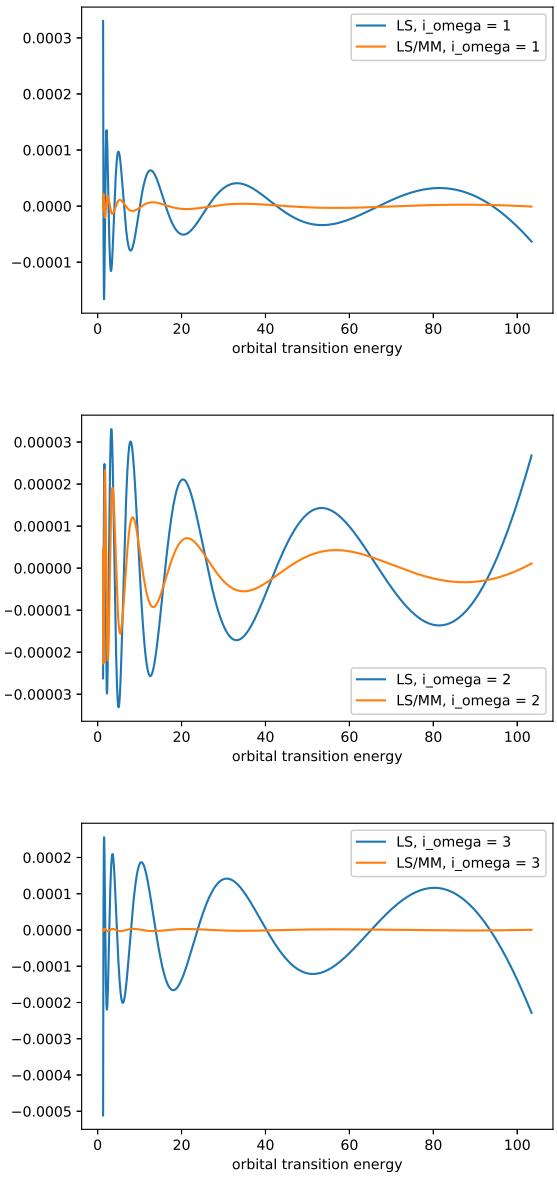

Figure 3.2: Error distribution functions $\eta^{(\omega)}(x;\sigma,\omega)$ for the Ne-atom using simple LS minimization (blue lines) and the combined LS/minimax-scheme (orange lines) for the first three frequency points (from top to bottom)

calculation, the LMA is then initialized with the pretabulated parameters which are closest to the x_{min}/x_{max} of the calculation.

To avoid unnecessarily large grids, the N_ω and N_τ are determined at run-time and the user only specifies an upper limit of points for both, imaginary time and frequency grids. More precisely, for small N_ω, grid points and weights are calculated and the L_2 norm of η^ω is calculated. Then we increase the imaginary frequency grid until the least square error is smaller than $\epsilon_\omega = 1e^{-10}$. The number of points which are required to reach this accuracy strongly depends on x_{min}/x_{max}. In our experience, the QP energies converge faster with respect to the imaginary time grid than with respect to the imaginary frequency grid. For example, for a Hydrogen-molecule in a triple-ζ (TZ) basis, $N_\omega = 7$ will already be sufficient to reach the desired accuracy, while for the Iodine molecule in a QZ basis $N_\omega = 31$ will be necessary.

Discrete Fourier Transforms

Since we want to switch between imaginary time and imaginary frequency, we write the discrete version of (2.231) as

$$F(i\omega_k) = -i \sum_j^{N_\tau} \left\{ \gamma_{kj}^{(c)} \cos(\omega_k \tau_j) \left(F(i\tau_j) + F(-i\tau_j)\right) + i\gamma_{kj}^{(s)} \sin(\omega_k \tau_j) \left(F(i\tau_j) - F(-i\tau_j)\right) \right\} , \tag{3.62}$$

where we have split the function F into even and odd parts. This is useful since it simplifies working with the bosonic quantities $P^{(0)}$, $W^{(0)}$ and their reducible counterparts. The Fourier transform from imaginary frequency to imaginary time can then be calculated by inverting the matrices with the elements $\gamma_{kj}^{(c)} \cos(\omega_k \tau_j)$ and $\gamma_{kj}^{(s)} \sin(\omega_k \tau_j)$ (In case $N_\tau \neq N_\omega$, a pseudo-inverse can be calculated). To calculate the matrices $\gamma^{(c)}$ we minimize

$$\left\| \eta^{(c)} \left(x; \gamma^{(c)}\right) \right\|_2 , \quad \eta^{(c)} \left(x, \gamma^{(c)}\right) = \frac{2x}{x^2 + \omega_k^2} - \sum_{j=1}^{N_\tau} \gamma_{kj}^{(c)} \cos(\omega_k \tau_j) e^{-x\tau_j} , \tag{3.63}$$

for all ω_k and for $\gamma^{(s)}$, we minimize

$$\left\| \eta^{(s)} \left(x; \gamma^{(s)}\right) \right\|_2 , \quad \eta^{(s)} \left(x, \gamma^{(s)}\right) = \frac{2\omega_k}{x^2 + \omega_k^2} - \sum_{j=1}^{N_\tau} \gamma_{kj}^{(c)} \sin(\omega_k \tau_j) e^{-x\tau_j} , \tag{3.64}$$

with a LMA. These forms of the error functions simply follow from the analytical sine and cosine transformations of $e^{-x\tau}$ eqs. (A.11) and (A.12). The procedure is the same as described in ref. [134]. In all cases, the LMA converges smoothly from arbitrary starting values.

3.2 Working Equations

In this section, we will express the approximations to the self-energy towards the end of section 2.2.3 in a form which is suitable for numerical implementations. This is straightforward

if these expressions are evaluated using interacting single-particle Green's functions. In case the Green's functions are non-interacting, one can make use of eqs. (2.204), (2.228), (2.230) and (2.231) to derive compact expressions. For each self-energy expression, we will also give the corresponding expression for the total energy in the section following the next one.

3.2.1 The *GW* Equations in the Atomic Orbital Basis

We now write down the *GW* equations in the AO basis using the discrete bases for the representation of imaginary time and frequency dependence. To start with, we repeat eqs. (2.228) and (2.229) in our new notation. Since the single-particle propagator is diagonal in spin, we will also replace x with $\boldsymbol{r}$,

$$\begin{aligned} G^{(0),>}(\boldsymbol{r},\boldsymbol{r}',i\tau) &= -i\sum_a \phi_a(\boldsymbol{r})\phi_a^*(\boldsymbol{r}')e^{-\epsilon_a\tau} \\ G^{(0),<}(\boldsymbol{r},\boldsymbol{r}',i\tau) &= -i\sum_i \phi_i^*(\boldsymbol{r})\phi_i(\boldsymbol{r}')e^{-\epsilon_i\tau} \end{aligned} \tag{3.65}$$

and

$$G^{(s)}(\boldsymbol{r},\boldsymbol{r}',i\tau) = -i\sum_a \phi_a(\boldsymbol{r})\phi_a^*(\boldsymbol{r}')e^{-\epsilon_a\tau} + i\sum_i \phi_i^*(\boldsymbol{r})\phi_i(\boldsymbol{r}')e^{-\epsilon_i\tau}\ . \tag{3.66}$$

Through (3.1) we obtain (using the fact that in the non-relativistic case the MOs are real)

$$G^{(0),<}(\boldsymbol{r},\boldsymbol{r}',i\tau) = -i\sum_i\sum_{\mu\nu} \chi_\mu(\boldsymbol{r})b_{\mu i}e^{-\epsilon_i\tau}b_{i\nu}\chi_\nu(\boldsymbol{r}') \tag{3.67}$$

$$G^{(0),>}(\boldsymbol{r},\boldsymbol{r}',i\tau) = -i\sum_a\sum_{\mu\nu} \chi_\mu(\boldsymbol{r})b_{\mu a}e^{-\epsilon_a\tau}b_{a\nu}\chi_\nu(\boldsymbol{r}') \tag{3.68}$$

and from the identity

$$G^{(0),\lessgtr}(\boldsymbol{r},\boldsymbol{r}',i\tau) = \sum_{\mu\nu}\chi_\mu(\boldsymbol{r})G^{(0),\lessgtr}_{\mu\nu,\tau}\chi_\nu(\boldsymbol{r}') \tag{3.69}$$

we obtain the representation of lesser and greater propagators in the STO basis,

$$G^{(0),<}_{\mu\nu,\tau} = -i\sum_i b_{\mu i}e^{-\epsilon_i\tau}b_{i\nu} \tag{3.70}$$

$$G^{(0),>}_{\mu\nu,\tau} = -i\sum_a b_{\mu a}e^{-\epsilon_a\tau}b_{a\nu}\ . \tag{3.71}$$

While Σ also transforms as a 2-point correlation function,

$$\Sigma_{\mu\nu,\tau} = \int d\boldsymbol{r}d\boldsymbol{r}'\chi_\mu(\boldsymbol{r})\Sigma(\boldsymbol{r},\boldsymbol{r}',i\tau)\chi_\nu(\boldsymbol{r}')\ . \tag{3.72}$$

all 2-electron operators transform as 4-point correlation functions in the AO basis,[15,69,294]

$$P^{(0)}_{\mu\kappa\nu\lambda,\tau} = \int d\boldsymbol{r}d\boldsymbol{r}'\chi_\mu(\boldsymbol{r})\chi_\nu(\boldsymbol{r})P^{(0)}(\boldsymbol{r},\boldsymbol{r}',i\tau)\chi_\kappa(\boldsymbol{r}')\chi_\lambda(\boldsymbol{r}') \tag{3.73}$$

$$v_{\mu\nu\kappa\lambda} = \int d\boldsymbol{r}d\boldsymbol{r}'\chi_\mu(\boldsymbol{r})\chi_\nu(\boldsymbol{r})v_c(\boldsymbol{r},\boldsymbol{r}')\chi_\kappa(\boldsymbol{r}')\chi_\lambda(\boldsymbol{r}') \tag{3.74}$$

$$W_{\mu\nu\kappa\lambda,\tau} = \int d\boldsymbol{r}d\boldsymbol{r}'\chi_\mu(\boldsymbol{r})\chi_\nu(\boldsymbol{r})W(\boldsymbol{r},\boldsymbol{r}',i\tau)\chi_\kappa(\boldsymbol{r}')\chi_\lambda(\boldsymbol{r}') \ . \tag{3.75}$$

In this representation, the calculation of the screened interaction (3.75) from $P^{(0)}$ and v_c requires the inversion of a matrix in the AO-product space $\mathcal{P} = \{\chi_\mu\}\otimes\{\chi_\nu\}$ for all frequency points whose dimension scales as N^2 with system size. Hence, the matrix inversion scales as N^6. For this reason, we use their representation in terms of the auxiliary basis instead,

$$P^{(0)}_{\alpha\beta\tau} = \int d\boldsymbol{r}d\boldsymbol{r}' f_\alpha(\boldsymbol{r})P^{(0)}(\boldsymbol{r},\boldsymbol{r}',i\tau)f_\beta(\boldsymbol{r}') \tag{3.76}$$

$$v_{\alpha\beta} = \int d\boldsymbol{r}d\boldsymbol{r}' f_\alpha(\boldsymbol{r})v_c(\boldsymbol{r},\boldsymbol{r}')f_\beta(\boldsymbol{r}') \tag{3.77}$$

$$W_{\alpha\beta,\tau} = \int d\boldsymbol{r}d\boldsymbol{r}' f_\alpha(\boldsymbol{r})W(\boldsymbol{r},\boldsymbol{r}',i\tau)f_\beta(\boldsymbol{r}') \ . \tag{3.78}$$

Using eqs. (3.13) and (3.14), the equations to be solved in a G_0W_0 calculation become

$$P^{(0)}_{\alpha\beta,\tau} = C_{\mu\nu\alpha}P^{(0)}_{\mu\nu\kappa\lambda,\tau}C_{\kappa\lambda\beta} = -iC_{\mu\nu\alpha}G^<_{\mu\kappa,\tau}G^>_{\nu\lambda,\tau}C_{\kappa\lambda\beta} \tag{3.79}$$

$$W_{\alpha\beta,\omega} = V_{\alpha\beta} + V_{\alpha\gamma}P^{(0)}_{\gamma\delta,\omega}W_{\delta\gamma,\omega} = \left[[v_c]^{-1} - P^{(0)}\right]^{-1}_{\alpha\beta,\omega} \tag{3.80}$$

$$\Sigma^x_{\mu\nu} = i\sum_{\kappa\lambda}\sum_{\alpha\beta} G^<_{\kappa\lambda,\tau=0}C_{\mu\kappa\beta}V_{\alpha\beta}C_{\nu\lambda\alpha} \tag{3.81}$$

$$\Sigma^c_{\mu\nu,\tau} = i\sum_{\kappa\lambda}\sum_{\alpha\beta} G_{\kappa\lambda,\tau}C_{\mu\kappa\beta}\widetilde{W}_{\alpha\beta,\tau}C_{\nu\lambda\beta} \ , \tag{3.82}$$

where we have split the screened electron-electron interaction according to $\widetilde{W} = W - V$. This isolates the Fock term from the GW self-energy. Also notice, that we only need $P^{(0)}(i\tau > 0)$ since $P^{(0)}(i\tau) = P^{(0)}(-i\tau)$. Therefore, (3.79) follows directly from (3.43). We now outline how the sparsity of the map from $\mathcal{P}$ to $\mathcal{A}$ can be exploited to reduce this scaling to N^2.

It should be noted that also in a plane-wave basis density-density response functions become matrices whose dimension only grows linearly with system size.[565] The challenge in such calculations is the size of the plane wave basis which is typically too large to allow for the solution of (3.80) in the space of all plane-waves.[565] Also in the plane-wave representation one can exploit the rank deficiency of the matrices to reduce their dimension, for instance using localized Wannier-type orbitals[247,566] or other low-rank approximations to the screened interaction.[567–569]

3.2.2 GW with pair atomic density fitting

Polarizability After the Green's function eqs. (3.70) and (3.71) have been constructed, $P^{(0)}$ can be evaluated. Using (3.32), the contribution of each atom pair (A,B) to $P^{(0)}$, eq. (3.79),

is given as the sum of four contributions (we will indicate the atomic indices in all following intermediates as superscripts),

$$P^{AB}_{\alpha\beta,\tau} = -i\left(P^{(0)^{AB,I}}_{\alpha\beta,\tau} + P^{(0)^{AB,II}}_{\alpha\beta,\tau} + P^{(0)^{AB,III}}_{\alpha\beta,\tau} + P^{(0)^{AB,IV}}_{\alpha\beta,\tau}\right) , \tag{3.83}$$

where

$$\begin{aligned} P^{(0)^{AB,I}}_{\alpha\beta,\tau} &= \sum_{\mu\in A}\sum_{\nu\in B}\sum_{\kappa\in C}\sum_{\lambda\in D} C^{DAA}_{\lambda\mu\alpha} G^{<,DC}_{\lambda\kappa,\tau} G^{>,AB}_{\mu\nu,\tau} C^{CBB}_{\kappa\nu\beta} \\ P^{(0)^{AB,II}}_{\alpha\beta,\tau} &= \sum_{\mu\in A}\sum_{\nu\in B}\sum_{\kappa\in C}\sum_{\lambda\in D} C^{DAA}_{\lambda\mu\alpha} G^{<,AC}_{\mu\kappa,\tau} G^{>,DB}_{\lambda\nu,\tau} C^{CBB}_{\kappa\nu\beta} \\ P^{(0)^{AB,IV}}_{\alpha\beta,\tau} &= \sum_{\mu\in A}\sum_{\nu\in B}\sum_{\kappa\in C}\sum_{\lambda\in D} C^{DAA}_{\lambda\mu\alpha} G^{<,AB}_{\mu\nu,\tau} G^{>,DC}_{\lambda\kappa,\tau} C^{CBB}_{\kappa\nu\beta} . \end{aligned} \tag{3.84}$$

The symmetry of $P^{(0)}$ implies $P^{(0)^{AB,III}} = \left[P^{(0)^{BA,II}}\right]^T$ and $P^{(0)^{AB}} = \left[P^{(0)^{BA}}\right]^T$. Also note, that Re $P^{(0)}(i\tau) = 0$. Defining the intermediates

$$F^{<,ABB}_{\mu\nu\beta,\tau} = \sum_{\kappa\in C} G^{<,AC}_{\mu\kappa,\tau} C^{CBB}_{\kappa\nu\beta} \tag{3.85}$$

$$F^{>,ABB}_{\mu\nu\beta,\tau} = \sum_{\kappa\in C} G^{>,AC}_{\mu\kappa,\tau} C^{CBB}_{\nu'\nu\beta} \tag{3.86}$$

$$H^{<,ACB}_{\mu\kappa\beta,\tau} = \sum_{\nu in B} F^{<,ABB}_{\mu\nu\beta,\tau} G^{>,BC}_{\nu\kappa,\tau} \tag{3.87}$$

$$H^{>,ACB}_{\mu\kappa\beta,\tau} = \sum_{\nu\in B} F^{>,ABB}_{\mu\nu\beta,\tau} G^{<,BC}_{\nu\kappa,\tau} , \tag{3.88}$$

(3.84) is most conveniently evaluated as

$$\begin{aligned} P^{(0)^{AB,I}}_{\alpha\beta,\tau} + P^{(0)^{AB,IV}}_{\alpha\beta,\tau} &= \sum_{\nu\in B}\sum_{\kappa\in C}\left(H^{<,CBA}_{\kappa\nu\alpha,\tau} + H^{>,CBA}_{\kappa\nu\alpha,\tau}\right) C^{CBB}_{\kappa\nu\beta} \\ P^{(0)^{AB,II}}_{\alpha\beta,\tau} &= \sum_{\mu\in A}\sum_{\nu\in B} F^{>,BAA}_{\nu\mu\alpha,\tau} F^{<,ABB}_{\mu\nu\beta,\tau} . \end{aligned} \tag{3.89}$$

We parallelize the outermost loop over all atoms and perform all tensor contractions using level-3 BLAS. No tensor contraction involves more than three atomic centers and since contractions corresponding to distant centers (for which all elements in C are zero) can be skipped, the operation count scales asymptotically as N^2. We always evaluate the intermediates eqs. (3.85)–(3.88) on the fly since storage of 2-center quantities with more than 2 indices would become prohibitive very quickly.

Screened Coulomb interaction After having evaluated $P^{(0)}$ for all atom pairs, $\widetilde{W}$ can be evaluated as in conventional approaches using matrices of dimension $N_{\text{aux}} \times N_{\text{aux}}$. After transforming the matrix $P^{(0)}$ (which is even in imaginary time) to the imaginary frequency axis using (3.62), the screened interaction W_ω can be obtained by inversion,

$$\widetilde{W}_{i\omega_k} = \left[v_c^{-1} - P^{(0)}_{i\omega_k}\right]^{-1} - v_c \; . \tag{3.90}$$

(3.90) has been used in all calculations presented in this work. Only recently, we have replaced it by

$$\widetilde{W}_\omega = \left\{ \left[1 - v_c P^{(0)}_{i\omega_k}\right]^{-1} - 1 \right\} v_c \; , \tag{3.91}$$

which seems to slightly improve the numerical stability and does not require the inversion of the bare electron-electron interaction. $W(i\omega_k)$ is stored in distributed memory. Note, that on the imaginary frequency axis, Im $P^{(0)} = 0$ and thus Im $W = 0$ as well. To evaluate (3.90), the dielectric function is not constructed explicitly as it is not symmetric and its inversion would be computationally demanding. We invert $[v_c]^{-1} - P^{(0)}_\omega$ (and v_c which only needs to be done once) using an LU decomposition with partial pivoting as implemented in SCALAPACK. Note, that inversion using CD would be numerically unstable since our C is not full-rank and therefore it does not conserve the positive semi-definiteness of W. We subsequently transform W back to imaginary time. In order to optimize the memory requirements of our algorithm and in contrast to our original implementation,[36] in our current implementation we retrieve all matrices $P(i\omega_k)$ and $W(i\omega_k)$ from disk when they are needed. This strategy can come with substantial computational overhead especially on disk-less compute nodes.

Self-energy Next, the contributions to Σ for all atom pairs,

$$\Sigma^{c,AB}_{\mu\nu,\tau} = i\Sigma^{AB,I}_{\mu\nu,\tau} + i\Sigma^{c,AB,II}_{\mu\nu,\tau} + i\Sigma^{c,AB,III}_{\mu\nu,\tau} + i\Sigma^{c,AB,IV}_{\mu\nu,\tau} \; , \tag{3.92}$$

are evaluated, where $\Sigma^{AB,III} = \left[\Sigma^{BA,II}\right]^T$, $\Sigma^{AB} = \left[\Sigma^{BA}\right]^T$. Also, Im $\Sigma^c = 0$, since Re $G^{\lessgtr} = 0$ and Re $W = 0$. We only give here the equations for $\Sigma^c(i\tau)$ as Σ^x is obtained in exactly the same way by replacing W with v_c and $G(i\tau)$ with $G(i\tau \to 0^-)$. To express the individual contributions to Σ we define the intermediate

$$I^{ABC}_{\mu\nu\gamma,\tau} = \sum_{\beta\in B} C^{ABB}_{\mu\nu\beta} \widetilde{W}^{BC}_{\beta\gamma,\tau} \; , \tag{3.93}$$

and together with (3.86) and (3.85) we obtain

$$\Sigma^{c,\lessgtr,AC,I}_{\mu\kappa,\tau} = \sum_{\nu\in B}\sum_{\lambda\in D}\sum_{\alpha\in A}\sum_{\gamma\in C} G^{\lessgtr,DB}_{\lambda\nu,\tau} C^{DAA}_{\lambda\mu\alpha} \widetilde{W}^{AC}_{\alpha\gamma,\tau} C^{BCC}_{\nu\kappa\gamma} = \sum_{\nu\in B}\sum_{\alpha\in A} F^{\lessgtr,BAA}_{\nu\mu\alpha,\tau} I^{BCA}_{\nu\kappa\alpha,\tau} \tag{3.94}$$

$$\Sigma^{c,\lessgtr,AC,II}_{\mu\kappa,\tau} = \sum_{\nu\in B}\sum_{\lambda\in D}\sum_{\alpha\in A}\sum_{\beta\in B} G^{\lessgtr,DB}_{\lambda\nu,\tau} C^{DAA}_{\lambda\mu\alpha} \widetilde{W}^{AB}_{\alpha\beta,\tau} C^{CBB}_{\kappa\nu\beta} = \sum_{\nu\in B}\sum_{\alpha\in A} F^{\lessgtr,BAA}_{\nu\mu\alpha,\tau} I^{CBA}_{\kappa\nu\alpha,\tau} \tag{3.95}$$

$$\Sigma^{c,\lessgtr,AC,IV}_{\mu\kappa,\tau} = \sum_{\nu\in B}\sum_{\lambda\in D}\sum_{\delta\in D}\sum_{\beta\in B} G^{\lessgtr,DB}_{\lambda\nu,\tau} C^{ADD}_{\mu\lambda\delta} \widetilde{W}^{DB}_{\delta\beta,\tau} C^{CBB}_{\kappa\nu\beta} = \sum_{\lambda\in D}\sum_{\delta\in D}\left[\sum_{\nu\in B} G^{\lessgtr,DB}_{\lambda\nu,\tau} I^{CBD}_{\kappa\nu\delta,\tau}\right] C^{ADD}_{\mu\lambda\delta} \ . \tag{3.96}$$

As for $P^{(0)}$ we parallelize the outermost loop over all atoms and completely rely on level-3 BLAS for all tensor contractions. Due to its prefactor of $N^2_{bas,l} \times N^2_{aux,l}$, where $N_{aux,l}$ ($N_{bas,l}$) denote the number of ABFs (AOs) on one atomic center, the calculation of I is the most expensive step. For weakly interacting atom pairs, we rely on multipole expansions of the Coulomb potential to reduce the prefactor of all contractions involving W (and v_c for Σ^x) considerably. We however found this approximation to introduce numerical instabilities for qsGW, where we switch it off. Still, also for qsGW Σ can be evaluated with a quadratic operation count only but the prefactor is somewhat higher compared to diagonal approximations to GW.

In a scGW calculation the self-energy is processed further in the AO basis. For all other types of GW calculations, the self-energy is transformed to the MO basis according to

$$\Sigma^{\lessgtr}_{pq} = \sum_{\mu\nu} b_{\mu p} \Sigma^{\lessgtr}_{\mu\nu} b_{\nu q} \ . \tag{3.97}$$

In a G_0W_0 or evGW calculation, only the diagonal elements are relevant, while in qsGW the whole self-energy matrix in the MO basis is needed.

Self-Energy in Imaginary Frequency

The first step in the transformation of the self-energy (3.97) to the real frequency axis is its Fourier transform to the imaginary axis. For this, we introduce the time-ordered self-energy,

$$\Sigma(i\tau) = \Theta(\tau)\Sigma^{>}(i\tau) - \Theta(-\tau)\Sigma^{<}(i\tau) \ , \tag{3.98}$$

which becomes

$$\begin{aligned}\Sigma_{pq}(i\omega) =& -\frac{i}{2}\int d\tau \cos(\omega\tau)\left[\Sigma_{pq}(i\tau) + \Sigma_{pq}(-i\tau)\right] + \frac{1}{2}\int d\tau \sin(\omega\tau)\left[\Sigma_{pq}(i\tau) - \Sigma_{pq}(-i\tau)\right] \\ =& -i\int_0^\infty d\tau \left[\Sigma^{>}_{pq}(i\tau) - \Sigma^{<}_{pq}(-i\tau)\right]\cos(\omega\tau) + \int_0^\infty d\tau \left[\Sigma^{>}_{pq}(i\tau) + \Sigma^{<}_{pq}(-i\tau)\right]\sin(\omega\tau)\end{aligned} \tag{3.99}$$

and through (3.62) the last equation becomes

$$\Sigma_{pq}(i\omega_k) = -i\sum_j^{N_\tau} \gamma^{(c)}_{kj} \cos(\omega_k\tau_j)\left[\Sigma^{>}_{pq}(i\tau_j) - \Sigma^{<}_{pq}(i\tau_j)\right] + \sum_j^{N_\tau} \gamma^{(s)}_{kj} \sin(\omega_k\tau_j)\left[\ \Sigma^{>}_{pq}(i\tau_j) + \Sigma^{<}_{pq}(i\tau_j)\right] \ . \tag{3.100}$$

In our implementation, this is actually rewritten as

$$\begin{aligned}\Sigma_{pq}(i\omega_k) = &\sum_j^{N_\tau} \gamma_{kj}^{(c)} \cos(\omega_k \tau_j) \left[\left(-i\Sigma_{pq}^{>}(i\tau_j)\right) - \left(-i\Sigma_{pq}^{<}(i\tau_j)\right)\right] \\ &+ i \sum_j^{N_\tau} \gamma_{kj}^{(s)} \sin(\omega_k \tau_j) \left[\left(-i\Sigma_{pq}^{>}(i\tau_j)\right) + \left(-i\Sigma_{pq}^{<}(i\tau_j)\right)\right] \ ,\end{aligned} \tag{3.101}$$

since we work with real quantities whenever possible. Therefore, we calculate $-i\Sigma = GW$ instead of $\Sigma = iGW$.

Analytical Continuation

Σ is now known on a discrete set of points $\mathcal{W} = \{i\omega_\beta\}_{\beta=1,N_\omega}$ on the imaginary frequency axis. In a next step, we will need to analytically continue the self-energy to the whole complex plane since we are interested in its behavior on the real frequency axis. To this end, we seek to find a function f which is analytic in the largest possible domain $\mathcal{A} \subset \mathbb{C}$ and coincides with Σ in $\mathcal{W}$. For a meromorphic function (as the self-energy) which is known on the whole imaginary axis, it is always possible to find such a function so that $\mathcal{A} = \mathbb{C}$, but since we only know the self-energy on a small subset of points, only an approximate solution can be found. The problem here is, that the AC is exceptionally ill-conditioned, i.e. numerical noise in the input data might significantly affect the output[466].

Among the many developed algorithms (see for instance ref.[467] for an overview), the construction of a continued fraction[570,571] *via* a Padé approximant is most common in implementations of the GWA. While in many codes Thiele's reciprocal difference method is implemented,[134,427,430] we have implemented the variant by Vidberg and Serene[570], which has for example also been implemented by Kutepov[428]. In the latter variant, the coefficients of the continued fraction are calculated while the former method returns the value of the continued fraction[571]. While it has been claimed that the former variant is numerically more stable[134], we did not experience any numerical issues in our implementation with the latter. AC typically yields good results for states close to the HOMO-LUMO gap[545] while it becomes unreliable for core states[572,573]. Exceptions are cases for which the self-energy has a pole close to the position of a QP energy[574]. Partial self-consistency in G pushes the poles away from the QP peak[296], and consequently, these issues should not be present in qsGW as well. This is different from situations in which the independent QP picture breaks down and the spectral weight of a single excited electrons is distributed between multiple peaks. The former is a purely numerical issue while the latter is caused by strong correlation and can not be overcome by partial self-consistency. It has also been shown in ref. [269] that AC yields accurate results for semi-core and inner valence states in case the real part of the self-energy does not have poles in the vicinity of the QP solutions.

In the continued fraction method, the self-energy at a point z in the complex plane is given

as

$$C(z) = \cfrac{a_1}{1 + \cfrac{a_2(z - i\omega_1)}{1 + \cfrac{a_3(z-i\omega_2)}{1+\ldots}}} , \tag{3.102}$$

where $\{\omega_k\}_{k=1,\ldots N_\omega}$ is the set of imaginary frequencies on which we have evaluated the self-energy. The continued fraction expansion needs to fulfil

$$C(i\omega_k) = \Sigma(i\omega_k) \quad \forall k \; .$$

The N_ω complex coefficients $\{a_k\}_{k=1,\ldots N_\omega}$ are determined recursively. We define

$$g_i(i\omega_k) = \begin{cases} \Sigma(i\omega_k) & i = 1 \\ \frac{g_{i-1}(\omega_{i-1}) - g_{i-1}(z)}{(z - i\omega_{i-1}) g_{i-1}(z)} & i \geq 2 \end{cases} \tag{3.103}$$

In the end, we set $a_k = g_k(i\omega_k)$ and identify Σ with C.

If one is only interested in accurate valence states, AC *via* Padé approximants is not problematic for G_0W_0 since the equtions for different single-particle levels do not couple. In evGW, the situation is only slightly different. The N_{MO} equations are still independent, but information from all QP energies enters the polarizability so that there is an implicit dependence of the QP energies on each other. In practice, this is also not an issue since the numerical errors are typically orders of magnitude smaller than the absolute values of the QP energies.

The situation is different for qsGW. The off-diagonal elements of Σ_c are often equal to or very close to zero[575] and generally small compared to the diagonal elements. For these off-diagonal elements, numerical errors from AC can be orders of magnitudes larger than their values. Since there are many of them, this might significantly alter the solutions of eq. (3.115). Due to the non-linear nature of the QP equations, this can complicate convergence of the SCF procedure or even lead to erroneous results. The development of more reliable methods for AC is a very active field of research[467,576–580] and it would certainly be interesting to investigate whether other techniques are more suitable for qsGW. For now, we restrict ourselves to the techniques of Padé-approximants. To ensure numerical stability, two aspects need to be considered:

First, it seems reasonable to assume that AC close to the Fermi energy is also more reliable for the off-diagonal elements of Σ. To this end, using (2.342) to construct the exchange-correlation potential seems to be more suitable for our implementation than (2.341). As we will see later on, both constructions of the exchange-correlation potential lead to similar results, but using(2.342), the SCF procedure is significantly easier to converge. In fact, applying the same reasoning one could justify to use $\Sigma(\omega = 0)$[272] instead. However, as we will show below, using (2.342) is sufficiently numerically stable.

Second, after evaluating eq. (2.342) or (2.341), numerical noise needs to be removed rigorously from v^{QP}. At self-consistency, the off-diagonal elements of v^{QP} need to be zero: In the $(n+1)^{\mathrm{th}}$ iteration, v^{QP} is expressed in the basis which diagonalizes the operator defined in (3.116) in the n^{th} iteration. At self-consistency $b^{(n+1)} = b^{(n)}$, which will not be the case when the off-diagonal

elements of v^{QP} will be different from zero. In our present implementation, we set all values with magnitude smaller than $1e^{-6}$ to zero. This cut-off is of the order of the numerical noise introduced by the AC. As we will show later on, despite this drastic cut-off the HOMO and LUMO energies can be converged to a degree that the QP energies are converged within a few meV.

Fully Self-Consistent *GW*

In a fully self-consistent *GW* calculation, the Dyson equation (2.131) for the interacting single-particle Green's function is typically solved by inversion.[243,244,387] This requires the adjustment of the chemical potential in each self-consistency cycle[387] and generally seems to be very sensitive to numerical noise. We therefore prefer to directly solve (2.259) for the amplitudes and conjugated amplitudes. This can be done directly using a Schur decomposition[581] (LAPACK routine ZGGES) which yields a set of complex eigenvectors $\psi_k, \psi_p^\dagger$ and complex eigenvalues ϵ_p^{QP} for all ω_k. More precisely, the Schur decomposition of a matrix $\mathbf{A}$ is

$$\mathbf{A} = \mathbf{Q}\mathbf{U}\mathbf{Q}^\dagger \ ,$$

where $\mathbf{U}$ is upper triangular and $\mathbf{Q}$ unitary. The columns of $\mathbf{Q}$ and $\mathbf{Q}^\dagger$ span the eigenspace and dual space of $\mathbf{A}$ while the diagonal elements of $\mathbf{U}$ can be identified with the eigenvalues of (2.259). These can then be used directly to construct the interacting single-particle Green's function in imaginary frequency in the spectral representation (2.236).

Expanding the Dyson amplitudes in the first equation in (2.259) using (3.1), multiplying from the left with χ_μ^* and integrating over $\boldsymbol{r}_1$, turns it into a generalized eigenproblem for the coefficients of the expansion (3.1),

$$\sum_\nu \left[h_{\mu\nu} + \Sigma^\sigma_{\mu\nu}(\epsilon_p^{QP})\right] b_{p\nu} = \sum_\nu S_{\mu\nu} b_{p\nu} \epsilon_p^{QP} \tag{3.104}$$

with

$$h_{\mu\nu} = \int d\boldsymbol{r}_1 \chi_\mu^*(\boldsymbol{r}_1) h_1(\boldsymbol{r}_1) \chi_\nu(\boldsymbol{r}_1) \tag{3.105}$$

$$S_{\mu\nu} = \int d\boldsymbol{r}_1 \chi_\mu^*(\boldsymbol{r}_1) \chi_\nu(\boldsymbol{r}_1) \tag{3.106}$$

$$\Sigma^\sigma_{\mu\nu}(\epsilon_p^{QP}) = \int d\boldsymbol{r}_1 d\boldsymbol{r}_3 \chi_\mu^*(\boldsymbol{r}_1) \Sigma(\boldsymbol{r}_1, \boldsymbol{r}_2, \sigma, \epsilon_p^{QP}) \chi_\nu(\boldsymbol{r}_2) \ . \tag{3.107}$$

The second equation in (2.259) turns into an analogous expression for the expansion coefficients of the conjugated Dyson amplitudes

$$\sum_\mu b^*_{p\mu} \left[h_{\mu\nu} + \Sigma^\sigma_{\mu\nu}(\epsilon_p^{QP})\right] = \sum_\mu b^*_{p\mu} S_{\mu\nu} \epsilon_p^{QP} \ , \tag{3.108}$$

or in matrix notation

$$\mathbf{\Sigma}\left[\epsilon\right]\mathbf{b} = \mathbf{S}\mathbf{b}\epsilon \tag{3.109}$$

$$\mathbf{b}^*\mathbf{\Sigma}\left[\epsilon\right] = \mathbf{b}^*\mathbf{S}\epsilon\ . \tag{3.110}$$

Therefore, we do not calculate the Schur factorization of Σ but rather of $\mathbf{S}^{-1}\mathbf{\Sigma}$. This is inefficient when solving generalized eigenproblems of the form of eq. (3.104) with $\mathbf{\Sigma}$ and $\mathbf{S}$ Hermitian, since generally $\mathbf{S}^{-1}\mathbf{\Sigma}$ will be non-Hermitian. Since in our case $\mathbf{\Sigma}$ is already non-Hermitian, there is no reason not to calculate $\mathbf{S}^{-1}\mathbf{\Sigma}$.

To obtain the corresponding density, we first sort all eigenpairs $(\psi_k, \psi_p^\dagger, \epsilon_p^{QP})_{p=1,\dots N_{\mathrm{MO}}}$ according to the magnitude of the real part of the eigenvalues. For N electrons, the lowest N eigenvalues are then associated with N occupied QP states. We then analytically continue the Green's function to the real frequency axis and evaluate the density-matrix P using the occupied eigenstates which is used to calculate Σ_H and Σ_x.

The next self-consistency cycle starts with the calculation of the Green's function in imaginary time. Notice, that $\mathrm{Re}\ G(i\tau) \neq 0$ as it is the case for $G^{(s)}$ since the ϵ^{QP} are complex. To Fourier transform the Green's function to imaginary time, we use (2.230),

$$\begin{aligned} G(i\tau) =& \frac{i}{2\pi}\int d\omega G(i\omega)e^{-i\omega\tau} \\ =& \frac{i}{2\pi}\int d\omega \cos(\omega\tau)\left[G(i\omega)+G(-i\omega)\right] + \frac{1}{2\pi}\int d\omega \sin(\omega\tau)\left[G(i\omega)-G(-i\omega)\right] \\ =& \frac{i}{2\pi}\int_0^\infty d\omega \mathrm{Re}\ G(i\omega)\cos(\omega\tau) + \frac{i}{2\pi}\int_0^\infty d\omega \mathrm{Im}\ G(i\omega)\sin(\omega\tau)\ . \end{aligned} \tag{3.111}$$

We then have

$$\begin{aligned} G(i\tau>0) = G^{>}(i\tau) =& \frac{i}{2\pi}\int_0^\infty d\omega \mathrm{Re}\ G(i\omega)\cos(\omega\tau) + \frac{i}{2\pi}\int_0^\infty d\omega \mathrm{Im}\ G(i\omega)\sin(\omega\tau) \\ G(i\tau<0) = G^{<}(i\tau) =& \frac{i}{2\pi}\int_0^\infty d\omega \mathrm{Re}\ G(i\omega)\cos(\omega\tau) - \frac{i}{2\pi}\int_0^\infty d\omega \mathrm{Im}\ G(i\omega)\sin(\omega\tau)\ , \end{aligned} \tag{3.112}$$

since cos is even and sin is uneven. The same equations can also be found in ref. [427] albeit without the factor of i which is due to the fact that the Green's function in ref. [427] is defined without the prefactor of $-i$.

Quasi-particle self-consistent *GW*

As in evGW, also in qsGW the full self-energy needs to calculated self-consistently. However, we only need the Hermitian part. We therefore only need (3.104) with the matrix elements of the self-energy replaced by

$$v^{QP}(\epsilon_p^{QP}) = \frac{1}{2}\left[\Sigma(\epsilon_p^{QP}) + \Sigma^\dagger(\epsilon_p^{QP})\right]$$

with the exact dependence on the ϵ_p^{QP} given by one of eqs. (2.341) and (2.342)

We will write this equation in the basis of MOs in which the Hamiltonian of the preceding iteration is diagonal (and in which S is diagonal as well). In the first iteration, we obtain a correction to the QP energies corresponding to $G^{(s)}$,

$$\sum_q v_{pr}^{QP}(\epsilon_p^{QP}) U_{rq} = \left(\epsilon_p^{QP} - \epsilon_p\right) U_{pq} \; .$$

We then define

$$H^{QP}\left[G^{(s)}\right] = H_H[n(\boldsymbol{r})] + v_{xc}^{QP}\left[G^{(s)}\right] \tag{3.113}$$

where we have defined the Hartree Hamiltonian

$$H_H[n(\boldsymbol{r})] = t(\boldsymbol{r}) + v_{ext}(\boldsymbol{r}) + V_H[n(\boldsymbol{r})] \tag{3.114}$$

and update H^{QP} in each iteration according to

$$\sum_r H_{pr}^{QP^{(n+1)}} U_{rq}^{(n+1)} = \omega_p^{(n+1)} U_{pq}^{(n+1)} \; , \tag{3.115}$$

with

$$H^{QP^{(n+1)}} = H_H + \Delta V_H^{(n+1)} + v_{xc}^{QP^{(n+1)}} \tag{3.116}$$

and

$$V_{xc}^{QP^{(n+1)}} = V_x[P^{(n)}] + v_c^{QP}[G_0^{(n)}] \; . \tag{3.117}$$

In each iteration, H^{QP} is expressed in the basis in which $G_0^{(n)}$ is diagonal. That is, at the $(n+1)^{\text{th}}$ iteration, H^{QP} is expressed in terms of the $\left\{\phi_i^{(n)}\right\}$ and unless self-consistency has been reached, $U^{(n)}$ will not be unity and defines a rotation of the molecular orbitals. We now set

$$\begin{aligned} b_{\mu p}^{(n+1)} &= \sum_q b_{\mu q}^{(n)} U_{qp}^{(n+1)} \\ \epsilon_p^{(n+1)} &= \omega_p^{(n+1)} \quad \forall p \end{aligned} \tag{3.118}$$

and evaluate $G_0^{(n+1)}$ using eqs. (3.70) and (3.71) which in turn is used to evaluate eq. (3.92) as described in section‘3.2.1 and finally eqs. (2.341) and (2.342). The 1RDM is then evaluated and the change in the Hartree-potential is calculated as

$$\Delta v_H^{(n+1)} = v_H[\Delta n(\boldsymbol{r})^{(n+1)}] \; , \tag{3.119}$$

with

$$\Delta n(\boldsymbol{r})^{(n+1)} = n(\boldsymbol{r})^{(n+1)} - n(\boldsymbol{r})^{(n)} \; . \tag{3.120}$$

The cycle is repeated until self-consistency is reached.

G_0W_0 and eigenvalue-only self-consistent GW

In a G_0W_0 or evGW calculation, the diagonal elements of the self-energy (3.101) are analytically continued to the real frequency axis, where (2.334) is solved using bisection. In a G_0W_0 calculation, these are the final QP energies. In an evGW calculation, the resulting QP energies are used in eqs. (3.70) and (3.71) and the procedure outlined in section 3.2.1 is repeated until the QP energies are stationary.

To summarize this section, a pseudocode of our implementation together with theoretical asymptotic scaling with system size is given in figure 1.

Convergence Acceleration

As outlined so far, in each iteration of the self-consistency cycle the previous qsGW Hamiltonian is replaced by the new one. Similarly, in evGW, the QP energies of the previous iteration are replaced by the new ones. The procedure is the same as in the Roothaan algorithm for the HF approximations[582] which is well known to be numerically unstable[583] and where convergence difficulties are encountered already for the simplest molecules[584,585]. Also in many GW implementations, convergence has been shown to be much slower than with a simple linear mixing scheme[244,540]. While the latter seems to work reasonably well for evGW[277], it seems that there is room for improvement, especially for qsGW[277]. We therefore implemented an iterative fixed point procedure of the general form

$$\left\{G_0^{(m)}\right\}_{0\leq m\leq n+1} \rightarrow \widetilde{H}^{QP^{n+1}} \rightarrow \epsilon^{(n+1)}\,, b^{(n+1)}\,. \tag{3.121}$$

We replace (3.115) by

$$\sum_r \widetilde{H}_{pr}^{QP^{(n+1)}} U_{rq}^{(n+1)} = \omega_p^{(n+1)} U_{pq}^{(n+1)}\,, \tag{3.122}$$

with

$$\widetilde{H}^{QP^{(n+1)}} = \sum_{m=n-n_0}^{n+1} \alpha_m H^{QP^{(m)}}\,, \tag{3.123}$$

where

$$\sum_{m=n-n_0}^{n} \alpha_m = 1\,, \tag{3.124}$$

needs to be fulfilled and n_0 is the maximum number of previous iterations taken into account. We determine the expansion coefficients α_m using Pulay's DIIS method[468]. In the DIIS method, we seek to minimise the residual error

$$r^{(n+1)} = \sum_{m=n-n_0}^{n} \alpha_m r^{(m)}\,, \tag{3.125}$$

Algorithm 1 Pseudocode for the evaluation of the self-energy on the real frequency axis using PADF. The asymptotic operation count of some key steps is given on the right.

Compute C, v_c, $[v_c]^{-1}$
Input MO coefficients $b_{\mu n}$, orbital energies ϵ_n
Compute $\{\tau_i\}_{i=1,\ldots,N_\tau}$, $\{\omega_k\}_{k=1,\ldots,N_\omega}$, $\left\{\gamma_{ki}^{(c)}, \gamma_{ki}^{(s)}\right\}_{k=1,\ldots,N_\omega, i=1,\ldots N_\tau}$

for $\tau = \tau_1, \tau_2, \tau_3 \ldots, \tau_{N_\tau}$ **do**
  Calculate G using (3.70), (3.71) ▷ $N^3 N_\tau$
  for $A \in N_{atom}, B \in N_{atom}$ **do**
    Evaluate $P^{AB}(\tau_i)$ using (3.83)-(3.89) ▷ $N^2 N_\tau$
  end for
  for $\omega = \omega_1, \omega_2, \omega_3 \ldots, \omega_{N_\omega}$ **do**
    Calculate contribution to $P(\omega_i)$ using (3.62) ▷ $N^2 N_\tau N_\omega$
  end for
end for
for $\omega = \omega_1, \omega_2, \omega_3 \ldots, \omega_{N_\omega}$ **do**
  Calculate $W(\omega_k)$ using (3.90) ▷ $N^3 N_\omega$
end for
for $\tau = \tau_1, \tau_2, \tau_3 \ldots, \tau_{N_\tau}$ **do**
  for $\omega = \omega_1, \omega_2, \omega_3 \ldots, \omega_{N_\omega}$ **do**
    Calculate $W(\tau_i)$ using (3.62) ▷ $N^2 N_\tau N_\omega$
  end for
  for $A \in N_{atom}, B \in N_{atom}$ **do**
    Evaluate $\Sigma^{AB}(\tau_i)$ using eqs. (3.92) and (3.94)–(3.96) ▷ $N^2 N_\tau$
  end for
end for
if qsGW **then**
  Calculate Σ_{pq,τ_i}
end if
if G_0W_0 or evGW **then**
  Calculate Σ_{pp,τ_i}
end if
Evaluate (3.101) to obtain $\Sigma(i\omega)$
AC to obtain $C(z) = \Sigma(z)$

subject to the constraint eq. (3.124). One might additionally require the α_m to be positive (what is usually called EDIIS)[553] but we did not find any improvement over the simple DIIS.

Different implementations of DIIS differ in the definition of the residual error. For qsGW,

since G_0 uniquely determines H^{QP}, we would ideally define

$$r^{qsGW^{(n+1)}} = G_0^{(n+1)} - G_0^{(n)} \,, \tag{3.126}$$

however, storage (or recalculation) of this quantity for n_0 iterations is inefficient. Therefore, one can use

$$r^{qsGW^{(n+1)}} = P^{(n+1)} - P^{(n)} \,, \tag{3.127}$$

which is related to the time-ordered Green's function by taking the limit $\tau \to 0^-$. In this work, we have used a different definition for the residual which is, however, identical to (3.127). In the calculations performed in this work, we have used

$$r^{qsGW^{(n+1)}} = \left[P^{(n+1)} + Q^{(n+1)}\right] - \left[P^{(n)} + Q^{(n)}\right] \,.$$

Here, Q is defined like P, but with the summation spanning the virtual orbital space,

$$Q_{\mu\nu} = \sum_a b_{\mu a} \left[b^\dagger\right]_{a\nu} \,.$$

This is based on the intuitive assumption that convergence could be improved by including information about the virtual orbitals in the residual. However, note that $S^{-1} = \frac{1}{2}P + Q$, so that we obtain $P + Q = \frac{1}{2}P + S^{-1}$. Apart from the factor of 1/2, (3.127) is therefore completely equivalent to this expression.

Technically, in the n^{th} iteration we solve (3.115) and evaluate the corresponding $b^{(n)}$ from which we calculate $P^{(n)}$ and $Q^{(n)}$. We check for convergence by evaluating the Frobenius norm of the residual (3.127),

$$N_F = \frac{1}{N_{MO}^2} \sqrt{\sum_{\mu\nu} \left[r_{\mu\nu}^{(n+1)}\right]^2} \,, \tag{3.128}$$

and terminate the SCF as soon as $N_F < \epsilon_{SCF}$ for two subsequent iterations. As we will show later on, $\epsilon_{SCF} = 1e^{-7}$ leads to QP energies which are converged within a few meV for all systems in the GW100 database[545]. Subsequently, we store $r^{(n+1)}$ and $H^{QP^{(n+1)}}$ and determine the expansion coefficients α_m using the DIIS method, setting $n_0 = 10$. Finally, we solve (3.122) and use the resulting U to evaluate (3.118).

For evGW, the definition of the residual is straightforward, since only the QP energies change in each iteration. We therefore define the vector of QP energies

$$\bar{\epsilon}^{QP} = [\epsilon_1^{QP}, \dots \epsilon_{N_{\text{MO}}}^{QP}]$$

amd the residual as

$$r^{evGW^{(n+1)}} = \bar{\epsilon}^{QP^{(n+1)}} - \bar{\epsilon}^{QP^{(n)}} \,. \tag{3.129}$$

As for qsGW, we use $n_0 = 10$ by default. We consider the QP energies as converged when the difference between the HOMO QP energy of two subsequent iterations falls below 1 meV.

3.2.3 Vertex Corrections to the Self-Energy

We now give the working equations for the vertex corrections. These are all different variants of SOSEX with different versions of screening, ranging from SOSEX(W,v_c) to SOX. Since evaluation of these expressions is rather inefficient in the AO basis[4], they are evaluated in the MO basis directly with N^5 scaling with system size. However, the efficient frequency integration as well as the DF approximation result in a very low prefactor which makes these approaches applicable to systems with up to 50-100 atoms with large basis sets on standard hardware.

The derivation of these equations uses the fact that the single-particle Green's functions eqs. (3.65) and (3.66) are diagonal in the MO basis,

$$G^{>}_{aa'}(i\tau) = i\delta_{a,a'\in virt}e^{-\epsilon_a\tau} \tag{3.130}$$

and

$$G^{<}_{ii'}(i\tau) = i\delta_{i,i'\in occ}e^{-\epsilon_i\tau} \ , \tag{3.131}$$

with

$$G_{pp'} = \Theta(i\tau)G^{>}_{aa'}(i\tau) - \Theta(-i\tau)G^{<}_{ii'}(i\tau) \ . \tag{3.132}$$

we note again, that all QP energies are given relative to the chemical potential.

MP2 and statically screened second-order exchange

Using the definitions above eqs. (3.130)–(3.132), the SOX contribution to the self-energy in a given basis (this might be either the AO or the MO basis and we denote it here with x, y) can be evaluated as

$$\Sigma^{\mathrm{G3W2}}_{xy}(\tau_{12}) = -\sum_{prq}\int d\tau_3 d\tau_4 G^{(s)}_p(\tau_{14})W_{xpqr}(\tau_{13})G^{(s)}_q(\tau_{43})G^{(s)}_r(\tau_{32})W_{pqry}(\tau_{42}) \ . \tag{3.133}$$

Using a time-independent interaction, like with a statically screened or unscreened interaction (we use the bare Coulomb interaction in the following) and after transformation to the imaginary

[4]We refer to the discussion in ref. [35].

frequency axis through eq. (2.231), eq. (2.232)

$$\begin{aligned}
\Sigma^{\mathrm{SOX}}_{xy}(i\omega) =& i\sum_{prq}\int d\tau e^{i\omega\tau} G^{(s)}_{p}(i\tau) W^{(0)}_{xpqr} G^{(s)}_{q}(-i\tau) G^{(s)}_{r}(i\tau) W^{(0)}_{pqry} \\
=& +\sum_{prq} v_{xpqr} v_{pqry} \int_0^\infty d\tau e^{i\omega\tau} G^{(s)}_{>,p}(i\tau) G^{(s)}_{<,q}(-i\tau) G^{(s)}_{>,r}(i\tau) \\
& -\sum_{prq} v_{xpqr} v_{pqry} \int_0^\infty d\tau e^{-i\omega\tau} G^{(s)}_{<,p}(-i\tau) G^{(s)}_{>,q}(i\tau) G^{(s)}_{<,r}(-i\tau) \\
=& \sum_{i}^{occ}\sum_{ab}^{virt} v_{xaib} v_{aiby} \int_0^\infty d\tau e^{-(\epsilon_a - \epsilon_i + \epsilon_b - i\omega)\tau} \\
& -\sum_{ij}^{occ}\sum_{a}^{virt} v_{xiaj} v_{iajy} \int_0^\infty d\tau e^{-(-\epsilon_i + \epsilon_a - \epsilon_j + i\omega)\tau}
\end{aligned} \tag{3.134}$$

the SOX term becomes

$$\Sigma^{\mathrm{SOX}}_{xy}(i\omega) = \sum_{i}^{occ}\sum_{ab}^{virt} \frac{v_{xaib} v_{aiby}}{\epsilon_a + \epsilon_b - \epsilon_i - i\omega} - \sum_{ij}^{occ}\sum_{a}^{virt} \frac{v_{xiaj} v_{iajy}}{\epsilon_a - \epsilon_i - \epsilon_j + i\omega} \,. \tag{3.135}$$

Notice, that we have just proved the result of section 2.4.5 which we have illustrated in figure 2.7: Using a static electron-electron interaction, only the terms involving alternating greater and lesser propagators remain in the self-energy expression for the $G3W2$ term.

The statically screened $G3W2$ contribution to the self-energy is then obtained by replacing v_c with $W(i\omega = 0)$. We thereby rely on the assumption that GW already gives rather accurate QP energies. We thus expand Σ^{G3W2} around the GW QP energies. At zeroth order, we obtain

$$\epsilon_p^{GW+G3W2} = \epsilon_p^{GW} + \Sigma_{pp}^{sG3W2}(\epsilon_p^{GW}) \,, \tag{3.136}$$

where Σ_{pp}^{G3W2} is evaluated using the GW QP energies,

$$\Sigma_{pp}^{sG3W2}(\epsilon_p^{GW}) = \sum_{i}^{occ}\sum_{ab}^{virt} \frac{W(i\omega=0)_{paib} W(i\omega=0)_{aiby}}{\epsilon_a^{GW} + \epsilon_b^{GW} - \epsilon_i^{GW} - \epsilon_p^{GW}} - \sum_{ij}^{occ}\sum_{a}^{virt} \frac{W(i\omega=0)_{piaj} W(i\omega=0)_{iajy}}{\epsilon_a^{GW} - \epsilon_i^{GW} - \epsilon_j^{GW} + \epsilon_p^{GW}} \,, \tag{3.137}$$

and where we have used the analytical continuation of (3.135) from the imaginary axis to the complex plane. Using the $\Sigma^{GW+G3W2}$ self-energy in (2.334) is possible as well and has been done in ref. [379]. Due to its much smaller computational cost, all values presented in this work have been obtained using equation (3.136).

SOSEX

The expression for the SOSEX(W,v_c) self-energy is slightly more involved due to the presence of an integral over imaginary time which does not contain a δ-function. We obtain

$$\begin{aligned}\Sigma_{xy}^{SOSEX(W,v_c)}(i\omega) =& i\sum_{qrs}\int d\tau_{12}d\tau_3 e^{i\omega\tau_{12}}G_q^{(s)}(\tau_{12})W_{xqrs}(\tau_{13})v_{qrys}G_r^{(s)}(\tau_{32})G_s^{(s)}(\tau_{23}) \\ =& -\frac{1}{2\pi}\sum_{qrs}\int d\tau_{12}\int d\omega' e^{i\omega\tau_{12}}e^{-i\omega'\tau_1}G_q^{(s)}(\tau_{12})W_{xqrs}(i\omega')v_{qrys} \\ & \times \underbrace{\int d\tau_3 e^{i\omega'\tau_3}G_r^{(s)}(\tau_{32})G_s^{(s)}(\tau_{23})}_{I(\tau_2)} \ .\end{aligned} \tag{3.138}$$

The integral over τ_3 is split at τ_2, and using eqs. (2.204), (2.214), (A.9) and (A.10) we obtain

$$\begin{aligned}I(\tau_2) =& \int_{\tau_2}^{\infty} d\tau_3 e^{i\omega'\tau_3}G_r^{(s)}(\tau_{32})G_s^{(s)}(\tau_{23}) + \int_{-\infty}^{\tau_2} d\tau_3 e^{i\omega'\tau_3}G_r^{(s)}(\tau_{32})G_s^{(s)}(\tau_{23}) \\ =& \int_{\tau_2}^{\infty} d\tau_3 e^{i\omega'\tau_3}G_{>,r}^{(0)}(\tau_{32})G_{<,s}^{(0)}(\tau_{23}) + \int_{-\infty}^{\tau_2} d\tau_3 e^{i\omega'\tau_3}G_{<,r}^{(0)}(\tau_{32})G_{>,s}^{(0)}(\tau_{23}) \\ =& e^{-(\epsilon_r-\epsilon_s)\tau_2}\left\{\Theta(\epsilon_r)\Theta(-\epsilon_s)\int_{\tau_2}^{\infty} d\tau_3 e^{-(\epsilon_s-\epsilon_r-i\omega')\tau_3} + \Theta(\epsilon_s)\Theta(-\epsilon_r)\int_{-\infty}^{\tau_2} d\tau_3 e^{-(\epsilon_s-\epsilon_r-i\omega')\tau_3}\right\} \\ =& \frac{e^{i\omega'\tau_2}}{\epsilon_s-\epsilon_r-i\omega'}\left\{\Theta(\epsilon_r)\Theta(-\epsilon_s) - \Theta(\epsilon_s)\Theta(-\epsilon_r)\right\} \ .\end{aligned} \tag{3.139}$$

Combing this result with the previous expression, we therefore obtain

$$\begin{aligned}\Sigma_{xy}^{\mathrm{SOSEX}}(i\omega) =& \frac{1}{2\pi}\sum_{q}^{all}\sum_{i}^{occ}\sum_{a}^{virt}\int d\omega' \underbrace{\int d\tau e^{-i(\omega'-\omega)\tau}G_q^{(s)}(\tau)}_{I} \\ & \times\left\{\frac{W_{xqai}(i\omega')v_{qayi}}{\epsilon_i-\epsilon_a-i\omega'} + \frac{W_{xqia}(i\omega')v_{qiya}}{\epsilon_i-\epsilon_a+i\omega'}\right\} \ .\end{aligned} \tag{3.140}$$

The integral over τ can be written as

$$I = -i\Theta(\epsilon_q)\int_{-\infty}^{0} e^{-(i\omega'-i\omega-\epsilon_q)\tau}d\tau + i\Theta(-\epsilon_q)\int_{0}^{\infty} e^{-(i\omega'-i\omega-\epsilon_q)\tau}d\tau \ . \tag{3.141}$$

Integrating out τ and inserting the solution into the previous expression we get

$$\begin{aligned}\Sigma^{\mathrm{SOSEX}}_{xy}(i\omega) =& \frac{i}{2\pi}\sum_{i}^{occ}\sum_{ab}^{virt}\int d\omega' \frac{W_{xbai}(i\omega')v_{bayi}}{(\epsilon_i-\epsilon_a-i\omega')(i\omega'-i\omega-\epsilon_b)} \\ &+ \frac{i}{2\pi}\sum_{i}^{occ}\sum_{ab}^{virt}\int d\omega' \frac{W_{xbia}(i\omega')v_{biya}}{(\epsilon_i-\epsilon_a+i\omega')(i\omega'-i\omega-\epsilon_b)} \\ &+ \frac{i}{2\pi}\sum_{ij}^{occ}\sum_{a}^{virt}\int d\omega' \frac{W_{xjai}(i\omega')v_{jayi}}{(\epsilon_i-\epsilon_a-i\omega')(i\omega'-i\omega-\epsilon_j)} \\ &+ \frac{i}{2\pi}\sum_{ij}^{occ}\sum_{a}^{virt}\int d\omega' \frac{W_{xjia}(i\omega')v_{jiya}}{(\epsilon_i-\epsilon_a+i\omega')(i\omega'-i\omega-\epsilon_j)} \,.\end{aligned} \tag{3.142}$$

Our final expression is obtained by combining the sums over occupied and virtual single-particle states,

$$\begin{aligned}\Sigma^{\mathrm{SOSEX}}_{xy}(i\omega) =& -\frac{i}{2\pi}\sum_{q}^{all}\sum_{i}^{occ}\sum_{a}^{virt}\int d\omega' \frac{W_{xqai}(i\omega')v_{yiaq}}{(\epsilon_i-\epsilon_a-i\omega')(i\omega'-i\omega-\epsilon_q)} \\ &- \frac{i}{2\pi}\sum_{q}^{all}\sum_{i}^{occ}\sum_{a}^{virt}\int d\omega' \frac{W_{xqai}(i\omega')v_{yaqi}}{(\epsilon_i-\epsilon_a+i\omega')(i\omega'-i\omega-\epsilon_q)} \,.\end{aligned} \tag{3.143}$$

3.2.4 Correlation Energies

RPA and direct MP2 Correlation Energies

After constructing the polarizability in imaginary time, we can already use it to calculate the RPA correlation energy or equivalently it's second-order contribution $E_c^{(2)}$ only. For the former, we need to transform the matrix $P^{(0)}$ to the imaginary frequency axis using (3.62) (which reduces to a cosine transform since $P^{(0)}$ is bosonic). Defining the intermediate

$$Z_{\alpha\beta}(i\omega) = \sum_{\gamma} P^{(0)}_{\alpha\gamma,i\omega} v_{\gamma\beta}$$

(2.355) becomes

$$\begin{aligned}E_c^{RPA} =& \frac{1}{2\pi}\int_0^\infty d\omega \mathrm{Tr}\left\{[\ln\left(\mathbf{1}-\mathbf{Z}(i\omega)\right)]+\mathbf{Z}(i\omega)\right\} \\ =& \sum_{k}^{N_\omega}\sigma_k \mathrm{Tr}\left\{[\ln\left(\mathbf{1}-\mathbf{Z}(i\omega_k)\right)]+\mathbf{Z}(i\omega_k)\right\}\end{aligned} \tag{3.144}$$

in the auxiliary basis. Since matrix logarithms are difficult to calculate, we use that (assuming Z can be diagonalized with eigenvalues λ_j)

$$\mathrm{Tr}\left[\ln \mathbf{Z}\right] = \sum_j \ln(\lambda_j) = \ln\left(\prod_j \lambda_j\right) = \ln\det\left(\mathbf{Z}\right) \ ,$$

and evaluate the determinant of Z instead. For the same reason for which we do not invert W by CD, we also calculate the determinant of Z by LU decomposition. $P^{(0)}(i\tau)$ is stored on disk for all imaginary time points before it is Fourier transformed to the imaginary frequency axis and (3.144) is calculated.

$E_c^{(2)}$ is directly evaluated directly in imaginary time and is given by

$$\begin{aligned} E_c^{(2)} &= -\frac{1}{2}\sum_k^{N_\tau} \alpha_k \mathrm{Tr}\left(\sum_\gamma Z_{\alpha\gamma,\tau_k} Z_{\gamma\beta,\tau_k}\right) \\ &= -\frac{1}{2}\sum_k^{N_\tau} \alpha_k \sum_{\alpha\beta} Z_{\alpha\beta,\tau_k} Z_{\beta\alpha,\tau_k} \ . \end{aligned} \tag{3.145}$$

Here, $P^{(0)}(i\tau)$ is evaluated for a single imaginary time point and (3.145) is evaluated directly for each point, i.e. $P^{(0)}(i\tau)$ does not need to be stored on disk. Using (2.282) we also have

$$Z_{\alpha\beta,\sigma,\tau_k} = \sum_\gamma P^{(0)}_{\alpha\gamma,\sigma,\tau_k} v_{\gamma\beta} \tag{3.146}$$

and

$$Z_{\alpha\beta,\tau_k} Z_{\beta\alpha,\tau_k} = \sum_{\sigma=\alpha,\beta} \sum_{\sigma'=\alpha,\beta} Z_{\alpha\beta,\sigma,\tau_k} Z_{\alpha\beta,\sigma',\tau_k} \ . \tag{3.147}$$

When working in the AO basis, we are only interested in the contribution to $E_c^{(2)}$ from electrons with unpaired spins which is used for instance in spin-opposite scaled (SOS) MP2[394] or in DOD-DHs.[586] In that case, only the terms with $\sigma \neq \sigma'$ contribute and the resulting correlation energy expression is scaled by an empirical factor. These factors for different DOD double hybrids can be found in table 1 of ref. [218].

Vertex Corrections

We now use the different flavors of the $G3W2$ expression to the self-energy to obtain vertex corrections to the energy expression (2.355). Inserting the AC-SOSEX self-energy (2.364) into

(2.351), we obtain

$$\begin{aligned} E_c^{SOSEX(W,v_c)} =& \frac{1}{2}\int d1\ldots d4\; G^{(s)}(1,2)G^{(s)}(2,3)G^{(s)}(3,4)G^{(s)}(4,1) \\ & \times \left\{ \frac{1}{2} W^{(0)}(3,1)W^{(0)}(2,4) \right. \\ & \left. + \frac{1}{3} W^{(0)}(3,1) \int d5d6\; W^{(0)}(2,5)P^{(0)}(5,6)W^{(0)}(6,4) + \ldots \right\} . \end{aligned} \tag{3.148}$$

In contrast to the RPA energy expression, the terms in this equations can not be summed exactly due to the presence of the $1/n$-terms. However, defining

$$\Sigma_{Hxc}^{\lambda} = \sum_{n=1}^{\infty} \lambda^n \Sigma_{Hxc}^{(n)} \left[G^{(s)}, v_c \right] . \tag{3.149}$$

we can rewrite (2.351) as an integral over a coupling constant λ,

$$E_c = \frac{1}{2} \sum_{n=2} \frac{1}{n} \int d1d2 G^{(s)}(1,2)\Sigma_{Hxc}^{(n)}(2,1)[G^{(s)}] = \frac{1}{2}\int_0^1 \frac{d\lambda}{\lambda} \int d1d2 G^{(s)}(1,2)\Sigma_{Hxc}^{(\lambda)}(2,1)[G^{(s)}] . \tag{3.150}$$

Eq. (3.149) then becomes

$$\Sigma_{Hxc}^{\lambda} = \sum_{n=1}^{\infty} \Sigma_{Hxc}^{(n)} \left[G^{(s)}, \lambda v_c \right] = \sum_{n=1}^{\infty} \Sigma_{Hxc}^{(n)} \left[G^{(s)}, W^{(\lambda)} \right] , \tag{3.151}$$

where $W^{(\lambda)}$ is defined by

$$W^{(\lambda)}(1,2) = \lambda W^{(0)}(1,2) + \lambda W^{(0)}(1,3)P^{(0)}(3,4)W(4,2) . \tag{3.152}$$

Defining

$$\overline{W} = \int_0^1 d\lambda W^{(\lambda)} , \tag{3.153}$$

and

$$\overline{\Sigma} = \Sigma \left[\overline{W} \right] \tag{3.154}$$

the correlation energy becomes

$$E_c = \frac{1}{2} \int d1d2\; G^{(s)}(1,2)\overline{\Sigma}_c(2,1) . \tag{3.155}$$

The integral in (3.153) needs to be computed numerically, but converges typically very fast when Gauss-Legendre grids are employed.[334] In ref. [587] a trapezoidal rule for the solution of this integral has been used and also ref. [335] suggests that this choice is often suitable for the

calculation of correlation energies within the RPA and beyond. Below, we will assess the effect of such approximate coupling constant integration on absolute and relative correlation energies. Notice, that using a trapezoidal rule, (3.155) reduces to

$$E_c = \frac{1}{4}\int d1d2\; G^{(s)}(1,2)\Sigma_c(2,1)\;, \tag{3.156}$$

and when the statically screened $G3W2$ self-energy (2.365) is used in this expression, the energy expression of ref. [40] is obtained. When additionally both $W(0)$ are replaced by $W^{(0)}$, (3.156) gives the SOX term of MP2 (evaluated with $G^{(s)}$).[290]

Using (3.155), simple expressions for the AC-SOSEX energy in the canonical basis of KS orbitals can be obtained. The derivations are similar to the ones of section 3.2.3 With (3.155), the AC-SOSEX self-energy (2.364) and eqs. (3.130)–(3.132) we obtain for the AC-SOSEX correlation energy

$$\begin{aligned} E^{\mathrm{SOSEX}(W,v_c)} =& \frac{i}{2}\sum_{pqrs}\int d\tau_{12}d\tau_3 G_p^{(s)}(\tau_{13})G_q^{(s)}(\tau_{31})G_r^{(s)}(\tau_{12})G_s^{(s)}(\tau_{21})v_{spqr}\overline{W}_{rspq}(\tau_{23}) \\ =& -\frac{1}{4\pi}\sum_{pqrs}\int d\omega' W^{(0)}_{spqr}\overline{W}_{rspq}(i\omega')\int d\tau_{12}G_r^{(s)}(\tau_{12})G_s^{(s)}(\tau_{21}) \\ & \times \underbrace{\int d\tau_3 e^{-i\omega'\tau_{23}}G_p^{(s)}(\tau_{13})G_q^{(s)}(\tau_{31})}_{I(i\tau_{12})}\;. \end{aligned} \tag{3.157}$$

The integral over τ_3 is the same as in section 3.2.3, eq. 3.139,

$$I(i\tau_{12}) = \frac{\left[\Theta(\epsilon_p)\Theta(-\epsilon_q) - \Theta(\epsilon_q)\Theta(-\epsilon_p)\right]e^{i\omega'\tau_{12}}}{\epsilon_p - \epsilon_q + i\omega'} = -e^{i\omega'\tau_{12}}\frac{\Theta(-\epsilon_p) - \Theta(-\epsilon_q)}{\epsilon_p - \epsilon_q + i\omega'} \tag{3.158}$$

The remaining integral over τ_{12} is

$$I_{\tau_{12}} = -\int G_r^{(s)}(\tau_{12})G_s^{(s)}(\tau_{21})e^{i\omega'\tau_{12}}d\tau_{12} = \frac{\Theta(-\epsilon_r) - \Theta(-\epsilon_s)}{\epsilon_r - \epsilon_s - i\omega'}\;, \tag{3.159}$$

so that the correlation energy becomes

$$E^{\mathrm{SOSEX}(W,v_c)} = -\frac{1}{4\pi}\sum_{pqrs}\int d\omega' v_{spqr}\overline{W}_{rspq}(i\omega')\frac{\Theta(-\epsilon_r) - \Theta(-\epsilon_s)}{\epsilon_r - \epsilon_s - i\omega'}\frac{\Theta(-\epsilon_p) - \Theta(-\epsilon_q)}{\epsilon_p - \epsilon_q + i\omega'} \tag{3.160}$$

Each of the nominators can only give a non-vanishing contribution if one of the two occupation numbers is zero. If the difference of the occupation numbers is -1, we simply flip sign in the denominator. Without loss of generality we can then decide that the indices r and p belong to

occupied and the indices s and q to virtual single-particle states. This gives us a factor of 4. We can then use the symmetry of the Coulomb interaction to obtain

$$E^{\mathrm{SOSEX}(W,v_c)} = -\frac{1}{4\pi}\sum_{ij}^{occ}\sum_{ab}^{virt}\int_0^\infty d\omega \overline{W}_{iajb}(i\omega)W^{(0)}_{jaib}\frac{4(\epsilon_i-\epsilon_a)(\epsilon_j-\epsilon_b)}{[(\epsilon_i-\epsilon_a)^2+\omega^2]\,[(\epsilon_j-\epsilon_b)^2+\omega^2]}\,. \quad (3.161)$$

For a closed-shell system we can integrate out spin which gives an additional factor of 2. This can be seen by writing out the spin-dependence of the electron-electron interactions in the SOX term explicitly,

$$\begin{aligned} v_{spqr}v_{rspq} &= \int d\boldsymbol{r}_1\ldots d\boldsymbol{r}_4 \phi_s^*(\boldsymbol{r}_1)\phi_p(\boldsymbol{r}_1)\phi_q^*(\boldsymbol{r}_3)\phi_r(\boldsymbol{r}_3)\phi_r^*(\boldsymbol{r}_2)\phi_s(\boldsymbol{r}_2)\phi_p^*(\boldsymbol{r}_4)\phi_q(\boldsymbol{r}_4) \\ &\qquad \times \sum_{\sigma_1,\ldots\sigma_4=\alpha,\beta} s_s^*(\sigma_1)s_p(\sigma_1)s_q^*(\sigma_3)s_r(\sigma_3)s_r^*(\sigma_2)s_s(\sigma_2)s_p^*(\sigma_4)s_q(\sigma_4) \\ &= \int d\boldsymbol{r}_1\ldots d\boldsymbol{r}_4 \phi_s^*(\boldsymbol{r}_1)\phi_p(\boldsymbol{r}_1)\phi_q^*(\boldsymbol{r}_3)\phi_r(\boldsymbol{r}_3)\phi_r^*(\boldsymbol{r}_2)\phi_s(\boldsymbol{r}_2)\phi_p^*(\boldsymbol{r}_4)\phi_q(\boldsymbol{r}_4) \\ &\qquad \times \sum_{\sigma_1,\ldots\sigma_4=\alpha,\beta} \delta_{\sigma_1,\sigma_2}\delta_{\sigma_1,\sigma_4}\delta_{\sigma_3,\sigma_4}\delta_{\sigma_3,\sigma_2} \\ &= \int d\boldsymbol{r}_1\ldots d\boldsymbol{r}_4 \sum_{\sigma=\alpha,\beta} \phi_s^*(\boldsymbol{r}_1,\sigma)\phi_p(\boldsymbol{r}_1,\sigma)\phi_q^*(\boldsymbol{r}_3,\sigma)\phi_r(\boldsymbol{r}_3,\sigma) \\ &\qquad\qquad \times \phi_r^*(\boldsymbol{r}_2,\sigma)\phi_s(\boldsymbol{r}_2,\sigma)\phi_p^*(\boldsymbol{r}_4,\sigma)\phi_q(\boldsymbol{r}_4,\sigma)\,. \end{aligned} \quad (3.162)$$

Therefore, we recover the well-known SOSEX correlation energy expression for a closed-shell system[334,587] as

$$E^{\mathrm{SOSEX}(W,v_c)} = -\frac{1}{2\pi}\sum_{ij}^{N/2}\sum_{ab}^{virt}\int_0^\infty d\omega \overline{W}_{iajb}(i\omega)W^{(0)}_{jaib}\frac{4(\epsilon_i-\epsilon_a)(\epsilon_j-\epsilon_b)}{[(\epsilon_i-\epsilon_a)^2+\omega^2]\,[(\epsilon_j-\epsilon_b)^2+\omega^2]}\,, \quad (3.163)$$

where we have indicated that only $N/2$ orbitals are occupied and indices with upper bars denote spatial orbitals. In a spatial orbital basis (summing over spins), the SOSEX($W(0), W(0)$) Correlation energy is obtained from (2.362) and (2.65) as

$$\begin{aligned} E^{\mathrm{SOSEX}(W(0),W(0))} &= -\frac{1}{2}\sum_{pqrs}\int d\tau_{12} G_p^{(s)}(\tau_{12})G_q^{(s)}(\tau_{21})G_r^{(s)}(\tau_{12})G_s^{(s)}(\tau_{21}) \\ &\qquad \times \overline{W}_{spqr}(i\omega=0)\overline{W}_{rspq}(i\omega=0) \\ &= -\sum_{ij}^{occ}\sum_{ab}^{virt}\frac{\overline{W}_{spqr}(i\omega=0)\overline{W}_{rspq}(i\omega=0)}{\epsilon_i+\epsilon_j-\epsilon_a-\epsilon_b}\,. \end{aligned} \quad (3.164)$$

This expression is completely equivalent to the SOX in MP2 with the bare electron-electron interaction replaced by the statically screened, coupling constant averaged one. The SOX contribution to the correlation energy in the spin-orbital basis is

$$E^{SOX} = -\frac{1}{2}\sum_{ij}^{occ}\sum_{ab}^{virt}\frac{v_{iajb}v_{jaib}}{\epsilon_i+\epsilon_j-\epsilon_a-\epsilon_b}\ . \tag{3.165}$$

This can be combined with the direct term $E_c^{(2)}$, which we have already written down in the basis of spin-orbitals in (3.44). The same expression is obtained through (2.351) from the full second-order self-energy. We obtain

$$E^{MP2} = \frac{1}{2}\sum_{ij}^{occ}\sum_{ab}^{virt}\frac{v_{iajb}\left[v_{iajb}-v_{jaib}\right]}{\epsilon_i+\epsilon_j-\epsilon_a-\epsilon_b}\ . \tag{3.166}$$

Notice, that one often encounters the expression

$$E^{MP2} = \frac{1}{4}\sum_{ij}^{occ}\sum_{ab}^{virt}\frac{\left[v_{iajb}-v_{jaib}\right]^2}{\epsilon_i+\epsilon_j-\epsilon_a-\epsilon_b}\ . \tag{3.167}$$

The equivalence of both expressions follows from

$$v_{iajb}v_{iajb} - 2v_{iajb}v_{jaib} + v_{jaib}v_{jaib} = 2v_{iajb}v_{iajb} - 2v_{iajb}v_{jaib}$$

where we have permuted i and j in the third term on the *l.h.s.* Summing over spin (see (2.282) for the direct term), we obtain for a closed shell system

$$E^{MP2} = \sum_{ij}^{N/2}\sum_{ab}^{virt}\frac{v_{iajb}\left[2v_{iajb}-v_{jaib}\right]}{\epsilon_i+\epsilon_j-\epsilon_a-\epsilon_b}\ . \tag{3.168}$$

In all of these expressions the matrix elements of the type M_{pqrs} are evaluated using eqs. (3.20) and (3.21). In practice, we fix the indices i,j and evaluate all integrals as well as the energy denominator for the fixed pair i,j so that each contribution to E^{MP2} becomes a vector product, i.e.

$$E^{MP2} = \sum_{i\leq j} e_{ij}^{(2)}\ , \tag{3.169}$$

where

$$e_{ij}^{(2)} = \sum_{ab}^{virt}\frac{v_{iajb}\left[v_{iajb}-v_{jaib}\right]}{\epsilon_i+\epsilon_j-\epsilon_a-\epsilon_b}\ .$$

This can be parallelized efficiently over all pairs of occupied single-particle states.

3.2.5 The Bethe-Salpeter Equation as an effective 2-particle Problem

We now move on to the implementation of (2.316). As already discussed, in practice one typically builds $\chi^{(0)}_{eh}$ using the non-interacting propagators. Repeating the derivation (2.276) and using (2.229), we obtain

$$\begin{aligned}
&\chi^{(0)}_{eh}(x_1, x_2, x_{1'}, x_{2'}, i\tau) = -iG^{(s)}(1, 2')G^{(s)}(2, 1') \\
&= i\Theta(\tau)G^{(s)}_{>}(x_1, x_{2'}, \tau)G^{(s)}_{<}(x_{1'}, x_2, -\tau) + i\Theta(-\tau)G^{(s)}_{<}(x_{2'}, x_1, \tau)G^{(s)}_{>}(x_2, x_{1'}, -\tau) \\
&= -i\Theta(\tau)\sum_{ia} e^{-(\epsilon_a-\epsilon_i)\tau}\phi_a(\boldsymbol{r}_1)\phi^*_a(\boldsymbol{r}_{2'})\phi^*_i(\boldsymbol{r}_{1'})\phi_i(\boldsymbol{r}_2) \\
&\quad -i\Theta(-\tau)\sum_{ia} e^{-(\epsilon_a-\epsilon_i)\tau}\phi^*_a(\boldsymbol{r}_{2'})\phi_a(\boldsymbol{r}_1)\phi_i(\boldsymbol{r}_2)\phi^*_i(\boldsymbol{r}_{1'}) \ .
\end{aligned} \tag{3.170}$$

We now introduce a basis of resonant (particle-hole) excitations, and anti-resonant (hole-particle) excitations $\mathcal{B} = \mathcal{R}\oplus\mathcal{A}$. Bases for $\mathcal{R}$ and $\mathcal{A}$ are conveniently built from the single-particle orbitals, more precisely $\mathcal{R} = \{\phi_i\}_{i=1,\dots,N_{occ}} \otimes \{\phi^*_a\}_{i=1,\dots,N_{virt}}$ and $\mathcal{A} = \{\phi_a\}_{a=1,\dots,N_{virt}} \otimes \{\phi^*_i\}_{i=1,\dots,N_{occ}}$. The elements of this basis can be interpreted as non-interacting two-particle amplitudes,

$$\begin{aligned}
\chi^{(r)}_S(\boldsymbol{r}_1, \boldsymbol{r}_{1'}) &= \phi_i(\boldsymbol{r}_1)\phi^*_a(\boldsymbol{r}_{1'}) \\
\chi^{(a)}_S(\boldsymbol{r}_1, \boldsymbol{r}_{1'}) &= \phi_a(\boldsymbol{r}_1)\phi^*_i(\boldsymbol{r}_{1'}) \ .
\end{aligned} \tag{3.171}$$

We now express the interacting amplitudes $\chi_S(\boldsymbol{r}, \boldsymbol{r}')$ in terms of elements of $\mathcal{B}$,

$$\chi_S(\boldsymbol{r}, \boldsymbol{r}') = \sum_{S'} A^{(r)}_{SS'}\chi^{(r)}_{S'}(\boldsymbol{r}, \boldsymbol{r}') + \sum_{S'} A^{(a)}_{SS'}\chi^{(a)}_{S'}(\boldsymbol{r}, \boldsymbol{r}') \ , \tag{3.172}$$

i.e. as linear combination of non-interacting two-particle amplitudes. In this basis, every map $F : \mathcal{B} \mapsto \mathcal{B}$ can be written as

$$F = \begin{pmatrix} F^{(r,r)} & F^{(r,a)} \\ F^{(a,r)} & F^{(a,a)} \end{pmatrix} \ , \tag{3.173}$$

where (x, y) denotes the respective sector of $\mathcal{B}$. With the general basis transformation of a 4-point correlation function F,

$$F_{pqrs} = \int dx_1 x_2 x_3 x_4 \phi^*_p(x_1)\phi^*_q(x_2)F(x_1, x_2, x_3, x_4)\phi_r(x_3)\phi_s(x_4) \ , \tag{3.174}$$

The transformations to the different sectors of $\mathcal{B}$ are obtained as

$$\begin{aligned}
\left[F^{(rr)}\right]_{SS'} &= \int dx_1 x_2 x_3 x_4 \chi^{(r)^*}_S(x_2, x_4)F(\boldsymbol{r}, \boldsymbol{r}', x_3, x_4)\chi^{(r)}_{S'}(x_3, x_1) \\
\left[F^{(ra)}\right]_{SS'} &= \int dx_1 x_2 x_3 x_4 \chi^{(r)^*}_S(x_2, x_4)F(\boldsymbol{r}, \boldsymbol{r}', x_3, x_4)\chi^{(a)}_{S'}(x_3, x_1) \\
\left[F^{(ar)}\right]_{SS'} &= \int dx_1 x_2 x_3 x_4 \chi^{(a)^*}_S(x_2, x_4)F(\boldsymbol{r}, \boldsymbol{r}', x_3, x_4)\chi^{(r)}_{S'}(x_3, x_1) \\
\left[F^{(aa)}\right]_{SS'} &= \int dx_1 x_2 x_3 x_4 \chi^{(a)^*}_S(x_2, x_4)F(\boldsymbol{r}, \boldsymbol{r}', x_3, x_4)\chi^{(a)}_{S'}(x_3, x_1) \ .
\end{aligned} \tag{3.175}$$

From the definition (3.171) as well as the orthonormality of the single-particle orbitals the relations

$$\chi_S^{(r)}(\boldsymbol{r},\boldsymbol{r}') = \chi^{(a)^*}(x_2,x_1) \tag{3.176}$$

$$\int dx_1 x_2 \chi_S^{(x)^*}(\boldsymbol{r},\boldsymbol{r}')\chi_{S'}^{(y)}(\boldsymbol{r},\boldsymbol{r}') = \delta_{SS'}\delta_{\mu\nu} \quad x,y=[r,a] \tag{3.177}$$

follow. Using (3.171) and defining the differences of non-interacting particle-energies,

$$\Omega_S^{(0)} = \epsilon_a - \epsilon_i \ , \tag{3.178}$$

allows us to write

$$\begin{aligned}\chi_{eh}^{(0)}(x_1,x_2,x_{1'},x_{2'},i\tau) = &-i\Theta(\tau)\sum_S e^{-\Omega_S^{(0)}\tau}\chi_S^{(a)}(x_1,x_{1'})\chi_S^{(a)^*}(x_{2'},x_2)\\ &-i\Theta(-\tau)\sum_S e^{\Omega_S^{(0)}\tau}\chi_S^{(r)}(x_1,x_{1'})\chi_S^{(r)^*}(x_{2'},x_{2'}) \ .\end{aligned} \tag{3.179}$$

To transform the expressions to the imaginary frequency axis, we use again (2.232) and obtain

$$\chi_{eh}^{(0)}(x_1,x_2,x_{1'},x_{2'},i\omega) = \sum_S \frac{\chi_S^{(a)}(x_1,x_{1'})\chi_S^{(a)^*}(x_{2'},x_2)}{i\omega-\Omega^{(0)}} - \sum_S \frac{\chi_S^{(r)}(x_1,x_{1'})\chi_S^{(r)^*}(x_{2'},x_{2'})}{i\omega+\Omega^{(0)}} \ . \tag{3.180}$$

This expression closely resembles (2.275). The only differences are the replacement of all interacting quantities with non-interacting ones and the states S over which is summed. Recall, that in the expression of the generalized interacting susceptibility we do not sum over $S=0$ since we have subtracted the static contribution from the product $G(1,1')G(2,2')$. Using section 3.2.5 and eq. (3.175) the diagonal blocks of eq. (3.180) are

$$\begin{aligned}\left[L_0^{(rr)}\right]_{SS'} = &\sum_{S''}\int dx_1x_2x_3x_4 \frac{\chi_S^{(r)^*}(x_2,x_4)\chi_{S''}^{(r)}(x_2,x_4)\chi_{S''}^{(r)^*}(x_3,x_1)\chi_{S'}^{(r)}(x_3,x_1)}{i\omega+E_{S''}}\\ &+\sum_{S''}\int dx_1x_2x_3x_4 \frac{\chi_S^{(r)^*}(x_2,x_4)\chi_{S''}^{(a)}(x_2,x_4)\chi_{S''}^{(a)^*}(x_3,x_1)\chi_{S'}^{(r)}(x_3,x_1)}{-i\omega+E_{S''}}\\ &=\frac{\delta_{SS'}}{i\omega+E_S} \ ,\end{aligned} \tag{3.181}$$

and

$$\begin{aligned}\left[L_0^{(aa)}\right]_{SS'} &= \sum_{S''}\int dx_1x_2x_3x_4\frac{\chi_S^{(a)^*}(x_2,x_4)\chi_{S''}^{(r)}(x_2,x_4)\chi_{S''}^{(r)^*}(x_3,x_1)\chi_{S'}^{(a)}(x_3,x_1)}{i\omega+E_{S''}} \\ &+ \sum_{S''}\int dx_1x_2x_3x_4\frac{\chi_S^{(a)^*}(x_2,x_4)\chi_{S''}^{(a)}(x_2,x_4)\chi_{S''}^{(a)^*}(x_3,x_1)\chi_{S'}^{(a)}(x_3,x_1)}{-i\omega+E_{S''}} \\ &= \frac{\delta_{SS'}}{-i\omega+E_S}\end{aligned}$$

,

and the off-diagonal blocks are zero,

$$\begin{aligned}\left[L_0^{(ra)}\right]_{SS'} &= \int dx_1x_2x_3x_4\sum_{S''}\frac{\chi_S^{(r)^*}(x_2,x_4)\chi_{S''}^{(r)}(x_2,x_4)\chi_{S''}^{(r)^*}(x_3,x_1)\chi_{S'}^{(a)}(x_3,x_1)}{i\omega+E_{S''}} \\ &+ \int dx_1x_2x_3x_4\sum_{S''}\frac{\chi_S^{(r)^*}(x_2,x_4)\chi_{S''}^{(a)}(x_2,x_4)\chi_{S''}^{(a)^*}(x_3,x_1)\chi_{S'}^{(a)}(x_3,x_1)}{-i\omega+E_{S''}} = 0\ ,\end{aligned} \tag{3.182}$$

and

$$\begin{aligned}\left[L_0^{(ar)}\right]_{SS'} &= \sum_{S''}\int dx_1x_2x_3x_4\frac{\chi_S^{(a)^*}(x_2,x_4)\chi_{S''}^{(r)}(x_2,x_4)\chi_{S''}^{(r)^*}(x_3,x_1)\chi_{S'}^{(r)}(x_3,x_1)}{i\omega+E_{S''}} \\ &+ \sum_{S''}\int dx_1x_2x_3x_4\frac{\chi_S^{(a)^*}(x_2,x_4)\chi_{S''}^{(a)}(x_2,x_4)\chi_{S''}^{(a)^*}(x_3,x_1)\chi_{S'}^{(r)}(x_3,x_1)}{-i\omega+E_{S''}} = 0\ ,\end{aligned} \tag{3.183}$$

In other words, the non-interacting generalized susceptibility is diagonal in the space of resonant and antiresonant transitions. For the matrix elements of the Kernel of (2.316),

$$\Gamma^{(0)^{GW}}(1,2,1',2') = W^{(0)}(1,1')\delta(1,2)\delta(1',2') - W(1,1')\delta(1,2')\delta(2,1')\delta(t_1-t_{1'})\ , \tag{3.184}$$

we obtain

$$\begin{aligned}\Gamma_{SS'}^{(0)^{(rr)}} &= \int dx_1dx_2\phi_b^*(x_1)\phi_i^*(x_2)\left[v_c(\boldsymbol{r}_1,\boldsymbol{r}_2)\phi_j(x_1)\phi_a(x_2) - W(\boldsymbol{r}_1,\boldsymbol{r}_2,i\omega=0)\phi_a(x_1)\phi_j(x_2)\right] \\ \Gamma_{SS'}^{(0)^{(ra)}} &= \int dx_1dx_2\phi_j^*(x_1)\phi_i^*(x_2)\left[v_c(\boldsymbol{r}_1,\boldsymbol{r}_2)\phi_b(x_1)\phi_a(x_2) - W(\boldsymbol{r}_1,\boldsymbol{r}_2,i\omega=0)\phi_a(x_1)\phi_b(x_2)\right] \\ \Gamma_{SS'}^{(0)^{(ar)}} &= \int dx_1dx_2\phi_b^*(x_1)\phi_a^*(x_2)\left[v_c(\boldsymbol{r}_1,\boldsymbol{r}_2)\phi_j(x_1)\phi_i(x_2) - W(\boldsymbol{r}_1,\boldsymbol{r}_2,i\omega=0)\phi_i(x_1)\phi_j(x_2)\right] \\ \Gamma_{SS'}^{(0)^{(aa)}} &= \int dx_1dx_2\phi_j^*(x_1)\phi_a^*(x_2)\left[v_c(\boldsymbol{r}_1,\boldsymbol{r}_2)\phi_b(x_1)\phi_i(x_2) - W(\boldsymbol{r}_1,\boldsymbol{r}_2,i\omega=0)\phi_i(x_1)\phi_b(x_2)\right]\ .\end{aligned} \tag{3.185}$$

For real orbitals

$$\Gamma^{(0)^{(rr)}} = \Gamma^{(0)^{(aa)}} \quad \text{and} \quad \Gamma^{(0)^{(ar)}} = \Gamma^{(0)^{(ra)}} \ , \tag{3.186}$$

and summing over spins, we obtain

$$\begin{aligned}
\Gamma^{(0)^{(rr)}}_{iajb} =& \int d\boldsymbol{r}_1 d\boldsymbol{r}_2 \sum_{\sigma_i,\sigma_j,\sigma_a,\sigma_b=\alpha,\beta} \phi^*_b(\boldsymbol{r}_1)\phi_j(\boldsymbol{r}_1)v_c(\boldsymbol{r}_1,\boldsymbol{r}_2)\phi^*_i(\boldsymbol{r}_2)\phi_a(\boldsymbol{r}_2)\delta_{\sigma_b,\sigma_j}\delta_{\sigma_i,\sigma_a} \\
&- \int d\boldsymbol{r}_1 d\boldsymbol{r}_2 \sum_{\sigma_i,\sigma_j,\sigma_a,\sigma_b=\alpha,\beta} \phi^*_b(\boldsymbol{r}_1)\phi_a(\boldsymbol{r}_1)W(\boldsymbol{r}_1,\boldsymbol{r}_2,i\omega=0)\phi^*_i(\boldsymbol{r}_2)\phi_j(\boldsymbol{r}_2)\delta_{\sigma_a,\sigma_b}\delta_{\sigma_i,\sigma_j} \\
\Gamma^{(0)^{(ra)}}_{iajb} =& \int d\boldsymbol{r}_1 d\boldsymbol{r}_2 \sum_{\sigma_i,\sigma_j,\sigma_a,\sigma_b=\alpha,\beta} \phi^*_j(\boldsymbol{r}_1)\phi_b(\boldsymbol{r}_1)v_c(\boldsymbol{r}_1,\boldsymbol{r}_2)\phi^*_i(\boldsymbol{r}_2)\phi_a(\boldsymbol{r}_2)\delta_{\sigma_b,\sigma_j}\delta_{\sigma_i,\sigma_a} \\
&- \int d\boldsymbol{r}_1 d\boldsymbol{r}_2 \sum_{\sigma_i,\sigma_j,\sigma_a,\sigma_b=\alpha,\beta} \phi^*_j(\boldsymbol{r}_1)\phi_a(\boldsymbol{r}_1)W(\boldsymbol{r}_1,\boldsymbol{r}_2,i\omega=0)\phi^*_i(\boldsymbol{r}_2)\phi_b(\boldsymbol{r}_2)\delta_{\sigma_a,\sigma_j}\delta_{\sigma_i,\sigma_b} \ .
\end{aligned} \tag{3.187}$$

The BSE can then be written as

$$\begin{aligned}
L = \left[L_0^{-1} - K\right]^{-1} &= \left[\begin{pmatrix} E_S & 0 \\ 0 & E_S \end{pmatrix} - i\omega \begin{pmatrix} 1 & 0 \\ 0 & 1 \end{pmatrix} + \begin{pmatrix} \Gamma^{(0)^{(rr)}} & \Gamma^{(0)^{(ra)}} \\ -\Gamma^{(0)^{(ra)}} & -\Gamma^{(0)^{(rr)}} \end{pmatrix}\right]^{-1} \\
&= \left[-i\omega\mathbb{I} + M\right]^{-1} \ ,
\end{aligned} \tag{3.188}$$

with $\mathbb{I}$ being the identity matrix and

$$M = \begin{pmatrix} A & B \\ -B & -A \end{pmatrix} \ , \tag{3.189}$$

with

$$A_{SS'} = \quad A_{iajb} = \quad \delta_{ab}\delta_{ij}\left(\epsilon_i - \epsilon_a\right) + v_{iajb} - W(i\omega=0)_{ijab} \tag{3.190}$$

$$B_{SS'} = \quad B_{iajb} = \quad v_{iajb} - W(i\omega=0)_{ajbi} \ . \tag{3.191}$$

Following the derivations of section 2.3.1 leading to (2.259), we make us of the spectral representation of χ (2.275) we can now reformulate the Dyson equation (3.188) as an effective 2-particle problem,

$$\sum_{S'} \left[\left[M - i\omega\mathbb{I}\right]^{-1}\right]_{SS'} \chi_{S'} = \frac{1}{\Omega_S - i\omega}\chi_S \ , \tag{3.192}$$

with $\chi_S \in \mathcal{B}$. Consequently,

$$\sum_{S'} \left[M - i\omega\mathbb{I}\right]_{SS'} \chi_{S'} = \left[\Omega_S - i\omega\right]\chi_S \ , \tag{3.193}$$

and since $i\omega$ only results in a constant shift of the eigenvalues, we obtain

$$\sum_{S'} M_{SS'} |\chi_{S'}\rangle = \Omega_S |\chi_S\rangle \ . \tag{3.194}$$

Diagonalization of M yields a set of eigenvectors and excitation energies Ω_S, from which the spectral representation of the interacting 2-particle Green's function is readily constructed. One huge advantage of this form of the BSE is that it eliminates the dependence on ω. This is however only possible in the static approximation for W. If the dynamic W is used, one ends up with an eigenproblem of the same form as (3.194), however, with a frequency dependent M.[127,128] In this case, M would need to be diagonalized for each ω separately and it is more convenient to construct L by direct inversion of $L_0^{-1} - K$ for each ω. This is of course the same situation as for the Dyson equation for the single-particle Green's function. In a fully self-consistent GW calculation, the Dyson equation for the interacting single-particle Green's function is often solved by inversion. When the self-energy is approximated as static, Dyson's equation is more easily solved by diagonalizing the resulting Hamiltonian which gives the spectral representation of the new Green's function.

Notice, that we have only derived the working equations for the BSE with static screening but not the dynamical version which starts from (2.315). For thorough discussions as well as derivations of the working equations for this case we refer to the work of Strinati on this subject, especially ref. [156] or ref. [128]. The implementation of this equation in plane-wave code has for instance been described by Kutepov.[424]

It is convenient to rewrite (3.194) as

$$A |\chi_S^{(r)}\rangle + B |\chi_S^{(a)}\rangle = \quad \Omega_S |\chi_S^{(r)}\rangle \tag{3.195}$$

$$B |\chi_S^{(r)}\rangle + A |\chi_S^{(a)}\rangle = \quad -\Omega_S |\chi_S^{(a)}\rangle \tag{3.196}$$

where we have introduced

$$\chi_S = \chi_S^{(r)} + \chi_S^{(a)} \ . \tag{3.197}$$

This definition makes sense due to the orthogonality of the spaces of resonant and antiresonant transitions, i.e. $\chi_S^{(r)} \in \mathcal{R}$ and $\chi_S^{(a)} \in \mathcal{A}$. The equations are simplified under the assumption that resonant and antiresonant transitions do not couple, or equivalently, that excitons can be described as a superposition of particle-hole transitions only. This is the so-called Tamm-Dancoff approximation[365,588] (TDA).[5] Equations (3.195) and (3.196) then become

$$A |\chi_S^{(r)}\rangle = \quad \Omega_S |\chi_S^{(r)}\rangle \tag{3.198}$$

$$A |\chi_S^{(a)}\rangle = \quad -\Omega_S |\chi_S^{(a)}\rangle \ . \tag{3.199}$$

[5]The Tamm-Dancoff approximation has first been introduced by Igor Tamm and Sidney Dancoff to describe collective excitations in nucelar physics in Hartree-Fock theory.[588,589]. Head-Gordon and Hirata introduced it to molecular physics in the framework of time-dependent DFT.[365]

Therefore, since

$$\Omega_S \left|\chi_S^{(r)}\right\rangle \left\langle\chi_S^{(a)}|\chi_S^{(a)}\right\rangle = -\Omega_S \left|\chi_S^{(a)}\right\rangle \tag{3.200}$$

and because of equation (2.260),

$$\left|\chi_S^{(r)}\right\rangle = -\left|\chi_S^{(a)}\right\rangle \ . \tag{3.201}$$

The pair of equations (3.196) and (3.195) can be rewritten (subtracting/adding both equations) as

$$(A-B)\left|\chi_S^{(r)} - \chi_S^{(a)}\right\rangle = \quad \Omega_S \left|\chi_S^{(r)} + \chi_S^{(a)}\right\rangle \tag{3.202}$$

$$(A+B)\left|\chi_S^{(r)} + \chi_S^{(a)}\right\rangle = \quad \Omega_S \left|\chi_S^{(r)} - \chi_S^{(a)}\right\rangle \ , \tag{3.203}$$

from were one obtains

$$(A+B)(A-B)\left|\chi_S^{(r)} - \chi_S^{(a)}\right\rangle = \quad \Omega_S^2 \left|\chi_S^{(r)} - \chi_S^{(a)}\right\rangle \tag{3.204}$$

$$(A-B)(A+B)\left|\chi_S^{(r)} + \chi_S^{(a)}\right\rangle = \quad \Omega_S^2 \left|\chi_S^{(r)} + \chi_S^{(a)}\right\rangle \ . \tag{3.205}$$

These versions of (3.194) are useful since they reduce the matrix sizes one needs to work with by a factor of two.

To write down the working equations for a close-shell system, we need to explicitly take into account the spin-strucure of the matrices $\Gamma^{(0)^{(rr)}}$ and $\Gamma^{(0)^{(ra)}}$. It is clear that all terms with one spin-up and three spin-down indicies (or the other way round) need to be zero. This leaves us with 8 terms, and using (3.187) as well as the shorthand notation $W = W(i\omega = 0)$we obtain the following structure of $\Gamma^{(0)^{(rr)}}$ in the basis of spin indicies

$$\Gamma^{(0)^{(rr)}}_{iajb,\sigma_i\sigma_a\sigma_j\sigma_b} = \begin{array}{c|cccc} & \alpha\alpha & \alpha\beta & \beta\alpha & \beta\beta \\ \alpha\alpha & v_{iajb} - W_{ijab} & 0 & 0 & v_{iajb} \\ \alpha\beta & 0 & -W_{ijab} & 0 & 0 \\ \beta\alpha & 0 & 0 & -W_{ijab} & 0 \\ \beta\beta & v_{iajb} & 0 & 0 & v_{iajb} - W_{ijab} \end{array} \tag{3.206}$$

and for $\Gamma^{(0)^{(ra)}}$

$$\Gamma^{(0)^{(ra)}}_{iajb,\sigma_i\sigma_a\sigma_j\sigma_b} = \begin{array}{c|cccc} & \alpha\alpha & \alpha\beta & \beta\alpha & \beta\beta \\ \alpha\alpha & v_{iajb} - W_{ajbi} & 0 & 0 & v_{iajb} \\ \alpha\beta & 0 & 0 & -W_{ajbi} & 0 \\ \beta\alpha & 0 & -W_{ajbi} & 0 & 0 \\ \beta\beta & v_{iajb} & 0 & 0 & v_{iajb} - W_{ajbi} \end{array} \ . \tag{3.207}$$

Since $A \pm B = E_S + \Gamma^{(0)^{(rr)}} \pm \Gamma^{(0)^{(ra)}}$, we also calculate

$$\left[\Gamma^{(0)^{(rr)}} \pm \Gamma^{(0)^{(ra)}}\right]_{iajb,\sigma_i\sigma_a\sigma_j\sigma_b} =$$

$$\begin{array}{c|cccc} & \alpha\alpha & \alpha\beta & \beta\alpha & \beta\beta \\ \alpha\alpha & fv_{iajb} - W_{ijab} \mp W_{ajbi} & 0 & 0 & fv_{iajb} \\ \alpha\beta & 0 & -W_{ijab} & \mp W_{ajbi} & 0 \\ \beta\alpha & 0 & \mp W_{ajbi} & -W_{ijab} & 0 \\ \beta\beta & fv_{iajb} & 0 & 0 & fv_{iajb} - W_{ijab} \mp W_{ajbi} \end{array}, \tag{3.208}$$

with $f = 2$ in the plus case and $f = 0$ in the minus case. Diagonalization results in

$$\left[\Gamma^{(0)^{(rr)}} \pm \Gamma^{(0)^{(ra)}}\right]_{iajb,\sigma_i\sigma_a\sigma_j\sigma_b} =$$

$$\begin{array}{c|cccc} & \frac{1}{\sqrt{2}}(\alpha\alpha + \beta\beta) & \frac{1}{\sqrt{2}}(\alpha\alpha - \beta\beta) & \frac{1}{\sqrt{2}}(\alpha\beta + \beta\alpha) & \frac{1}{\sqrt{2}}(\alpha\beta - \beta\alpha) \\ \frac{1}{\sqrt{2}}(\alpha\alpha + \beta\beta) & 2fv_{iajb} - W_{ijab} \mp W_{ajbi} & 0 & 0 & 0 \\ \frac{1}{\sqrt{2}}(\alpha\alpha - \beta\beta) & 0 & -W_{ijab} \mp W_{ajbi} & 0 & 0 \\ \frac{1}{\sqrt{2}}(\alpha\beta + \beta\alpha) & 0 & 0 & -W_{ijab} \mp W_{ajbi} & 0 \\ \frac{1}{\sqrt{2}}(\alpha\beta - \beta\alpha) & 0 & 0 & 0 & -W_{ijab} \mp W_{ajbi} \end{array}, \tag{3.209}$$

which shows that there only two different types of solutions: In the basis of spatial orbitals singlet exciations are described by the matrix elements

$$(A+B)^s_{iajb} = (\epsilon_a - \epsilon_i)\delta_{ab}\delta_{ij} - W_{ijab} - W_{ajbi} + 4v_{iajb} \tag{3.210}$$

$$(A-B)^s_{iajb} = (\epsilon_a - \epsilon_i)\delta_{ab}\delta_{ij} - W_{ijab} + W_{ajbi} \tag{3.211}$$

and triplet excitations are described by

$$(A+B)^t_{iajb} = (\epsilon_a - \epsilon_i)\delta_{ab}\delta_{ij} - W_{ijab} - W_{ajbi} \tag{3.212}$$

$$(A-B)^t_{iajb} = (\epsilon_a - \epsilon_i)\delta_{ab}\delta_{ij} - W_{ijab} + W_{ajbi}\ . \tag{3.213}$$

Singlet and triplet excitation energies are then obtained by solving (3.205) or (3.204) with these matrix elements.

Diagonalization of the 2-particle Hamiltonian

The dimension of the eigenproblems section 3.2.5 grows as $n = N_{occ}N_{virt}$, i.e. linear with basis set and quadratic with system size. For instance, a calculation of the excited states of the C_{60} molecule in a TZ3P basis set will already lead to matrices of dimension $180x1620 = \approx 3 \times 10^5$ whose diagonalization would already require 720 GB of storage. Such matrices can be stored and diagonalized using highly efficient distributed solvers[590] based on for instance the CHASE

algorithm[591] but performing such large calculations on standard hardware probably won't become routine anytime soon.

In applications where the full interacting generalized susceptibility is needed, for instance when one solves the *GW* equations with screening calculated within BSE@*GW* instead of within the RPA,[361,362] there is no way around the diagonalization of the full BSE Hamiltonian. However, some approaches to circumvent the N^6 scaling of these calculations by compressing the BSE Hamiltonian have been suggested over the last years.[442,444] A strategy which has been pursued to calculate optical spectra is to use iterative Lanczos-type solvers,[441,592,593] for instance Haydock recursion,[594] which only scales as N^4 with system size or even cubic in an AO based implementation.[441]

In practical applications one is however often interested in $m \ll n$ low-lying excitonic states. These can be found using iterative eigensolvers which only scale as mn^2. Such solvers will still require storage of the whole matrix to be diagonalized. Further savings of CPU time and memory can be achieved by removing high-energy transitions from the particle-hole basis which are not contributing significantly to the low-lying excitation energies.

Even with such techniques, application of the BSE@GW method to larger systems with a few thousand virtual states is not possible. For such systems, one can however resort to iterative eigenvalue solvers which have been developed for TD-HF over the last decades. Indeed, replacing the matrix elements of the screened Coulomb interaction by the ones of the bare one in (3.205), the TD-HF method is obtained (compare (2.316) to (2.293)). It is therefore clear that any solver which can be used to solve (3.194) in the TD-HF case, can also be used for BSE@GW. We use an extension of the Davidson algorithm[595] originally proposed by Stratmann and Scuseria.[596] It projects the generalized eigenproblem (3.205) on a sequence of orhonormal subspaces

$$\text{span}\left\{b_1^{(n)}, \dots b_k^{(n)}\right\} , \tag{3.214}$$

in which (3.205) is solved. k denotes the size of the n^{th} subspace and the b_k are linear combinations of particle-hole states. The vectors forming the subspace are then updated until the subspaces are converged. The procedure can be interpreted as an iterative optimization of the basis of particle-hole states, where the part which does not carry useful information (i.e. the particle-hole transitions which do not contribute to the low-lying excitons) is projected out.

Matrix Elements Equations (3.210)–(3.213) in the Davidson Method

The time-determining step in the Davidson diagonalization is the projection of the eigenproblem in the full space on the subspaces. The term containing the bare Coulomb potential is easily evaluated following the procedure in ref. [597]. For the matrix elements of the screened interaction in the $(n+1)^{\text{th}}$ subspace iteration, we define a column in the subspace labeled by $s_i, s_j, \dots$, $s_a, s_b, \dots$, respectively, as

$$(\mathbf{A} \pm \mathbf{B})^{(n+1)}_{s_i s_a} = \sum_{s_j, s_b} \left\{ -W(i\omega = 0)^{(n)}_{s_a s_b, s_j s_i} \mp W(i\omega = 0)^{(n)}_{s_a s_j, s_b s_i} \right\} b^{(n)}_{s_i s_a} . \tag{3.215}$$

In the minus case, this is equivalent to the evaluation of the greater or lesser component of self-energy for a single imaginary time point. In the plus case, a similar algorithm can be used, but the resulting matrix needs to be antisymmetrized.

Since we do not use the screened interaction at zero frequency in our GW implementation, we calculate the zero-frequency component of $P^{(0)}$ from the imaginary time representation of the polarizability by

$$P(\omega = 0) = \frac{1}{2\pi} \int P^{(0)}(i\tau) d\tau \ , \tag{3.216}$$

and we then use (2.301) to obtain $W(\omega = 0)$. We solve (3.215) in the basis of Slater functions and then transform to the basis functions which span the subspace. Let us write (3.215) in the primary basis as

$$K^{(\pm)}_{\mu\nu} = -\sum_{\kappa\lambda} b_{\kappa\lambda} W(i\omega = 0)_{\mu\kappa\nu\lambda} \pm W(i\omega = 0)_{\nu\kappa\mu\lambda} \ . \tag{3.217}$$

Within the PADF approximation, the contribution to $\mathbf{K}^{(\pm)}$ for all atom pairs (A, B) is

$$\mathbf{K}^{(\pm)^{\mathrm{AB}}} = \mathbf{K}^{(\pm)^{\mathrm{AB,I}}} + \mathbf{K}^{(\pm)^{\mathrm{AB,II}}} + \mathbf{K}^{(\pm)^{\mathrm{AB,III}}} + \mathbf{K}^{(\pm)^{\mathrm{AB,IV}}} \ , \tag{3.218}$$

where

$$\begin{aligned} \mathbf{K}^{(+)^{\mathrm{AB,III}}} &= \left[\mathbf{K}^{(+)^{\mathrm{AB,II}}}\right]^T \\ \mathbf{K}^{(-)^{\mathrm{AB,III}}} &= -\left[\mathbf{K}^{(-)^{\mathrm{AB,II}}}\right]^T \ . \end{aligned} \tag{3.219}$$

In these and in the following quantities the matrices are restricted to the primary basis functions centered on the atoms denoted by the indices in the superscripts. Defining the intermediates

$$I^{ABC}_{\mu\nu\gamma} = \sum_{\beta \in B} c^{ABB}_{\mu\nu\beta} W(\omega = 0)^{BC}_{\beta\gamma} \ , \tag{3.220}$$

and

$$F^{BAA}_{\nu\mu\alpha} = \sum_{\lambda \in D} b^{DB}_{\lambda\nu} c^{DAA}_{\lambda\mu\alpha} \ . \tag{3.221}$$

We can then write

$$K^{\pm,AC,I}_{\mu\kappa} = \sum_{\nu \in B} \sum_{\lambda \in D} \sum_{\alpha \in A} \sum_{\gamma \in C} b^{DB}_{\lambda\nu} c^{DAA}_{\lambda\mu\alpha} W(\omega = 0)^{AC}_{\alpha\gamma} c^{BCC}_{\nu\kappa\gamma} \tag{3.222}$$

$$= \sum_{\nu \in B} \sum_{\alpha \in A} F^{BAA}_{\nu\mu\alpha} I^{BCA}_{\nu\kappa\alpha,\tau} \tag{3.223}$$

$$K^{\pm,AC,II}_{\mu\kappa} = \sum_{\nu \in B} \sum_{\lambda \in D} \sum_{\alpha \in A} \sum_{\beta \in B} b^{DB}_{\lambda\nu} c^{DAA}_{\lambda\mu\alpha} W(\omega = 0)^{AB}_{\alpha\beta} c^{CBB}_{\kappa\nu\beta} \tag{3.224}$$

$$= \sum_{\nu \in B} \sum_{\alpha \in A} F^{BAA}_{\nu\mu\alpha} I^{CBA}_{\kappa\nu\alpha} \tag{3.225}$$

$$K^{\pm,AC,IV}_{\mu\kappa} = \sum_{\nu\in B}\sum_{\lambda\in D}\sum_{\delta\in D}\sum_{\beta\in B} b^{DB}_{\lambda\nu} c^{ADD}_{\mu\lambda\delta} W(\omega=0)^{DB}_{\delta\beta} c^{CBB}_{\kappa\nu\beta} \tag{3.226}$$

$$= \sum_{\lambda\in D}\sum_{\delta\in D}\sum_{\nu\in B} b^{DB}_{\lambda\nu} I^{CBD}_{\kappa\nu\delta} b^{ADD}_{\mu\lambda\delta} \,, \tag{3.227}$$

where in the + case b is symmetric, and antisymmetric otherwise. Note the close similarity to the equations leading to the GW self-energy eqs. (3.92) and (3.94)–(3.96). However, eqs. (3.222), (3.224) and (3.226) are evaluated using W instead of $\widetilde{W}$, i.e., they include the exx contribution to the SEX self-energy.

We point out, that for systems with $N_{occ}N_{virt}$ of the order of a few 10000, direct diagonalization of the full BSE Hamiltonian is computationally much more efficient than the Davidson method. For Benzene with a QZ6P basis set, the dimension of the BSE Hamiltonian is around $n = 10000$. The calculation of the three lowest singlet and triplet states (six states in total) took less than 4 minutes on 8 cores of a intel skylake node. This is around 15-20 times faster than the corresponding calculation using the Davidson method. For details we refer to A.4.3

Chapter 4

Technical Validation

Ideally, the result of a MBPT calculation should be independent of the particular implementation of the method. As explained in detail in the last chapter, choices regarding the numerical representation of the involved quantities must be made, including the choice of a single-particle basis as well as a discretization of frequency and/or time-variables. The choice of the single-particle basis also entail a choice regarding the representation of the core electrons as well as of the treatment of virtual states. Both factors are decisive since it is known that core correlation plays a major role in MBPT calculations[545] but also since many quantities like charged excitations or correlation energies converge very slowly to the complete basis set (CBS) limit within MBPT.[296,545,598,599] For these reasons, achieving consensus between different MBPT codes is challenging and requires careful convergence of a calculation with respect to all technical parameters. Due to limited resources and/or time constraints, it might not always be possible in applications to only work with converged parameters. In that case, one would like to know how a certain technical parameter affects the final result.

For these reasons, comparison between different codes through systematic benchmarks is highly desirable. First, it allows to verify that the results from these codes agree within a reasonable margin of error. Second, such benchmarks are crucial in order to quantify the influence of the various technical parameters on a certain property. It is useful to thereby focus on the comparison of different GW implementations. First of all, individual GW QP energies are very sensitive to technical errors and their correctness also imply the correct calculations of derived quantities like QP gaps which enter the working equations for correlation energies and 2-particle response functions. Furthermore, the GW method has been implemented in many codes and achieving consensus between these implementations has received much attention over the last years.

Significant efforts towards comparing GW results from different codes in a systematic way have been initiated by van Setten et al.[545] in 2015 with the publication of the GW100 database for finite systems. In their work, van Setten et al. compared the IPs and EAs of 100 small and medium-sized molecules on the G_0W_0@PBE level of theory, calculated with three different

codes, the GTO based all-electron code TURBOMOLE[501,600], the NAO based all-electron code FHI-AIMS[492,498,499], and the PW code BerkeleyGW.[225,601] Later, benchmarks for many more codes followed, including the PW implementations in VASP[134,602–604] in 2017[605] and WEST[565] in 2018,[574] and the real-space finite-element (RSFE) implementation in nanoGW[474] in 2019.[606] Also the accuracies of many low-order scaling implementations of the G_0W_0 method were tested for the GW100 database.[6,36,269,433]

These studies established the choice of single-particle basis as a crucial factor causing major differences between different implementations. For instance, the results from TURBOMOLE, FHI-AIMS and MOLGW,[542] but also from the low-scaling implementations by Wilhelm *et al.*[269] in CP2K[607] and by Duchemin and Blase[433], all using the same def2[608]-GTO type basis sets, agree within a few ten meV on average for GW100, even though these implementations differ in frequency treatment as well as calculation of four-center integrals. The differences between codes using different basis sets are considerably larger. The discrepancy between the TURBOMOLE and BerkeleyGW results of nearly 300 meV on average reported in ref.[545] for the Highest Occupied Molecular Orbital (HOMO) were not necessarily insightful since the BerkeleyGW results were not CBS limit extrapolated. With only around 60 meV on average, the agreement between the CBS limit extrapolated PW results obtained with VASP and TURBOMOLE was found to be significantly better.[605] However, for EAs the disagreement between different codes is considerable larger and differences for systems with a positive LUMO can easily exceed several eV. It has also been pointed out in ref. [605] that the type of GTO-type basis set has a major influence on these EAs and that Dunning's correlation consistent basis sets[512] are more suitable than the def2-series which has been used in ref. [545]. Beside the choice of the basis set, the treatment of core electrons (pseudopotentials[609] vs. all-electron) also plays a decisive role for many systems.[574,610]

The purpose of this chapter is to assess the errors introduced by the numerical approximations outlined in section 3. In section 4.1 we first compare our results for G_0W_0@PBE for the GW100 database to the ones from other codes with implement the *GW* equations with GTOs, PWs, and RSFEs. Since G_0W_0@PBE generally do not give accurate QP energies (see discussion in section 2.4.4) we will only focus on numerical aspects and abstain from comparison to experimental or other reference values calculated with other quantum chemical methods.[287,611,612] In section 4.2 we compare our qs*GW* results to the ones from TURBOMOLE.[540,575] In section 4.4 we then continue with validating our RPA correlation energies for single atoms and also perform some preliminary tests of SOSEX($W(0)$,$W(0)$). All of these systems are rather small. Therefore, to complement the results of this section we also calculate IPs and EAs of small to medium molecules from the GW5000 database.[598] in section 4.3. These larger systems allow us to assess the suitability of the sparsity thresholds for the PADF method introduced in section 3.1.3.

4.1 Quasiparticle energies - G_0W_0

4.1.1 Computational Details

We follow the protocol for the GW100 benchmark as described by van Setten et al.[545] and perform non-relativistic G_0W_0@PBE[189,190] calculations. We use the structures as available on the web page for the GW100 database and also use the updated structures for Phenol and Vynilbromide.[1] For consistency with other benchmarks for GW100, we always use the QP energy obtained from the KS LUMO energy, which is usually, but not always, the energetically lowest virtual QP energy. For a detailed discussion of the effect of orbital reordering we refer to ref. [606].

We performed calculations with the augmented versions of the basis sets described in this work and extrapolated them to the CBS limit as described for instance in ref. [501]: We calculate the QP energies ϵ_n with the aug-TZ3P and aug-QZ6P basis sets and estimate the CBS limit as

$$\epsilon_n^{CBS} = \epsilon_n^{QZ} - \frac{1}{N_{bas}^{QZ}} \frac{\epsilon_n^{QZ} - \epsilon_n^{TZ}}{\frac{1}{N_{bas}^{QZ}} - \frac{1}{N_{bas}^{TZ}}} = \epsilon_n^{QZ} - \left(\epsilon_n^{QZ} - \epsilon_n^{TZ}\right) \left(1 - \frac{N_{bas}^{QZ}}{N_{bas}^{TZ}}\right)^{-1} , \tag{4.1}$$

4.1.2 Convergence with respect to Imaginary Time and Frequency Grids

We first comment on the suitable of our numerical treatment of imaginary time and imaginary frequency variables. In implementations based on the space-time method grids similar to ours have been used by other researchers[6,269,433] to implement the G_0W_0 method for finite systems. Recently, Wilhelm *et al.* benchmarked the convergence of QP energies in the GW100 database with respect to the grid sizes.[269] They could clearly show that grids with 20-30 points are sufficient to convergence all IPs and EAs in GW100. Our imaginary time and frequency grid implementation allow us to use up to 40 points which ensures that the results are converged with respect to this parameter.[269] In ref. [269], Wilhelm et al. could also reproduce the results obtained by van Setten et al.[545] with the TURBOMOLE code with an accuracy of a few meV. Since TURBOMOLE performs the frequency integration fully analytically, we conclude that the frequency integration is a numerical parameter which is well under control in our updated implementation.

4.1.3 Basis Set Errors

Before we discuss in detail the comparison of the STO results to the ones from other codes, we consider the basis set errors and basis set convergence properties of aug-TZ3P and aug-QZ6P. Using eq. (4.1), one implicitly assumes that when going to a larger basis set, each additional basis function reduces the basis set error on average by the same amount. In other words, one assumes uniform convergence of the basis set expansion, i.e. that eq. (3.4) holds. It is clear that such an assumption will only be justified for rather large basis sets and, for the same reason,

[1] Data downloaded from the website of the GW100 project by Van Setten et al., https://gw100.wordpress.com

extrapolation is generally more reliable for larger systems. Usually one would also like to use three or even more data points instead of using (4.1). It has, however, been pointed out[511] that including a calculation with a basis set of quality lower than TZ will deteriorate the quality of the fit. Therefore, we calculate QP energies at the CBS limit from TZ and QZ results only.

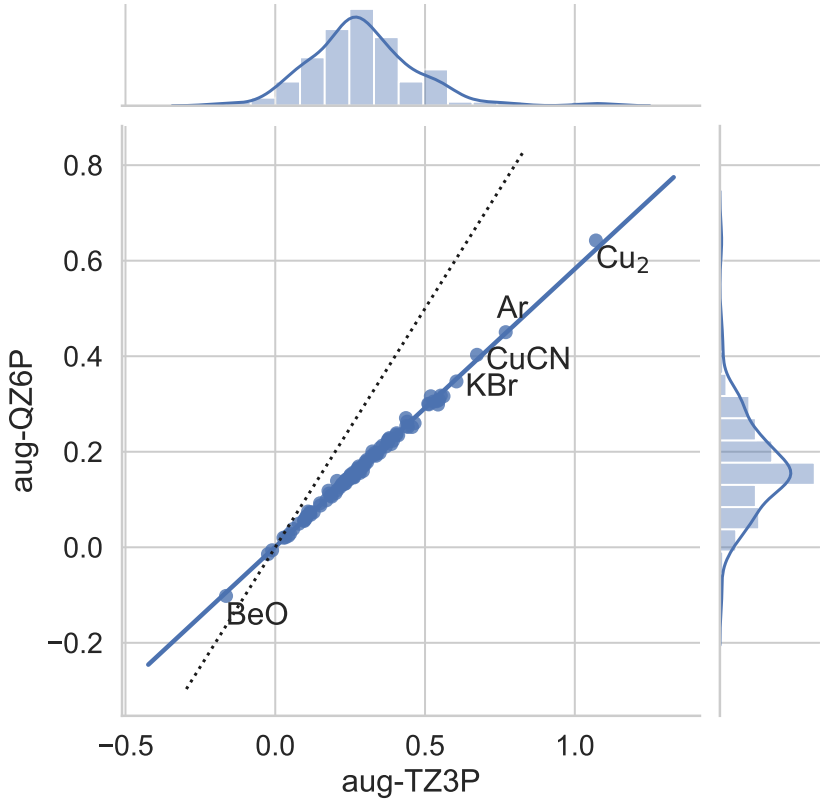

Figure 4.1: Basis set errors with respect to the CBS limit extrapolated IPs in the GW100 database using the aug-TZ3P and aug-QZ6P basis sets. The univariate plots show the distributions of errors with respect to the CBS limit extrapolated values. All values are in eV. The blue straight line is a linear fit and the dotted line is defined by $\Delta_{TZ} = \Delta_{QZ}$. All values are in eV.

To demonstrate the accuracy of an extrapolation scheme, the extrapolated result should ideally be compared to one obtained in a very large basis which already gives a result very close to the CBS limit. Due to the limitations of our basis sets to angular momenta ≤ 3, this is not possible for us. As a rule of thumb, extrapolation with basis sets of cardinality X and $X-1$ can provide the accuracy of a calculation using a basis set of accuracy $X+1$.[489] Recently, Bruneval et al.[599] found basis set errors of about 60 meV for the IPs of a large set of small to medium organic molecules with the cc-pV5Z basis set. This is of the same order as the typical accuracy

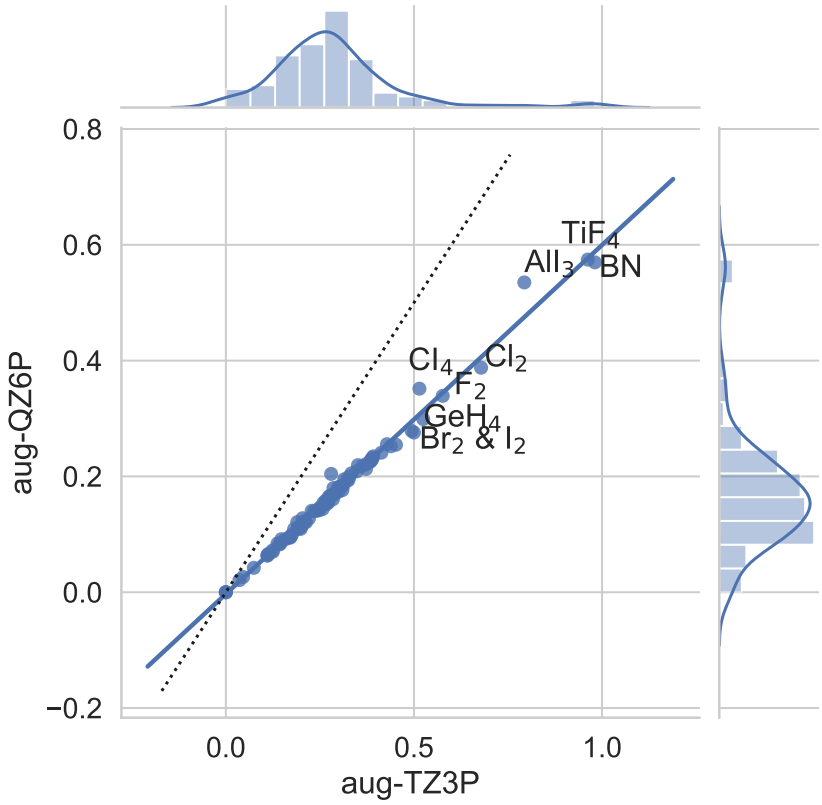

Figure 4.2: Basis set errors with respect to the CBS limit extrapolated EAs in the GW100 database using the aug-TZ3P and aug-QZ6P basis sets. The univariate plots show the distributions of errors with respect to the CBS limit extrapolated values. All values are in eV. The blue straight line is a linear fit and the dotted line is defined by $\Delta_{TZ} = \Delta_{QZ}$. All values are in eV.

in a photo-ionization experiment[599] and considerably lower than the 150 meV for IPs which are usually found using the cc-pVQZ basis set.[598,599] For EAs, one can usually expect errors of the same order of magnitude than IPs when augmented basis sets are used.[613] It is thus reasonable to use this number as an estimate of the average error in our extrapolation.

The distributions of basis set errors with respect to the CBS limit extrapolated IPs and EAs (excluding noble gases and the hydrogen molecule in the latter) for the GW100 database are shown in figures 4.1 and 4.2, respectively. The average basis set error reduces from 300 (290) meV to 170 (170) meV for IPs (EAs), i.e. there seems to be no qualitative difference in the convergence to the CBS limit for IP and EA as one would expect for augmented basis sets. With the exception of the IP of BeO, the basis set error with aug-QZ6P is always smaller than the one with aug-TZ3P, i.e. aug-QZ6P gives higher QP energies. In both plots, we also highlight some

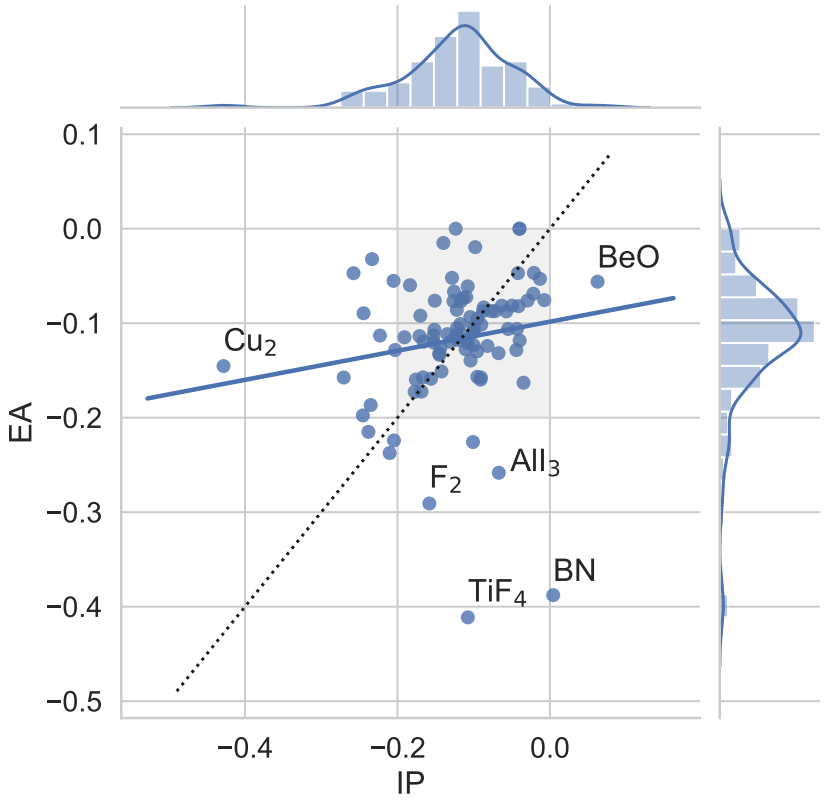

Figure 4.3: Correlation between differences between the aug-TZ3P and aug-QZ6P results Δ_{T-Q} for EAs (y-axis) and IPs (x-axis). The univariate plots show the corresponding distributions. The blue straight line is a linear fit and the dotted line is defined by $\Delta_{IP} = \Delta_{EA}$. All values are in eV.

systems for which the convergence to the CBS limit seems to be rather slow, i.e. the differences between QP energies on the TZ and QZ level are very large. For these systems, CBS limit extrapolation will be less accurate. Without exception, the problematic systems are composed of only a few atoms.

Also a good correlation between the basis set errors for IPs and EAs is desirable since it implies a fast convergence of the HOMO-LUMO QP gap to the CBS limit. Fast convergence of this quantity with basis sets augmented with diffuse functions has been demonstrated before.[613] At first glance, the distributions of IP and EA BSEs appear rather similar, suggesting that such an error cancellation might also be found for our basis sets. To investigate this further, we plot all pairs $(\Delta(QZ-TZ)_{IP_i}, \Delta(QZ-TZ)_{EA_i})$ (bivariate plot) together with the corresponding error distributions (univariate plots) in figure 4.3 (omitting again all noble gases and H_2). The

blue solid line is a linear fit, the dotted black line is defined by the equation $\Delta(QZ-TZ)_{IP_i} = \Delta(QZ-TZ)_{EA_i}$, and Gaussian kernels are fitted to the univariate distributions. A few molecules with large BSE for the IP but small basis set error for the EA (Cu_2) or vice-versa (BN, TiF_4, F_2, AlI_3) aside, most systems cluster around the dotted line in the grey shaded area in which IP and EA BSEs should cancel each other to a large extent.

4.1.4 Comparison to GTO-Type Basis Sets

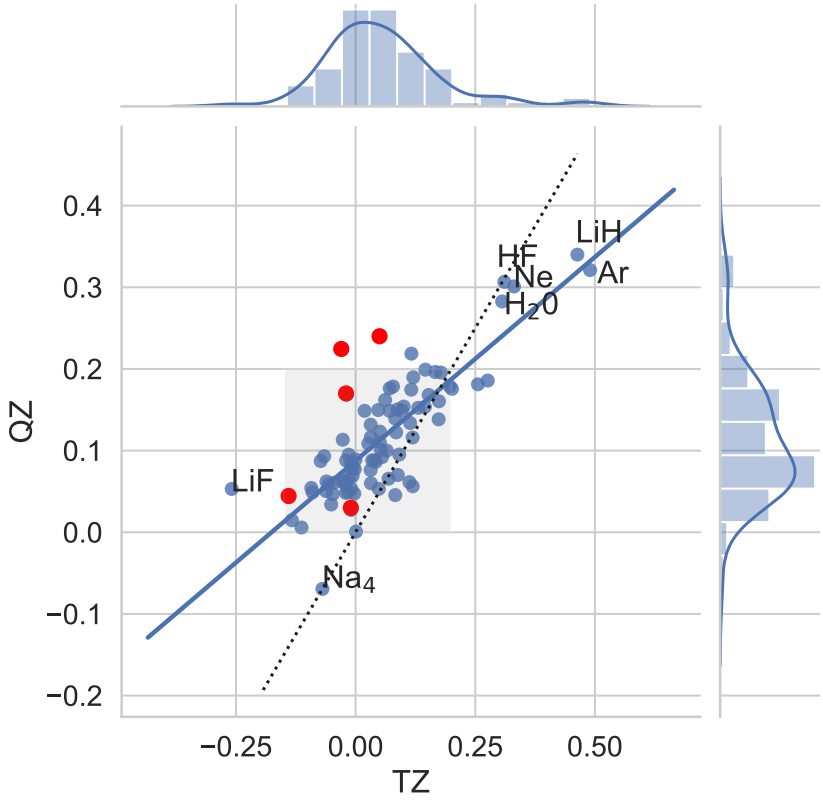

Figure 4.4: Distribution of deviations of the ADF IPs to the def2-GTO IPs for the GW100 database for TZ and QZ basis sets ($\Delta_{X,i}$, X = TZ,QZ). The univariate plots show the distribution of the $\Delta_{TZ,i}$ (upper histogram) and the $\Delta_{QZ,i}$ (left histogram). The bivariate plots shows the pairs $(\Delta_{TZ,i}, \Delta_{QZ,i})$ and the blue line is a linear fit. The dotted line is defined by $\Delta_T = \Delta_Q$. Systems containing 5th row elements are highlighted in red. All values are in eV.

Additional insight into the convergence properties of the STO type basis sets is provided when comparing them to GTO type ones of the same cardinality. Such a comparison is made in figure 4.4 for results on the TZ and and for the QZ level. The univariate plot on top of figure 4.4

shows the deviation of the aug-TZ3P IPs to the ones obtained with def2-TZVP and the univariate plot on the right side of figure 4.4 shows the same for aug-QZ6P and def2-QZVP (here and in the remainder of this paper, we use the results calculated with the TURBOMOLE code whenever we refer to def2-GTO basis sets. We could have equally well used results obtained with other codes like FHI-AIMS or MOLGW). Again, Gaussian kernels are fitted to the univariate distributions. The bivariate plot shows the individual pairs $(\Delta_{T,i}, \Delta_{Q,i})$, with $\Delta_{T,i}$ ($\Delta_{Q,i}$) being the differences between the IPs calculated with aug-TZ3P and def2-TZVP (aug-QZ6P and def2-QZVP) for the i^{th} datapoint in the GW100 database. The dotted line is defined by $\Delta_{T,i} = \Delta_{Q,i}$. The systems for which the QP equations (2.334) can have multiple solutions (CI_4, KBr, NaCl, BN, O_3, BeO, MgO, Cu_2, and CuCN) are excluded from this comparison.[574] Also Ag_2 is not shown since the deviations on the TZ and QZ level are exceptionally large.

We observe that the maximum of the Gaussian kernel function is close to zero eV for the TZ and closer to 0.1 eV for the QZ basis sets. In other words, the aug-QZ6P IPs are consistently smaller than the def2-QZVP IPs (with a mean deviation (MD) of 120 eV), while the aug-TZ3P ones are with a MD of 60 meV only slightly smaller than the def2-TZVP IPs on average. The missing g functions in the aug-QZ6P basis sets might be a reason for this discrepancy. We will see in the next subsection that the CBS limit extrapolated IPs calculated with our basis sets are on average lower than the def2-GTO results. This section clearly shows that this discrepancy is mostly caused by the differences on the QZ level.

The deviations of the STO-type to the respective def2- basis sets are strongly correlated. In cases in which the aug-TZ3P IPs are considerably smaller than their def2-TZVP counterparts, also the aug-QZ6P IPs will be much smaller than the def2-QZVP ones. Good examples are the five molecules represented by the points in the upper right corner of the bivariate plot. Since it is known that the GTO-type basis sets allow for a reliable CBS limit extrapolation, this fact is highly important since it guarantees that the same CBS limit extrapolation can be performed using our STO-type basis sets.

We also shortly comment on the systems containing 5th-row elements, highlighted in red. With the exception of one of them (Rb_2), the agreement on the TZ is rather good, while they agreement on the QZ level is significantly worse. This is again due to the inconsistent polarization for the heavier elements mentioned above; approaching the CBS limit for heavier elements becomes difficult without Slater functions with angular momentum larger than $l = 3$.

To summarize the key points of this section, our STO type basis sets seem to behave qualitatively similar to the GTO-type basis sets, although the improvement when going from TZ to QZ is smaller for the STO- than for the GTO-type basis sets. Together with the good correlation of deviations on the TZ and QZ level, this indicates that our basis sets allow indeed for a meaningful CBS limit extrapolation. However, the CBS limit extrapolated IPs from the STO-type basis sets will on average be lower than their counterparts calculated using GTOs.

4.1.5 Comparison to Other Codes

KS Eigenvalues

Before we dive into our comparison of the *GW* QP energies, we shorty compare our KS eigenvalues for the systems in GW100 to the ones from other codes. Here and in the following, we do not include Phenol and Vynilbromide in the statistical analysis since different structures have been used in the past for both systems.[605] Our results (see supporting information of ref. [37] for the raw data for all 100 systems) only confirm what is already well known; For KS eigenvalues, the agreement between different codes is generally excellent. For example, the CBS limit extrapolated KS HOMO energies from the WEST code agree with the ones obtained from def-GTO calculations within 30 meV on average, with a maximum deviations of 176 meV.[574] These figures reduce to 24 meV and 92 meV when the plane-wave results are compared to def2-QZVP.[574] With only 19 meV, the agreement from VASP to def2-QZVP is even better.[605] One should keep in mind that the extrapolation schemes for correlated-electron methods and localized basis functions are not necessarily useful to extrapolate KS eigenvalues as has already been pointed out in ref. [605] and in ref. [574]. Such a comparison should rather be based on non-extrapolated results.[614,615]

Our KS HOMO eigenvalues calculated on the aug-QZ6P level of theory show a MAD of 26 meV to the ones on the def2-QZVP level and of 22 meV to the CBS limit extrapolated values calculated with the WEST code. Our LUMO eigenvalues only differ to the ones from WEST by 35 meV on average. Major deviations of more than 150 meV are only found for Helium (340 meV), H_2 (280 meV) and Ag_2 (340 meV). With deviations of more than 420 meV to WEST and 490 meV to def-QZVP, the latter system is also the only outlier for IPs. However, when the ZORA is made, the deviations to WEST reduce to 15 meV for the HOMO and 17 meV for the LUMO, respectively. Also, the deviation to the def2-QZVP IP reduces to an acceptable value of 50 meV which is rather strange, given that the latter has been calculated without relativistic corrections.

Ionization Potentials

We now turn our attention to the IPs calculated within the GWA. In addition to Phenol and Vynilbromide, we again exclude the systems for which the QP equations (2.334) can have multiple solutions (CI_4, KBr, NaCl, BN, O_3, BeO, MgO, Cu_2, and CuCN)[574] from the following statistical comparison, but also TiF_4 and OCS for which no IPs from the WEST code are available. Due to large discrepancies between WEST and VASP, we also exclude the systems containing Iodine, Gallium and Xenon. Finally, we also exclude all remaining systems containing 5th-row elements from our analysis since for these systems (especially the ones containing Iodine and Ag_2) the different treatment of relativistic effects have been shown to significantly affects QP energies.[605] This leaves us with a set of 81 molecules whose IPs we include in the statistical analysis in this section.

Table 4.1: G_0W_0@PBE ionization potentials (IP) for the GW100 database (third column) Columns four to seven denote deviations of the ADF IPs to the ones from reference X, $\Delta_X = IP_X - IP_{ADF}$. All values are in eV.

	Name	ADF	$\Delta_{def2-GTO}$	Δ_{VASP}	Δ_{WEST}	Δ_{nanoGW}
1	Helium	23.31	0.18	0.07	0.11	−011
2	Neon	20.06	0.27	0.11	0.27	0.39
3	Argon	15.26	0.02	0.06	0.11	0.19
4	Krypton	13.71	0.18	0.22	0.05	−006
5	Xenon	11.88	0.45	0.26	1.24	0.23
6	Hydrogen	15.88	−003	−003	−004	−013
7	Lithium dimer	5.08	−002	0.01	−004	−004
8	Sodium dimer	4.89	0.02	0.04	0.09	0.05
9	Sodium tetramer	4.25	−004	−008	−001	−003
10	Sodium hexamer	4.30	0.04	0.04	0.07	0.05
11	Potassium dimer	3.99	0.09	0.13	0.15	0.07
12	Rubidium dimer	3.78	0.10	0.24	0.23	0.08
13	Nitrogen	14.79	0.26	0.14	0.15	0.04
14	Phosphorus dimer	10.26	0.12	0.09	0.17	0.06
15	Arsenic dimer	9.58	0.08	0.01	−003	−009
16	Fluorine	14.99	0.12	−006	0.01	0.03
17	Chlorine	11.18	0.13	0.14	0.23	0.13
18	Bromine	10.46	0.10	0.11	−002	−017
19	Iodine	9.04	0.54	0.48	1.37	0.23
20	Methane	13.89	0.11	0.13	0.10	0.26
21	Ethane	12.35	0.11	0.15	0.09	−019
22	Propane	11.85	0.04	0.05	−001	−032
23	Butane	11.52	0.07	0.09	−011	−027
24	Ethylene	10.28	0.12	0.14	0.11	−001
25	Acetylene	11.14	−005	−007	−005	−021
26	Tetracarbon	10.74	0.17	0.15	0.16	0.06
27	Cyclopropane	10.63	0.02	0.09	0.04	−015
28	Benzene	9.07	0.03	0.04	0.01	−011
29	Cyclooctatetraene	8.16	0.02	0.03	0.00	−014
30	Cyclopentadiene	8.43	0.02	0.04	0.01	−013
31	Vinyl fluoride	10.24	0.08	0.04	0.05	−006
32	Vinyl chloride	9.82	0.08	0.10	0.12	−001
33	Vinyl bromide	9.03	0.11	0.72	0.61	0.49
34	Vinyl iodide	8.93	0.26	0.34	0.88	0.09
35	Tetrafluoromethane	15.43	0.17	−002	0.08	−004
36	Tetrachloromethane	11.24	−003	−004	0.05	0.00
37	Tetrabromomethane	10.05	0.17	0.20	0.06	−001
38	Tetraiodomethane	8.74	0.31	0.37		0.07
39	Silane	12.37	0.02	0.03	0.05	−012
40	Germane	12.09	0.03	0.04	0.23	−018
41	Disilane	10.46	−005	−002	0.06	−014
42	Pentasilane	9.07	−002	0.06	0.12	−008
43	Lithium hydride	6.52	0.07	−006	0.11	0.15
44	Potassium hydride	4.88	0.09	0.09	0.09	−020
45	Borane	12.93	0.03	0.02	0.02	−015
46	Diborane(6)	11.92	0.01	0.02	0.00	−025
47	Amonia	10.27	0.12	0.05	−009	−020
48	Hydrazoic acid	10.44	0.11	0.06	0.04	−026
49	Phosphine	10.27	0.08	0.08	0.16	0.04

Continued on next page

	Name	ADF	$\Delta_{def2-GTO}$	Δ_{VASP}	Δ_{WEST}	Δ_{nanoGW}
50	Arsine	10.31	−011	−005	0.02	−011
51	Hydrogen sulfide	10.12	0.01	−001	0.11	0.07
52	Hydrogen fluoride	15.14	0.23	0.23	0.09	0.12
53	Hydrogen chloride	12.36	0.00	0.09	0.12	0.11
54	Lithium fluoride	10.03	0.24	0.04	0.08	0.03
55	Magnesium fluoride	12.44	0.07	−003	0.02	−014
56	Titanium tetrafluoride	13.93	0.15	0.08		0.00
57	Aluminum fluoride	14.33	0.15	0.00	0.07	−013
58	Boron monofluoride	10.59	0.14	−013	−003	−017
59	Sulfur tetrafluoride	12.34	0.05	−014	−002	−018
60	Potassium bromide	7.85	−024	−005		−074
61	Gallium monochloride	9.81	−007	0.08	0.36	−006
62	Sodium chloride	8.32	0.03	0.15		−014
63	Magnesium chloride	11.07	0.12	0.12	0.18	0.04
64	Aluminum iodide	9.38	0.20	0.20	0.93	−007
65	Boron nitride	10.94	0.15			0.25
66	Hydrogen cyanide	13.10	0.22	0.19	0.12	0.12
67	Phosphorus mononitrid	11.10	0.20	0.14	0.16	0.11
68	Hydrazine	9.40	−003	−007	−013	−030
69	Formaldehyde	10.46	0.00	−004	−005	−025
70	Methanol	10.54	0.13	0.07	0.07	−023
71	Ethanol	10.17	0.10	0.04	0.04	−020
72	Acetaldehyde	9.61	0.05	0.02	0.00	−022
73	Ethoxy ethane	9.41	0.02	0.02	−002	−030
74	Formic acid	10.84	0.03	−003	−003	−013
75	Hydrogen peroxide	10.96	0.14	0.00	0.04	0.02
76	Water	11.94	0.11	−010	−007	−012
77	Carbon dioxide	13.37	0.09	−001	0.00	−025
78	Carbon disulfide	9.80	0.15	0.16	0.25	0.09
79	Carbon oxide sulfide	10.90	0.21	0.16	0.26	0.08
80	Carbon oxide selenide	10.40	0.03	0.02	−003	−022
81	Carbon monoxide	13.66	0.05	−004	0.00	−018
82	Ozone	11.74	−023			0.33
83	Sulfur dioxide	11.86	0.20	0.05	0.10	0.05
84	Beryllium monoxide	8.99	−048			0.76
85	Magnesium monoxide	6.82	−007			0.24
86	Toluene	8.72	0.00	0.03	−001	−014
87	Ethylbenzene	8.65	0.01	0.04	0.01	−016
88	Hexafluorobenzene	9.70	0.04	−007	−005	−013
89	Phenol	8.47	0.04	−009		−024
90	Aniline	7.72	0.07	0.06	0.01	−014
91	Pyridine	9.18	0.00	−002	−005	−019
92	Guanine	7.77	0.10	0.08	0.05	−012
93	Adenine	8.14	0.01	−002	−005	−020
94	Cytosine	8.44	0.01	−004	−004	−019
95	Thymine	8.86	0.01	−003	−004	−022
96	Uracil	9.26	0.12	0.10	−007	−002
97	Urea	9.25	0.21	0.10	0.14	−003
98	Silver dimer	7.06	0.91	0.77	0.98	0.81
99	Copper dimer	8.20	−157	−101		−033
100	Copper cyanide	10.25	−073			0.40

Table 4.1 shows the results for all 100 IPs in the GW100 database obtained with our code next to the deviations to def2-GTO, VASP, WEST and nanoGW, if available. To facilitate a discussion of the data, figures 4.5 shows MADs and maximum absolute errors (MAE) between

all codes, while figure 4.6 visualizes the distribution of the deviations of the ADF IPs to the ones from other codes. The IPs from ADF, def2-GTO, VASP and WEST are all in good agreement with each other, with MADs to each other between 56 and 86 meV, while the deviations to nanoGW are about twice as large. Figure 4.6 also shows, that the deviations of the ADF IPs to the ones from other codes (again, with the exception of nanoGW) show a small spread and no outliers can be found. We note again, that we assume the CBS limit extrapolation error to be of the order of at least 60 meV on average and all the values reported and compared here should only be interpreted with these error bars. For the plane-wave codes, the CBS limit extrapolation error is likely smaller than for the localized basis sets, but there are additional sources of error, most notably pseudopotentials and box-size effects. In light of these uncertainties, the agreement between all four codes can be considered as excellent.

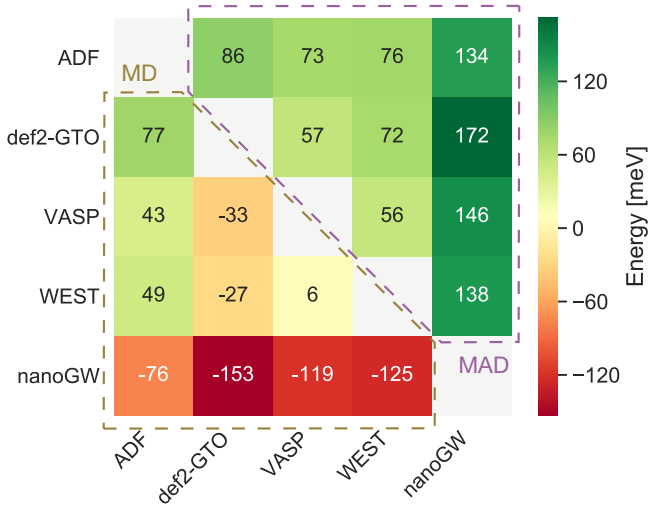

Figure 4.5: MADs, (upper triangle) and mean deviations (MD) (lower triangle) of the CBS limit extrapolated IPs in the GW100 database (18 molecules have been excluded from the comparison, see explanations above) computed with different codes. All values are in meV.

Looking at the mean deviations to the other codes in the lower triangle of figure 4.5 as well as at the boxplots in figure 4.6, we see that ADF IPs are generally smaller than the ones from def2-GTO, VASP and WEST. The reasons for the discrepancy between ADF and def2-GTO have already been discussed above. We also see that the nanoGW IPs are on average much smaller than the ones from all others codes. This is in line with the fact that the nanoGW results were apparently obtained without basis set limit extrapolation,[606] although the numerical parameters determining the convergence to the CBS limit (grid spacing, chosen cut-off for virtual states and radius of the sphere around a given finite systems) where tested for convergence separately.[606] Still, our data analysis suggests that the nanoGW IPs are not as well converged as the ones from

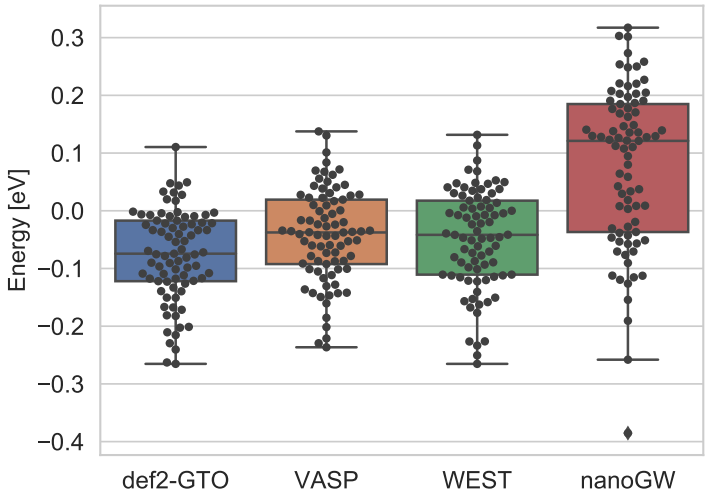

Figure 4.6: Deviation of IPs calculated with ADF to different codes. Black dots denote the individual data points. The horizonal line in each box denotes the median deviation, the box contains all data points between the first quartile (Q1) and third quartile (Q2) and the whiskers are at $Q1 \pm \frac{3}{2}|Q1 - Q3|$ (in case of a normal distribution, the whiskers include 99.3 % of all data points). All values are in eV.

the other codes.

Systems containing Fluorine and Nitrogen generally show rather pronounced disagreements between different codes (For example, consider the following deviations from ADF to def2-GTO: N_2: 260 meV, HCN: 220 meV, TiF_4: 150 meV, AlF_3: 150 meV, LiF: 240 meV, HF: 230 meV). For Fluorine, this has already been observed by Maggio and Kresse in ref. [605], who pointed at the default pseudopotentials in VASP as a potential source of these discrepancies. Another possible explanation might be found in a a recent study by Bruneval *et al.*[599] which suggests, that molecules predominantly composed of Carbon and Hydrogen converge to the CBS limit rather quickly, whereas the convergence is considerably slower for systems to a large part composed of Fluorine and Nitrogen.

Finally, we shortly comment on some systems which we have excluded from the statistical comparisons in figures 4.5 and figures 4.6. We find large differences for system containing 5th row elements, e.g. Xe, ceAg2, I_2, or CI_4. Here, the ADF IPs are considerably lower than the ones from other codes, indicating that the ADF results are not properly converged to the CBS limit which is due to the missing basis functions with angular momentum higher than $l = 3$.

With 1.57 eV, the by far largest deviation reported in table 4.1 can be found between ADF (8.20 eV) and TURBOMOLE (6.63 eV) for Cu_2. FHI-AIMS gives an IP of 7.78 eV for this system,[545] which is in considerably better agreement with ADF. FHI-AIMS relies on an analytical continuation from the imaginary to the real frequency axis with 16 sampling points (AIMS-P16),

not much different from the procedure in ADF. We can conclude, that for this particular system, the large deviation of ADF and FHI-AIMS to TURBOMOLE are caused by inaccuracies from non-converged frequency grids. The ADF IP reported in table 4.1 has been obtained from aug-TZ3P and aug-QZ6P calculation with 24 and 27 imaginary frequency points, respectively. When 24 imaginary frequency points are used for the aug-QZ6P calculation as well, the IP of Cu_2 reduces to 8.05 eV, which is already in reasonable agreement with FHI-AIMS. Similar conclusions can be drawn for CuCN. Another interesting case is BeO, with deviation of 0.48 eV to def-GTO. Again, the large deviation is due to non-converged frequency grids. the ADF IP is with 8.99 eV very close to the 9.07 eV obtained by AIMS-P16. With 128 imaginary frequency points (AIMS-P128), FHI-AIMS gives an IP of 9.63 eV which is then in perfect agreement with TURBOMOLE. Furthermore, in ref.[545], three solutions are reported for BeO, while ADF only recovers one of them. These three examples show, that the current frequency treatment in ADF can not properly describe the IPs of systems for which the single QP picture breaks down in the valence region.

Electron Affinities

We now turn our attention to the EAs. As for the IPs, table 4.2 shows the EAs calculated with ADF and the differences to the other four codes excluding all noble gases and H_2. However, it is known, that the def2-GTO basis sets sometimes severely overestimate positive LUMO energies which then deviate from results from plane-wave codes by more than 1 eV. Furthermore, since EAs converge slower to the CBS limit than IPs when non-augmented basis sets are used,[599] also CBS limit extrapolation errors are larger for the remaining systems. On the other hand, PW calculations require very large box sizes for these systems which makes it harder to converge the EAs with respect to this parameter and for this reason results from VASP are often not available.[605]

Table 4.2: G_0W_0@PBE electron affinities (EA) for the GW100 database (third column) Columns four to seven denote deviations of the ADF EAs to the ones from reference X, $\Delta_X = EA_X - EA_{ADF}$. All values are in eV.

	Name	ADF	$\Delta_{def2-GTO}$	Δ_{VASP}	Δ_{WEST}	Δ_{nanoGW}
7	Lithium dimer	0.52	0.23	0.09	0.12	0.14
8	Sodium dimer	0.64	0.02	−004	−003	0.00
9	Sodium tetramer	0.92	0.23	0.15	0.16	0.20
10	Sodium hexamer	0.95	0.18	0.12	0.09	0.11
11	Potassium dimer	0.59	0.16	0.15	0.16	0.16
12	Rubidium dimer	0.67		0.07	0.06	0.07
13	Nitrogen	−240	0.28		0.25	0.17
14	Phosphorus dimer	0.64	0.44	0.35	0.45	0.38
15	Arsenic dimer	1.08	0.44	−001	0.01	−004
16	Fluorine	0.54	0.69		0.52	0.58
17	Chlorine	0.83	0.57	0.42	0.55	0.52

Continued on next page

	Name	ADF	$\Delta_{def2-GTO}$	Δ_{VASP}	Δ_{WEST}	Δ_{nanoGW}
18	Bromine	1.40	0.56	0.59	0.48	0.29
19	Iodine	1.56		0.65	1.65	
20	Methane	−078	−125	0.15	0.02	−010
21	Ethane	−077	−116		−001	−011
22	Propane	−072	−115		−003	−011
23	Butane	−070	−113		−004	−013
24	Ethylene	−191	0.09		0.11	−004
25	Acetylene	−248	−008		−002	−020
26	Tetracarbon	2.62	0.53	0.47	0.48	0.52
27	Cyclopropane	−073	−123		−002	−014
28	Benzene	−096	0.07		0.03	−010
29	Cyclooctatetraene	0.03	0.09	0.02	0.04	−010
30	Cyclopentadiene	−091	0.06		0.01	−015
31	Vinyl fluoride	−192	0.04		0.03	−009
32	Vinyl chloride	−131	0.14	0.12	0.10	0.00
33	Vinyl bromide	−123	0.12		0.17	0.09
34	Vinyl iodide	−077		0.40	0.55	0.44
35	Tetrafluoromethane	−088	−300		0.05	−010
36	Tetrachloromethane	0.04	0.50	0.28	0.37	0.41
37	Tetrabromomethane	0.99	0.57	0.48	0.46	0.41
38	Tetraiodomethane	2.16		0.28	0.88	0.32
39	Silane	−072	−154		−004	−011
40	Germane	−047	−138		−014	−036
41	Disilane	−075	−076		−002	−083
42	Pentasilane	−008	0.08	0.05	0.15	−002
43	Lithium hydride	0.05	0.11	0.02	0.02	0.13
44	Potassium hydride	0.17	0.15	0.08	0.08	0.35
45	Borane	−026	0.23	0.23	0.25	0.21
46	Diborane(6)	−087	0.13		0.15	0.00
47	Amonia	−076	−124		−005	−009
48	Hydrazoic acid	−140	0.30		0.25	0.23
49	Phosphine	−067	−159		−003	−006
50	Arsine	−058	−136		−008	−016
51	Hydrogen sulfide	−073	−152		−005	−011
52	Hydrogen fluoride	−106	−098		−005	−012
53	Hydrogen chloride	−119	−034		0.10	−003
54	Lithium fluoride	−004	0.05	−013	−003	0.11
55	Magnesium fluoride	0.26	0.05	0.03	0.07	0.18
56	itanium tetrafluorid	0.09	0.97		0.83	1.14
57	Aluminum fluoride	0.06	0.17	−014	0.10	0.01
58	Boron monofluoride	−121	0.16		0.28	0.24
59	Sulfur tetrafluoride	−029	0.39	0.22	0.37	0.35
60	Potassium bromide	0.34	0.08	−002	0.06	0.59
61	Gallium monochloride	0.02	0.37	0.17	0.42	0.20
62	Sodium chloride	0.42	0.00	0.04	0.05	0.61
63	Magnesium chloride	0.68	0.00	−007	0.02	0.05
64	Aluminum iodide	1.18		−016	0.48	0.02
65	Boron nitride	4.05	−010		0.03	0.05
66	Hydrogen cyanide	−231	0.09		0.06	−006
67	hosphorus mononitrid	0.12	0.47		0.40	0.35
68	Hydrazine	−070	−098		−002	−008
69	Formaldehyde	−106	0.35		0.30	0.15
70	Methanol	−081	−100		−010	−019
71	Ethanol	−073	−094		−011	−019

Continued on next page

	Name	ADF	$\Delta_{def2-GTO}$	Δ_{VASP}	Δ_{WEST}	Δ_{nanoGW}
72	Acetaldehyde	−116	0.33	0.29	0.29	0.25
73	Ethoxy ethane	−062	−108		−009	−018
74	Formic acid	−182	0.23	0.18	0.18	0.04
75	Hydrogen peroxide	−206	0.11		0.26	0.28
76	Water	−088	−113	−016	−003	−008
77	Carbon dioxide	−103	0.10		0.06	−003
78	Carbon disulfide	0.10	0.45	0.32	0.40	0.32
79	Carbon oxide sulfide	−122	0.39		0.28	0.20
80	arbon oxide selenide	−093	0.41		0.29	0.22
81	Carbon monoxide	−084	0.47		0.40	0.38
82	Ozone	2.03	0.66	0.47	0.53	0.52
83	Sulfur dioxide	0.86	0.63	0.39	0.51	0.36
84	Beryllium monoxide	1.99	0.73	0.74	0.52	0.54
85	Magnesium monoxide	1.74	0.39	0.31	0.21	0.52
86	Toluene	−091	0.08		0.04	−009
87	Ethylbenzene	−087	0.00		−003	−018
88	Hexafluorobenzene	−003	−033		0.00	−008
89	Phenol	−078	0.04		−007	−018
90	Aniline	−091	−003		−007	−019
91	Pyridine	−044	0.14		0.08	−005
92	Guanine	−048	0.02		−003	−015
93	Adenine	−028	0.07		−001	−013
94	Cytosine	−018	0.17	0.06	0.09	−003
95	Thymine	0.02	0.16	0.04	0.08	−006
96	Uracil	0.05	0.20	0.06	0.10	−002
97	Urea	−049	−068		−004	−012
98	Silver dimer	0.91		0.44	0.58	0.41
99	Copper dimer	1.00	0.23	0.24	0.41	0.25
100	Copper cyanide	1.47	0.38	0.44	0.51	0.34
MAD			0.48	0.21	0.16	0.21

Thus, for the full database, only comparison to WEST and nanoGW is possible. Excluding again all compounds containing Iodine, Copper, Gallium and Xenon as well as remaining systems containing 5^{th} row elements, we find a MAD of 160 meV to the former and of 210 meV to the latter code. These MADs are about twice as large as for the IPs but in light of the difficulties mentioned above certainly not surprising and in line with the previous benchmark studies on GW100.[545,574,605,606] Figure 4.7 shows that the ADF EAs, as for the IPs, are on average smaller than the ones from WEST while no trend in that direction can be observed when comparing to nanoGW.

We furthermore observe significant deviations of the STO to the def2-GTO results of up to several eVs for the molecules with with positive LUMOs. Contrariwise, the raw data in table 4.2 shows that the agreement with WEST is especially good for systems with positive LUMO. As an example, consider the series of linear alkane chains, C_nH_{2n+1} for $n = 1, \ldots, 4$. With deviations from 10 to 40 meV, the agreement with WEST is excellent, while def2-GTO overestimates the EAs of these systems by more than 1 eV. In this context, it is interesting to investigate the effect of the diffuse functions. This is shown in table 4.3 for some systems with LUMO well above the vacuum level. Only comparing the basis set extrapolated values, the effect of the diffuse functions seem to be rather small; for N_2 the EA calculated from the basis set without

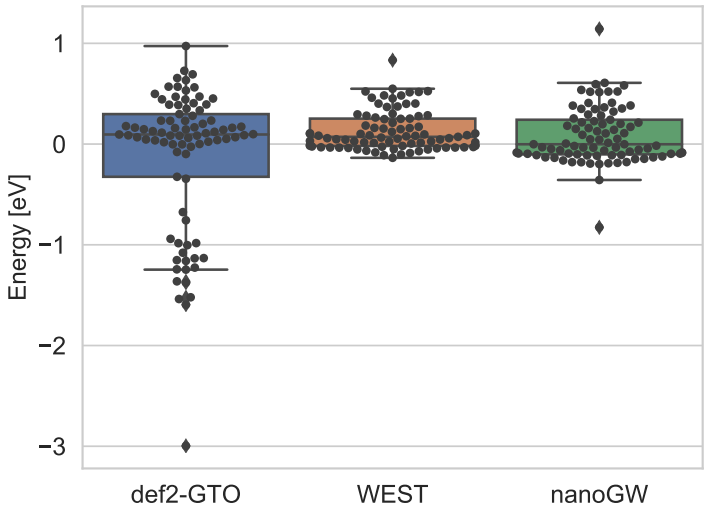

Figure 4.7: Deviation of EAs calculated with ADF to different codes. Black dots denote the individual data points. The horizonal line in each box denotes the median deviation, the box contains all data points between the first quartile (Q1) and third quartile (Q2) and the whiskers are at $Q1 \pm \frac{3}{2}|Q1 - Q3|$ (in case of a normal distribution, the whiskers include 99.3 % of all data points). All values are in eV. The deviations to VASP have been excluded due to the lack of reference values for too many systems in GW100.

the diffuse functions is with 250 meV even higher than the augmented basis sets, and overall, the average difference is only 50 meV which is well within the expected error range from the CBS limit extrapolation. However, comparing the results form the finite basis sets, the differences are exorbitant. Especially, on the TZ level, the addition of diffuse functions results in a lowering of the EAs by nearly 1 eV on average. For the non-augmented basis sets, the average difference between TZ and QZ basis set is 480 meV, resulting in differences of sometimes more than 1 eV between the EAs on the TZ and on the extrapolated level. In light of these differences, the good agreement between the CBS limit extrapolated EAs is remarkable. Despite this good agreement, the augmented basis sets should be the preferred choice to calculate EAs of systems with unbound LUMOs since the extrapolation procedure generally becomes less reliable with increasing difference between the results for the finite basis sets.

Finally, we compare our EAs for systems with a bound LUMO to WEST, nanoGW, and def-GTO results. The MADs and MDs in figure 4.8 show that def2-GTO, nanoGW and and WEST are generally in good agreement for these systems while the MADs to ADF are large. As the MDs show, ADF significantly overestimates these EAs compared to the other codes, which indicates that the results are not entirely converged to the CBS limit. This interpretation is also in line with the raw data in table 4.2 showing that the deviations are generally largest for di- and triatomic systems as well as molecules containing Fluorine and Chlorine, while the agreement

		aug.				non.aug.						
		T	Q	Ex.	Δ_{TQ}	T	Q	Ex.	Δ_{TQ}	Δ_{TT}	Δ_{QQ}	Δ_{EE}
13	N_2	-2.65	-2.54	-2.40	-0.11	-3.00	-2.58	-2.15	-0.42	0.36	0.04	-0.25
20	CH_4	-0.97	-0.89	-0.78	-0.08	-2.20	-1.59	-0.95	-0.61	1.23	0.70	0.17
21	C_2H_6	-0.96	-0.88	-0.77	-0.08	-2.13	-1.52	-0.87	-0.62	1.17	0.64	0.10
22	C_3H_8	-0.92	-0.83	-0.72	-0.08	-2.06	-1.44	-0.78	-0.62	1.14	0.61	0.06
23	C_4H_{10}	-0.89	-0.81	-0.70	-0.08	-2.04	-1.41	-0.74	-0.63	1.15	0.60	0.04
24	C_2H_4	-2.12	-2.03	-1.91	-0.09	-2.40	-2.12	-1.81	-0.28	0.28	0.09	-0.10
25	C_2H_2	-2.76	-2.65	-2.48	-0.11	-3.24	-2.87	-2.44	-0.37	0.48	0.22	-0.04
27	C_3H_3	-0.98	-0.88	-0.73	-0.10	-2.29	-1.61	-0.87	-0.68	1.31	0.73	0.14
31	C_2H_3F	-2.21	-2.09	-1.92	-0.12	-2.50	-2.22	-1.91	-0.28	0.29	0.13	-0.01
39	SiH_4	-0.92	-0.83	-0.72	-0.09	-1.75	-1.42	-1.08	-0.33	0.83	0.59	0.36
47	NH_3	-0.93	-0.85	-0.76	-0.08	-1.85	-1.35	-0.85	-0.51	0.93	0.50	0.09
66	HCN	-2.59	-2.48	-2.31	-0.12	-2.96	-2.61	-2.23	-0.35	0.37	0.14	-0.08
70	CH_4O	-1.05	-0.95	-0.81	-0.10	-2.00	-1.49	-0.93	-0.52	0.95	0.54	0.12
71	C_2H_6O	-0.97	-0.87	-0.73	-0.10	-1.90	-1.39	-0.84	-0.51	0.93	0.52	0.11
76	H_2O	-1.02	-0.96	-0.88	-0.06	-1.75	-1.34	-0.89	-0.41	0.73	0.38	0.01
	MD				0.09				0.48	0.81	0.43	0.05

Table 4.3: Comparison of EAs for selected molecules from the GW100 database calculated with ADF with and without diffuse functions. All values are in eV.

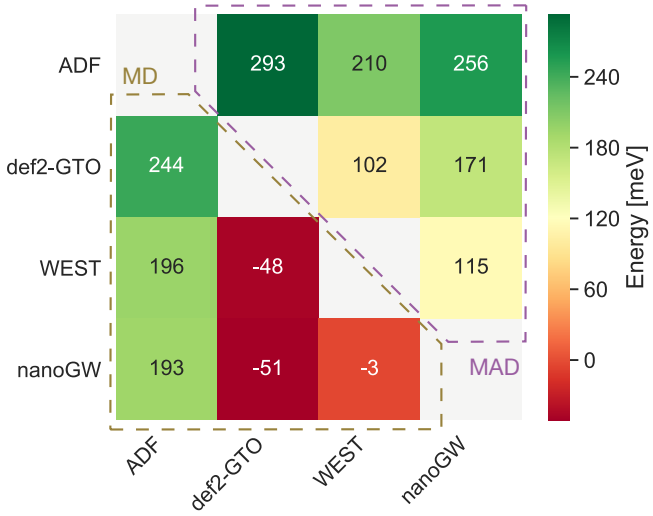

Figure 4.8: MADs, (upper triangle) and mean deviations (MD) (lower triangle) of the CBS limit extrapolated EAs of the subset of systems with bound LUMO and medium sized organic molecules (in total 48 data points) in the GW100 dataset computed with different codes. All values are in eV.

for the medium organic molecules like the nucleo-bases is satisfactory. Adding additional diffuse or tight functions would possible not result in an improved description of the EAs of the former

system	T	Q	ex.	ex. (no gh.)	def2-GTO	WEST
F_2	0.20	0.51	0.90	0.54	1.23	1.06
Cl_2	0.74	0.95	1.21	0.83	1.40	1.38
Br_2	1.27	1.45	1.69	1.40	1.96	1.88
TiF_4	-0.33	-0.10	0.19	0.09	1.06	0.92
SO_2	0.84	1.07	1.38	0.86	1.49	1.37

Table 4.4: Effect of the addition of additional off-center Slater functions *via* Ne ghost atoms on the EAs of selected systems form GW100. All values are in eV.

systems. Instead, reaching the CBS limit is most likely only possible using basis functions with higher angular momenta than $l = 3$ which are not available to us. However, we can try to simulate the effect of these functions by adding additional off-center Slater functions to the basis set which can be achieved conveniently by adding ghost atoms. This approach is reminiscent of bond-centred basis functions which have for example been used by Dunlap and coworkers.[616]

As examples, we consider the dihalogens F_2, Cl_2 and Br_2, SO_2, as well as TiF_4 and we augment these structures with Ne ghost atoms for which we use the same basis set than for the real atoms. For each atom A in a systems, we place two ghost atoms G, G' on a straight line defined by the position of A and every neighboring atom B so that the distance between A and G (G') equals one third (minus one third) of the distance between A and B. The results of this augmentation is shown in table 4.4 and we clearly see that it reduces the basis set errors considerably. Of course, such an augmentation should not be seen as a practical solution but it shows that agreement between ADF and the other codes can in principle be reached also for these systems.

4.2 Quasiparticle Energies - qsGW

4.2.1 Computational Details

We use the non-augmented TZ3P and QZ6P basis sets described in this work. CBS limit extrapolated results are obtained using (4.1). In all calculations, we set the *numericalQuality* key to *Good*. Exceptions are a few systems for which we observed inconsistencies with the *Good* fit set: For Pentasilane, Na_2, Na_4, and Na_6, we used the *Excellent* fit set, and for the nucleobases we used the *VeryGood* auxiliary basis set. We used 32 imaginary time and 32 imaginary frequency points each. For all TZ3P calculations, we set *Dependency Bas=1e-3* and for QZ6P we set *Dependency Bas=5e-3* in the AMS input as described in ref.[36]. All calculations using augmented basis sets (aug-TZ3P and aug-QZ6P) have been performed in the same way, but using the *excellent* auxiliary fit set and *numericalQuality VeryGood*.

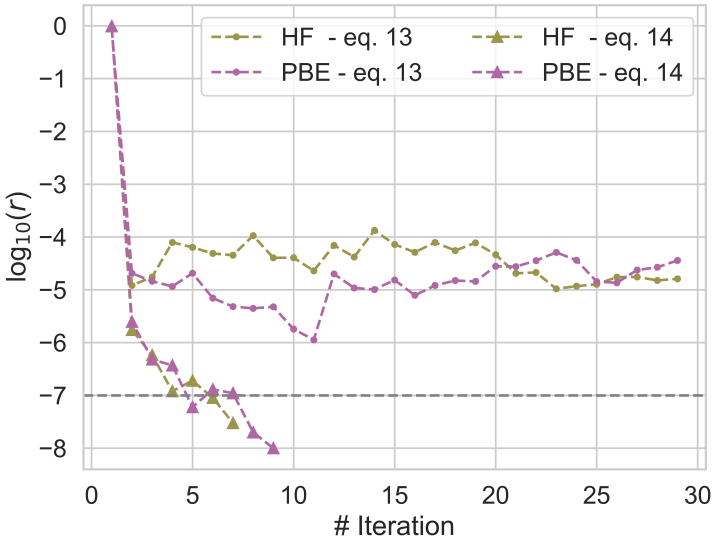

Figure 4.9: Convergence of the qsGW SCF for Methane for different initial guesses and constructions of the correlation potential. $\log_{10} r$, r defined in eq. (3.127), is plotted against the number of iterations.

4.2.2 Comparison of exchange-correlation potentials in qsGW

We already noticed in section 2.4.4 that the correlated part of the exchange-correlation potential of qsGW can be defined in different ways. Here we compare the two approaches to construct this quantity introduced by Kotani et al.[142] (eq. (2.341) and (2.342)) for a subset of molecules from the GW100 database. For the reasons discussed in section 2.4.4, we do not assess the approaches by Shishkin and Kresse[176,177] and Kutepov et al.[271,272]. The data is shown in the supporting information of ref. [38] and shows that the QP equations are significantly harder to converge when the exchange-correlation potential obtained from (2.341) is used. An example of the convergence behavior of both variants is shown in figure 4.9. Figure 4.9 plots $\log_{10} r$ with r defined in eq. (3.127) against the number of iterations with two different initial guesses for Methane. We see, that using (2.342), the SCF rapidly converges towards a fixed point, while $\log_{10} r$ always remains much larger than -6 for (2.341). On the other hand, for the 10 converged calculations differences in the final QP energies are small; for both, IPs and EAs, both variants differ by only 20 meV on average, i.e the error introduced by averaging over the off-diagonal elements of the self-energy are small. For this reason, we decided to use the correlation potential as defined in (2.342) in all subsequent calculations.

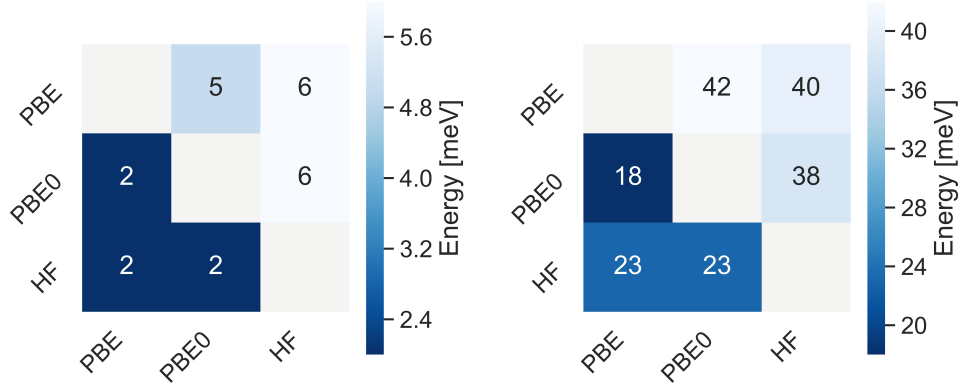

Figure 4.10: Mean absolute deviations (left plot) and maximum absolute deviations (right plot) of qs*GW* IPs (upper triangle) and EAs (lower triangle) obtained with different initial guesses for the GW100 database. All values are in meV.

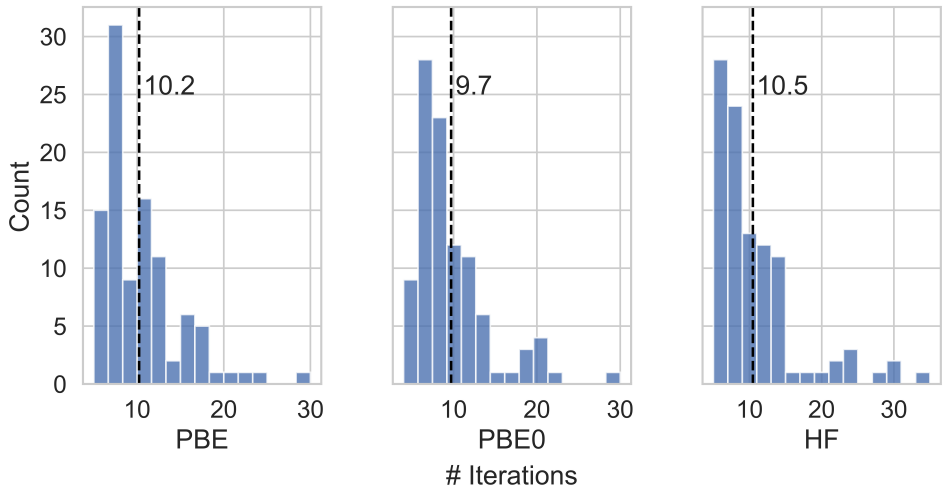

Figure 4.11: Number of iterations needed to attain convergence of the SCF for different initial guesses.

4.2.3 SCF Convergence

Next, we comment on the convergence of the qs*GW* SCF procedure. To this end, we compare IPs and electron affinities (EA) for the molecules in the GW100 database for 3 different starting points, PBE, PBE0, and HF. At self-consistency, the QP energies should be independent from the initial guess and their differences will therefore provide information about the obtained convergence of the QP energies for a given ϵ_{SCF}. In all calculations we set $\epsilon_{SCF} = 1e^{-7}$ and

restrict all calculations to a maximum of 30 iterations.

Independent of the starting point, we could not reach convergence for Mgo, BeO, BN, Cu_2, and CuCN with our DIIS implementation. Employing a linear mixing procedure as implemented in ref.[540] with $\alpha = 0.35$ we could reach convergence for these systems, albeit with a large number of iterations. These systems are problematic for *GW* approaches since the spectral weight of the single excited electron is distributed between multiple peaks[574]. qs*GW* relies on the validity of the single QP picture. In situations, in which the quasi-particle equations might have multiple solutions[296,574] corresponding to the same non-interacting state, different solutions may be found in different iterations of the qs*GW* SCF procedure. qs*GW* should select the solution with largest QP weight[270] but in situations where there are at least two solutions with (almost) equal QP weight, the "physical" solution might change in each iteration. In such cases, the DIIS algorithm tries to minimize the the residual SCF error by interpolating between different solutions and no fixed point of the map (3.121) is found.[617] To overcome this issue with QP self-consistent schemes, a regularization procedure has recently been proposed.[617] On the other hand, linear mixing results in a smooth but slow convergence pattern, if only α is chosen small enough to make sure that in all iterations the "physical" solution is the same. We do not know, how to best solve this issue but we do not consider it to be a major concern as such convergence problems are only encountered for systems in which the single QP picture is not valid. An erratic convergence then rather indicates that qs*GW* is not an appropriate level of theory.

Figure 4.10 shows mean absolute deviations (MAD) as well as maximum absolute deviations of the IPs and EAs obtained from different starting points. With MAD of 6 meV and 2 meV, respectively, EAs are better converged than IPs. Also the maximum error is about twice as small for EAs than for IPs. These differences are related to the AC procedure which gives smaller errors for unoccupied states with usually featureless self-energy matrix elements. The maximum error never exceeds 50 meV and is of the same order of magnitude than the experimental resolution of photoionization experiments[242] of the typical basis set errors of *GW* calculations after extrapolation.[37,242,574,599,605]. The distribution of iterations required for convergence is displayed in figure 4.11. This includes the 5 problematic cases discussed above. The calculations on average converge in around 10 iteration, with little dependence on the initial guess.

4.2.4 Comparison of Ionization Potentials for the GW100 Database

We now compare the IPs from our algorithm to the ones obtained with the TURBOMOLE code for GW100. The TURBOMOLE results have been obtained with the GTO-type def2-TZVPP basis sets. For some systems, TURBOMOLE results are not available and we exclude these from our discussion. We use the TZ3P basis sets which we have shown to give comparable results to def2-TZVP for GW100[37]. However, quantitative accuracy can not be expected.

The deviations to TURBOMOLE are shown in figure 4.12. The average deviation between both codes is close to zero, and with one exception, for all IPs deviations are considerably smaller than 300 meV, with the deviations for the majority of systems being smaller than 100 meV. Thus, our results are qualitatively similar and deviations can be attributed to different

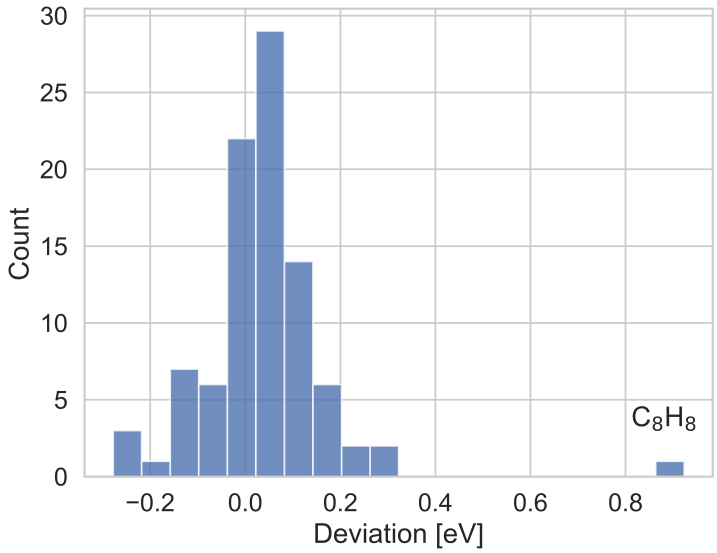

Figure 4.12: Distribution of deviations (in eV) of the IPs from TURBOMOLE and with our implementation.

basis set errors and different constructions of the qs*GW* exchange-correlation potential. The IP of Cyclooctatetrane is the only exception. Here, TURBOMOLE gives an IP of 9.30 eV, while the ADF IP is with 8.38 eV nearly one eV smaller. For different starting points, we obtained the same result within an accuracy of only a few meV, indicating that our IP is well converged. The TURBOMOLE qs*GW* IPs on average overestimate the CCSD(T) reference values for GW100 by Klopper and coworkers[543] in the same basis set by only a little more than 100 meV, while the deviation for Cycloocatetrane is nearly one eV. The CCSD(T) IP for this system, is 8.35 eV, which is in very good agreement with our value. These numbers indicate that our IP is reasonable, despite the large deviation to TURBOMOLE.

Ideally, we would also like to compare our EAs against literature data, however, with only one exception (were optimized structures do not seem to be available)[276], we are not aware of any published EAs for molecular systems.

4.2.5 Basis set limit extrapolated Quasiparticle Energies

Table 4.5: Complete Basis set limit extrapolated ionization potentials and electron affinities for the GW100 database using the non-augmented basis sets.

		IP			EA		
	Name	TZ3P	QZ6P	extra	TZ3P	QZ6P	extra
1	Helium	24.320	24.560	24.790	−8720	−2770	2.780
2	Neon	21.740	21.650	21.550	−1350	−3780	4.600
3	Argon	15.480	15.600	15.720	−8770	−1910	5.950
4	Krypton	13.940	13.980	14.040	−7420	−1470	5.790
5	Xenon	12.270	12.290	12.320	−5600	−1370	6.320
6	Hydrogen	16.490	16.480	16.460	−3070	−2420	−1700
7	Lithiumdimer	5.260	5.340	5.420	0.120	0.180	0.250
8	Sodiumdimer	5.000	5.040	5.100	0.220	0.270	0.330
9	Sodiumtetramer	4.250	4.340	4.450	0.470	0.520	0.580
10	Sodiumhexamer	4.390	4.450	4.530	0.470	0.480	0.490
11	Dipotassium	4.040	4.120	4.230	0.290	0.340	0.410
12	Dirubidium	3.840	3.910	4.010	0.280	0.330	0.400
13	Nitrogen	15.740	15.860	15.980	−3230	−2260	−1180
14	Phosphorusdimer	10.270	10.370	10.480	0.130	0.360	0.600
15	Arsenicdimer	9.650	9.650	9.660	0.590	0.630	0.670
16	Fluorine	16.210	16.260	16.310	0.050	0.050	0.050
17	Chlorine	11.490	11.600	11.720	0.210	0.430	0.660
18	Bromine	10.670	10.720	10.770	1.010	1.050	1.090
19	Iodine	9.600	9.630	9.680	1.280	1.360	1.510
20	Methane	14.560	14.620	14.690	−2300	−1620	−0780
21	Ethane	12.980	13.020	13.080	−2270	−1560	−0650
22	Propane	12.320	12.350	12.390	−2230	−1510	−0560
23	Buthane	11.850	11.900	11.970	−2240	−1500	−0520
24	Ethylene	10.540	10.650	10.790	−2430	−1670	−0700
25	Acetylene	11.290	11.420	11.590	−2440	−1960	−1320
26	Tetracarbon	11.200	11.390	11.640	1.970	2.220	2.570
27	Cyclopropane	10.980	11.070	11.180	−2420	−1650	−0610
28	Benzene	9.240	9.360	9.520	−1820	−1350	−0690
29	Cyclooctatetraene	8.380	8.490	8.640	−0900	−0710	−0460
30	Cyclopentadiene	8.620	8.730	8.880	−1850	−1500	−1040
31	Vynilfluoride	10.580	10.660	10.770	−2300	−1620	−0760
32	Vynilchloride	10.080	10.160	10.270	−2160	−1490	−0650
33	Vynilbromide	9.270	9.370	9.490	−2030	−1570	−0980
34	Vyniliodide	9.370	9.430	9.520	−1450	−1120	−0620
35	Carbontetrafluoride	16.750	16.760	16.780	−2270	−2920	−3690
36	Carbontetrachloride	11.660	11.730	11.800	−0840	−0570	−0270
37	Carbontetrabromide	10.610	10.640	10.690	0.480	0.520	0.570
38	Carbontetraiodide	9.380	9.410	9.460	1.490	1.580	1.760
39	Silane	13.060	13.100	13.140	−1830	−1460	−1040
40	Germane	12.740	12.760	12.790	−1590	−1450	−1280
41	Disilane	10.860	10.890	10.930	−1610	−0930	−0130
42	Pentasilane	9.470	9.520	9.570	−0830	0.670	2.500
43	Lithiumhydride	8.090	8.160	8.230	0.100	0.120	0.150
44	Potassiumhydride	6.260	6.380	6.530	0.130	0.190	0.250
45	Borane	13.560	13.580	13.610	−0620	−0430	−0200
46	Diborane6	12.610	12.640	12.690	−1470	−1310	−1100
47	Amonia	11.030	11.080	11.130	−1880	−1310	−0650
48	Hydrogenazide	10.750	10.870	11.010	−1720	−1230	−0670
49	Phosphine	10.630	10.670	10.710	−1580	−1380	−1170
50	Arsine	10.490	10.590	10.700	−1540	−1280	−0980

Continued on next page

		IP			EA		
	Name	TZ3P	QZ6P	extra	TZ3P	QZ6P	extra
51	Hydrogensulfide	10.310	10.410	10.520	−1660	−1110	−0460
52	Hydrogenfluoride	16.400	16.380	16.360	−1640	−1360	−1060
53	Hydrogenchloride	12.610	12.710	12.820	−1650	−1180	−0670
54	Lithiumfluoride	11.770	11.790	11.810	0.170	0.220	0.280
55	Magnesiumfluoride	14.110	14.080	14.040	0.120	0.170	0.220
56	Titaniumfluoride	15.730	15.820	15.920	0.580	0.670	0.770
57	Aluminumtrifluoride	15.770	15.750	15.720	−0530	−0260	0.050
58	Fluoroborane	11.080	11.130	11.200	−1670	−1290	−0830
59	Sulfertetrafluoride	13.130	13.120	13.120	−0850	−0630	−0380
60	Potassiumbromide	8.290	8.310	8.330	0.460	0.490	0.510
61	Galliummonochloride	9.810	9.940	10.100	−0130	−0050	0.050
62	Sodiumchloride	9.110	9.220	9.360	0.540	0.590	0.660
63	Magnesiumchloride	11.680	11.800	11.940	0.220	0.300	0.410
64	Aluminumtriiodide	9.880	9.900	9.920	0.270	0.360	0.510
65	Boronnitride	11.680	11.820	11.980	3.140	3.330	3.550
66	Hydrogencyanide	13.600	13.710	13.850	−2170	−1470	−0620
67	Phosphorusmononitride	11.900	11.990	12.100	−0420	−0130	0.190
68	Hydrazene	10.000	10.040	10.090	−1710	−1150	−0500
69	Formaldehyde	11.200	11.230	11.260	−1640	−1450	−1210
70	Methanol	11.430	11.440	11.460	−2000	−1460	−0750
71	Ethanol	11.070	11.110	11.160	−1970	−1400	−0640
72	Acetaldehyde	10.580	10.630	10.710	−1910	−1450	−0850
73	Ethoxyethane	10.200	10.270	10.360	−2180	−1510	−0600
74	FormicAcid	11.810	11.870	11.950	−1960	−1530	−0960
75	Hydrogenperoxide	11.970	11.980	12.010	−1810	−1340	−0730
76	Water	12.890	12.880	12.870	−1640	−1290	−0850
77	Carbondioxide	14.010	14.080	14.180	−4180	−1410	2.550
78	Carbondisulfide	9.890	10.040	10.230	−0430	−0160	0.180
79	Carbonoxysulfide	11.180	11.330	11.520	−1930	−1080	0.020
80	Carbonoxyselenide	10.540	10.600	10.690	−1450	−1280	−1040
81	Carbonmonoxide	14.450	14.520	14.620	−1310	−1040	−0710
82	Ozon	13.140	13.250	13.400	1.890	2.020	2.190
83	Sulferdioxide	12.620	12.670	12.730	0.530	0.690	0.910
84	Berylliummonoxide	10.230	10.220	10.200	1.930	2.060	2.220
85	Magnesiummonoxide	8.100	8.140	8.200	1.580	1.720	1.910
86	Tuloene	8.880	8.990	9.140	−1760	−1370	−0840
87	Ethybenzene	8.780	8.950	9.180	−1790	−1310	−0640
88	Hexafluorobenzene	10.200	10.270	10.360	−0900	−0810	−0680
89	Phenol	8.740	8.840	8.990	−1630	−1320	−0890
90	Aniline	8.040	8.170	8.350	−1780	−1210	−0420
91	Pyridine	9.650	9.760	9.910	−1230	−1010	−0720
92	Guanine	8.100	8.200	8.330	−1160	−0750	−0190
93	Adenine	8.390	8.460	8.550	−1230	−1060	−0830
94	Cytosine	8.970	9.050	9.170	−0930	−0750	−0500
95	Thymine	9.280	9.340	9.420	−0760	−0600	−0370
96	Uracil	9.650	9.740	9.870	−0710	−0550	−0330
97	Urea	10.460	10.520	10.600	−1480	−0970	−0330
98	Silverdimer	7.000	7.060	7.150	0.490	0.570	0.690
99	Copperdimer	7.610	7.660	7.730	0.350	0.440	0.560
100	Coppercyanide	11.000	11.070	11.160	0.940	1.100	1.300

In table 4.5 we report CBS limit extrapolated EAs and IPs for the GW100 database. The qsGW QP energies seem to converge faster to the CBS limit than their G_0W_0 counterparts. Going from TZ3P to QZ6P, the basis set incompleteness error reduces by 80 meV on average,

while for G_0W_0@PBE, we found an average reduction of 130 meV in the last section. Self-consistent approaches might converge faster than G_0W_0 - Caruso et al. have already observed that scGW QP energies converge faster to the CBS limit than G_0W_0[244].

Table 4.6: Complete Basis set limit extrapolated ionization potentials and electron affinities for selected systems in the GW100 database using the augmented basis sets .

		IP			EA		
	Name	TZ3P	QZ6P	extra	TZ3P	QZ6P	extra
Methane	14.58	14.610	14.660	−0790	−0580	−0260	
Ethane	13.00	13.020	13.070	−0720	−0570	−0350	
Propane	12.33	12.350	12.380	−0720	−0550	−0300	
Buthane	11.86	11.890	11.950	−0710	−0550	−0300	
Ethylene	10.56	10.630	10.730	−0850	−0610	−0220	
Acetylene	11.36	11.430	11.530	−0990	−0630	−0050	
Vynilfluoride	10.65	10.670	10.690	−0570	−0570	−0560	
Vynilchloride	10.09	10.180	10.330	−0760	−0420	0.090	
Vynilbromide	9.27	9.340	9.440	−0760	−0540	−0220	
Carbontetrafluoride	16.68	16.760	16.890	−0500	−0840	−1350	
Carbontetrachloride	11.66	11.750	11.890	−0530	−0240	0.170	
Silane	13.00	13.110	13.280	−0650	−0550	−0390	
Germane	12.75	12.770	12.790	−0530	−0480	−0410	
Disilane	10.83	10.900	11.000	−0510	−0500	−0480	
Borane	13.54	13.580	13.640	−0340	−0270	−0180	
Diborane6	12.59	12.630	12.680	−0710	−0540	−0300	
Amonia	11.03	11.080	11.160	−0660	−0460	−0180	
Hydrogenazide	10.78	10.850	10.930	−0580	−0390	−0120	
Phosphine	10.65	10.680	10.740	−0570	−0490	−0370	
Arsine	10.49	10.580	10.710	−0560	−0460	−0310	
Hydrogensulfide	10.37	10.400	10.460	−0570	−0280	0.150	
Hydrogenfluoride	16.37	16.320	16.260	−0450	−0430	−0410	
Hydrogenchloride	12.63	12.730	12.870	−0570	−0300	0.050	
Fluoroborane	11.08	11.160	11.300	−0540	−0660	−0870	
Hydrogencyanide	13.63	13.720	13.860	−0700	−0430	−0030	
Formaldehyde	11.18	11.190	11.210	−0700	−0490	−0130	
Methanol	11.39	11.450	11.540	−0680	−0500	−0220	
Ethanol	11.07	11.110	11.160	−0650	−0490	−0240	
Acetaldehyde	10.58	10.630	10.710	−0660	−0450	−0130	
Ethoxyethane	10.21	10.260	10.340	−0700	−0520	−0230	
Water	12.85	12.900	12.970	−0560	−0410	−0190	
Urea	10.47	10.510	10.570	−0460	−0270	0.010	

For the EAs, the average differences are much larger which is also due to the many systems with negative EA in the GW100 database. For these systems CBS limit extrapolation is not reliable without adding diffuse functions. Repeating these calculations with augmented basis sets[37] yields smaller differences between the aug-TZ3P and aug-QZ6P basis sets.[37]. In table 4.6, these differences are shown for the series of linear alkanes from Methane to Butane. On both the TZ and QZ level the augmented basis sets give a much higher EA. Also, the differences between aug-TZ3P and aug-QZ6P are only modest with in between 150 and 200 meV, but they are huge for the non-augmented basis sets. Also the extrapolated values are much smaller using the augmented basis sets. The effect of augmentation is also profound for other systems. For

example, using the non-augmented basis sets, the EA of carbontetrachloride is negative (-0.27 eV). Using the augmented basis sets, it becomes positive (0.17 eV) which is in much better agreement with experiment (0.80 ± 0.34 eV)[618].

4.3 QP Energies for Large Molecules

4.3.1 Computational Details

We also performed G_0W_0@PBE0[192,193] calculations for a subset of of 250 molecules from the GW5000 database[598] using the zeroth order regular approximation (ZORA),[619–621] which we describe in the appendix A.1. Calculations are performed with the non-augmented TZ3P and QZ6P basis sets. Eq. (4.1) is used for CBS limit extrapolation. We use 24 points in imaginary frequency and imaginary time each, *numericalQuality Good* and the *Normal* auxiliary basis set which is sufficient for non-augmented basis sets.[36] We set *Dependency Bas=5e-4*.

4.3.2 Thresholds

We have so far assessed the validity of our numerical approximations for small molecules only. However, the aim of these approximations is to perform MBPT calculations for large systems. Therefore, we also need to assess the accuracy of our algorithms for large molecules. We focus here on G_0W_0 only and restrict ourselves to rather small basis sets.

As a first test, we calculate the HOMO and LUMO QP energies of 20 organic molecules with in between 85 and 99 atoms from the GW5000 database.[598] These tests are crucial for our purpose sine they allow us to assess the effect of the values of the thresholds controlling distance effects. As explained in detail in section 3.1.3, we essentially rely on three thresholds in our implementation, which we organize in three tiers, denoted as *Basic*, *Normal* and *Good*.

The convergence with respect to these threshold tiers for HOMO and LUMO QP energies is shown in figure 4.13. As shown in the lower panel, the HOMO energies from different threshold tiers agree within 0.1 eV and the HOMO energies from the *Normal* and the *Good* threshold tier usually agree within an accuracy of 60 mEV. Using the *Basic* threshold tier, the LUMO QP energies show a maximum deviation of roughly 0.15 meV with respect to the *Good* tier. On the other hand, the LUMO energies from the *Normal* and *Good* tier are in even better agreement than the corresponding HOMO energies. Thus, using the *Normal* tier ensures an internal precision of our implementation of 60 meV for HOMO and LUMO QP energies. However, if it can be afforded it is the safer choice to use the *Good* threshold quality instead. In our experience, it also leads to better convergence of qsGW.

4.3.3 Accuracy with smaller basis sets

Finally, we investigate the accuracy of our algorithm as a function of systems size. To this end, we randomly selected 250 molecules from the GW5000 database and sorted these systems from

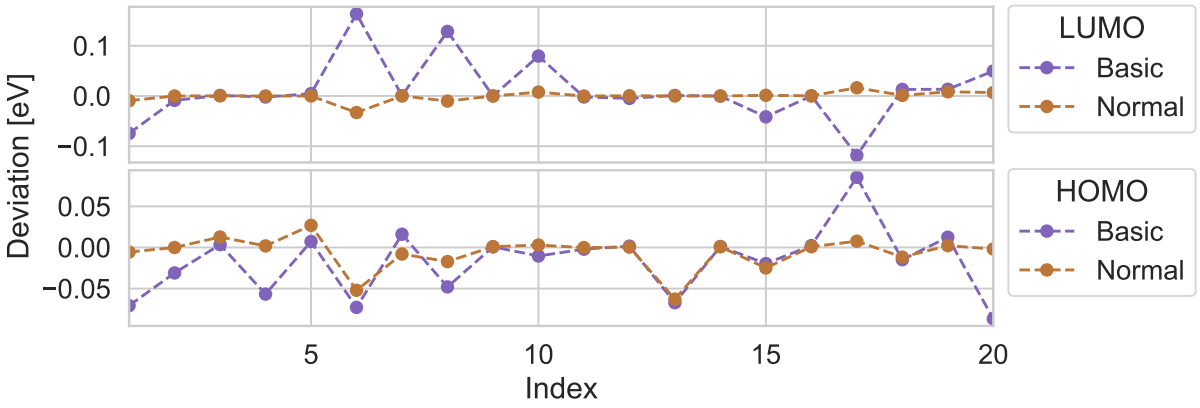

Figure 4.13: Deviations of the *Basic* and *Normal* threshold tiers with respect to the *Good* tier for HOMO (bottom) and LUMO (top) QP energies on the G_0W_0/PBE0 level of theory (all values in eV).

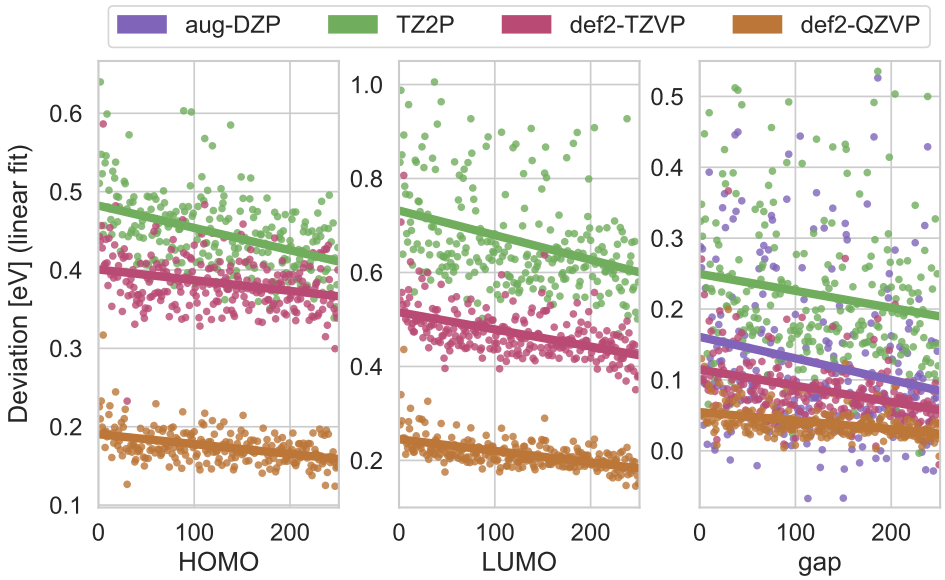

Figure 4.14: HOMO (left), and LUMO QP energies (middle) as well as HOMO-LUMO QP gaps (right) with different basis sets for 250 randomly selected molecules from the GW5000 database (dots) as well as linear fits, $f(x) = a \times x + b$. The systems have been sorted according to increasing size.

smallest (12 atoms) to largest (99 atoms). Figure 4.14 shows the deviations to the CBS limit of

our G_0W_0@PBE0 results for HOMO, LUMO and HOMO-LUMO QP gap with the TZ2P and aug-DZP basis sets as well as FHI-AIMS results using the def2-TZVP and def2-QZVP basis sets[598]. Additionally, we performed linear fits as implemented in Numpy[622], which are also shown in figure 4.14. Essentially we obtain the same picture as for the 20 large molecules: TZ2P performs nearly as good as def2-TZVP for the HOMO QP energies and considerably worse for the LUMO level which translates into a worse description of the HOMO-LUMO gap. While it is observed that the STO-results show a larger spread than their GTO counterparts especially for LUMO energies, we also observe that the deviation to the CBS limit decreases with growing system size for all basis sets. For all subplots in figure 4.14, the TZ2P fit is more or less parallel (also see the fit-parameters in the supporting information of ref. [36]) to the GTO fits, while the slope in the aug-DZP fit for the HOMO-LUMO gap is slightly more negative. As for the subset of 20 large molecules, aug-DZP produces HOMO-LUMO gaps which on average agree with the CBS limit extrapolated reference within 0.15 eV for systems larger than a few tens of atoms. However, in some cases the errors can still be rather large (e.g. larger than 0.4 eV in 7 out of 250 cases), while the def2-QZVP BSE practically never exceeds 0.1 eV.

The decreasing errors are most likely due to basis set superposition which leads to a more complete basis when the system increases and the assumption that this effect is more pronounced for basis sets with many diffuse functions such as aug-DZP is reasonable. Thus, we can conclude that the accuracy of our algorithm is not negatively affected by the system size. We note, that local over-completeness and the associated numerical issues can already be encountered for very small systems like the ones the left side of the plots in figure 4.14. On the other hand, it is highly unlikely that they become more pronounced for larger systems due to the locality of the AOs and auxiliary fit functions.

4.3.4 Accuracy with converged basis sets

For the GW100 database that discrepancies to other codes are more pronounced for smaller systems than for medium sized ones. To confirm this observation for a larger number of systems, we present here IPs and EAs of a subset of 250 medium to large organic molecules from the GW5000 database[598] for which CBS limit extrapolated references values calculated with FHI-AIMS using the def2-GTO basis sets are available. We have already considered this subset in ref[36]. We used here the TZ3P and QZ6P basis sets without diffuse functions since the LUMOs of the considered systems are negative. As expected, we find better agreement with FHI-AIMS than for GW100: For IPs, ADF deviated to FHI-AIMS by 62 meV on average as opposed to the 86 meV for GW100. For EAs, the MAD is with 93 meV slightly worse but the agreement is much better than for GW100.

4.4 Total Energies - Benchmark Results for Atoms

Before we move on to benchmarking the accuracy of some of the more advanced methods described in section 2.4 we shortly assess the accuracy of our algorithms for correlation energies.

4.4.1 Computational Details

The correlation energies presented here are evaluated based on exact exchange (EXX) only OEP[136,171] orbitals obtained in the implementation of Scuseria and coworkers[623] within the Krieger Lee Iafrate (KLI)[624] approximation.

Relative energies

Correlation energies are calculated using,[503]

$$E_{CBS} = E_{QZ} - E^c_{QZ} + \frac{E^c_{QZ} * 4^3 - E^c_{TZ} * 3^3}{4^3 - 3^3} \,, \tag{4.2}$$

where E^c_{QZ} (E^c_{TZ}) denotes the correlation energy at the QZ6P (TZ3P) level and E_{QZ} is the total energy at the QZ6P level. The extrapolation scheme has been shown to be suitable for correlation consistent basis sets.[489,503] We use here double augmented TZ3P and QZ6P basis sets, with additional diffuse functions as well as additional tight 1s and 2p functions (see below). Numerical quality and auxiliary fit set quality are set to *excellent*. No dependency thresholds have been set. We use 32 points for imaginary time and imaginary frequency each.

To see how the inclusion of the Σ^{G3W2} self-energy influences the description of electron correlation effects, we calculate the total correlation energies of 16 atoms with in between 2 and 36 electrons. For all systems with less or equal than 18 electrons, we compare the RPA and RPA+SOSEX($W(0)$,$W(0)$) correlation energies to almost exact values by Froese-Fischer and coworkers[625] and for the heavier elements we use the CCSD(T) values by McCarthy and Thakkar as reference.[627] For Argon, their CCSD(T) energy deviates from the value from ref.[625] by only 0.01 %. We also compare them to different beyond-RPA approaches by Jiang and Engel[298] (RPA+RSOX and RPA+SOX) and Gould et al.[626] (gRPA+). To be consistent with ref.[298] and ref.[626], we evaluate the correlation energies with exx only OEP orbitals, implemented within the KLI approximation.[623,624]

To first obtain an idea about the numerical quality of our RPA correlation energies, we compare them against the ones from Engel and coworkers which are free of basis set errors.[298] We find deviations between 3 and 15 % for neutral atoms and much larger ones for cations. Clearly, our standard basis sets are not compact enough for these systems (especially for the cations) and do not capture the full correlation energy. Therefore, we augment them with four tight 1s and two 2p functions each for TZ3P and QZ6P. Using these basis sets, total energies for all atoms deviate to the ones from ref.[298] by about 7 % on average. This is not perfect but accurate enough for a qualitative comparison of the different beyond-RPA approaches.

The relative errors of correlation energies with respect to the reference values are shown in figure 4.15. Simple RPA@EXX overestimates the correlation energies by typically between 25 % and 100 %. In accordance with the expectation that the correlation energy is more and more dominated by charge screening with increasing electron number, the agreement with the exact values becomes better for larger atomic numbers. RPA+SOSEX($W(0)$,$W(0)$) reduced the RPA

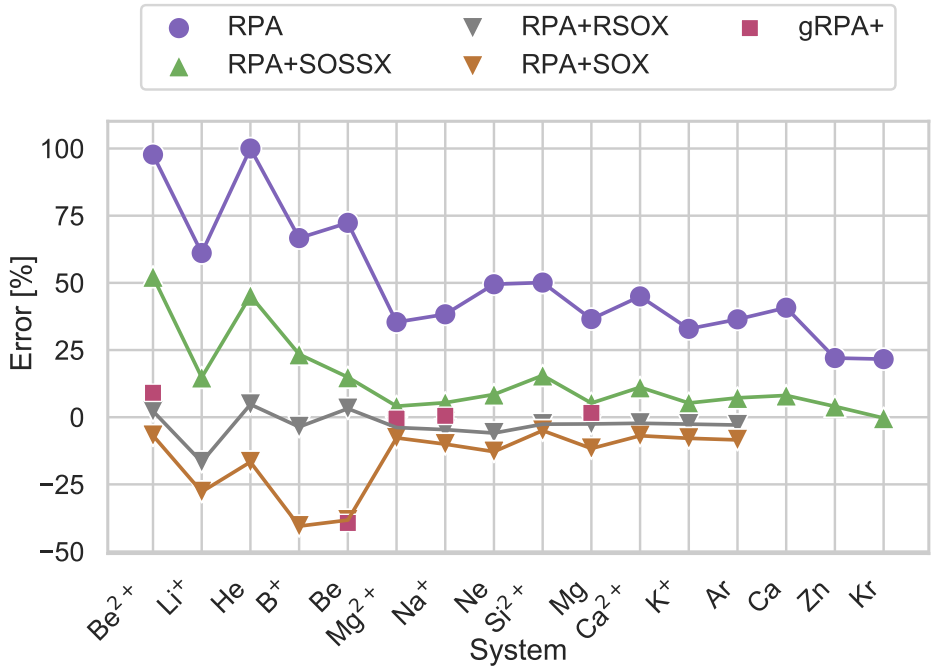

Figure 4.15: Relative errors [in percent] of correlation energies calculates with different methods compared to the exact values.[625] The RPA+SOX and RPA+RSOX values are taken from Engel and coworkers[298] and the gRPA+ values are from Gould et al.[626]

correlation energy by 29 % on average, improving agreement with the reference considerably. Especially for the systems with 2 or 4 electrons, the total correlation energies are still too high. For the last three systems with 18 electrons or more, the agreement becomes much better, but the correlation energy is still overestimated by a small amount. However, the SOSEX($W(0)$,$W(0)$) results have been evaluated with a single $\lambda-$integration point only. As we will see in the next chapter, a larger λ-grid generally leads to a SOSEX($W(0)$,$W(0)$) correction of higher magnitude and therefore to lower RPA+SOSEX($W(0)$,$W(0)$) correlation energies.

As one can expect, RPA+SOX considerably underestimates the correlation energies. RPA+RSOX shows a tendency to underestimate the correlation energies and out of all assessed methods, the deviations to the reference energies are clearly the smallest. For gRPA+, no clear trend in any direction can be identified.

While gRPA+ is not diagrammatic, SOSEX($W(0)$,$W(0)$) and RSOX are two different strategies to renormalize the SOX term. RPA+RSOX is based on the resummation of the Epstein-Nesbet series[582] of hole-hole ladder diagrams[407, 408] while SOSEX($W(0)$,$W(0)$) results from the resummation of ring diagrams, with the additional approximation of static screening. Both classes of diagrams are contained in CCD which also includes particle-particle ladder diagrams

and a third class of diagrams, coupling ladder and ring diagrams.[423] Thus, CCD can be seen as a first-principle method to couple both renormalization strategies. Unfortunately, CCD scales as N^6, as opposed to N^5. Since RPA+SOSEX($W(0)$,$W(0)$) overestimates, and RSOX underestimates the correlation energies, it seems worthwhile to look for alternative ways to combine SOSEX($W(0)$,$W(0)$) with RSOX while retaining the N^5 scaling.

In summary, the results presented here demonstrate that our implementation of RPA correlation energies gives numerically good results and second, that the $GW + G3W2$ self-energy massively improves over GW for the description of electron correlation. This, however, does not necessarily imply improvements for properties like relative energies and charged excitations in realistic systems. For example, RPA is often very accurate for relative energies since errors in the correlation energies tend to cancel.[299] On the other hand, beyond-RPA methods, while improving total correlation energies, often do not yield improvements for relative energies.[333] We will assess the accuracy of the different flavors of RPA+SOSEX for relative energies in the next chapter.

Chapter 5

Accuracy

In the last chapter, we have demonstrated that the numerical approximations we have introduced in chapter 3 are well under control. We have explicitly shown that we can eliminate the basis set incompleteness error to a large extent by extrapolation. Therefore, we are now in the position to assess the accuracy of the techniques we have implemented without the results being skewed by numerical errors. This is the purpose of the current section. We focus here on the accuracy which can be achieved with qsGW as well as the effect of the vertex corrections on charged excitations and electron-electron interaction energies. While the quality of qsGW has been assessed before for optical excitations,[277] charged excitations,[276,628] benchmark results for large datasets and a direct comparison to G_0W_0 for these datasets is missing.

Most importantly, we herein assess the effect of the statically screened $G3W2$ correction to the GW self-energy for charged excitations and relative total energies for a wide range of different binding characteristics, ranging from atomization energies to non-covalent interactions. The results for total energies of atoms presented in the last chapter have already revealed that the resulting correction to the RPA correlation energies, SOSEX($W(0)$,$W(0)$), corrects for the major part of the overestimation of the correlation energies. Also Grüneis *at al.*[360] have found the statically screened $G3W2$ correction to give improvements over GW for the band structure of solids. We will assess here whether it also outperforms GW for the calculation of QP energies in finite systems.

Next, we assess the resulting expression for the correlation energy for relative energies, for which the RPA has found widespread use in quantum chemistry.[299,333,335,629–634] As already discussed, the RPA is generally believed to describe long-range electron correlation very accurately since the effect of charge screening dominates in this limit.[291] This property together with the relation (2.356) is very desirable for the description of long-range dispersion effects or hydrogen bonding, which are omnipresent in chemistry and biology, determining for instance the structure of DNA or tertiary structures of proteins.[399,635] The magnitude of dispersion interactions does generally grow super-linearly with system size[636] and it's relative importance compared to covalent bonding therefore increases with the number of electrons. Especially for larger systems, it

becomes decisive to take into account the screening of the electron-electron interaction. CC and MBPT based methods describe this screening by resummation of certain classes of self-energy diagrams to infinite order.[112,406,637]

The RPA is the simplest first principle method which accounts for these effects and it is known to indeed work reasonably well for non-covalent interactions. For AC-SOSEX, it is already known that the improvements of absolute energies also translate into better relative energies for many but not all reaction types[333,334] and we assess in the following if this is also the case for RPA+SOSEX($W(0)$,$W(0)$). To this end, we compare the performance of this method to RPA and RPA+AC-SOSEX for for a wide range ot chemical systems, using datasets which are commonly used to assess the accuracy of new methods for the calculation of ground state energies.[218,334,393,638]

5.1 Computational Details

5.1.1 Quasiparticle Energies

Charged excitations in this work are calculated using (3.136). For qsGW, we set the dependency threshold to $5e^{-3}$ and perform a maximum of 15 iterations of the self-consistency cycle. Following the recommendations given in ref.[38], we use *VeryGood* numerical quality and the corresponding auxiliary basis set. We perform G_0W_0 calculations using PBE, PBE0, LRC-ωPBEh[200] and ωB97 - X[219] orbitals and eigenvalues. We use *Good* numerical quality and the corresponding auxiliary basis set for all G_0W_0 calculations and set the dependency threshold to $5e^{-4}$. All QP energies are calculated using (4.1).

5.1.2 Relative Energies

We use in all calculations grids of 24 points in imaginary time and imaginary frequency which is more then sufficient for convergence.[35] The final correlation energies are then extrapolated to the complete basis set limit using (4.2). Since the basis set error is not completely eliminated with this approach, we also counterpoise correct all energies, taking into account 100 % of the counterpoise correction. With these settings, we assume all our calculated values to be converged well enough to be able to draw quantitative conclusions about the performance of the methods we benchmark herein. We use the *VeryGood* numerical quality for integrals over real space and distance cut-offs. Dependency thresholds[36] have been set to $5e^{-4}$.

All Full configuration interaction calculations have been performed with the code by Knowles and Handy.[639,640] The 1- and 2-electron integral which are required as input have been generated with ADF.

5.2 Quasiparticle Energies

5.2.1 Organic Acceptor Molecules

We first assess the performance of the $G3W2$ QP energies in comparison to qsGW for a set of 24 organic acceptor molecules.[641] The reference values are of CC singles doubles and perturbative triples [CCSD(T)] quality and have been extrapolated to the CBS limit. Comparing these values to the experimental data shown in figure 5.1, we see that there are sizable differences to the CC values, especially for the fundamental gaps. Among the factors which might contribute to the discrepancies are errors in the optimized geometries, missing zero point vibrational energy corrections, and geometry relaxation after oxidation/reduction. For benzonitrile, the authors of ref.[641] calculated the values of the latter two corrections to be of the order of 0.18 and 0.14 eV, respectively. The errors in geometry or thermodynamical contributions are more difficult to assess but can be sizable as well: For example, the structure used in the calculations might not correspond to a global minimum on the potential energy surface. Finally, we note that the basis set extrapolation can also introduce some errors, especially for the larger systems where no basis sets larger than QZ were used.[242] We estimate the error of our own CBS limit extrapolation to be of the order of 50 meV for IPs and EAs of medium organic molecules.[37]. Due to all these factors that affect the direct comparison to experiment, we exclusively use the CCSD(T) reference values for the following quantitative discussion and only show the experimental values for comparison.

Performance of qsGW

For a variety of solids and metals it has been found that qsGW commonly overestimates band gaps and IPs by about about 15-20 % when screening is calculated within the RPA.[175,176,284,642,643] In contrast, the qsGW IPs shown in figure 5.1a are in excellent agreement with the CC reference values, with no systematic overestimation. The fundamental gaps in figure 5.1c are even (a few exceptions aside) systematically underestimated by qsGW. The overestimation of band gaps by qsGW is usually explained by missing electron-hole interaction via vertex corrections in the polarizability. Inclusion of an effective two-point kernel from time-dependent (TD) DFT or the Bethe-Salpeter equation (BSE) has been demonstrated to significantly improve the agreement of band gaps and IPs with experiment,[176,282,356,360–362] demonstrating the importance of beyond-RPA screening. For polar materials, i.e. materials with strong longitudinal-optical (LO) and transverse-optical (TO) phonon splitting,[644] electron-phonon coupling and phonon contributions to the frequency-dependent screening can have a sizable effect on the QP spectrum as well.[644,645] For example, qsGW overestimates the experimental band gap of V_2O_5 by about 100 %, which to a large extent is due to LO-TO splitting.[254]

The systems we consider here are rather small and have a planar geometry. The reduction of charge screening in low-dimensional materials has often been emphasized, for example in comparative studies on bulk and layered V_2O_5[253,254], MoS_2[252] or polythiophene.[251] Anti-screening has been observed in a spin chain[141] and also in finite conjugated systems.[250] Finally, LO-TO splitting will be absent entirely. These qualitative differences most likely explain the much higher

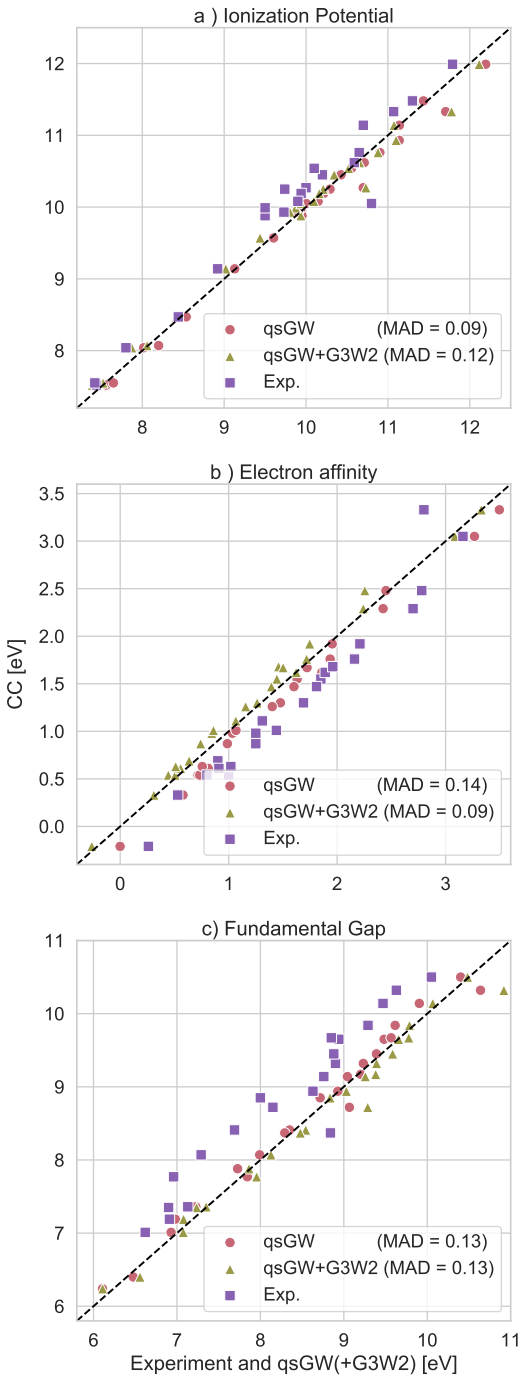

Figure 5.1: Ionization potentials (top), electron affinities (middle) and fundamental gaps (bottom) from qsGW and qsGW + $G3W2$ for a dataset of 24 organic acceptor molecules. The dashed black diagonal lines are CCSD(T) reference values. Experimental results are given for comparison as well. The values in parantheses denote mean absolute deviations (MAD) with respect to CCSD(T). All values are in eV.

accuracy of qsGW for the systems studied herein as compared to periodic systems.

The data clearly demonstrates qsGW to be an excellent first-principle method for the description of charged excitations for these weakly correlated, organic molecules. It is worthwhile to compare the performance of this method for to previous benchmark results of different GW methods. The accuracy of a large number of GW methods has been assessed for the same dataset in ref.[242]. Out of all GW based methods, the authors found G_0W_0@LRC-ωPBE to perform best (with optimized range separation parameter), with a MAD of 0.13 eV for IPs, and 0.18 eV for EAs. All in all, qsGW seems to be superior.

The effect of the statically screened $G3W2$ correction

Now we look at the effect of adding the $G3W2$ correction. As can be seen in figure 5.1, on average it lowers the qsGW IPs (see also the MDs in table 5.1) by a small amount and decreases the EAs by a relatively larger amount, implying increasing fundamental gaps. For IPs, this slightly worsens the agreement with the CC reference values, increasing the mean absolute deviation (MAD) from 0.09 eV to 0.12 eV. However, given the errors from the basis set limit extrapolation, this difference is not significant. Also, the $G3W2$ correction does not alter the MAD for the fundamental gaps. Since the statically screened $G3W2$ correction tends to increase the QP energies, a method which systematically overestimates IPs and EAs will be systematically improved by the $G3W2$ correction. This is demonstrated in figure 5.2 for G_0W_0@ωB97-X and G_0W_0@LRCωPBEh. Here, the $G3W2$ correction slightly improves the MAD with respect to the CC reference values for the IPs from 0.26 to 0.16 eV, and from 0.16 to 0.13 eV. For the EAs, the improvements are tremendous, and the inclusion of the $G3W2$ term leads to almost perfect agreement with the reference values. In table 5.1, these results are summarized. Despite the great performance of the $G3W2$ correction for the range-separated hybrids, the description of fundamental gaps is actually deteriorated, which can be considered as a serious drawback of this method.

Comparison of dynamically and statically screened SOX

In table 5.2 we compare a few beyond-GW approaches for the same dataset. These are GW + SOSEX from ref.[381] and GW + dynamically screened $G3W2$ from ref.[379] (denoted as $G_0W_0\Gamma_0^{(1)}$ by the authors of ref.[379]). These methods have all been implemented perturbatively and only differ in the way the electron-electron interaction in the SOX-term is screened (see figure 2.7). The results from ref.[381] and ref.[379] clearly demonstrate that especially methods with bad or only mediocre performance, like G_0W_0@PBE or G_0W_0@PBE0, profit immensely from vertex corrections with fully dynamical self-energy: $G_0W_0\Gamma_0^{(1)}$@PBE0 is very accurate, with a MAD of 0.16 eV for the IPs and 0.09 eV for EAs. Especially $G_0W_0\Gamma_0^{(1)}$@PBE performs much better than G_0W_0PBE. For EAs, the MAD improve from 0.60 eV to 0.06 meV, however, with 0.28 eV for IPs, $G_0W_0\Gamma_0^{(1)}$@PBE is not very accurate. For EAs, with a MAD of 0.06 eV, G_0W_0@PBE + SOSEX performs excellent, but it is considerably less accurate for IPs (MAD = 0.33 eV). In

	GW			$GW + G3W2$		
	qsGW	$\omega B97X$	ωPBEH	qsGW	$\omega B97X$	ωPBEH
Ionization Potentials						
MAD	0.09	0.26	0.16	0.12	0.16	0.13
MD	0.08	0.26	0.16	0.00	0.14	0.05
MAX	0.43	0.54	0.41	0.46	0.57	0.54
Electron Affinities						
MAD	0.14	0.29	0.27	0.09	0.05	0.07
MD	0.14	0.29	0.27	-0.09	-0.03	-0.06
MAX	0.25	0.38	0.36	0.23	0.15	0.20
Fundamental Gaps						
MAD	0.13	0.11	0.16	0.13	0.19	0.16
MD	-0.06	-0.03	-0.12	0.09	0.17	0.11
MAX	0.35	0.25	0.28	0.60	0.66	0.62

Table 5.1: Mean absolute deviations (MAD), mean signed deviattions (MD), and maximum errors (MAX) for IPs, EAs, and fundamental gaps for the 24 acceptor molecules for three different starting points for several GW based methods plus the respective $G3W2$ corrections. All values are in eV.

$G^{(s)}$	G_0W_0		G_0W_0+SOSEX		$G_0W_0 + dG3W2$		$G_0W_0 + sG3W2$	
	IP	EA	IP	EA	IP	EA	IP	EA
PBE	0.56/0.66	0.44/0.60	0.33	0.08	0.28	0.06	0.67	0.09
PBE0	0.19/0.22	0.39/0.39	0.12	0.16	0.16	0.09	0.28	0.06

Table 5.2: Comparison of MADs with respect to the CC reference values for different beyond-GW method in comparison to G_0W_0 for different starting points. All values are in eV. The prefix d denote that the screened interaction is dynamic, whereas s denotes the static interaction. For G_0W_0, the two numbers denote MADs with ADF/FHI-AIMS.

summary, $G_0W_0\Gamma_0^{(1)}$@PBE0 is the most accurate of these methods. However, it can not beat qsGW and also not G_0W_0@ωB-97-X + $G3W2$ and G_0W_0@LRCωPBEh + $G3W2$.

For the sake of a direct comparison of dynamically and statically screened $G3W2$ corrections, we also calculated G_0W_0@PB + $G3W2$ or G_0W_0@PBE0 + $G3W2$ with our implementation. First, we note the reasonable agreement of the results obtained with our implementation and FHI-AIMS on the GW level, which allows for a qualitative comparison. The differences mainly result from the different basis sets used in the calculations.[379,381] The MADs in table 5.2 clearly show, that the statically screened $G3W2$ correction does not give good results for these starting points. For EAs, the performance of the statically screened correction is comparable to the dynamical one. However, the description of IPs is even worsened. Here, the methods with dynamical screening are significantly better.

In ref.[379], it was found that the magnitude of the $G3W2$ correction was much smaller, when the statically screened interaction instead of the dynamically screened one was used. This is in line with our results. For the HOMO QP energies, the correction often changes sign, i.e. the HOMO QP energy is increased when the interaction is statically screened. Also in this case, the correction for the LUMO level is typically much larger than the one for the HOMO level,

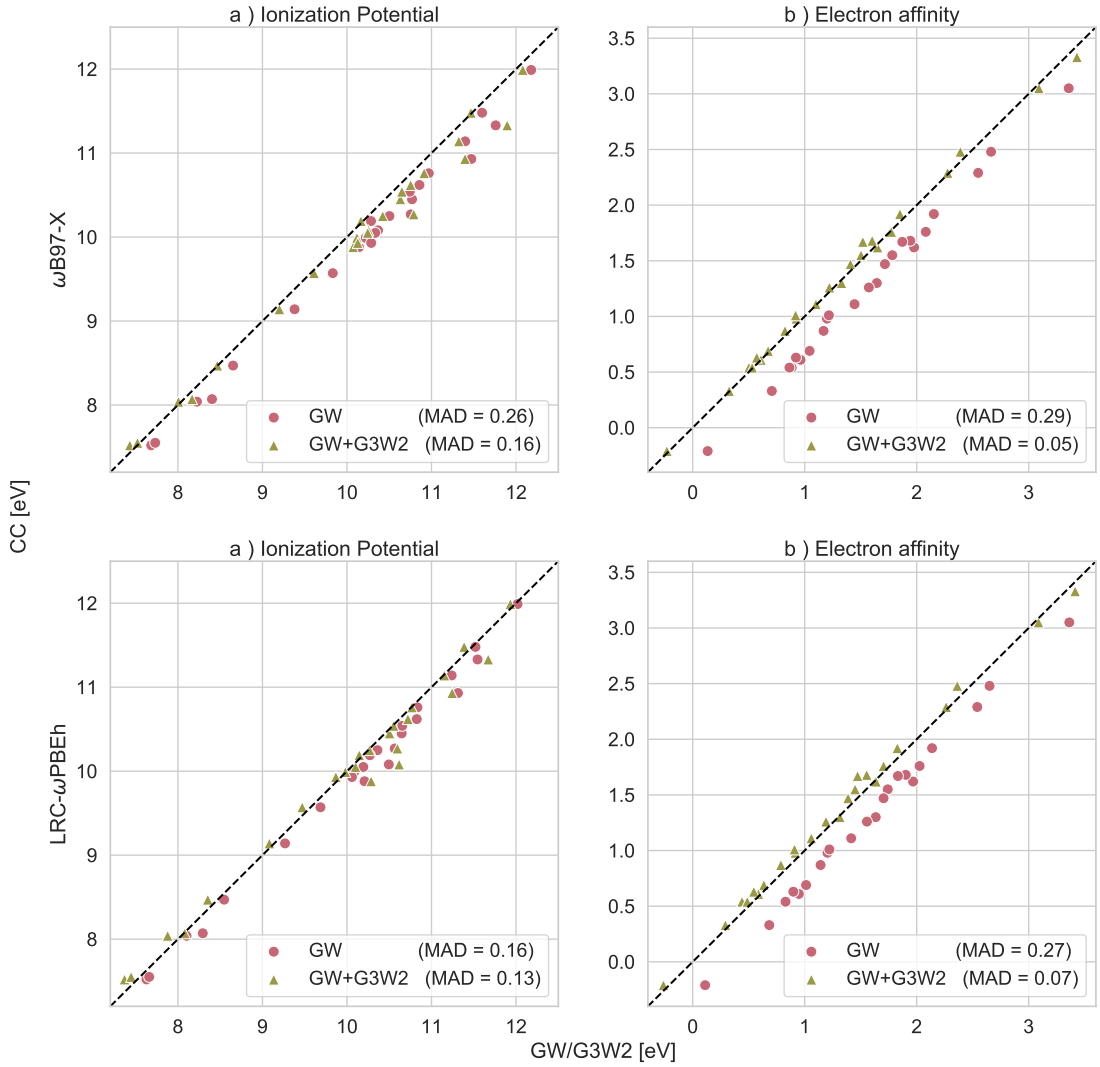

Figure 5.2: Ionization potentials (left) and electron affinities (right) from G_0W_0@ωB97-X (+ Σ^{G3W2}) (top) and G_0W_0@LRCω-PBEh (+ Σ^{G3W2}) (bottom) and G_0W_0@ωB97-X + Σ^{G3W2}, for a dataset of 24 organic acceptor molecules. The dashed black diagonal lines are CCSD(T) reference values and the values in parantheses denote mean absolute deviations (MAD) with respect to CCSD(T). All values are in eV.

increasing the fundamental gaps. Due to the small magnitude of the correction, the statically screened $G3W2$ correction works well if QP energies are already well described on the GW level. The dynamically screened $G3W2$ term leads to a correction of larger magnitude and works best for GW methods which severely underestimate IPs and overestimate EAs. This is the case for

G_0W_0@PBE and (to a smaller extent) also for G_0W_0@PBE0[242] and consequently, the addition of SOSEX or dynamically screened $G3W2$ leads to large improvements.[379] On the other hand, G_0W_0@HF underestimates the HOMO QP levels and overestimates LUMO QP levels.[242,379] Therefore, the addition of dynamically screened SOX deteriorates the results for this starting point.

5.2.2 Ionization Potentials of Small Molecules

Starting Point	GW	$GW + G3W2$
qsGW	0.21	0.27
ωB97-X	0.20	0.27
LRC-ωPBEh	0.12	0.21

Table 5.3: MADs with respect to the EOM-CCSDT reference for the first ionization potentials of a set of 40 small molecules. All values are in eV.

So far, the performance of the $G3W2$ self-energy correction has only been assessed for a very specific type of molecules. We now also consider a second database curated by Bartlett and coworkers.[646] They calculated the IPs of 40 small organic and inorganic molecules, using EOM-CCSD/cc-pVTZ & cc-pVQZ and EOM-CCSDT/cc-pVTZ. The reference values we use here are obtained as follows: From the EOM-CCSD results obtained with the cc-pVTZ and cc-pVQZ basis sets, we extrapolate the IPs to the CBS limit with the formula by Helgaker et al.[503], eq. (4.2). Note, that we used eq.(4.1) to obtain our own STO results. Subsequently, we add the difference between the EOM-CCSD and EOM-CCSDT IPs to the CBS limit extrapolated EOM-CCSD IPs. Thus, the reference values should be close to EOM-CCSDT quality at the CBS limit. The MADs of the considered methods with respect to the EOM-CCSDT reference values are shown in table 5.3. The qsGW IPs are with a MAD of 0.21 eV still in reasonable agreement with the reference values, but the agreement is worse than for the acceptor molecules. For all tested GW starting points, the $G3W2$ term worsens the IPs.

In summary, the results presented in this section reveal qualitative differences between the dynamically screened $G3W2$ correction as recently tested in ref.[379] and the statically screened one for charged excitations. The magnitude of the $G3W2$ correction becomes much smaller when the electron-electron interaction is statically screened. The addition of the dynamically screened SOX term consistently lowers EAs and increases IPs, while the statically screened one often decreases the IPs.

Popular methods like G_0W_0 based on PBE and PBE0 starting points predict too low ionization potentials and too high electron affinities[379] and the addition of dynamically screened $G3W2$ correction results in major improvements for these methods.[379] The statically screened $G3W2$ correction, on the other hand, gives improvements over GW calculations which consistently underestimate QP energies. This is the case for G_0W_0@$LRC\omega$PBEh and G_0W_0@ωB97-X. Especially for EAs, improvements are tremendous. For IPs and fundamental gaps, the improvements are not consistent and seem to be system-specific. For molecules with nearly 100 atoms,

evaluating the perturbative $G3W2$ correction for a few states does not come with significantly increased computational costs compared to a GW calculation. This is a big advantage over the dynamically screened SOX correction.[379]

5.3 Relative energies

5.3.1 Dissociation Curves

The potential energy curves of small diatomic molecules serve as an important test for electronic structure methods. We first consider molecules with different bonding types for which we were able to calculate FCI reference values: H_2 is covalently bound, LiH is an ionic molecule, and He_2 has a very weak, non-covalent bond.

The dissociation curve of H_2 calculated with RPA+SOSEX($W(0)$,$W(0)$)@PBE is the red line in figure 5.3. Our calculations are not converged with respect to the basis set size but comparison of our dissociation curves calculated with RPA@PBE and RPA+SOSEX(W,v_c)@PBE to the ones presented in ref. [385] and [647] clearly shows that their qualitative behavior is reproduced correctly. It is known that RPA describes the dissociation of covalently bonded molecules qualitatively correctly while RPA+SOSEX(W,v_c) and other exchange-corrected RPA approaches fail.[340,385,647] Here we find that also RPA+SOSEX($W(0)$,$W(0)$) dissociates the hydrogen molecule correctly and that the potential energy curve has a similar shape than the RPA one. Henderson and Scuseria have argued that the self-correlation in the RPA mimics static correlation effects[647] whose good description is necessary to dissociate H_2 correctly. The fact that in RPA+SOSEX($W(0)$,$W(0)$ the self-correlation error is eliminated to some large extent (also see table 1 in the SI) but not completely therefore explains the similarity to the RPA dissociation curve.

To rationalize this result further, we also calculated the dissociation curve within the static limit of RPA+SOSEX(W,v_c), RPA+SOSEX($W(0)$,v_c) (blue curve). This shows that the screening of the second electron-electron interaction line is responsible for the qualitative differences between SOSEX(W,v_c) and SOSEX($W(0)$,$W(0)$). It should also be noted that the RPA+SOSEX($W(0)$,$W(0)$) dissociation curve of H_2 very closely resembles the one calculated by Bates and Furche using the approximate exchange kernel (AXK) correction to the RPA.[341] SOSEX($W(0)$,$W(0)$) and the AXK kernel have in common that both electron-electron interaction lines are screened. For LiH, we find a similar behavior than for H_2. For He_2 (notice that we plotted here the binding energy and not the total energy) we see that all approaches give the correct dissociation limit.

From these potential energy curves, we also extracted the equilibrium bond lengths via cubic spline interpolation. These are shown in table 5.4 Around the equilibrium distances, RPA+SOSEX(W,v_c) generally gives the best energies but this does not necessarily translate into the best bond lengths. For the covalently bound molecules LiH and F_2 as well as LiH RPA+SOSEX(W,v_c) underestimates and RPA+SOSEX($W(0)$,$W(0)$) overestimates the bond lengths. Again, RPA+SOSEX($W(0)$,$W(0)$) behaves qualitatively similar to RPA. For He_2, both approaches give similar results, while RPA+SOSEX($W(0)$,v_c) fails completely. On the other

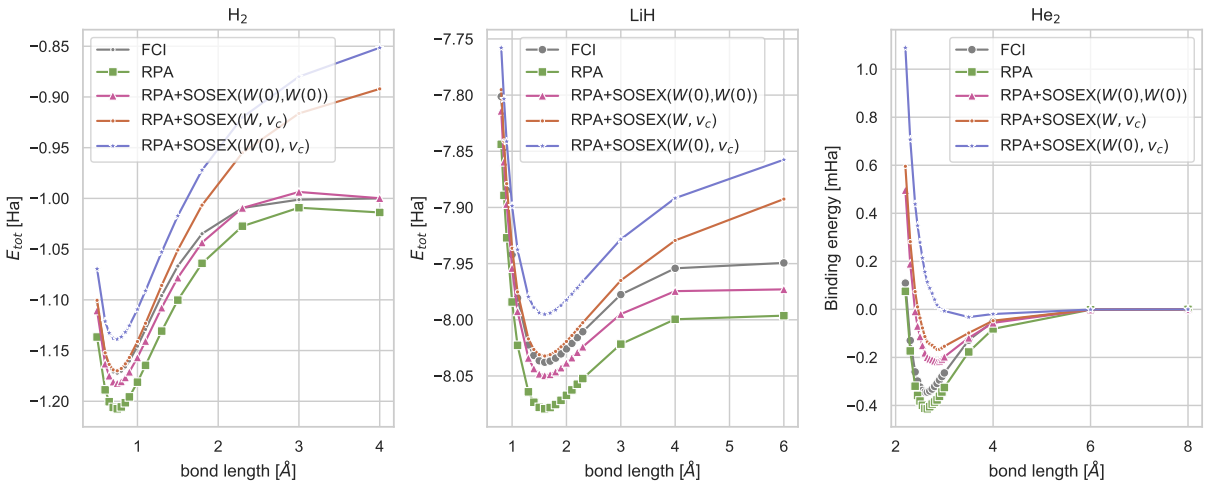

Figure 5.3: Potential energy curves (in Hartree) of H_2 (left) and LiH (middle), as well as binding energy (in mHartree) as a function of system size for He_2 on the right using FCI, RPA@PBE and different variants of RPA+SOSEX@PBE. For H_2 and He_2, all calculations have been performed with the TZ3P basis set. For Lih, all calculations have been performed using the TZP basis set.

method	H_2	LiH	He_2	F_2	Be_2
exp.				1.413[648]	2.320[649]
accurate	0.741	1.601	2.626	1.413[648]	2.320[650]
RPA	0.742	1.597	2.632	1.437	2.403
RPA + SOSEX$(W(0), W(0))$	0.744	1.605	2.852	1.444	2.424
RPA + SOSEX(W, v_c)	0.738	1.594	2.871	1.364	–
RPA + SOSEX$(W(0), v_c)$	0.735	1.599	3.542	1.348	–

Table 5.4: Equilibrium bond length of selected molecules. All values are in Å. The bond lengths for H_2, He_2, and LiH have been calculated using the TZ3P and TZP basis sets to make them comparable to the FCI result. The bond lengths for F_2 and Be_2 have been obtained using the QZ6P basis set. All RPA(+SOSEX) calculations have been performed with a PBE Green's function.

hand, unlike RPA+SOSEX($W(0)$,$W(0)$), RPA+SOSEX(W,v_c) does predict an unbound Be_2 dimer.

5.3.2 Dissociation of charged Dimers

In table 5.5 we investigate the dissociation of four charged dimers by means of the SIE4x4 dataset.[638] Here, the self-correlation error of RPA leads to considerable underbinding,[299,385,647] whereas RPA+SOSEX(W,v_c) is exact,[386] the remaining error for H_2 being due to basis set errors

	RPA	SOSEX(W,v_c)	SOSEX($W(0)$,v_c)	SOSEX($W(0)$,$W(0)$)
H_2^+				
1.0	5.19	0.76	-2.58	3.09
1.25	7.59	-0.26	-5.33	5.19
1.50	11.21	-1.31	-8.23	8.89
1.75	16.15	-2.30	-11.14	14.27
He_2^+				
1.0	13.23	0.23	-5.30	14.34
1.25	25.40	-2.84	-12.91	27.56
1.50	40.60	-5.64	-20.32	44.79
1.75	56.76	-7.65	-25.76	63.38
$(NH_3)_2^+$				
1.0	5.89	15.17	24.91	16.23
1.25	13.00	20.08	36.23	33.50
1.50	20.61	21.89	42.78	50.41
1.75	30.88	15.14	28.73	61.48
$(H_2O)_2^+$				
1.0	10.19	29.79	51.70	33.79
1.25	20.62	12.16	21.61	38.68
1.50	31.88	2.35	4.58	50.58
1.75	42.08	0.50	5.47	65.61
MAD	21.95	8.63	19.22	33.24

Table 5.5: Errors in kcal/mol for the charger dimers in the SIE4x4 benchmark set calculated with RPA and different variants of RPA+SOSEX. PBE orbitals have been used in all calculations

as well as the fact that PBE orbitals have been used. Furche and coworkers have observed a catastrophic failure of RPA+SOX for $(NH_3)_2^+$ and $(H_2O)_2^+$[651] and also SOSEX($W(0)$,$W(0)$) considerably deteriorates the RPA results for those systems. Only for H_2^+, one finds that the partial cancellation of the RPA self-correlation leads to small improvements over RPA.

5.3.3 Thermochemistry and Kinetics

We move on to assess the performance of RPA+SOSEX($W(0)$,$W(0)$) for reaction types which are relevant for thermochemistry and kinetics. Total atomization energies, ionization potentials and electron affinities as well as barrier heights of different reactions serve hereby as important testing grounds. For this work, we calculated the atomization energies (defined as the total energy of the molecule minus the sum of the energies of the atomic fragments) of the 144 small and medium molecules in the W4-11 dataset.[652] The reference values have been calculated using the highly accurate W4 protocol.[653] For barrier heights, we use the BH76 database which is a compilation of the HTBH38[654] and NHTBH38[655] databases for barrier heights by Truhlar and coworkers, which are typically used in benchmarks of (beyond-)RPA methods.[299,333,334,631] The reference values have been calculated with the W2-F12 protocol.[638,656] To benchmark the performance for ionization potentials and electron affinities we employ the G21IP and G21EA databases by Pople and coworkers and use the original experimental reference values.[657]

To start with, we assess the effect of the Green's function G^s used to calculate the correlation

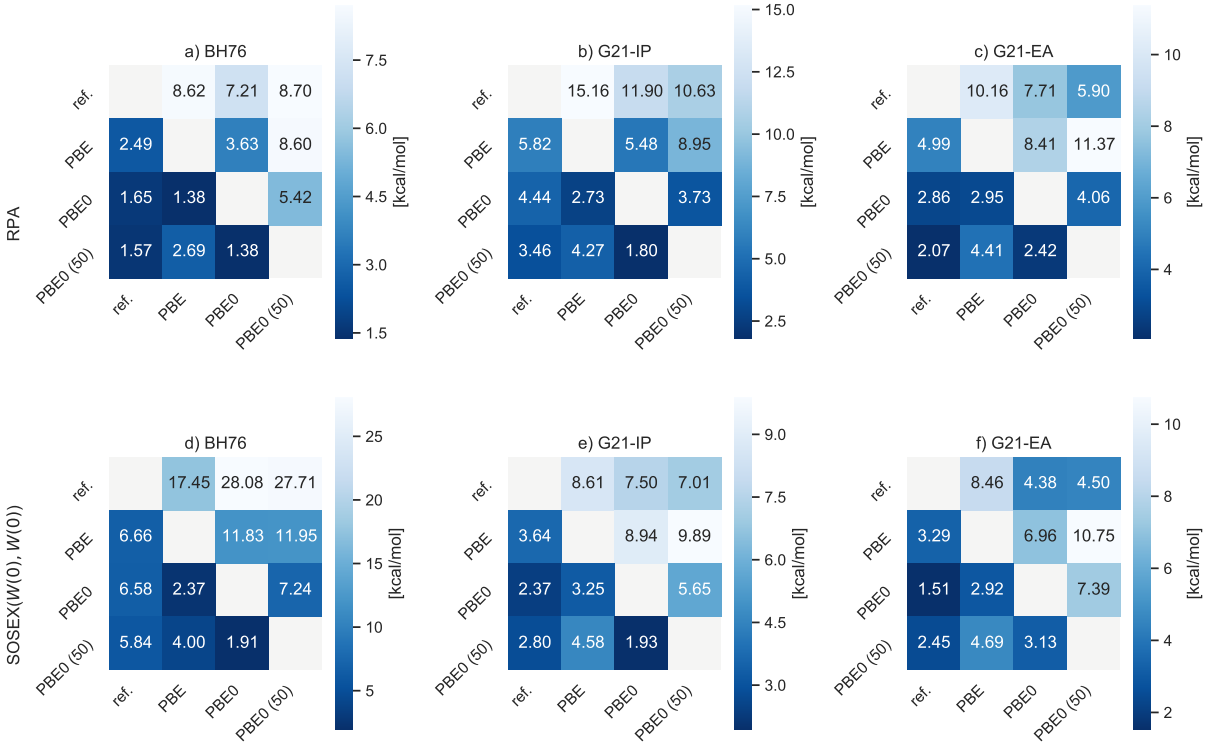

Figure 5.4: Mean absolute deviations (MAD) (lower triangle in each plot) and Maximum deviations (MAX) (upper triangle) with respect to the reference values as well as using different KS Green's functions as input for BH76 (left), G21-IP (middle) and G21-EA (right) for RPA (top) and RPA+SOSEX($W(0)$,$W(0)$) (bottom). All values are in kcal/mol.

energies. RPA calculations can in principle be performed self-consistently using a variety of approaches.[168,234,274,337,658–662] (see ref. [663] for a review) This is rarely done in practice since self-consistent RPA calculations are computationally demanding and since the resulting energies are often worse than the ones evaluated using a Green's function from a generalized gradient approximation (GGA) or hybrid calculation.[660] GGAs like PBE or TPSS are often used to construct G^s.[334,393,634] Using hybrid orbitals can be seen as a pragmatic way to compensate for the lack of self-consistency in the RPA calculation and therefore we assess here whether they lead to improvements over GGA orbitals.

For W4-11, the differences between different starting points are minor, but PBE tends to give the best results. For the BH76, G21IP, and G21EA datasets, we show mean absolute deviations (MAD) and maximum deviations (MAX) with respect to the reference values and

with respect to the different starting points in figure 5.4. The RPA results generally improve with increasing amount of Fock exchange, while 25 % (PBE0) generally seems to work best for RPA+SOSEX($W(0)$,$W(0)$). The differences are often substantial, for instance in case of the RPA barrier heights (fig 5.4a) or the RPA+SOSEX($W(0)$,$W(0)$) electron affinities (fig 5.4f).

For charged excitations, this observation aligns very well with the experience from G_0W_0 calculations where hybrid functional with 25 - 50 % are typically a much better starting point than GGAs.[241,257] However, when $G3W2$ corrections are added to the G_0W_0 QP energies, using a hybrid functional with a smaller fraction of exact exchange might often be beneficial.[40,379] For barrier heights, hybrid functionals with a larger fraction of exact exchange are usually required to obtain qualitatively correct barrier heights[638,664] and it therefore not surprising that hybrid orbitals serve as a suitable starting point for RPA calculations.

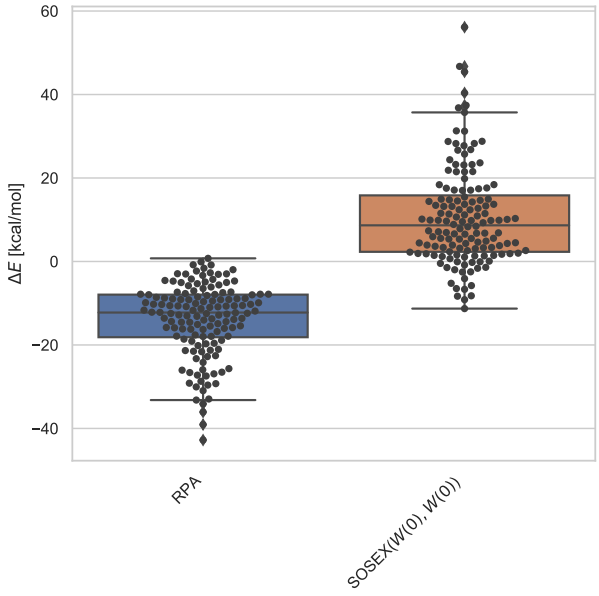

Figure 5.5: Errors of RPA@PBE and RPA+SOSEX(W,v_c)@PBE for the atomization energies in the W4-11 dataset. Black dots denote the individual data points and the horizonal line in each box denotes the median deviation. the box contains all data points between the first quartile ($Q1$) and third quartile ($Q2$) and the whiskers are at $Q1 \pm |Q1 - Q3|$. (in case of a normal distribution, the whiskers include 99.3% of all data points). All values are in kcal/mol.

Our atomization energies for the W4-11 dataset are shown in figure 5.5. It has first been observed by Furche[629] that RPA underestimates atomization energies (indicated here by negative errors). This has been confirmed later by Ren at al.[299] and Paier et al.[333] for the 55 covalently bound molecules in the G2-I set.[657] The same holds for RPA+SOSEX(W,v_c), but compared to RPA the magnitude of the error is reduced on average.[299,333] We observe here that unlike SOSEX(W, v_c), the addition of SOSEX($W(0), W(0)$ substantially overcorrects the

RPA atomization energies which are now much too high in magnitude. Notice, that our non-counterpoise corrected calculations based on (T,Q) extrapolation will still include a sizable basis set incompleteness error for atomization energies. However, our qualitative conclusions will be valid. Adding bare SOX to RPA leads to underestimated correlation energies.[298] This effect is expected to be more pronounced for the molecule than for the individual atoms since more electrons are correlated in the former. Therefore, RPA+SOX will substantially overestimate atomization energies and due to underestimated screening of the SOX term in SOSEX($W(0), W(0)$, RPA+SOSEX($W(0), W(0)$ inherits this problem.

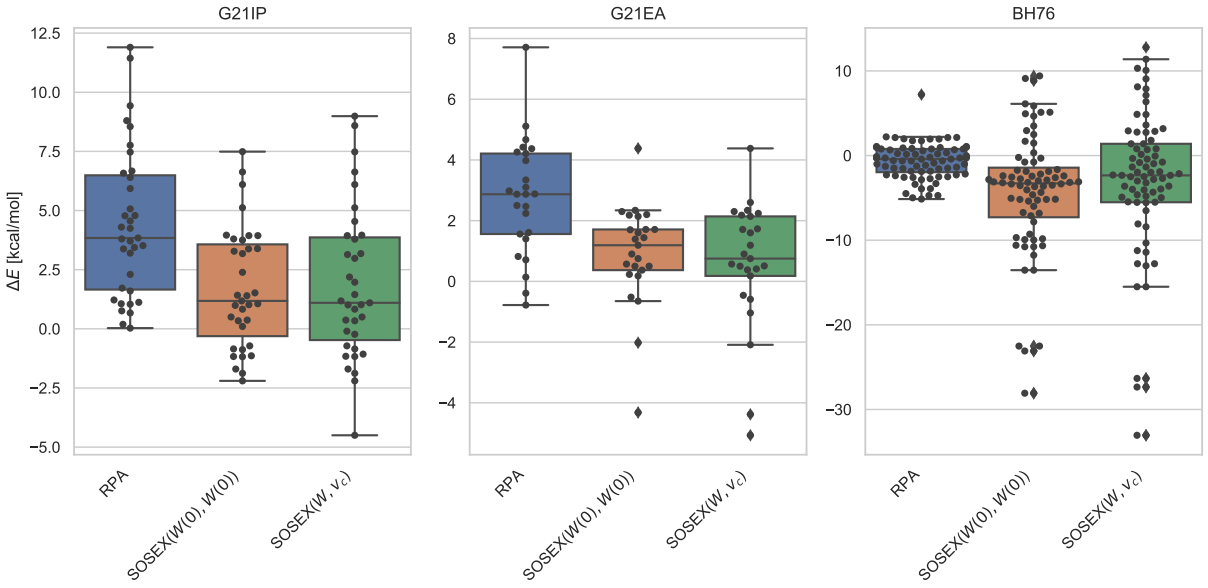

Figure 5.6: Errors of RPA@PBE and different RPA+SOSEX variants for barrier heights (BH76, left), ionization potentials (G21-IP, middle) and electron affinities (G21-EA, right). For an explanation of the boxplots, see the caption of figure 5.5. All values are in kcal/mol.

As also shown in more detail in figure 5.6, the performance of RPA+SOSEX($W(0)$,$W(0)$) is in all cases comparable to RPA+SOSEX(W,v_c), for which the trends presented here are well known:[299,334,385,631,665] RPA+SOSEX(W,v_c), fails for barrier heights, where the inclusion of renormalized singles excitations is necessary to obtain good results[299,333,334] and works very well for charged excitations.[299,631] We note, that RPA+SOSEX($W(0)$,$W(0)$)@PBE0 performs very well for charged excitations, with an accuracy challenging modern double-hybrid functionals.[638]

5.3.4 Non-covalent Interactions

λ-dependence of the S66 Interaction Energies

We now discuss the dependence of the SOSEX correlation energies on the λ-integration for non-covalent interactions. The magnitude of the SOSEX contribution to the correlation energy as a function of the size of the λ-grid is shown in table 5.6 for three selected systems. One can show, that for a 2-electron system like H_2, the SOSEX(W, v_c) correction equals minus half of the RPA correlation energy (In other words, RPA+SOSEX is self-correlation free). This relation is fulfilled for SOSEX(W, v_c) with already 4 Gauss-Legendre points.

	SOSEX(W, v_c)			SOSEX($W(0), W(0)$)		
N_λ	H_2	$(H_2O)_2$	Benzene	H_2	$(H_2O)_2$	Benzene
1	15.51400	147.15253	287.90735	10.74228	101.45448	204.17377
2	16.63810	157.79684	307.48549	12.83037	119.99186	239.22546
4	16.63421	157.71007	307.35326	12.82006	119.79484	238.91728
6	16.63421	157.70997	307.35313	12.82006	119.79451	238.91688
$\frac{1}{2}E^{RPA}$	16.63421			16.63421		

Table 5.6: Total magnitude of SOSEX correction in kcal/mol as a function of the size of the λ-grid for selected systems.

The magnitude of the SOSEX correction is underestimated when the λ-integration is carried out using a trapezoidal rule. This is illustrated in fig. 5.7 for H_2 and $(H_2O)_2$. Using a single λ-point corresponds to approximating the λ-dependence of the correlation energy as a straight line, which leads to a small integration error. Also in section 5.3.4, we show the effect of the number of points used for the λ-integration on the relative energies in the S66 dataset to be indeed very small. Also the accuracy of the interaction energies with respect to the CCSD(T) reference values is not negatively affected when only a single integration point is used and therefore all benchmark results for the S66x8 database are carried out using the trapezoidal rule.

The effect of the number of points in the λ-integration on relative energies for SOSEX(W, v_c) and SOSEX($W, W(0)$) for the S66 test set is shown in figure 5.8. Fig. 5.8a) shows the error in the covalent bonding energies with respect to the converged $\lambda-$integration when only a single integration point is used. Generally, the resulting integration errors are very small and do not exceed 0.1 kcal/mol for most complexes. In parts b) and c) of figure 5.8, the relative errors of the interaction energies with respect to the CCSD(T) reference values are shown. One can clearly see, that the error in the λ-integration is negligible when looking at the accuracy of relative energies. This is also reflected in the MADs with respect to the CCSD(T) reference shown in figure 5.8.

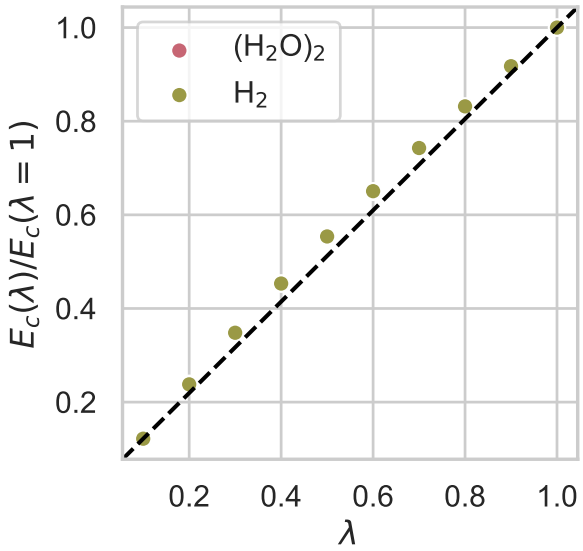

Figure 5.7: Magnitude of the SOSEX(W, v_c) correlation energy as a function of λ relative to its value at $\lambda = 1$ for H_2 and $(H_2O)_2$.

S66 Interaction Energies

We now turn to our benchmark results for non-covalent interactions. As for the previous datasets, we also assess the dependence of RPA and RPA+SOSEX correlation energies on the choice of the KS Green's function G^s. In figure 5.9 the interaction energies in the S66 database[666] obtained using different G^s are compared to each other as well as to the CCSD(T) reference values by Hobza and coworkers.[666] Following the discussion in 5.3.4, all values have been obtained using a single integration point for the λ-integral. RPA and RPA+SOSEX$(W(0), W(0))$ are equivalently independent of the choice of the KS Green's function, with MADs between 0.20 and 0.39 kcal/mol between the different functionals. However, individual values can differ by almost 2 kcal/mol which is a sizable difference, given that the largest interaction energies in the S66 database are of the order of 20 kcal/mol only. The performance of RPA compared to the CCSD(T) reference is rather insensitive to the KS Green's function, even though the hybrid starting points lead to slightly better results. With 0.52 kcal/mol, the MAD for RPA@PBE is in excellent agreement with the 0.61 kcal/mol MAD obtained by Nguyen *et. al.* in ref. [393], which has been obtained with GTO-type basis sets and 50 % counterpoise correction instead of 100 %. This shows, that our interaction energies are well converged with respect to the basis set size. The RPA+SOSEX$(W(0), W(0))$ results are much better using the hybrid functionals than with PBE. RPA+SOSEX(W, v_c)@PBE, is slightly more accurate than RPA+SOSEX(W, v_c)@PBE0, but unlike for the datasets discussed before, the differences between the different starting points are negligibly small. Also, the dependence of SOSEX(W, v_c) on the starting point is smaller than

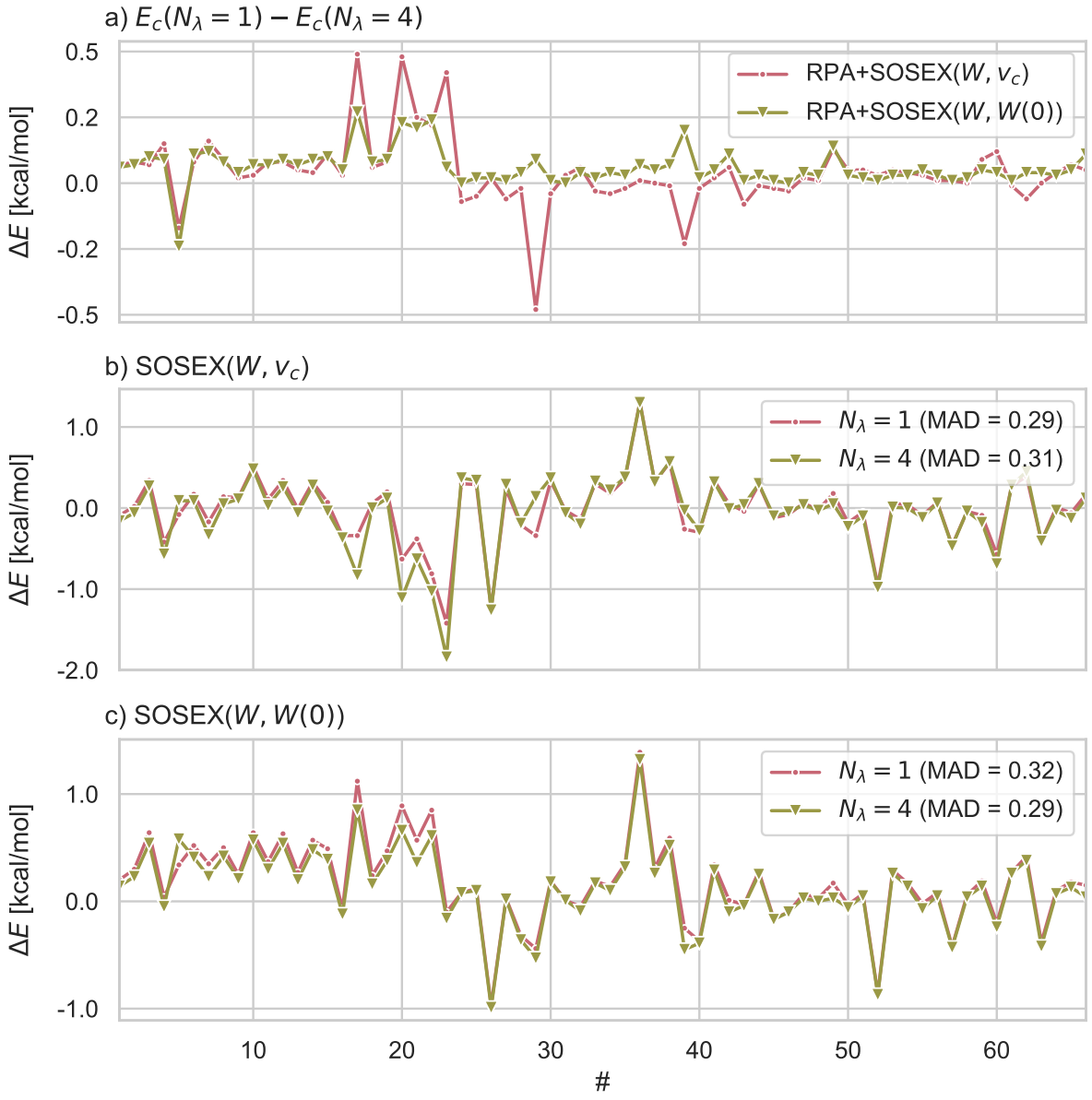

Figure 5.8: a) Difference in relative correlation energies for the S66 test set for both SOSEX variants when using 1 and 4 integration points for the λ-integration. b) Error of relative SOSEX(W, v_c) correlation energies with respect to the CCSD(T) reference values when using 1 and 4 integration points for the λ-integration. c) Same as b), but for SOSEX$(W, W(0))$. All values are in kcal/mol.

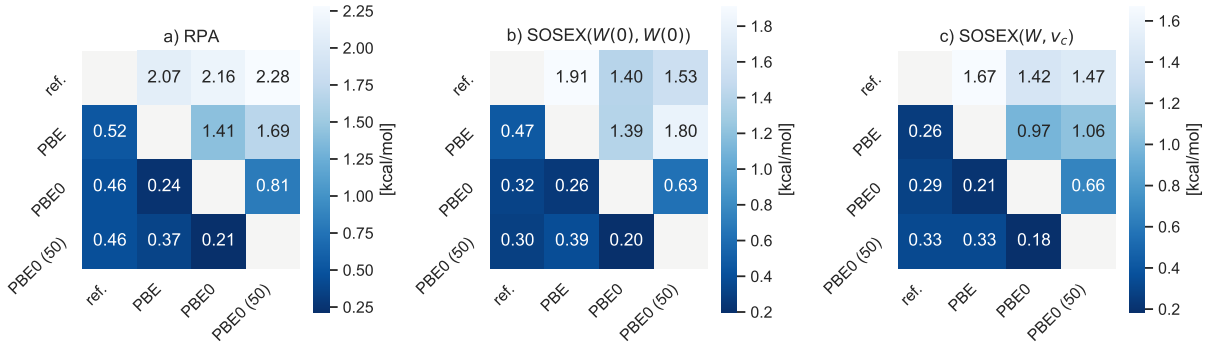

Figure 5.9: Mean absolute deviations (MAD) (lower triangle in each plot) and Maximum deviations (MAX) (upper triangle) for a) RPA, b) SOSEX($W(0), W(0)$) and c) SOSEX($W(0), v_c$) interaction energies for the S66 database using different KS Green's functions as well as to the CCSD(T) reference values (ref.). All values are in kcal/mol.

for SOSEX($W(0), W(0)$).

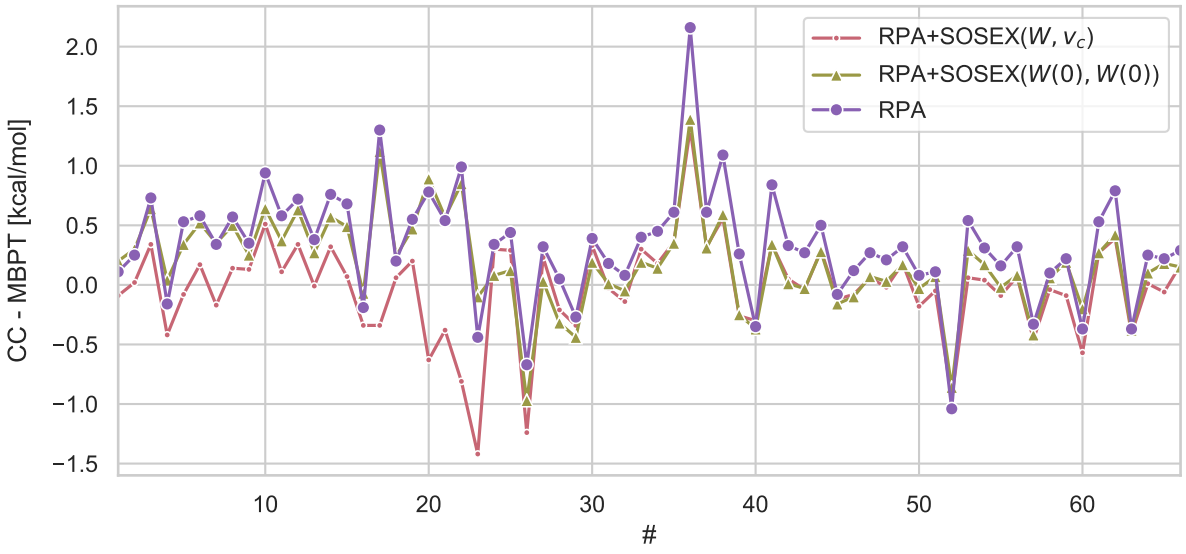

Figure 5.10: Deviations of RPA@PBE0 and both RPA + SOSEX@PBE0 variants for the S66 database with respect to the CCSD(T) reference. All values are in kcal/mol.

Figure 5.10 shows the deviations of RPA and both RPA+SOSEX variants with respect to CCSD(T) for all datapoints in the S66 database. MADs and mean absolute percentage deviations (MAPD) for the whole database as well as for the individual categories are presented in table 5.7.

	MAD							
	S66		hydr. bond		dispersion		mixed	
Method	$[\frac{kcal}{mol}]$	[%]	$[\frac{kcal}{mol}]$	[%]	$[\frac{kcal}{mol}]$	[%]	$[\frac{kcal}{mol}]$	[%]
SOSEX$(W(0), W(0))$@PBE0	0.32	7.28	0.45	5.76	0.29	10.33	0.21	5.50
SOSEX$(W(0), v_c)$@PBE0	0.28	6.88	0.30	3.42	0.34	11.77	0.20	5.25
SOSEX(W, v_c)@PBE0	0.29	6.85	0.31	3.39	0.33	11.63	0.21	5.33
SOSEX(W, v_c)@PBE	0.26	6.25	0.23	3.51	0.33	10.16	0.17	4.26
RPA	0.46	11.54	0.55	7.19	0.47	17.74	0.34	9.41
PBE0-D3(BJ)	0.28	5.09	0.47	4.80	0.18	5.09	0.18	5.42
DSD-PBE-P86-D3(BJ)	0.23	5.07	0.31	3.71	0.21	6.99	0.16	4.43

Table 5.7: MADs (absolute and in %) of different electronic structure methods with respect to the CCSD(T) reference values for the whole S66 database and for its subcategories.

The interactions of the first 22 complexes in the database are dominated by Hydrogen bonds which are predominantly of electrostatic origin.[667] The next 22 complexes are mostly bound by dispersion interactions and the remaining interactions are of mixed nature.[666] It is useful to distinguish between these different interaction patterns in the following comparison.

For the whole database, RPA gives a MAPD of 11.5 % and the SOSEX corrections sizably reduce the MAPDs with respect to the CCSD(T) reference values to in between 7.3 % and 6.3 %. SOSEX(W, v_c) outperforms SOSEX$(W(0), W(0))$ by far for the hydrogen-bonded complexes, and is even slightly more accurate than the double-hybrid DSD-PBE-P86-D3(BJ),[208] one of the best double hybrid functionals for weak interactions.[413] For dispersion interactions, the performance of SOSEX$(W(0), W(0))$ and SOSEX(W, v_c) is comparable. Here, the empirically dispersion corrected[207,213] functionals, the hybrid PBE0-D3(BJ) and DSD-PBE-P86-D3(BJ), are much more accurate than all MBPT based methods. A few exceptions aside, fig. 5.10 shows that RPA understabilizes the complexes in the S66 database (indicated by positive errors). SOSEX corrections lower the interaction energies, i.e. the complexes are predicted to be more stable. SOSEX(W, v_c) shows a tendency to overstabilize the hydrogen-bonded complexes. For these systems, the RPA+SOSEX$(W(0), W(0))$ energies are almost identical to the ones from RPA.

Also from the sizable differences of SOSEX(W, v_c) (green points) to its static limit (with only a single screened interaction line, blue points) shown in figure 5.10 it is clear that the dynamical screening effects are important for the hydrogen-bonded complexes. As can be seen from the MAPD in table 5.7, this does however not improve agreement with the CCSD(T) reference values. For the dispersion bound complexes, there are only negligible differences between both variants, demonstrating that the dynamical variations of the screening average out. For the last 22 complexes in the database the differences are slightly larger. In all cases, dressing the second electron-electron interaction line does not alter the results decisively.

S66x8 Interaction Energy

The S66x8 dataset contains the complexes in the S66 database at 8 different geometries.[666] The separations of the monomers in the complexes are given relative to their equilibrium distances, i.e. a relative separation of 2.0 means that the monomers separation in the complex is twice as large as the equilibrium separation. For our assessment of the SOSEX($W(0), W(0)$) correction, we divide the separations of the potential energy curve in three regions, which we denote as short (equilibrium distance scaled by a factor 0.9-0.95), middle (1.0-1.25) and long (1.5-2.0). All RPA (+SOSEX) calculation discussed here have been performed using a PBE0 Green's function.

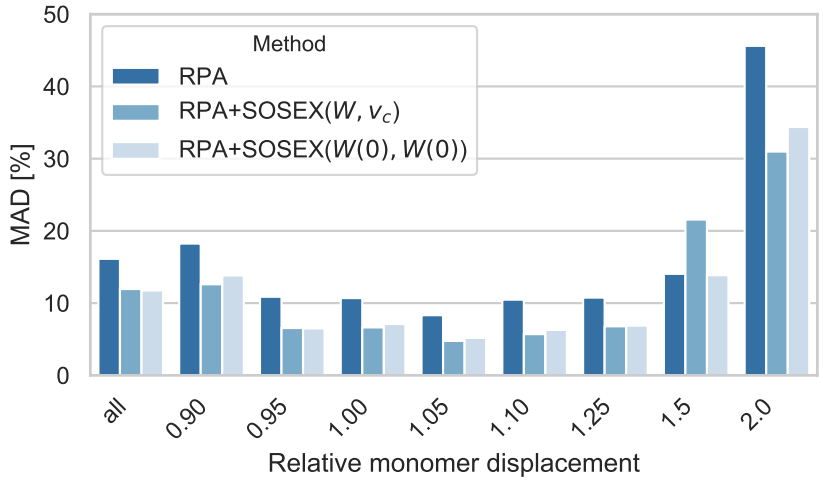

Figure 5.11: MADs (in percent) for the S66x8 database with respect to the CCSD(T) reference values for RPA, RPA+SOSEX(W, v_c) and RPA+SOSEX($W(0), W(0)$). MADs are shown separately for the whole database (columns on the left) and for different monomer-monomer separations.

	short [%]	middle [%]	long [%]
SOSEX(W, v_c)	35.2	42.8	13.5
SOSEX($W(0), W(0)$)	31.0	37.9	19.1

Table 5.8: Relative improvements obtained with different SOSEX variants over RPA for different groups of monomer-monomer separations.

The results of our comparison are shown in figure 5.11, where the MAPDs with respect to CCSD(T) for the whole database as well as for the scaled monomer-monomer separations are shown. For the whole database, the average relative deviations with respect to the reference values are larger than for S66. With in between 31 and 43 %, both SOSEX correction lead to siz-

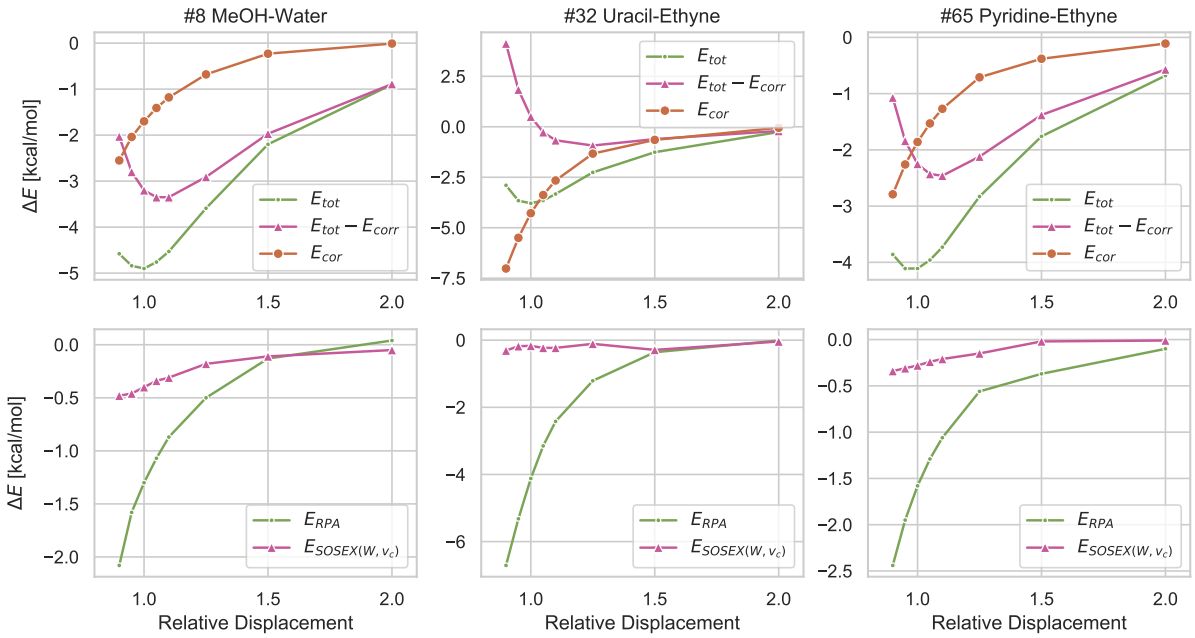

Figure 5.12: Upper plots: three RPA+SOSEX(W,v_c)@PBE0 potential energy curves in the S66x8 database (green), separated in correlation contributions (yellow) and HF energy (evaluated with PBE0 orbitals). Lower plots: decomposition of the correlation energies into RPA and SOSEX(W,v_c) contributions. All values are in kcal/mol.

able improvements over the RPA in the short and medium regime. For large monomer-monomer separations, the improvements become much smaller, with 14 % for SOSEX(W, v_c) and 19 % for SOSEX($W(0), W(0)$). This can be rationalized by observing that for large electron-electron distances the correlation contributions to the interaction energies quickly decay to zero. This is shown in figure 5.12 where we have plotted three of the RPA+SOSEX(W,v_c) potential energy curves (Green curves in the upper plots) in the S66x8 database and separated the correlation contributions (The Green curves are the sums of the red and yellow curves). The lower plots separately show the RPA and SOSEX(W,v_c) contributions to the correlation energy differences.

In all three plots, the potential energy curves are dominated by the difference of the correlation energy of the dimer and the sum of correlation energies of the monomers. Therefore, the approximation used for the calculation of the correlation energy plays a large role. However, this difference quickly goes to zero for larger separations. At two times of the equilibrium distance, the correlation contributions to the potential energy curves are almost zero in all three considered examples. Therefore, the expression used for the correlation energy becomes less and less important with increasing monomer separation. This argument also holds if one expresses the contributions in % of the total interaction energy.

One would expect the SOSEX contribution to decay faster than the RPA one, since the former is of exchange nature and therefore fundamentally short-ranged.[298] However, the plots in the lower part of figure 5.12 shows that this is only the case for the potential energy curve on the right, but not for the two curves on the left, where SOSEX and RPA contributions seem to decay equally fast.

In conclusion, we have here assessed the accuracy of the SOSEX($W(0), W(0)$) correction to RPA correlation energies for a wide range of chemical problems including bond dissociation, thermochemistry, kinetics, and non-covalent interactions. In situation where the addition of SOSEX(W, v_c) leads to major improvements over the RPA, the addition of SOSEX($W(0), W(0)$) does as well. This is the case for the calculation of ionization potentials and electron affinities where RPA+SOSEX approaches challenge the accuracy of modern double-hybrid functionals.[638] Also for non-covalent interactions both SOSEX variants lead to the same substantial improvements over RPA. SOSEX(W, v_c) is most accurate for the hydrogen-bonded complexes while SOSEX($W(0), W(0)$) is slightly more accurate for dispersion interactions. We also showed that the frequency-dependence of the screened interactions does seem to be an important factor for hydrogen-bonding but not for dispersion interactions.

We have observed differences in both SOSEX variants for the dissociation of diatomic molecules. As RPA and unlike RPA+SOSEX(W,v_c),[385,647] RPA+SOSEX($W(0), W(0)$) dissociates the Hydrogen molecule correctly. RPA does so because the self-correlation error effectively describes static correlation.[647] The situation seems to be similar for RPA+SOSEX ($W(0), W(0)$) since in contrast to RPA+SOSEX(W,v_c) it is not completely self-correlation free for 1-electron systems. We have also shown that this qualitative difference is due to the screening of the second electron-electron interaction line.

The incomplete cancellation of self-correlation error does however negatively affect the dissociation of charged dimers for which RPA+SOSEX(W,v_c) fixes most of the deficiencies of RPA.[385,651] Here, RPA+SOSEX($W(0), W(0)$) performs even worse than RPA. Furthermore, the good dissociation of diatomic molecules does not automatically carry over to accurate barrier heights[654,655] where both SOSEX variants considerably worsen the RPA results.

Our results suggest that the statically screened SOSEX is a suitable alternative to dynamically screened SOSEX. While both formally scale as N^5 with system size, the computation of the SOSEX(W, v_c) correction requires a numerical imaginary frequency integration. The calculation of the SOSEX($W(0), W(0)$) correction is therefore much cheaper, comparable to MP2. MP2 is however inadequate for large molecules since it neglects screening effects entirely.[111,393] RPA+SOSEX($W(0), W(0)$) is in principle applicable also to large molecules. A stochastic linear scaling implementation of the SOSEX self-energy has already been developed[382] and a recent RPA+SOSEX implementation by Ochsenfeld and co-workers[668] allowed applications to the L7 dataset,[399] albeit with small basis sets. Other low-scaling MP2 implementations[669–671] could potentially be generalized to SOSEX as well.

Finally, it should be mentioned that the accuracy of the dynamically screened SOSEX correction to the RPA can be improved upon by the addition of renormalized single excitations.[299,334] Other methods which have been shown to outperform SOSEX, in particular for barrier heights,

are the AXK kernel method[341,651,672] or a SOSEX variant in which the terms of RPA and SOSEX beyond second order in v_c are scaled down.[672] It remains to be investigated whether the concept of static screening can also be combined with those approaches and leads to good results.

Chapter 6

Applications

In chapter 3, we have shown how the formalism developed in chapter 2 is translated into efficient algorithms for the calculation of charged and optical excitations of large molecules. In chapter 5, we have furthermore scrutinized the reliability of the implemented numerical approximations by means of detailed comparisons to other codes. We have then assessed the accuracy of the implemented algorithms for charged excitations and electron-electron interaction energies by comparison to reference results obtained from computationally more involved approaches (mostly high-level CC methods). Before concluding this thesis and in order to showcase both, the computational efficiency as well as the predictive power of the developed algorithms, we present applications to relatively large, biologically relevant systems: In section 6.1, we use the *GW* formalism to calculate ionization potentials of large DNA oligomers and in section 6.2 we calculate the low-lying excitonic states of a six-chromophore model of the photosystem II (PSII) reaction center (RC) with nearly 500 atoms and 2000 correlated electrons in total.

6.1 DNA

Oxidation of DNA is related to genetic damage[673] and to investigate the mechanisms behind these processes quantum chemically, electron addition and removal energies need to be computed with high accuracy. A necessary first step for such studies is the selection of appropriate model system which should represent DNA under physiological conditions as accurately as possible while still being computationally feasible. As an illustrative example how the new qs*GW* implementation can be used effectively in practice, we investigate the dependence of IP and EA of oligomers of Adenine-Thymine (AT) base pairs on the oligomer size.

6.1.1 Computational Details

The structures of the DNA fragments have been taken from ref.[669]. We performed qs*GW* calculations using the TZ2P[487], TZ3P and QZ6P basis sets, starting from a PBE0[192,193] initial guess.

We set the numerical quality to *VeryGood*, but used the *Good* auxiliary basis set, with the exception of the QZ6P calculations were we also used the *VeryGood* auxiliary basis set. We also set *MBPT.ThresholdQuality=Normal*. In ref.[36] we have shown that these thresholds are sufficient to converge quasi-particle energies within a few ten meV. 16 grid points in imaginary time and imaginary frequency have been used. Solvent effects have been accounted for exclusively on the KS level using the conductor like screening model (COSMO)[674–676] (see appendix A.2 for a brief introduction) as implemented in ADF[677] using the BLYP[187,678,679] functional with D3(BJ) dispersion correction and the TZ2P basis set. *Numericalquality Good* has been used. The solvent correction ΔE_s is then obtained as $\Delta E_s = E_s^{(+)} - E_s^{(0)}$, i.e. as the difference between the solvent contributions to the bonding energies of the oxidized species and the neutral species both at the equilibrium geometry of the neutral species.

6.1.2 Results

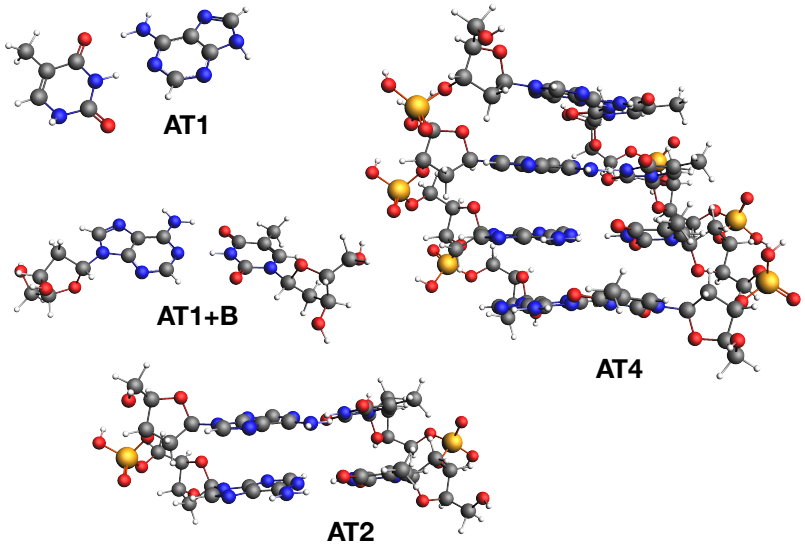

Figure 6.1: DNA model systems used in this work.

The calculated charged excitations are shown in table 6.1 for different basis sets and fragment sizes between 1 and 4 AT pairs (We refer to these systems as ATx, were x denotes the number of AT base pairs). These systems are shown in figure 6.1. For all fragments, we calculated the IPs with the TZ2P and TZ3P basis set with 1d1f, and 2d1f shells of polarization functions for 2nd and 3rd row atoms (and analogously for other atoms). We see, that going from TZ2P to TZ3P only has a small effect on the IPs and EAs, reducing the basis set incompleteness error by

	IP				EA			
calculation	AT1	AT1+B	AT2	AT4	AT1	AT1+B	AT2	AT4
TZ2P		7.84	7.34	6.94		-0.84	-0.65	-0.45
TZ3P	8.47	7.90	7.35	6.97	-0.41	-0.80	-0.63	-0.40
QZ6P	8.50	7.96			-0.26	-0.62		
extra	8.55	8.04	(7.49)	(7.11)	-0.07	-0.38	(-0.21)	(0.02)
Δsol.	1.82	-0.99	-0.52	-0.01	1.55		1.87	1.62
$\epsilon + \Delta$sol.	6.73	7.05	6.97	7.10	1.62		1.66	1.64

Table 6.1: Ionization potentials (IPs) and electron affinities (EAS) of DNA fragments consisting of different numbers of adenine-thymine base pairs calculated with different basis sets and contributions of solvent from ΔBLYP calculations. Extra(TQ) denotes extrapolation to the CBS limit based on TZ3P and QZ6P calculations and numbers in parentheses are obtained by adding the difference between $\epsilon_i^{CBS} - \epsilon_i^{TZ3P}$ to the result obtained at the TZ3P level. Δsol. has been calculated using COSMO. All values are in eV.

only a few ten meV. These calculations with two rather similar basis sets are necessary to rule out the possibility that a result is simply an artefact of a chosen basis set. Going from TZ3P to QZ6P, the IP of the AT1+B increases by a modest 60 meV, while the EA reduces by 180 meV. Based on the TZ3P and QZ6P calculations, we can estimate the QP energies at the CBS limit by extrapolation. Comparing the TZ3P results to the extrapolated ones, we find a basis set limit incompleteness error of 140 meV for the IP and of 420 meV for the EA of AT1. For AT1, we find a similar basis set limit incompleteness error of 80 meV for the IP and of 340 meV for the EA.

On standard hardware, calculations on the QZ level are not feasible for AT4 and already for AT2, the QZ calculation is cumbersome. This is not only due to the large number of diffuse AOs which make makes it difficult to exploit distance-based cut-offs[36] but also due to the large auxiliary basis sets which are required to make the calculations numerically stable. However, we can estimate the CBS limit based on the differences between the QP energies at the CBS limit and the largest affordable basis set for the larger systems for the smaller fragments. This is justified with the observations made in ref.[36] for G_0W_0 were we found the basis set incompleteness error on average to decrease with increasing system size[36] but only to a certain extent since basis functions are localised. Based on this assumption, we correct the IPs and EAs of AT2 and AT4 on the TZ3P level by the basis set limit incompleteness error found for AT1+B. (140 meV and 420 meV, respectively). There is of course a small uncertainty due to the different basis set errors for AT1 and AT1+B. For the extrapolation itself, we assume the error to be rather small for the IP, since the difference between TZ3P and QZ6P are rather small. For the EAs, the error might be larger. Still, we can safely assume, that the basis set errors for AT2 and AT4 are below 100 meV.

The energy required to remove or add an electron from a DNA oligomer in vacuum is strongly size dependent: The vertical IP in vacuum decreases rapidly with increasing oligomer size, with a difference of almost 1 eV between AT1 and AT4. For the EA, a difference of 0.4 eV is found. The

IPs of the solvated DNA oligomers, on the other hand, are almost independent of the number of base pairs. When an electron is removed from the oligomer, the surrounding cloud of electrons stabilizes the resulting hole. Increasing the oligomer size thus reduces the IP potential since the hole becomes more and more stabilized. In the aqueous environment, the solvent plays the same role and consequently, the inclusion of water via the COSMO effectively compensates for the effect of the DNA environment. Of course, the comparison is slightly skewed since the DNA environment and the solvent are not treated at the same level of theory. However, there is some evidence that COSMO and other polarizable continuum models are fairly accurate in describing the dielectric screening properties of water[680].

The IP of AT1+B, AT2, and AT4, all agree within 130 meV. In light of possible basis set errors and errors of the qsGW method itself, the difference is well within the error margin of our method. Only for AT1 we obtain a significantly lower IP, which indicates that the DNA backbone apparently plays an important role in stabilizing ionized DNA oligomers. For the EAs, we arrive at the same conclusion. The differences between the considered systems are even smaller, the aqueous EAs of AT1, AT2 and AT4 being with 1.62, 1.66 and 1.64 eV in excellent agreement. Recently, Pluhařová et. al.[673,681,682] also concluded that the effect of the DNA environment on the IPs of individual aqueous nucleobases seems to be modest. On the BMK[683]/6-31G* level of theory, they obtained an IP of 7.24 eV for a fragment of 2 solvated AT base pairs including backbone from the Dickerson dodecamer, but for the isolated AT base pair, they obtained and IP of 7.58 eV. The first number is in good agreement with ours, while the second one differs from our result for AT1 by almost 1 eV. However, the difference of only 340 meV between both fragments is of the same order as our difference between the IPs of AT1 and AT2 of 260 meV. Thus, our conclusions regarding the role of the explicit inclusion of the DNA environment on the calculated IPs are very similar.

In conclusion, we have shown that IPs and EAs of the considered DNA oligomers in vacuum are strongly size-dependent. Upon taking into account the effect of the aqueous environment, the QP energies become almost independent of the system size. This confirms the results of previous DFT studies.[673,682]

6.2 Chlorophylls

The absorption of photons by a molecule or a material upon interaction with electric radiation is a key process in the conversion of light into chemical or electrical energy. In the photosystem II (PSII) reaction center (RC), photons are captured by chromophoric complexes which then leads to the generation of free charge carriers.[684] In the first step of this process an electron-hole pair is formed, where electron and hole are bound due to their Coulombic interaction.[3] Such bound electron-hole states are commonly referred to as excitons and correspond to the energies of the absorbed photons.[685] In the current work we look at the characterization of such low-lying excited states of the RC of PSII which is at the heart of photosynthetic function.[686] As shown in figure 6.2, the PSII RC comprises six chromophores, a "special pair",[687,688] of two Chlorophyll a

(chla) molecules (P_{D1} and P_{D2}), flanked by two more chla (Chl_{D1} and Chl_{D2}) and two Pheophytin ($Pheo_{D1}$ and $Pheo_{D2}$) molecules, with around 2000 electrons in total. By now, it has been firmly established that the primary events of charge separation in PSII are determined by a complex interplay of all these six chromophores.[689] Therefore, all six chromophores should ideally be treated on a quantum mechanical level and their couplings need to be taken into account.

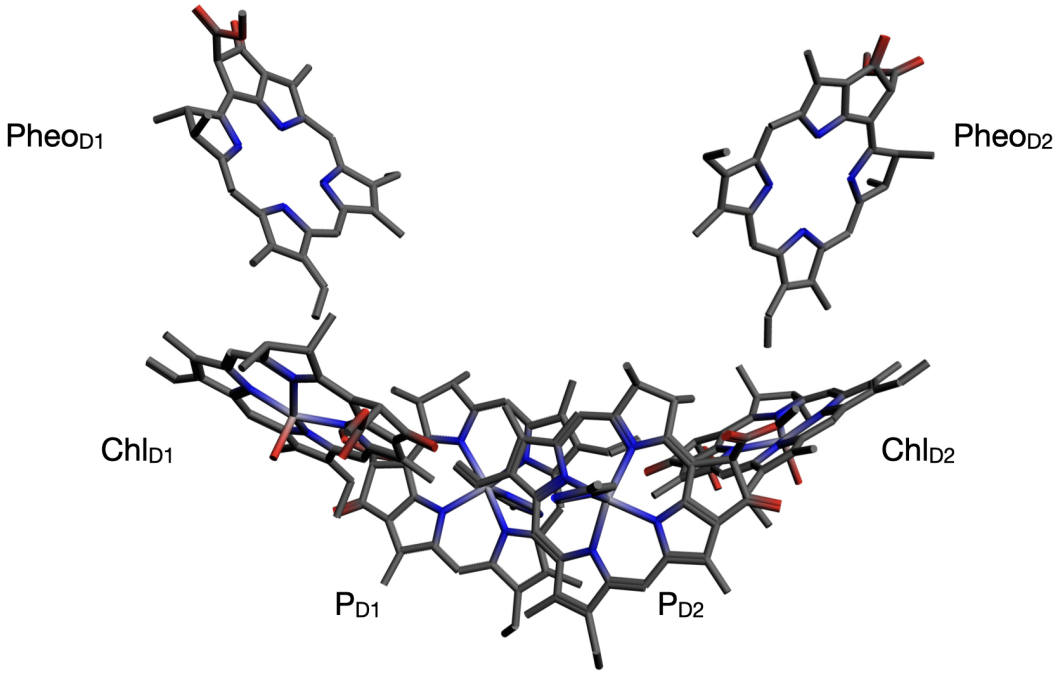

Figure 6.2: Chromophores of the Photosystem II reaction center.

In most current calculations of larger biomolecular complexes, one resorts to Hartree-Fock (HF)[690,691] or Time-dependent (TD) Density Functional Theory (DFT) with a range-separated hybrid (RSH) exchange-correlation kernel[689,692–696]. RSHs frequently offer good agreement with experiment for Chla monomers and dimers,[695,697,698] but also large deviations to more advanced multi-configurational[698,699] and wave-function based methods have been reported.[700] To mitigate such errors, RSHs can be parametrized empirically for each system under investigation (as for example done in references in[701] and[702]), but this makes them non-transferable and unreliable for general applications. More systematic parametrization procedures for range-separated functionals have been suggested as well[201–204] which always require to perform exploratory calculations to find the ideal range-separation parameter. Furthermore, heterogeneous systems like large complexes of Chromophores might require different range separation parameters for different parts of the complex.[206]

Turning to wave-function based methods for excited states, we find the second-order algebraic

diagrammatic construction scheme (ADC(2))[703,704] and coupled cluster[62–66] with approximate doubles (CC2)[705] easy to apply and reasonably cost-efficient. CC2 results are typically in good agreement with more involved methods like equation-of-motion (EOM) CC[706] with singles and doubles (EOM-CCSD) or similarity-transformed (ST) EOM[707,708]-CCSD[709,710]. For these methods we are aware of one study of a tetrameric model by Suomivuori et al.[711] using ADC(2) together with the spin-opposite-scaled[712] and reduced-virtual-space (RVS)[713] approximations. Unfortunately, they did not include the Pheophytin chromophores in their calculations, which are known to play a key role in the initial charge separation immediately after photoexcitation.[696,714–716] This is potentially possible, but we note that most applications of wave-function based methods[698,700,717,718] focus on single chromophores. Utilizing subsystem methods[719–725] the applicability of these methods can be extended. In this family of methods one describes the full RC by an effective Hamiltonian with a limited amount of levels for each chromophore. The information needed to build such an effective Hamiltonian are the monomeric excitation energies as well as the inter-monomeric couplings. These parameters can be computed in a first principles manner with various electronic structure methods[726–728]. While the subsystem approach can be used with high-level monomer calculations, a drawback is that commonly used approximations to calculate the couplings between the chromophores are often not accurate enough.[697,713,729] In the current work we will therefore examine how a large system can be treated directly without having to resort to partitioning and subsystem methods. As the states of interest are the lowest energy ones, we thereby focus on a limited number of states, but describe them in a supermolecular fashion that fully accounts for all intermolecular couplings of the chromophores.

Our approach is based on the BSE@*GW* method which has recently been shown to reproduce experimental low-lying excitation energies of Chls with high accuracy.[268,730] So far, it has only been applied to monomeric models of PSII.[268,730] In section 6.3 we first contrast the qs*GW* method to ev*GW* for monomers and then confirm the excellent agreement with experiment and other quantum chemical calculations for both methods. We then use the BSE@qs*GW* implementation to calculate the low-lying excitation of the hexameric complex. Finally, section 6.3 summarizes and concludes this work.

6.2.1 Computational Details

All calculations have been performed with a locally modified development version of ADF2022.1[496,731] Unlike in all other calculations reported in this thesis, the projection technique outlined in section 3.1.3 has been used here.

For the hexameric unit of PSII, we used the structure of ref. [732] which has been optimized at the PBE level of theory taking into account environment effects using a QM/MM approach. Dimer structures have been optimized in this work using CAM-B3LYP-D3(BJ), a triple-ζ + polarization (TZP)[487] basis set and *Good* numerical quality. The monomer structures used in section 6.3.1 and sec. 6.3.2 are taken from the structure by ref. [694] based on the experimental structure at 1.9 Å resolution by Umena et al.[733] and where the positions of the Hydrogen atoms have been optimized using a semi-empirical model with all other coordinates frozen. All

structures used in this work can be found in the supporting information of ref. [39].

We also benchmarked the basis set dependence of the BSE@*GW* calculations using the larger TZ3P and QZ6P basis sets[37] for Chla monomers in section 6.3.2. All BSE@qs*GW* results shown there have been obtained with the *veryGood* auxiliary basis. This allows us to reliably compare excitation energies obtained with different primary basis sets. TZ3P and QZ6P contain *f*-functions for second-row atoms and for such basis sets, the *Good* auxiliary fit set is generally insufficient. For monomers, we calculate the lowest 3 eigenstates of (3.194).

For chromophore dimers we calculated the lowest 6 eigenstates of (3.194), using TZP (triple-ζ + polarization)[487] as primary basis set, *Good* numerical quality and 16 imaginary time and frequency points each. In all calculations for monomers and dimers we terminate the sequence of subspace iterations if all eigenvalues are converged within 10^{-5} Hartree (0.27 meV).

In the BSE@*GW* calculations of the excited states of the hexamer, we used the TZP basis set, *Basic* numerical quality, and 12 imaginary time and frequency points each. We restrict the basis in which we solve the BSE to the subspace spanned by all particle-hole pairs with transition energies below 1.5 Hartree. In agreement with earlier BSE@*GW* studies for such systems,[288] we found this approximation to change the low-lying excitation energies by only around 10-20 meV compared to calculations including all particle-hole pairs. For instance, changing the cut-off for the inclusion of the particle-hole states from 1.5 to 2.0 Hartree changes each of the lowest three excitation energies of monomers by less than 10 meV. This improves numerical stability of our algorithm and accelerates the convergence of the subspace iterations in the Davidson algorithm. We perform eight subspace iterations in the Davidson algorithm and calculate the 24 lowest eigenstates of (3.194). This is sufficient to converge the low-lying excited states to within less than 5 meV. We also calculated the low-lying excited states of the same system using TD-DFT with the ωB97-X kernel using the same numerical settings. However, in contrast to our BSE@*GW* calculations, we calculated the 12 lowest states and converged all eigenvalues to within 10^{-6} Hartree.

In all calculations we took into account scalar relativistic effects in the zeroth-order regular approximation.[619–621] The threshold ϵ_s described in appendix 3.1.3 has been set to 5×10^{-3}. Also, in all KS calculations we set the threshold below which we set eigenvalues of the inverse of the overlap matrix to zero during he canonical orthonormalization procedure to 5×10^{-3}. If not stated otherwise, in all qs*GW* calculations we first perform a PBE0 calculation with 40 % exact exchange (PBEH40), which is a good preconditioner for qs*GW* and leads to fast convergence.[248] Aside from numerical inaccuracies, the final results are independent of this choice which we have verified in ref. [38] and which we will verify also for the case of Chla in the next section. For qs*GW*, we terminate the calculations when the Frobenius norm of the difference between the density matrices of two subsequent iterations falls below 5×10^{-9}.[38] We also performed BSE@ev*GW* calculations based on the LDA and PBEH40 functionals (ev*GW*@LDA, ev*GW*@PBEH40). We terminate the ev*GW* calculations if the HOMO QP energy difference between two subsequent iterations falls below 3 meV.

To compare our method to the RSH TD-DFT approach, we also performed calculations using the CAMY-B3LYP and ωB97-X kernel using the TZP basis set and *Good* numerical quality. We

also calculated the electrochromatic shifts due to the presence of the protein environment using the conductor like screening model (COSMO)[674–676] as implemented in ADF.[677] Following ref. [711], we set the dielectric constant of the environment to a value of 4.0 in these calculations which should approximately account for solvent and protein environment.

6.3 Results

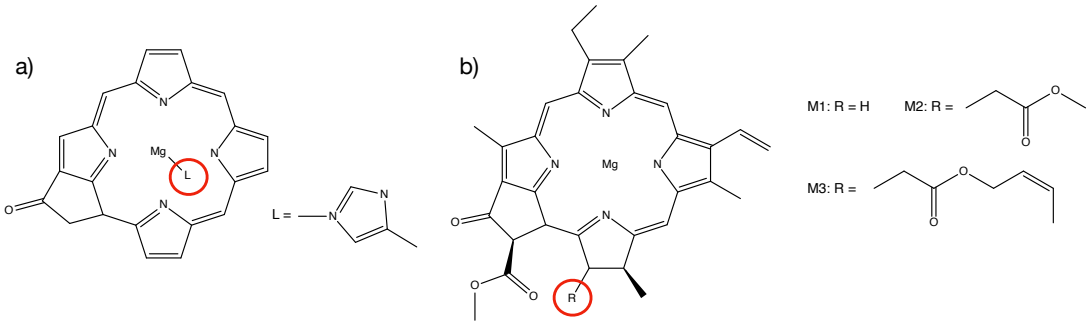

Figure 6.3: Different models of Chla used in this work: a) Model used by Suomivuori et al.[711] with ligating Histidine residue. b) Models without Histidine residue but containing all ligands at the chlorin core and different models for the phytyl chain (M1, M2, and M3, respectively).

6.3.1 Starting-point dependence

As discussed in the previous chapters, its starting point independence is a major advantage of qsGW over evGW. To verify the starting point independence of our implementation also for BSE@qsGW calculations, we report here vertical excitation energies (VEE) for qsGW and evGW for the M2 model in figure 6.3b) with 82 atoms in total for the LDA, PBE, PBEH40, and HF starting points. We thereby use a tighter convergence criterion of 1 meV for the HOMO QP energy for evGW than the default value. The results for the Q_y excitation are shown in table 6.2. The qsGW calculations converge to the same HOMO-LUMO gap within an accuracy of 10 meV within less than 10 iterations. This also results in Q_y excitation energies which are converged within 10 meV. The remaining differences are due to numerical noise in the imaginary frequency and time grids used in the GW calculations which then translates into uncertainties in the analytical continuation of the self-energy to the complex plane.[37,269] The differences in the HOMO-LUMO gaps of the evGW calculations are much larger and differ by almost 300 meV between evGW@LDA and evGW@HF, which results in Q_y excitations energies differing by about 80 meV. This is the most extreme case, for starting points other than HF there are only very small differences between the different evGW results. This has already been observed in ref. [268]. Since the computational overhead of a qsGW calculation is negligible compared

to evGW (5.79 vs. 5.67 core hours per iteration) and the number of iterations needed for convergence is essentially the same, there is little advantage to be gained by using evGW instead of the more robust qsGW approach.

	evGW				qsGW			
	gap	Q_y [eV]	n_I	t [h]	gap	Q_y [eV]	n_I	t [h]
LDA	4.405	1.764	9	5.67	4.499	1.752	9	5.79
PBE	4.417	1.837	9	-	4.501	1.745	10	-
PBEH40	4.476	1.772	7	-	4.493	1.760	8	-
HF	4.671	1.766	9	-	4.496	1.753	9	-

Table 6.2: HOMO-LUMO gap, Value of the Q_y excitation for different starting points, number of iterations until convergence and time per GW iteration, measured in core hours, for qsGW and evGW. Calculations were performed on a 2.2 GHz intel Xeon (E5-2650 v4) node (broadwell architecture) with 24 cores and 128 GB RAM.

6.3.2 Basis Set Errors

	BSE@evGW@LDA						BSE@qsGW					
	M1			M2			M1			M2		
	Q_y	Q_x	B	Q_y	Q_x	B	Q_y	Q_x	B	Q_y	Q_x	B
TZP	1.74	1.93	2.68	1.76	1.94	2.71	1.72	1.98	2.84	1.74	2.00	2.86
TZ3P	1.77	1.96	2.72	1.79	1.98	2.76	1.72	1.98	2.84	1.73	1.97	2.84
QZ6P	1.71	1.94	2.64	1.74	1.92	2.68	1.71	1.96	2.80	1.71	1.96	2.84
Δ_{TQ}	0.03	-0.01	0.04	0.02	0.02	0.03	0.01	0.02	0.04	0.03	0.04	0.02

Table 6.3: VEEs for M1 and M2 with different basis sets for BSE@qsGW and BSE@evGW@LDA. The values in the last row denote the differences in VEEs calculated with the TZP[487] and QZ6P[37] basis sets. All values are in eV.

Next, we investigate the dependence of the Q_y excitation energy on the basis set size. For GW calculations it is well known that individual QP energies converge slowly with respect of the size of the single-particle basis. In practice, extrapolation techniques are needed to obtain converged results.[545,598,599] For orbital energy differences which are entering the BSE, the situation is much better since the basis set error for the QP energies usually have the same sign.[598] In table 6.3 we compare the lowest excitation energies calculated with different basis sets for the two different Chla models M1 and M2 shown in figure 6.3b). For evGW and qsGW the QZ6P VEEs are only slightly lower than the TZP ones, indicating that they are almost converged also with the smaller basis set. These errors are certainly smaller then other possible sources of error in our calculations like shortcomings of BSE@GW or uncertainties in structural parameters. Therefore, to a very good approximation, we can ignore the basis set incompleteness error in all of the following TZP calculations.

6.3.3 Comparison to Experiment and different *ab-initio* Calculations

Monomers

Next, we assess the accuracy of BSE@qsGW by comparison to experimental gas-phase data for Chla by Gruber et al.[734] In table 6.4 we directly compare VEEs calculated with different computational methods to the experimental VEE which has recently been extracted from the experimental spectrum by Sirohiwal et al.[717]. The domain based local pair-natural orbital[414,415] (DLPNO)-STEOM-CCSD[735–737] results are taken from ref. [717], while the BSE@evGW@LDA/6-311++G(2d,2p) results calculated using MOLGW[542] are by Hashemi and Leppert.[268] Two different, gas-phase optimized structures have been used: One has been optimized at the CAM-B3LYP-D3(BJ)/def2-TZVP level of theory by Sirohival et al.[717], while the other has been optimized by Hashemi and Leppert using B3LYP/def2-TZVP.

	Q_y	Q_x	B	$\Delta_{Q_y-Q_x}$
exp. (VEE)	1.99	2.30	3.12	0.31
exp. (band max)	1.94	2.23	3.08	0.29
CAM-B3LYP-D3(BJ)/def2-TZVP optimized structure				
DLPNO-STEOM-CCSD	1.75	2.24	3.17	0.49
qsGW	1.97	2.29	3.15	0.32
evGW@PBEH40	1.98	2.29	3.15	0.31
evGW@LDA	1.94	2.20	3.01	0.26
CAMY-B3LYP	1.94	2.23	3.08	0.29
ωB97-X	2.10	2.71	3.57	0.61
B3LYP/def2-TZVP optimized structure				
BSE@evGW@LDA (ADF/TZP)	1.85	2.09	2.91	0.24
BSE@evGW@LDA (MOLGW/6-311++G(2d,2p))	1.85	2.13	2.91	0.28

Table 6.4: VEEs for Chla calculated with different quantum chemical methods for two different gas-phase optimized structures and experimental reference data. All values are in eV.

We performed BSE@evGW@LDA calculations for both structures. Our results for the CAM-B3LYP-D3(BJ) optimized structure are consistently around 0.1 eV lower than the ones for the B3LYP optimized structure. This illustrates the large influence of small changes in structural parameters on the final excitation energies. However, CAM-B3LYP has been shown to describe the structural features of Cholorpyll monomers very well.[717,738] For the B3LYP optimized structure, we can compare our herein calculated VEEs to the ones from Hashemi and Leppert calculated on the same level of theory. Except for the Q_x excitation energies which are slightly different (40 meV), we find perfect agreement between both implementations.

All evGW results agree very well with qsGW also for Chla. All BSE@GW results for the CAM-B3LYP-D3(BJ) optimized structure are in excellent agreement with the experimental values. For instance, the BSE@qsGW VEEs agree all with the experimental VEEs within 30 meV. On the other hand, DLPNO-STEOM-CCSD not only severly underestimates the Q_y excitation energy, but it also overestimates the gap between both Q-bands, $\Delta_{Q_y-Q_x}$, considerably. Con-

sidering this difference, we note that STEOM-CCSD is not necessarily a reliable reference for qsGW. In STEOM-CCSD, a much larger number of diagrams is considered in the single- and two-particle Green's functions compared to GW.[612] QP approximations to GW approximate the effect of these diagrams instead by neglecting the vertex.[142] The diagrams contained in GW are not a subset of the ones contained in EOM-CCSD but only of the ones contained in EOM-CCSDT.[612] Accounting for excitations to triples (at least to some extent) is known to be of high importance for the reliable description of charged[646] and neutral excitations.[709,710,739] Consequently, STEOM-CCSD shows mean signed errors compared to EOM-CCSDT calculations of around 0.1 eV for a set of medium organic molecules, but errors can be as large as 0.5 eV in some cases.[709] Moreover, apart from the neglect to triple excitations, the DLPNO approximation can also introduce some artifacts. The pairs which are treated on the CC level are selected based on an MP2 calculation[415] which is not always reliable for systems with strongly screened electron-electron interactions.[112,393]

Lastly, TD-DFT with the RSH kernels CAMY-B3LYP and ωB97-X which are typically used in computational studies of the PSII RC[693–695,732] give very different results. CAMY-B3LYP is actually in excellent agreement with experiment and the BSE@GW calculations, while ωB97-X gives much too high excitation energies and also massively overestimates the $\Delta_{Q_y-Q_x}$.

Dimers

	Ω_1	Ω_2	Ω_3	Ω_4	Ω_5	Ω_6
exp. (VEE)[740]	1.95	(estimated)				
exp. (band max)[740]	1.90					
B3LYP-D3(BJ)/def2-SVP optimized structure[a711]						
qsGW	1.89	1.92	2.07	2.10	2.83	2.92
evGW@PBEH40	1.92	1.95	2.09	2.11	2.84	2.93
evGW@LDA	1.87	1.88	1.90	1.90	2.72	2.75
CAMY-B3LYP	2.12	2.15	2.29	2.32	2.63	2.76
RVS-LT-SOS-ADC(2)[b]	2.04	2.06				
CAM-B3LYP-D3(BJ)/TZP optimized structure[c]						
qsGW	1.94	1.98	2.25	2.28	2.56	2.68
evGW@PBEH40	1.97	2.02	2.24	2.27	2.58	2.67
evGW@LDA	1.98	1.99	2.16	2.22	2.51	2.64
CAMY-B3LYP	2.12	2.16	2.38	2.43	2.51	2.61
ωB97-X	2.05	2.10	2.63	2.68	3.10	3.27

Table 6.5: The lowest six excitation energies for two different models of the Chla dimer. All values are in eV.[a,b,c]

[a]The B3LYP-D3(BJ)/def2-SVP structure has been taken from Suomivuori et al.[711].
[b]Results taken from Suomivuori et al.[711].
[c]The structure of the M3 dimer has been optimized in this work at CAM-B3LYP-D3(BJ)/TZP.

In table 6.5, we show the low-lying excitations of BSE@GW calculations for different models of P_{D1}-P_{D2}. The first dimer structure has been optimized in the gas phase by Suomivuori *et al.*

at the B3LYP-D3/def2-SVP level of theory and consists of two Chla monomers whose structure is shown in figure 6.3a. This structure lacks most substituents of the Chlorin core present in Chla (see figure 6.3b which, in principle, complicates comparison of excitation energies to experimental results. However, these calculations give some indication on the performance of BSE@GW in comparison to the RVS-LT-SOS-ADC(2) VEEs by Suomivuori *et al.* Comparison of experimental band maximum and VEE for a single Chla measured in ref. [734] suggests that the VEE of the chlorophyll dimer might be around 1.95 eV (50 meV higher than the band maximum).

	evGW@LDA				evGW@PBEH40			
	VEE	character	weight	f	VEE	character	weight	f
Ω_1	1.87	$238 \rightarrow 240$	0.49	0.08	1.92	$238 \rightarrow 240$	0.28	0.30
						$237 \rightarrow 239$	0.26	
Ω_2	1.88	$237 \rightarrow 240$	0.22	0.14	1.95	$238 \rightarrow 241$	0.41	0.03
		$237 \rightarrow 239$	0.17			$237 \rightarrow 239$	0.34	
Ω_3	1.90	$236 \rightarrow 239$	0.38	0.13	2.09	$235 \rightarrow 239$	0.53	0.04
Ω_4	1.90	$237 \rightarrow 240$	0.37	0.00	2.11	$236 \rightarrow 240$	0.49	0.03
		$235 \rightarrow 239$	0.31					
Ω_5	2.72	$238 \rightarrow 239$	0.51	0.37	2.84	$238 \rightarrow 239$	0.56	0.24
Ω_6	2.75	$237 \rightarrow 239$	0.27	0.14	2.93	$237 \rightarrow 240$	0.31	0.20
		$237 \rightarrow 242$	0.24					

Table 6.6: Characterization and comparison of the low-lying excited states of Chla dimer (structure by Suomivuori et al.[711]) calculated with BSE@evGW@LDA and BSE@evGW@PBEH40.[a]
[a]Shown are the excitation energies Ω_S (in eV), the dominant coefficients of the corresponding eigenvector and the associated particle-hole transitions, as well as the oscillator strengths f.

As for the monomer, the BSE@GW results are in excellent agreement with these values while the RVS-LT-SOS-ADC(2) VEEs are much too high. In contrast to the case of the Chla monomer, CAMY-B3LYP overestimates the VEEs by far. The VEEs Ω_3 and Ω_4 of the BSE calculation based on evGW@LDA are almost 0.2 eV lower than the ones based on evGW@PBEH40, and in the former calculation, the four lowest excited states are almost degenerate. The character of these excitations are compared in more detail in table 6.6 with the corresponding KS single-particle orbitals shown in figure 6.4. Comparison of the most important contributions to the eigenvector $|\mathbf{X}, \mathbf{Y}\rangle_1^T$ already shows that BSE@evGW@LDA predicts the lowest excitation to be localized on the P_{D1} fragment, while in the BSE@evGW@PBEH40 calculation it is delocalised over both monomers with almost equal weights. Using BSE@evGW@LDA, the second excited state has a large contribution of a particle-hole transition located on P_{D1}, while it is localized on P_{D2} using BSE@evGW@PBEH40. Also, the oscillator strengths in table 6.6 show that the different excitations differ substantially in their brightness. Together with the large difference in some of the VEEs, this shows that different KS starting points can lead to different excitations, even when the eigenvalues are updated self-consistently.

In table 6.5, we also show results for a more realistic model of the Chla dimer. Our model consists of two M3 monomers which includes the first four segments of the phytyl chain in stacked conformation. In table S1 of the supporting information of ref. [39], we show that the final excitation energies are however very insensitive to the particular structural model.

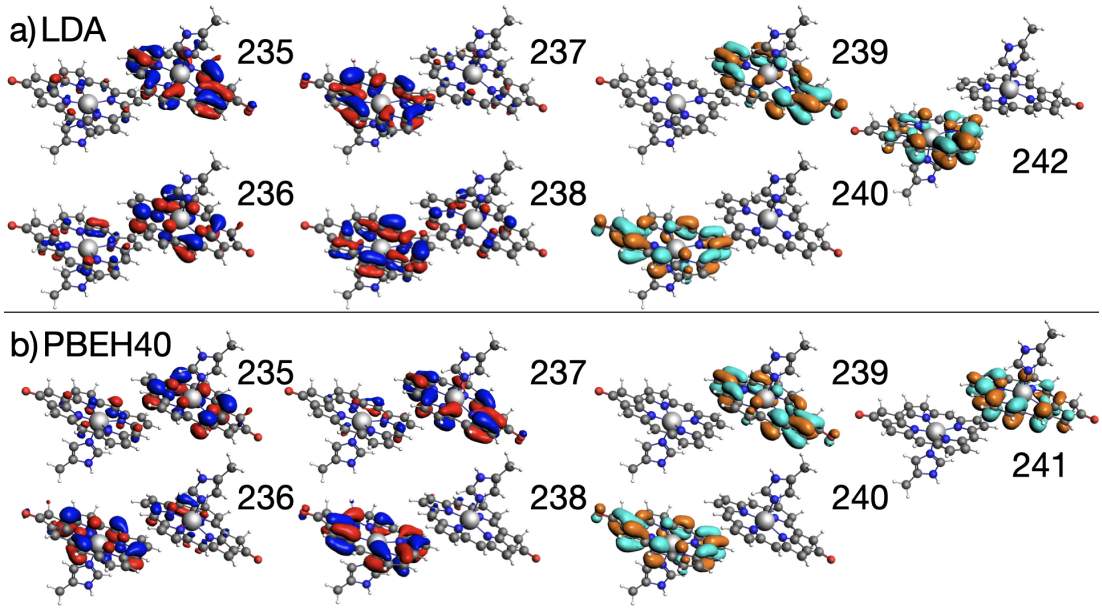

Figure 6.4: Selected valence single-particle KS orbitals for the Chla dimer (structure by Suomivuori et al.[711]) calculated using LDA and PBEH40.

The band maximum of ref. [740] which we used as reference has been measured for a charge tagged dimer. However, as shown in ref. [741] for Chla monomers, the final excitation energies are insensitive to the type of charge tag and omitting the charge tag entirely only results in a lowering of the excitation energies of around 30-40 meV.

The excitations have been calculated for a geometry optimized at the CAM-B3LYP/TZP level of theory. Excitation energies for geometries optimized with different methods can be found in table S2 of the supporting information of ref. [39]. In accordance with ref. [717] and our results shown in table 6.4 we found the VEEs to be very sensitive to the choice of the functional chosen for geometry optimization. For instance, using PBE-D4/TZP lowers the lowest 2 excitation energies by around 0.1 eV with respect to the CAM-B3LYP-D3(BJ) optimized structure. The data shown in table S3 in supporting information furthermore demonstrates that VEEs for crystal structures considerably underestimate the experimental values.

The lowest BSE@qsGW excitation energy of 1.94 meV is again in excellent agreement with the VEE of 1.95 eV estimated from the band maximum. As explicitly shown in the supporting information of ref. [39] and as for the monomers in table 6.3, the excitation energies are again rather insensitive to the basis set. Also notice that the remaining small basis set errors will largely cancel with the small error from omitting the charge tag. Again, the lowest two BSE@evGW VEEs are in excellent agreement with the BSE@qsGW one and each other, while there are larger differences in higher-lying VEEs. As for the monomer, CAMY-B3LYP massively overestimates

the VEEs compared to experiment.

6.3.4 Six-chromophore model of the PSII RC

	VEE	f	Character	weight
Ω_1	1.89	0.22	$P_{D2}{}^*$	0.39
			$Chl_{D2}{}^*$	0.22
Ω_3	1.90	0.77	$P_{D2}{}^*$	0.24
			$P_{D1}{}^*$	0.14
			$Pheo_{D2}{}^*$	0.09
			$P_{D1}{}^+$ - $P_{D2}{}^-$	0.09
Ω_3	1.91	0.04	$Chl_{D1}{}^*$	0.30
			$P_{D1}{}^*$	0.24
			$Chl_{D1}{}^+$ - $Pheo_{D1}{}^-$	0.08
Ω_4	1.92	0.22	$Pheo_{D2}{}^*$	0.39
			$Chl_{D2}{}^*$	0.16
			$Pheo_{D2}{}^*$	0.12
			$Chl_{D1}{}^*$	0.09
Ω_5	1.94	0.01	$Chl_{D1}{}^*$	0.23
			$Chl_{D2}{}^*$	0.18
			$P_{D1}{}^*$	0.16
			$P_{D2}{}^*$	0.15
Ω_6	1.97	0.20	$Pheo_{D1}{}^*$	0.54
			$Pheo_{D1}{}^-$ - $Chl_{D1}{}^+$	0.21
Ω_{13}	2.71	0.00	$P_{D2}{}^+$ - $Chl_{D2}{}^-$	0.81
			$P_{D1}{}^+$ - $Chl_{D2}{}^-$	0.13
Ω_{14}	2.73	0.00	$P_{D1}{}^+$ - $Chl_{D1}{}^-$	0.70
			$P_{D1}{}^+$ - $Pheo_{D1}{}^-$	0.20

Table 6.7: The lowest BSE@qsGW/TZP excited states of the hexameric chromophore complex in the RC of PSII.[a].

[a]Shown are the excitation energies Ω_S (in eV), the dominant coefficients of the corresponding eigenvector and the associated particle-hole transitions, as well as the oscillator strengths f.

The most complete model of the PSII RC we consider in this work comprises all six chromophores shown in figure 6.2 with 476 atoms in total. Time-resolved spectroscopic experiments[714–716] show that the primary electron transfer in the RC occurs from an exciton localized on Chl_{D1} to $Pheo_{D1}$, followed by a transfer of the hole to P_{D1}. This would point to the presence and possible mixing in of low-lying CT states with pronounced $Chl_{D1}{}^+$ -$Pheo_{D1}{}^-$ and $P_{D1}{}^+$ -$Pheo_{D1}{}^-$ character in calculations of excitation energies. In previous TD-DFT calculations using RSH kernels for similar multi-chromophoric models, no low-lying CT state which could be related to this charge separation pathway have been observed.[693,732] In recent computational studies, both Sirohiwal et al.[689,732] and Tamura et al.[696] demonstrated that the protein environment is crucial for observing the $Chl_{D1}{}^+$ -$Pheo_{D1}{}^-$ CT state at low energies.

	BSE@qsGW		BSE@qsGW@PBEH40		TD-DFT@ωB97-X	
	VEE	f	VEE	f	VEE	f
Ω_1	1.89	0.22	1.94	0.81	1.92	0.33
Ω_2	1.90	0.77	1.94	0.32	1.93	0.64
Ω_3	1.91	0.04	1.96	0.05	1.94	0.14
Ω_4	1.92	0.22	1.97	0.24	1.96	0.18
Ω_5	1.94	0.01	1.99	0.15	1.97	0.09
Ω_6	1.97	0.20	2.00	0.11	1.98	0.07

Table 6.8: The VEEs and oscillator strengths of the six lowest excited states of the hexameric complex at different levels of theory. All values are in eV.

The low-lying excitations of the hexameric complex at the BSE@qsGW/TZP level of theory are characterized in table 6.7. In the supporting information of ref. [39] we characterize these excitations in more detail by visualizing the involved single-particle qsGW orbitals. We also present results of our own TD-DFT calculations using the ωB97-X kernel as well as for BSE@evGW@PBEH40/TZP. The excitation energies and the oscillator strengths of the six lowest excited states using these different methods are compared in table 6.8.

In agreement with past[693,732] and our own TD-DFT calculations using the ωB97-X kernel, only states with local character can be found among the six lowest excitations of the hexamer using both, BSE@qsGW and BSE@evGW@PBEH40. As shown in table 6.8, also the VEEs using the different methods agree within 50 meV. In all methods, the low-lying states are linear combinations of excitonic states involving the frontier orbitals on each chromophore.

At the BSE@qsGW level, the two lowest states with pronounced CT character can be found at 2.7 eV and these cannot directly be linked to charge separation pathways in PSII which have been observed experimentally.[714–716] Only the third excited state at the BSE@qsGW level of theory at 1.91 eV contains a contribution from a Chl_{D1}^{+} -$Pheo_{D1}^{-}$ particle-hole transition with a small weight, which is entirely absent in our TD-DFT and BSE@evGW calculations. Future studies at the BSE@GW level with inclusion of the environment electrostatics are needed to rationalize how the Chl_{D1}^{+} -$Pheo_{D1}^{-}$ CT state is influenced by the protein environment at the BSE@qsGW level.

Chapter 7

Conclusions

In this thesis, we have given an overview over MBPT based methods for the description of many-electron systems and their implementation in the STO based quantum chemistry code ADF. In chapter 2 we have summarized the theoretical foundations on which these methods are based, discussed the physical content of the canonical approximations and gave an overview over their strength and weaknesses for the description of electron interaction effects in finite systems. Combining theoretical rigor and a thorough discussion of practical aspects, chapter 2 provides a concise introduction to MBPT with a focus on the treatment of finite systems. The other chapters of this thesis combine three novel developments:

First, we have implemented the standard methods of MBPT using STOs and with low-order scaling with system size. These are MP2 and RPA methods for the calculation of correlation energies, the GW method for of single particle excitations, and the BSE@GW method for excitonic states. The numerical approximations we have thereby introduced have been described in chapter 3 and their precision has been assessed in chapter 4 *via* a detailed comparison of GW QP energies to ones from other quantum chemistry codes implementing the GWA with different basis set types and also making different choices regarding other technical parameters like frequency treatment, description of core electrons, the algorithm used to solve the QP equations, and the numerical treatment of 4-point correlation functions.

We have shown herein that it is possible, though difficult, to reach consensus between these implementations and ours. In light of the differences in the MBPT implementations, the observed agreement of QP energies between 55 to 85 meV on average for IPs between STO- def2-GTO- and plane-wave results is excellent. Reaching the CBS limit is more difficult for EAs than for IPs. Still, EAs calculated with ADF are in excellent agreement with the plane-wave results from the WEST code for systems with positive LUMOs, with an overall MAD between both codes of 160 meV. These deviations mostly stem from large basis set errors for the EAs of small molecules with bound LUMO with the ADF code. For larger organic molecules, agreement to def2-GTO results is with a MAD of 93 meV significantly better. Good agreement is also observed for RPA correlation energies. Since the other methods we have implemented rely on the same

approximations, these results also imply their correct implementation. This close agreement between different codes is highly important in practice since it allows researchers to interpret the results of their MBPT calculations, without worrying that they might be skewed by technical aspects.

Second, we have described an efficient implementation of the qsGW method and assessed its accuracy for molecular systems. While low-scaling implementations of diagonal approximations to GW have been presented before, our implementation is the first which also achieves low-order scaling with system size for qsGW. We have shown that qsGW is an excellent method to calculate IPs and EAs for a set of medium organic acceptor molecules. With MADs of 0.09 eV for IPs and 0.14 eV for EAs, qsGW outperforms all other GW methods, previously benchmarked for this dataset.[242] Remarkably, fundamental gaps are underestimated by qsGW compared to CCSD(T) reference values. This is different from the common situation in extended systems and can be attributed to the much weaker charge screening in finite systems. Also for a second set of 40 small molecules where no reference data for EAs was available, qsGW gives excellent IPs.

This allows for the accurate and starting point independent computation of single particle excitations and - in combination with the BSE@qsGW method - the calculation of excitonic states for large molecules. The applications we have presented in chapter 6 illustrate this. As opposed to a recently developed simplified BSE@GW scheme,[742] our implementation does not introduce any empirical approximations to the matrix elements of the BSE Hamiltonian. We have illustrated the potential of this new implementation by applications to biologically relevant systems, a six-chromophore model of the photosystem II (PSII) reaction center (RC) and DNA oligomers. These systems contain several hundreds of atoms and the developments presented in this work made it possibly for the first time to investigate them on the (BSE@)qsGW level of theory.

Third, We went beyond the GW approximation and presented approaches based on the $G3W2$ contribution to the electronic self-energy which go beyond the canonical approximations. We have implemented the statically screened $G3W2$ self-energy and assessed its accuracy for single-particle excitations. For qsGW, the statically screened $G3W2$ correction does not lead to systematic improvements. However, we could show that this contribution to the self-energy is especially useful to improve over RPA correlation energies and gives the same level of accuracy as AC-SOSEX for a wide range of different bonding characteristics.

Building on these developments there are various directions of research which might be pursued in the future. An issue which appeared throughout this thesis is the slow convergence of the values of observables with respect to the single-particle basis. First of all, our STO-type basis sets are restricted to angular momenta smaller or equal to $l = 3$ which sets a limit to the accuracy currently attainable. It would be desirable to obtain results using even larger basis sets than the ones presented in this thesis. Currently, we are working on interfacing our MBPT code to the BAND code which uses numerical atomic orbitals. This would allow us to use larger basis sets of all types with angular momenta larger than $l = 3$ and would improve the attainable accuracy for small molecules.

Even more importantly, the slow convergence to the CBS limit is also an obstacle in practical

applications since calculations at (or even close to) the CBS limit are currently often out of reach and will most likely not become routine anytime soon for systems with hundreds of atoms. This is due to the fact that low-order scaling implementations like ours rely on sparsity in the primary basis and do not scale well with the size of the basis set. Furthermore, the equations we implemented tend to become numerically more unstable with increasing basis set size. To overcome this issue, finite basis set corrections[599,743,744] hold much promise and it is to hope that these techniques will be further developed and become more widespread available in the near future.

It should be noted that one might find ways around these issues in practical applications. We have for example seen in section 6.1 that basis set errors for large systems can also be accurately estimated based on results for smaller, chemically closely related systems. Also for BSE@GW calculations in which only differences in the QP energies are relevant, the situation is already much better. Our results in section 6.2 confirmed the results of previous studies which demonstrated that basis set errors for occupied and virtual states usually cancel to a large extent and that fundamental gaps are often sufficiently converged using relatively small basis sets.[258,263–265,268,613,745]

Another issue we have encountered in chapter 6 is that many system of practical interest are not isolated but are typically embedded in a solvent or in a protein matrix. We have seen in ref. 6.1 and also in ref. [248] that the effect of the solvent can be accurately modeled by using a combination of DFT and COSMO. However, this procedure is rather tedious and it would be highly desirable to take into account environmental effects more directly by combining GW directly with a polarizable continuum model (PCM). his would require to calculate the dielectric screening effects due to the environment on the system which is treated on the MBPT. Approaches to achieve this have already been suggested.[746,747] Modelling the effect of the protein environment is even more challenging since anisotropic effects can not be described *via* PCMs. It would therefore be desirable to include the the protein matrix into the MBPT calculations through explicit point charges along the lines of other BSE@GW implementations.[544,748,749] Finally, we mention approaches based on localized electronic states which allow to decompose a large system into subsystems. This then allows to calculate the self-energy of a subsystem including the effect of another system in which the first system is embedded.[438,725] Such a decomposition would be very useful to describe the effect of a solvent on the solute.

Exploring vertex corrections to the self-energy in a more systematic way would be another interesting direction for further research. Even though we have seen in chapter 5 that the statically $G3W2$ correction to the self-energy leads to improvements over GW in certain situations, our results confirm recent studies[319,368,372,383,424] which suggest that QP approximations to GW are difficult to improve upon diagrammatically. Systematic and reliable improvements over GW are most likely only possible starting from the fully self-consistent solution of the GW equations. We have written down all the necessary working equations in section 3.2.2 but haven't presented an actual implementation so far.

An scGW implementation would be a necessary first step to systematically investigate some of the more advanced vertex corrections we have introduced in section 2.4.5. So far, we have

only evaluated the statically screened $G3W2$ correction perturbatively but it is straightforward to calculate this term for the full self-energy as well. We note, that the working equations from section 3.2.3 assume a basis in which G is diagonal. Evaluating them with an interacting Green's function would require a representation in the AO basis[387] or, more efficiently,[750] in the natural orbital basis.[427,750] Since we have already implemented a solver for the full BSE Hamiltonian (also see appendix A.4.3 for timings) we could also evaluate the BSE@GW response function (2.316). This would lead to a statically screened version of Kutepov's $GW + G3W2$@BSE implementation.[368,424] Implementing this approach with full frequency dependence would be very challenging from a computational perspective but potentially highly interesting since it has been shown to work exceptionally well for solids.[368,370–372] Implementing the BSE@GW method with the dynamical GW kernel eq. (2.315) would also be useful in its own right since the dynamical BSE@GW approach gives access to double excitations which are not captured within the static approximation.[128]

Appendix A

Appendix

A.1 Zeroth-Order Regular Approximation to the Dirac Equation

We have derived all of our equations from the non-relativistic Schrödinger equation. Since we herein mostly focused on molecules containing first- and second-row atoms, this is an excellent approximation since relativistic effects will be negligible. For molecules containing heavy elements, for instance Iodine or Silver which are part of the GW100 database, relativistic effects can not be neglected (see discussion in section 4.1). We have then included relativistic effects approximately using the scalar zeroth-order regular approximation (ZORA) by van Lenthe *et. al.*[619–621] which we will shortly introduce here.

The scalar ZORA leads to a modification of the kinetic energy expression in the non-relativistic Schrödinger equation and therefore to a modified single-particle Schrödinger equation (2.7). Since only the single-particle part of the equations of chapter 3 is altered by scalar ZORA, non of the working equations of chapter 3 is affected.

We start from the Dirac equation for a free particle,

$$\begin{pmatrix} v_{ext}(\boldsymbol{r}) & c\vec{\sigma}\cdot\vec{p} \\ c\vec{\sigma}\cdot\vec{p} & v_{ext}-2c^2 \end{pmatrix}\begin{pmatrix}\psi_L\\ \psi_S\end{pmatrix} = E\begin{pmatrix}\psi_L\\ \psi_S\end{pmatrix} \tag{A.1}$$

in which

$$\Psi = \begin{pmatrix}\psi_L\\ \psi_S\end{pmatrix}$$

is the four-component wave function and the two-component wave functions ψ_L and ψ_S are respectively called large and small components. Solving the second equation for ψ_L and inserting the result in the first equation allows for the elimination of the small components

$$\left[\frac{1}{2}\vec{\sigma}\cdot\vec{p}K(E,\boldsymbol{r})\vec{\sigma}\cdot\vec{p}+v_{ext}(\boldsymbol{r})\right]\psi_L = E\psi_L\ , \tag{A.2}$$

with

$$K(E,\boldsymbol{r}) = \left[1 + \frac{E - v_{ext}(\boldsymbol{r})}{2c^2}\right]^{-1} .$$

K can be rewritten as

$$K(E,\boldsymbol{r}) = \left(1 - \frac{v_{ext}(\boldsymbol{r})}{2c^2}\right)^{-1} \left(1 + \frac{E}{2c^2 - v_{ext}(\boldsymbol{r})}\right)^{-1}$$

Expanding the second factor in this equation and noly retaining terms of zeroth order in v_{ext} we get

$$\left\{ v_{ext} + \frac{1}{2}\left(\vec{\sigma}\cdot\vec{p}\right)\left[1 - \frac{v_{ext}(\boldsymbol{r})}{2c^2}\right]^{-1}\left(\vec{\sigma}\cdot\vec{p}\right)\right\}\psi_L = E\psi_L . \tag{A.3}$$

Through the relation[751]

$$\left(\vec{\sigma}\cdot\vec{X}\right)\left(\vec{\sigma}\cdot\vec{Y}\right) = \vec{X}\cdot\vec{Y} + i\vec{\sigma}\left(\vec{X}\times\vec{Y}\right) \tag{A.4}$$

identifying $\vec{X}$ with

$$\vec{p}\times\left[1 - \frac{v_{ext}(\boldsymbol{r})}{2c^2}\right]^{-1}$$

and using

$$\frac{1}{2}\left[1 - \frac{v_{ext}(\boldsymbol{r})}{2c^2}\right]^{-1} = \frac{c^2}{2c^2 - v_{ext}(\boldsymbol{r})}$$

we can write the ZORA-Hamiltonian as[621]

$$\hat{h}_1^{ZORA}(\boldsymbol{r}) = \hat{h}_1^{ZORA,SR}(\boldsymbol{r}) + \hat{h}_1^{ZORA,SO}(\boldsymbol{r}) , \tag{A.5}$$

where the first term describes scalar relativistic effects

$$\hat{h}_1^{ZORA,SR}(\boldsymbol{r}) = v_{ext}(\boldsymbol{r}) + \vec{p}\frac{c^2}{2c^2 - v_{ext}(\boldsymbol{r})}\vec{p} \tag{A.6}$$

and the second one spin-orbit effects,

$$\hat{h}_1^{ZORA,SO}(\boldsymbol{r}) = \frac{c^2}{\left(2c^2 - v_{ext}(\boldsymbol{r})\right)^2}\vec{\sigma}\cdot\left(\nabla v_{ext}(\boldsymbol{r})\times\vec{p}\right) . \tag{A.7}$$

One sees that $\hat{h}_1^{ZORA,SR}$ reduced to the non-relativisitc expression (2.4) in the limit $c \to 0$. Whenever the ZORA is used in a calculation, $\hat{h}_1$ in eqs. (2.1) and (2.2) needs to be replaced with $\hat{h}_1^{ZORA,SR}$.

The inclusion of the second term (A.7) can be very important for the correct description of electron attachment and removal especially for molecules containing heavier p-block elements.[610] The implementation of the GW equations with explicit inclusion of spin-orbit coupling in ADF is currently in progress.

A.2 Polarizable Continuum Models

In the practical applications of MBPT of chapter 6 we have been faced with the problem that the systems we investigated were not isolated. It is then typically not feasible to treat this environment at the same level of theory unless the subsystem of interest consists of only a few electrons, as it is for instance the case for small molecules in solution.[438] The strategy we pursued in chapter 6 was to embed our system into a continuum model which approximately describes the effect of the environment on the many-electron system. This has been done only on the (TD-)DFT level of theory.

Environment effects can be described on different levels of approximation. A common approach is to represent the solvent as a homogeneous field with no explicit solvent molecules.[752] Using such so-called continuum solvation (CS) models is possibly the computationally most efficient way to account for solvent effects. We have used models of this type in chapter 6. In CS models, the solute is enclosed in a cavity inside a dielectric medium with the dielectric constant ϵ. In a special case, the field outside the cavity is represented as a conductor material ($\epsilon = \infty$), which is known as the conductor-like screening model (COSMO).[674].

The cavity, i.e. the interface between the solute and solvent, is created as an exterior of atom-centered spheres with the van der Waals atom radii which is segmented into smaller parts in such a way that a constant charge density is assumed for each segment. The solute then induces a polarization charge density on the interface to the conductor. The electrostatic energy of solvation is given by

$$E_s = \int d\boldsymbol{r}_s \sum \frac{Z_{\mathcal{A}} n_s(\boldsymbol{r}_s)}{|\boldsymbol{r}_{\mathcal{A}} - \boldsymbol{r}_s|} + \int\int d\boldsymbol{r} d\boldsymbol{r}_s \frac{n(\boldsymbol{r}) n_s(\boldsymbol{r}_s)}{|\boldsymbol{r} - \boldsymbol{r}_s|} + \int\int d\boldsymbol{r}_s d\boldsymbol{r}'_s \frac{n_s(\boldsymbol{r}_s) n'_s(\boldsymbol{r}'_s)}{|\boldsymbol{r}_s - \boldsymbol{r}'_s|} \tag{A.8}$$

where the three terms describe respectively the interaction of the surface charges with the nuclear charge, interaction of the surface charges with the electron density, and self-interaction of the surface charges, which are approximated by point charges.[677]

A.3 Starting-point Dependence of GW Calculations

In section 2.4.4, we have discussed the starting point dependence of different approximations to fully self-consistent GW. Here, we assess this for five different functionals - meta-GGAs, hybrids, and range-separated hybrids for different approximations, ranging from G_0W_0 to qsGW. For the latter method, we also compare the different QP Hamiltonians eqs. (2.341) and (2.342). We have calculated all IPs in the GW100 database using the TZ2P basis set,[1] *Good* numerical quality and standard numerical settings otherwise and compared our results to the ones from Berkelbach and coworkers[612] at the EOM-CCSD/def2-TZVP level of theory. As we have already discussed, this is not necessarily a suitable reference and the basis set incompleteness errors we are introducing do not allow an unbiased comparison of the accuracy of the approaches. However, we are only

[1] We have performed these calculations prior to the development of the correlation consistent basis sets.

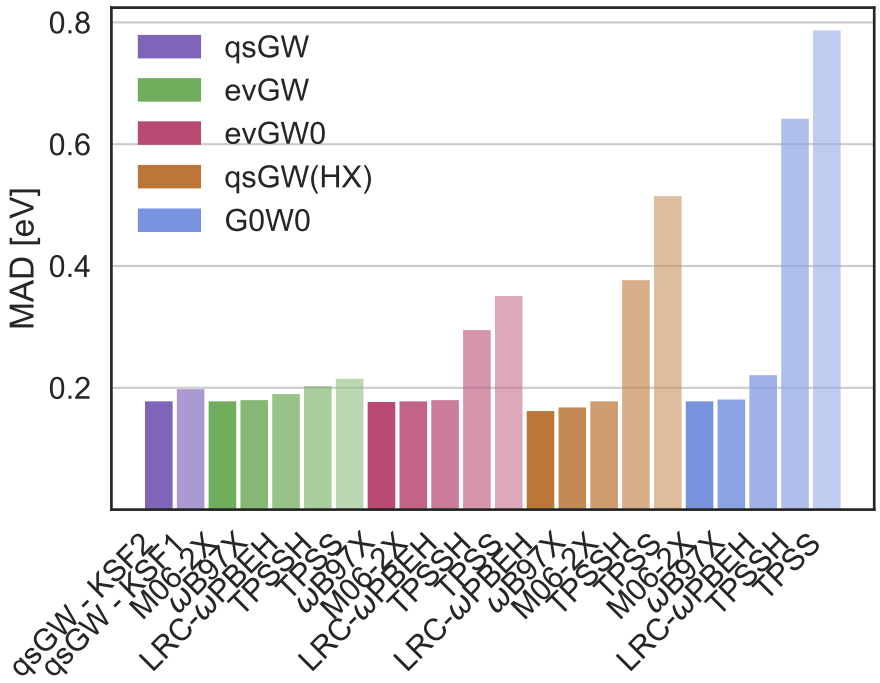

Figure A.1: Comparison of G0W0, evGW, evGW0, qsGW and qsGW(HX) for the IPs in the GW100 database for 5 different starting points, using the TZ2P basis set and *Good* numerical quality, with respect to the EOM-CCSD/def2-TZVP reference. All values are in eV.

interested in getting an idea about the starting point dependence for the different levels of self-consistency. For this purpose, the reference values are not important and only the differences in the deviations to the reference at each level of self-consistency with different starting points are relevant. To assess the relative accuracy for each level of self-consistency, our reference is good enough. Our results are shown in figure A.1.

For G_0W_0, we observe a tremendous starting point dependence, with MADs ranging from 0.8 eV for the meta-GGA TPSS to less than 0.2 eV for the hybrid M06-2X with 54 % exx. Even though TPSSH is also a hybrid functional, it does not improve much over TPSS. This is due to the fact that it only contains 10 % of exact exchange and therefore it significantly overestimates the screening of the electron-electron interaction.

In qsGW(HX), the starting point dependence is already reduced, even though the correlation contribution to the self-energy is only updated once. In evGW_0, the starting point dependence is reduced even more. The difference there is only due to the screening which is kept fixed at the level of $G^{(s)}$. At the evGW level, the starting point dependence is eliminated almost completely. In fact, the difference in qsGW with different constructions of the QP Hamiltonians (here referred to as KSF1 and KSF2, respectively) is only marginally smaller.

The reduced starting point dependence does however not imply an increased accuracy with respect to EOM-CCSD/def2-TZVP. The accuracy which can be reached with G_0W_0 is slightly below 0.2 eV. This is the same at all levels of self-consistency.

A.4 Timings

A.4.1 Asymptotic Scaling of G_0W_0

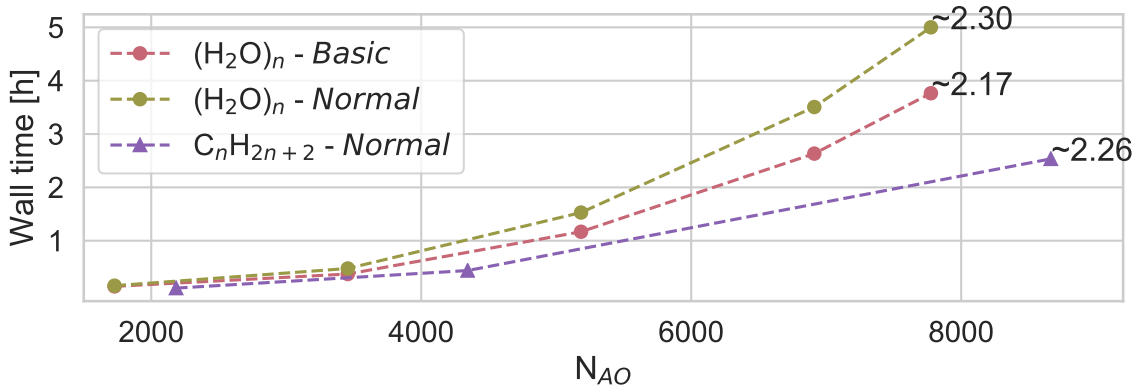

Figure A.2: Wall times in hours for G_0W_0@PBE/TZ2P calculations on a series of Water clusters and a linear alkane chain (exclusive the preceding SCF). All calculations have been performed on 2 bw nodes. The exponent of the polynomial describing the asymptotic scaling of the algorithm is given on the right of each plot.

In this appendix, we briefly comment on the computational time needed to perform MBPT calculations. In order to analyze the asymptotic scaling of our calculations we present G_0W_0@PBE calculations on series of water clusters[2] using the TZ2P basis set, *Normal* numerical quality, the *Basic* and *Normal* tiers of thresholds and 12 imaginary time and imaginary frequency points. All calculations presented in this subsection were performed on 2.2 GHz intel Xeon (E5-2650 v4) nodes (broadwell architecture) with 24 cores and 128 GB RAM each (bw nodes in short). Figure A.2 shows the wall times for the G_0W_0-part of the calculations and the exponents of the polynomials describing the asymptotic scaling of these calculations with increasing system size. Information on CPU time and asymptotic scaling of key steps of the algorithm for the largest of these systems are given in figure A.3

The largest water cluster here comprises 432 atoms with 7776 AOs and 36576 ABFs. Using the *Normal* threshold tier, the whole G_0W_0 calculation takes five hours on two nodes. As shown in figure A.3, the most expensive step is the calculation of Σ, being responsible for about half of

[2]The structures of the water clusters have been downloaded from the website of the ERGO program,[753] http://www.ergoscf.org (visited on may 19th, 2020).

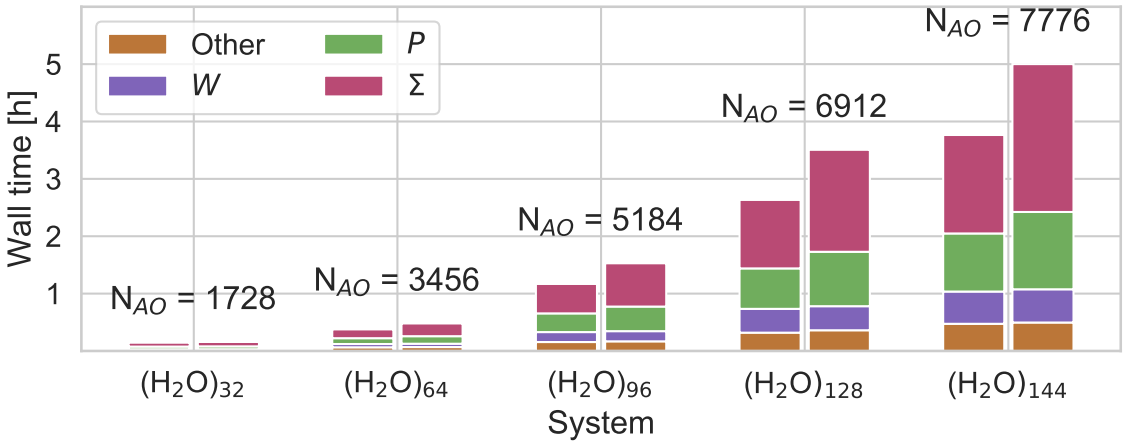

Figure A.3: Contributions to total G_0W_0 wall times from different key steps for a series of Water cluster using the TZ2P basis set. Left bar in each group: *Basic* threshold quality, right bar in each group: *Normal* threshold quality. All calculations have been performed on 2 bw nodes.

the wall time of the whole calculation, followed by the evaluation of $P^{(0)}$. The evaluation of Σ is also the step which is accelerated most when the thresholds are loosened. This is due to the contractions eq. (3.93) which are tremendously accelerated when the multipole approximation is used for an increasing number of atom pairs. Consequently, the asymptotic scaling of this step is decreased from $N^{2.34}$ to $N^{2.15}$. Also the asymptotic scaling of $P^{(0)}$ is reduced considerably (from $N^{2.19}$ to $N^{2.05}$), so that the wall time of the total calculation can be reduced to less than 4 hours. Note, that the evaluation of W is not affected by changing the thresholds and asymptotically scales as N^3. However, even for the largest water cluster the timings are clearly dominated by $P^{(0)}$ and Σ and W can not be expected to become a bottleneck even for systems much larger than the ones considered here.

Water clusters are very compact systems due to their spherical shapes. This takes an adverse effect on the asymptotic scaling properties of our algorithm, compared to low-dimensional systems, e.g. linear alkane chains as the most extreme example. The timings for a series of alkane chains is given for comparison in figure A.2 as well. With the same thresholds, the G_0W_0-calculation for $C_{160}H_{322}$ takes with roughly 2.5 hours only half the time as the one for $(H_2O)_{144}$ even though the former system is larger. In fact, $P^{(0)}$ is calculated in less than half an hour which is less wall time than is required for the calculation of $\widetilde{W}$.

A.4.2 CPU Times for BSE@*GW*

In this appendix, we briefly comment on the computational effort for different basis sets and methods to calculate the lowest N_Ω roots of the full hexamer with 476 atoms and 1872 correlated electrons, described in section 6. The computational timings in core hours are given in table A.1.

Method	Basis	N_{bas}	N_Ω	Iterations qsGW	Iterations BSE	CPU time GW	CPU time BSE	CPU time total
qsGW-BSE	TZ3P	11116	12	6	10	3401	3447	7283
qsGW-BSE	TZP	6256	24	6	8	1074	1729	2924
evGW-BSE	TZP	6256	24	5	8	826	1969	2917
ωB97-X	TZP	6256	12	–	21	–	2675	2846

Table A.1: CPU times (in core hours) to calculate the N_Ω lowest roots of the full hexamer with 476 atoms and 1872 correlated electrons with different basis sets and methods. 39884 auxiliary basis functions have been used in all calculations. All calculations have been performed on an 2.6 GHz AMD Rome 7H12 node with 64 cores and 16 GB RAM per node.

The calculation for the hexamer can be performed in less than 3000 core hours, i.e. in less than two days on a node with 64 cores. The qsGW part of the calculation is slightly cheaper than the BSE part. Notice, that the BSE part of the calculation is roughly as expensive as the TD-DFT calculation with the WB97-X kernel if the timings are normalized by the number of states and number of subspace iterations in the Davidson algorithm.

Notice, that low-order scaling implementations like ours which rely on sparsity in the primary basis usually do not scale well with the size of the basis set, as can be seen by comparing the timings of the qsGW-BSE calculations with different basis sets. We also performed a qsGW calculation for the full hexamer with more than 11000 basis functions using the TZ3P basis set. Here, a single qsGW iteration already takes around 540 core hours, which is about three times more than one iteration using the TZP basis set. While in this work the TZP basis set was already sufficient to obtain converged results, typically lager basis sets will be required. Finite basis set correction techniques for many-body perturbation theory might be a promising solution to circumvent this problem.[599, 743, 744, 754]

A.4.3 Diagonalization of the BSE Hamiltonian

The BSE Hamiltonian can either be diagonalized using the Davidson scheme or by direct solvers which build the full BSE Hamiltonian and then solve for a selected number of excitonic states or the full spectrum. In practical applications it is important to know which solver to use for what matrix dimension. It is important to notice that in our implementation of the BSE@GW method using the direct solver only eigenvalues and eigenvectors can be obtained but not oscillator strengths or excitonic life times which are always calculated when the Davidson algorithm is used.

The time required to build and diagonalize the BSE Hamiltonian is shown in table A.2 for three rather small systems for which the direct solver is clearly much faster than the Davidson solver. The main shortcoming of the direct solver is the amount of memory needed to store the BSE Hamiltionian. The decisive factor for the direct solver is here the size of the basis of electron-hole transitions in which the BSE Hamiltonian is diagonalized. For $C_{32}H_{18}N_4$ with a cut-off of 8 Ha, the number of relevant electron-hole transitions is already of the order of

System	basis set	range [Ha]	dim $\mathcal{R}$	Storage [GB]	N	CPU time [h] direct	CPU time [h] Davidson
C_6H_6	QZ6P	full	9210	0.7	3	0.5	7.7
					12	0.6	86.4
$C_{14}H_{10}$	TZ3P	full	23876	4.6	3	3.3	4.4
$C_{32}H_{18}N_4$	TZ3P	1.5	16027	2.1	12	4.8	330.1
		2.0	22958	4.2	12	8.3	
		4.0	42235	14.3	12	32.0	
		8.0	75887	46.1	12	328.0	
		4.0	42235	14.3	120	32.1	

Table A.2: Computational timings (in core hours) for the diagonalization of the BSE Hamiltonian using different solvers. We solve for different numbers of excitonic states, denoted here by N and for $C_{32}H_{18}N_4$ we also vary the range of particle-hole transition energies below which we include these particle hole pairs in the basis for building $\mathcal{R}$ ($\mathcal{A}$) (third column). All calculations have been performed on a single Intel Skylake node with 32 cores and 192 GB of RAM. For C_6H_6 and $C_{14}H_{10}$ we performed all calculations on 8 cores. For $C_{32}H_{18}N_4$ with an energy range of 8 Ha, we used two full nodes since the BSE Hamiltonian could not be stored in direct memory on a single node only.

	range[Ha] 1.5	2.0	4.0	8.0	full
singlet	3.571	3.567	3.564	3.564	3.565
	3.744	3.741	3.738	3.738	3.739
	4.002	3.999	3.996	3.996	3.997
triplet	2.899	2.886	2.871	2.868	2.869
	3.041	3.020	3.006	3.002	3.001
	3.042	3.022	3.008	3.004	3.003

Table A.3: Convergence of the three lowest singlet-singlet and singlet-triplet excitation energies of $C_{32}H_{18}N_4$ with the size of the particle-hole basis (BSE@@GW@PBE0(40 % exx)/TZ3P). All values are in eV.

75000 and the BSE Hamiltonian needs almost 50 GB of storage. Since in practice we need to provide three matrices of this size $(A-B)$, $(A+B)$ as well as $|\chi_S^{(r)}+\chi_S^{(a)}\rangle$, this was already too large to perform the calculation on a single node (Intel Skylake with 32 cores and 192 GB of RAM). We then performed the calculation on 2 nodes. This now takes almost as long as with the Davidson algorithm. However, it should be noted that we have not optimized the communication between multiple nodes. For this calculation, 80 % of the 328 core hours account for inter-node communication alone.

Another big advantage of the direct solver is that the timings only increase marginally with increasing number of excitonic states one solves for. For instance, the CPU time required to obtain the lowest 12 excitonic singlet and triplet states of $C_{32}H_{18}N_4$ is essentially the same than for 120 states each. On the other hand, as can be seen for C_6H_6, for the Davidson algorithm, it

takes around 9 times longer to obtain 12 singlet and triplet states each instead of three states each.

As shown in table A.3 this cut-off is however unnecessarily large. Already using a cut-off of 1.5 Ha (for which the direct solver is about 80 times faster than the Davidson algorithm) all excitation energies are converged within 40 meV and for a cut-off of 2.0 Ha all excitation energies are converged within 20 meV. Notice, that the results of both solvers typically differ by 1-2 meV for the same cut-off since the particle-hole exchange term is calculated differently: In the Davidson routine the so-called ZLMfit scheme is used[471] for this term while we use PADF in the direct solver.

In summary, the Davidson solver should only be used for rather large systems with dim $\mathcal{R}$ of the order of around 5×10^4 where the storage of the full BSE Hamiltonian becomes prohibitive. Especially for larger basis sets for which the BSE Hamiltonian tends to become more "dense", or when a large number of excitonic states is sought, the direct solver should be preferred. To obtain generalized susceptibilities, it would be very useful to implement Haydock recursion[594] which would potentially allow for treating larger systems than the ones which are currently feasible for the direct solver.

A.5 Table of Integrals

$$\int_b^\infty e^{-ax} dx = \frac{e^{-ab}}{a} \tag{A.9}$$

$$\int_{-\infty}^b e^{-ax} dx = -\frac{e^{-ab}}{a} \tag{A.10}$$

$$\int_0^\infty e^{-ax} \cos(bx) dx = 2\frac{a}{a^2 + b^2} \tag{A.11}$$

$$\int_0^\infty e^{-ax} \sin(bx) dx = 2\frac{b}{a^2 + b^2} \tag{A.12}$$

Bibliography

(1) Diamantis, P.; Tavernelli, I.; Rothlisberger, U. *J. Chem. Theory Comput.* **2020**, *16*, 6690–6701.

(2) Curutchet, C.; Mennucci, B. *Chem. Rev.* **2017**, *117*, 294–343.

(3) Croce, R.; van Amerongen, H. *Science (80-.).* **2020**, *369*, eaay2058.

(4) Decavoli, C.; Boldrini, C. L.; Manfredi, N.; Abbotto, A. *Eur. J. Inorg. Chem.* **2020**, *2020*, 978–999.

(5) Zhu, Q.-L.; Xu, Q. *Chem. Soc. Rev.* **2014**, *43*, 5468–5512.

(6) Wilhelm, J.; Golze, D.; Talirz, L.; Hutter, J.; Pignedoli, C. A. *J. Phys. Chem. Lett.* **2018**, *9*, 306–312.

(7) Ruggenthaler, M.; Flick, J.; Pellegrini, C.; Appel, H.; Tokatly, I. V.; Rubio, A. *Phys. Rev. A - At. Mol. Opt. Phys.* **2014**, *90*, 012508.

(8) Harris, F. E.; Monkhorst, H. J.; Freeman., D. L., *Algebraic and diagrammatic methods in many-fermion theory.* Courier Dover Publications: Dover, 2020.

(9) Olsen, J.; Jørgensen, P.; Simons, J. *Chem. Phys. Lett.* **1990**, *169*, 463–472.

(10) Lin, H. Q. *Phys. Rev. B* **1990**, *42*, 6561–6567.

(11) Zhang, J. M.; Dong, R. X. *Eur. J. Phys.* **2010**, *31*, 591–602.

(12) Kohn, W. *Phys. Rev. Lett.* **1996**, *76*, 3168–3171.

(13) Evangelista, F. A. *J. Chem. Phys.* **2018**, *149*, 030901.

(14) Ceperley, D.; Alder, B. *Quantum Monte Carlo* **1986**, *231*, 555–560.

(15) Martin, R. M.; Reining, L.; Ceperley, D. M., *Interacting electrons*; Cambridge University Press: 2016.

(16) White, S. R. *Phys. Rev. Lett.* **1992**, *69*, 2863–2866.

(17) White, S. R. *Phys. Rev. B* **1993**, *48*, 10345–10356.

(18) Verstraete, F.; Murg, V.; Cirac, J. I. *Adv. Phys.* **2008**, *57*, 143–224.

(19) Chan, G. K. L.; Keselman, A.; Nakatani, N.; Li, Z.; White, S. R. *J. Chem. Phys.* **2016**, *145*.

(20) Shi, Y. Y.; Duan, L. M.; Vidal, G. *Phys. Rev. A - At. Mol. Opt. Phys.* **2006**, *74*, 022320.

(21) Vidal, G. *Phys. Rev. Lett.* **2007**, *99*, 220405.

(22) Metzner, W.; Vollhardt, D. *Phys. Rev. Lett.* **1989**, *62*, 324–327.

(23) Müller-Hartmann, E. *Zeitschrift für Phys. B Condens. Matter* **1989**, *74*, 507–512.

(24) Georges, A.; Kotliar, G.; Krauth, W.; Rozenberg, M. J. *Rev. Mod. Phys.* **1996**, *68*, 13–113.

(25) Huron, B.; Malrieu, J. P.; Rancurel, P. *J. Chem. Phys.* **1973**, *5745*, 5745–5759.

(26) Buenker, R. J.; Peyerimhoff, S. D. *Theor. Chim. Acta* **1974**, *35*, 33–58.

(27) Carleo, G.; Troyer, M. *Science (80-.).* **2017**, *355*, 602–606.

(28) Hermann, J.; Schätzle, Z.; Noé, F. *Nat. Chem.* **2020**, *12*, 891–897.

(29) Pfau, D.; Spencer, J. S.; Matthews, A. G.; Foulkes, W. M. *Phys. Rev. Res.* **2020**, *2*, 033429.

(30) Harrison, R. J. *J. Chem. Phys.* **1991**, *94*, 5021–5031.

(31) Biermann, S.; Aryasetiawan, F.; Georges, A. *Phys. Rev. Lett.* **2003**, *90*, 086402.

(32) Dvorak, M.; Rinke, P. *Phys. Rev. B* **2019**, *99*, 115134.

(33) Dvorak, M.; Golze, D.; Rinke, P. *Phys. Rev. Mater.* **2019**, *3*, 70801.

(34) Kopietz, P., *Bosonization of Interacting Fermions in Arbitrary Dimensions*; Springer: Berlin, 2006.

(35) Förster, A.; Franchini, M.; van Lenthe, E.; Visscher, L. *J. Chem. Theory Comput.* **2020**, *16*, 875–891.

(36) Förster, A.; Visscher, L. *J. Chem. Theory Comput.* **2020**, *16*, 7381–7399.

(37) Förster, A.; Visscher, L. *J. Chem. Theory Comput.* **2021**, *17*, 5080–5097.

(38) Förster, A.; Visscher, L. *Front. Chem.* **2021**, *9*, 736591.

(39) Förster, A.; Visscher, L. *arXiv:2205.08360* **2022**, 1–53.

(40) Förster, A.; Visscher, L. *Phys. Rev. B* **2022**, *105*, 125121.

(41) Förster, A. *arXiv:2204.06810* **2022**, 1–49.

(42) Gell-Mann, M.; Low, F. *Phys. Rev.* **1951**, *84*, 350–354.

(43) Feynman, R. P. *Phys. Rev.* **1949**, *76*, 749–759.

(44) Dyson, F. J. *Phys. Rev.* **1949**, *75*, 1736–1755.

(45) Dyson, F. J. *Phys. Rev.* **1949**, *75*, 486–502.

(46) Schwinger, J. *Proc. Natl. Acad. Sci.* **1951**, *37*, 452–455.

(47) Schwinger, J. *Proc. Natl. Acad. Sci.* **1951**, *37*, 455–459.

(48) Houriet, A.; Kind, A. *Helv. Phys. Acta* **1949**, *22*, 319–330.

(49) Wick, G. C. *Phys. Rev.* **1950**, *80*, 268–272.

(50) Brueckner, K. A. *Phys. Rev.* **1955**, *100*, 36–45.

(51) Goldstone, J. *Proc. R. Soc. London. Ser. A. Math. Phys. Sci.* **1957**, *239*, 267–279.

(52) Hubbard, J. *Proc. R. Soc. London. Ser. A. Math. Phys. Sci.* **1957**, *240*, 539–560.

(53) Hugenholtz, N. *physica* **1957**, *XXIII*, 481–532.

(54) Bloch, C. *Nucl. Phys.* **1958**, *6*, 329–347.

(55) Farid, B. *arXiv:1912.00474v2* **2019**.

(56) Luttinger, J. M.; Ward, J. C. *Phys. Rev.* **1960**, *118*, 1417–1427.

(57) Klein, A. *Phys. Rev.* **1961**, *121*, 950–956.

(58) Baym, G.; Kadanoff, L. P. *Phys. Rev.* **1961**, *124*, 287–299.

(59) Baym, G. *Phys. Rev.* **1962**, *127*, 1391.

(60) Salpeter, E. E.; Bethe, H. A. *Phys. Rev.* **1951**, *84*, 1232–1242.

(61) De Dominicis, C.; Martin, P. C. *J. Math. Phys.* **1964**, *5*, 31–59.

(62) Coester, F. *Nucl. Phys.* **1958**, *7*, 421–424.

(63) Coester, F.; Kümmel, H. *Nucl. Phys.* **1960**, *17*, 477–485.

(64) Čížek, J. *J. Chem. Phys.* **1966**, *45*, 4256–4266.

(65) Čížek, J. *Adv. Chem. Physics, Vol. XIV* **1969**, *XIV*, 35–89.

(66) Paldus, J.; Čížek, J.; Shavitt, I. *Phys. Rev. A* **1972**, *5*, 50–67.

(67) Hedin, L. *Phys. Rev.* **1965**, *139*, A796.

(68) Phillips, J. C. *Phys. Rev.* **1961**, *123*, 420–424.

(69) Starke, R.; Kresse, G. *Phys. Rev. B* **2012**, *85*, 075119.

(70) Lewis, G. *J. Am. Chem. Soc.* **1916**, *38*, 762–785.

(71) Landau, L. D. *Sov. Phys. JETP* **1957**, *3*, 920.

(72) Landau, L. D. *Sov. Phys. JETP* **1957**, *5*, 101.

(73) Landau, L. D. *Sov. Phys. JETP* **1959**, *35*, 752–760.

(74) Abrikosov, A.; Khalatnikov, I. *Sov. J. Exp. Theor. Phys.* **1958**, *6*, 888.

(75) Abrikosov, A. A.; Gorkov, K. P.; Dzyaloshinskii, I. E. *Sov. Phys. JETP* **1959**, *36*, 636–641.

(76) Nozières, P.; Luttinger, J. M. *Phys. Rev.* **1962**, *127*, 1423–1431.

(77) Hohenberg, P.; Kohn, W. *Phys. Rev.* **1964**, *136*, 864–871.

(78) Kohn, W.; Sham. L. J. *Phys. Rev.* **1965**, *140*, A1133.

(79) Hartree, D. R. *Math. Proc. Cambridge Philos. Soc.* **1928**, *24*, 89–110.

(80) Slater, J. C. *Phys. Rev.* **1928**, *32*, 339–348.

(81) Slater, J. C. *Phys. Rev.* **1930**, *35*, 210–211.

(82) Fock, V. *Zeitschrift für Phys.* **1930**, *61*, 126–148.

(83) Slater, J. C. *Phys. Rev.* **1929**, *34*, 1293–1322.

(84) Dirac, P. A. *Proc. R. Soc. London. Ser. A, Contain. Pap. a Math. Phys. Character* **1926**, *112*, 661–677.

(85) Heisenberg, W. *Zeitschrift für Phys.* **1926**, *38*, 411–426.

(86) Fock, V. *Zeitschrift für Phys.* **1932**, *75*, 622–647.

(87) Kohlmann, M. Schrödinger Operators and their Spectra, lecture notes, 2017/2018, Göttingen.

(88) Schwinger, J. *Phys. Rev.* **1948**, *74*, 1439–1461.

(89) Baker, C. T. H., *The Numerical Treatment of Integral Equations*; Clarendon Press: Oxford, 1977, pp 358–360.

(90) Weisstein, E. W. Fredholm Integral Equation of the Second Kind.

(91) Weisstein, E. W. Integral Equation Neumann Series.

(92) Abrikosov, A. A.; Gorkov, P. L.; Dzyaloshinski, I. E., *Methods of quantum field theory in statistical physics*; Dover Publications INC. New York: 1975.

(93) Bogoliubov; N. N; Shirkov; D. V., *Introduction to the Theory of Quantized Fields*; John Willey & Sons Inc.: New York, 1980.

(94) Kong, L.; Nooijen, M.; Mukherjee, D. *J. Chem. Phys.* **2010**, *132*, 234107.

(95) Beloussov, I. V. *Spec. Matrices* **2015**, *3*, 169–174.

(96) Molinari, L. G. *J. Math. Phys.* **2007**, *48*, 052113.

(97) Brouder, C.; Stoltz, G.; Panati, G. *Phys. Rev. A - At. Mol. Opt. Phys.* **2008**, *78*, 042102.

(98) Brouder, C.; Panati, G.; Stoltz, G. *Phys. Rev. Lett.* **2009**, *103*, 230401.

(99) Brouder, C.; Panati, G.; Stoltz, G. *Ann. Henri Poincare* **2010**, *10*, 1285–1309.

(100) Szalay, P. G.; Müller, T.; Gidofalvi, G.; Lischka, H.; Shepard, R. *Chem. Rev.* **2012**, *112*, 108–181.

(101) Köhn, A.; Hanauer, M.; Mück, L. A.; Jagau, T. C.; Gauss, J. *Wiley Interdiscip. Rev. Comput. Mol. Sci.* **2013**, *3*, 176–197.

(102) Hirata, S.; Doran, A. E.; Knowles, P. J.; Ortiz, J. V. *J. Chem. Phys.* **2017**, *147*, 044108.

(103) Cancés, E.; Gontier, D.; Stoltz, G. *Rev. Math. Phys.* **2016**, *28*, 1650008.

(104) Nooijen, M.; Snijders, J. G. *Int. J. Quantum Chem.* **1992**, *44*, 55–83.

(105) Nooijen, M.; Snijders, J. G. *Int. J. Quantum Chem.* **1993**, *48*, 15–48.

(106) Peng, B.; Panyala, A.; Kowalski, K.; Krishnamoorthy, S. *Comput. Phys. Commun.* **2021**, *265*, 108000.

(107) Kozik, E.; Ferrero, M.; Georges, A. *Phys. Rev. Lett.* **2015**, *114*, 156402.

(108) Schäfer, T.; Ciuchi, S.; Wallerberger, M.; Thunström, P.; Gunnarsson, O.; Sangiovanni, G.; Rohringer, G.; Toschi, A. *Phys. Rev. B* **2016**, *235108*, 235108.

(109) Gunnarsson, O.; Rohringer, G.; Schäfer, T.; Sangiovanni, G.; Toschi, A. *Phys. Rev. Lett.* **2017**, *119*, 056402.

(110) Sham, L. J.; Schlüüter, M. *Phys. Rev. Lett.* **1983**, *51*, 1888–1891.

(111) Macke, W. *Zeitschrift fur Naturforsch.* **1950**, *5*, 192–208.

(112) Mattuck, R. D., *A Guide to Feynman Diagrams in the Many-body Problem*, 2nd; Dover Publications INC. New York: 1992.

(113) Grüneis, A.; Marsman, M.; Kresse, G. *J. Chem. Phys.* **2010**, *133*, 074107.

(114) Marie, A.; Burton, H. G.; Loos, P. F. *J. Phys. Condens. Matter* **2021**, *33*, 283001.

(115) Rohringer, G.; Hafermann, H.; Toschi, A.; Katanin, A. A.; Antipov, A. E.; Katsnelson, M. I.; Lichtenstein, A. I.; Rubtsov, A. N.; Held, K. *Rev. Mod. Phys.* **2018**, *90*, 25003.

(116) Gunnarsson, O.; Schäfer, T.; Leblanc, J. P.; Merino, J.; Sangiovanni, G.; Rohringer, G.; Toschi, A. *Phys. Rev. B* **2016**, *93*, 245102.

(117) Yang, S. X.; Fotso, H.; Liu, J.; Maier, T. A.; Tomko, K.; D'Azevedo, E. F.; Scalettar, R. T.; Pruschke, T.; Jarrell, M. *Phys. Rev. E - Stat. Nonlinear, Soft Matter Phys.* **2009**, *80*, 046706.

(118) Augustinský, P.; Janiš, V. *Phys. Rev. B - Condens. Matter Mater. Phys.* **2011**, *83*, 035114.

(119) Tam, K. M.; Fotso, H.; Yang, S. X.; Lee, T. W.; Moreno, J.; Ramanujam, J.; Jarrell, M. *Phys. Rev. E - Stat. Nonlinear, Soft Matter Phys.* **2013**, *87*, 013311.

(120) Li, G.; Kauch, A.; Pudleiner, P.; Held, K. *Comput. Phys. Commun.* **2019**, *241*, 146–154.

(121) Janiš, V.; Augustinský, P. *Phys. Rev. B - Condens. Matter Mater. Phys.* **2007**, *75*, 165108.

(122) Li, G.; Wentzell, N.; Pudleiner, P.; Thunström, P.; Held, K. *Phys. Rev. B* **2016**, *93*, 165103.

(123) Pariser, R.; Parr, R. G. *J. Chem. Phys.* **1953**, *21*, 466.

(124) Pople, J. A. *Trans. Faraday Soc.* **1953**, *49*, 1375–1385.

(125) Pudleiner, P.; Thunström, P.; Valli, A.; Kauch, A.; Li, G.; Held, K. *Phys. Rev. B* **2019**, *99*, 125111.

(126) Krien, F.; Valli, A.; Capone, M. *Phys. Rev. B* **2019**, *100*, 155149.

(127) Strinati, G. *La Riv. Del Nuovo Cim. Ser. 3* **1988**, *11*, 1–86.

(128) Romaniello, P.; Sangalli, D.; Berger, J. A.; Sottile, F.; Molinari, L. G.; Reining, L.; Onida, G. *J. Chem. Phys.* **2009**, *130*, 044108.

(129) Held, K.; Taranto, C.; Rohringer, G.; Toschi, A. In *LDA+DMFT approach to strongly Correl. Mater.* Pavarini, E., Koch, E., Vollhardt, D., Lichtenstein, A., Eds., 2011; Chapter 13, pp 13.1–13.22.

(130) Rohringer, G.; Valli, A.; Toschi, A. *Phys. Rev. B - Condens. Matter Mater. Phys.* **2012**, *86*, 125114.

(131) Maggio, E.; Kresse, G. *J. Chem. Theory Comput.* **2017**, *13*, 4765–4778.

(132) Rieger, M. M.; Steinbeck, L.; White, I. D.; Rojas, H. N.; Godby, R. W. *Comput. Phys. Commun.* **1999**, *117*, 211–228.

(133) H. N. Rojas; R.W.Godby; R. J.Needs *Phys. Rev. Lett.* **1995**, *74*, 1827–1831.

(134) Liu, P.; Kaltak, M.; Klimeš, J.; Kresse, G. *Phys. Rev. B* **2016**, *94*, 165109.

(135) Bruus, H.; Flensberg, K., *Many-Body Quantum Theory in Condensed Matter Physics: An Introduction*; OUP Oxford: Oxford, 2004.

(136) Engel, Eberhard and Dreizler, R. M., *Density functional theory An Advanced Course*; Springer: 2013.

(137) Stefanucci, G.; Pavlyukh, Y.; Uimonen, A. M.; van Leeuwen, R. *Phys. Rev. B* **2014**, *90*, 115134.

(138) Hüser, F.; Olsen, T.; Thygesen, K. S. *Phys. Rev. B - Condens. Matter Mater. Phys.* **2013**, *87*, 235132.

(139) Luttinger, J. M.; Nozières, P. *Phys. Rev.* **1962**, *127*, 1431–1440.

(140) Fabrizio, M. *Phys. Rev. B* **2020**, *102*, 155122.

(141) De Groot, H. J.; Bobbert, P. A.; van Haeringen, W. *Phys. Rev. B* **1995**, *52*, 11000–11007.

(142) Kotani, T.; van Schilfgaarde, M.; Faleev, S. V. *Phys. Rev. B* **2007**, *76*, 165106.

(143) Kaltak, M. M. Merging GW with DMFT, Ph.D. Thesis, Universität Wien, 2015.

(144) Sham, L. J.; Kohn, W. *Phys. Rev.* **1966**, *145*, 561–567.

(145) Galitskii, M. V.; A. B. Migdal *Sov. Phys. JETP* **1958**, *7*, 96–104.

(146) Layzer, A. J. *Phys. Rev.* **1963**, *129*, 897–907.

(147) Ashcroft, N. W.; Mermin, N. D. Solid State Physics, Toronto, 1976.

(148) Strinati, G.; Mattausch, H. J.; Hanke, W. *Phys. Rev. B* **1982**, *25*, 2867–2888.

(149) Hanke, W.; Sham, L. J. *Phys. Rev. Lett.* **1974**, *33*, 582–585.

(150) Hanke, W.; Sham, L. J. *Phys. Rev. B* **1975**, *12*, 4501–4511.

(151) Hanke, W.; Sham, L. J. *Phys. Rev. Lett.* **1979**, *43*, 387–390.

(152) Hanke, W.; Sham, L. J. *Phys. Rev. B* **1980**, *21*, 4656–4673.

(153) Sham, L. J.; Rice, T. M. *Phys. Rev.* **1966**, *144*, 708–714.

(154) Mattausch, H. J.; Hanke, W.; Strinati, G. *Phys. Rev. B* **1982**, *26*, 2302–2305.

(155) Strinati, G. *Phys. Rev. Lett.* **1982**, *49*, 1519–1522.

(156) Strinati, G. *Phys. Rev. B* **1984**, *29*, 5718–5726.

(157) Onida, G.; Reining, L.; Godby, R. W.; Del Sole, R.; Andreoni, W. *Phys. Rev. Lett.* **1995**, *75*, 818–821.

(158) Rohlfing, M.; Louie, S. G. *Phys. Rev. Lett.* **1998**, *80*, 3320–3323.

(159) Ma, Y.; Rohlfing, M.; Molteni, C. *Phys. Rev. B - Condens. Matter Mater. Phys.* **2009**, *80*, 241405(R).

(160) Baumeier, B.; Andrienko, D.; Rohlfing, M. *J. Chem. Theory Comput.* **2012**, *8*, 2790–2795.

(161) Baumeier, B.; Andrienko, D.; Ma, Y.; Rohlfing, M. *J. Chem. Theory Comput.* **2012**, *8*, 997–1002.

(162) Rohlfing, M.; Louie, S. G. *Phys. Rev. B* **2000**, *62*, 4927–4944.

(163) Loos, P.-F.; Blase, X. *J. Chem. Phys.* **2020**, *153,* 114120.

(164) Cudazzo, P.; Reining, L. *Phys. Rev. Res.* **2020**, *2*, 012032(R).

(165) Authier, J.; Loos, P.-F. *J. Chem. Phys.* **2021**, *153*, 184105.

(166) Godby, R. W.; Schlüter, M.; Sham, L. J. *Phys. Rev. B* **1988**, *37*, 10159–10175.

(167) Hellgren, M.; Baguet, L.; Calandra, M.; Mauri, F.; Wirtz, L. *Phys. Rev. B* **2021**, *103*, 075101.

(168) Riemelmoser, S.; Kaltak, M.; Kresse, G. *J. Chem. Phys.* **2021**, *154*, 154103.

(169) Vacondio, S.; Varsano, D.; Ruini, A.; Ferretti, A. *J. Chem. Theory Comput.* **2022**, *18*, 3703–3717.

(170) Kümmel, S.; Kronik, L. *Rev. Mod. Phys.* **2008**, *80*, 3–60.

(171) Talman, J. D.; Shadwick, W. F. *Phys. Rev. A* **1976**, *14*, 36–40.

(172) Casida, M. E. *Phys. Rev. A* **1995**, *51*, 2005–2013.

(173) Jin, Y.; Zhang, D.; Chen, Z.; Su, N. Q.; Yang, W. *J. Phys. Chem. Lett.* **2017**, *8*, 4746–4751.

(174) Faleev, S. V.; van Schilfgaarde, M.; Kotani, T. *Phys. Rev. Lett.* **2004**, *93*, 126406.

(175) Van Schilfgaarde, M.; Kotani, T.; Faleev, S. *Phys. Rev. Lett.* **2006**, *96*, 226402.

(176) Shishkin, M.; Marsman, M.; Kresse, G. *Phys. Rev. Lett.* **2007**, *99*, 246403.

(177) Shishkin, M.; Kresse, G. *Phys. Rev. B - Condens. Matter Mater. Phys.* **2007**, *75*, 235102.

(178) Levy, M.; Perdew, J. P.; Sahni, V. *Phys. Rev. A* **1984**, *30*, 2745–2748.

(179) Almbladh, C. O.; Von Barth, U. *Phys. Rev. B* **1985**, *31*, 3231–3244.

(180) Runge, E.; Gross, E. K. *Phys. Rev. Lett.* **1984**, *52*, 997.

(181) Mardirossian, N.; Head-Gordon, M. *Mol. Phys.* **2017**, *115*, 2315–2372.

(182) Vosko, S. H.; Wilk, L.; Nusair, M. *Can. J. Phys.* **1980**, *58*, 1200–1211.

(183) Ma, S. K.; Brueckner, K. A. *Phys. Rev.* **1968**, *165*, 18–31.

(184) Herman, F.; van Dyke, J. P.; Ortenburger, I. B. *Phys. Rev. Lett.* **1969**, *22*, 807–811.

(185) Becke, A. D. *J. Chem. Phys.* **1986**, *84*, 4524–4529.

(186) Becke, A. D. *J. Chem. Phys.* **1986**, *85*, 7184–7187.

(187) Becke, A. D.; Dickson, R. M. *J. Chem. Phys.* **1988**, *89*, 2993–2997.

(188) Perdew, J. P. *Phys. Rev. B* **1986**, *33*, 8822–8824.

(189) Perdew, J. P.; Burke, K.; Ernzerhof, M. *Phys. Rev. Lett.* **1996**, *77*, 3865–3868.

(190) Perdew, J. P.; Ernzerhof, M.; Burke, K. *Phys. Rev. Lett.* **1996**, *77*, 3865–3868.

(191) Tao, J.; Perdew, J. P.; Staroverov, V. N.; Scuseria, G. E. *Phys. Rev. Lett.* **2003**, *91*, 146401.

(192) Adamo, C.; Barone, V. *J. Chem. Phys.* **1999**, *110*, 6158–6170.

(193) Ernzerhof, M.; Scuseria, G. E. *J. Chem. Phys.* **1999**, *110*, 5029.

(194) Zhao, Y.; Truhlar, D. G. *Theor. Chem. Acc.* **2008**, *120*, 215–241.

(195) Csonka, G. I.; Perdew, J. P.; Ruzsinszky, A. *J. Chem. Theory Comput.* **2010**, *6*, 3688–3703.

(196) Savin, A.; Flad, H.-J. .-. *Int. J. Quantum Chem.* **1995**, *56*, 327–332.

(197) Leininger, T.; Stoll, H.; Werner, H. J.; Savin, A. *Chem. Phys. Lett.* **1997**, *275*, 151–160.

(198) Yanai, T.; Tew, D. P.; Handy, N. C. *Chem. Phys. Lett.* **2004**, *393*, 51–57.

(199) Chai, J. D.; Head-Gordon, M. *J. Chem. Phys.* **2009**, *131*, 174105.

(200) Rohrdanz, M. A.; Martins, K. M.; Herbert, J. M. *J. Chem. Phys.* **2009**, *130*, 054112.

(201) Stein, T.; Eisenberg, H.; Kronik, L.; Baer, R. *Phys. Rev. Lett.* **2010**, *105*, 266802.

(202) Refaely-Abramson, S.; Baer, R.; Kronik, L. *Phys. Rev. B - Condens. Matter Mater. Phys.* **2011**, *84*, 075144.

(203) Refaely-Abramson, S.; Sharifzadeh, S.; Govind, N.; Autschbach, J.; Neaton, J. B.; Baer, R.; Kronik, L. *Phys. Rev. Lett.* **2012**, *109*, 226405.

(204) Kronik, L.; Stein, T.; Refaely-Abramson, S.; Baer, R. *J. Chem. Theory Comput.* **2012**, *8*, 1515–1531.

(205) Prokopiou, G.; Hartstein, M.; Govind, N.; Kronik, L. *J. Chem. Theory Comput.* **2022**, *18*, 2331–2340.

(206) Karolewski, A.; Kronik, L.; Kümmel, S. *J. Chem. Phys.* **2013**, *138*, 204115.

(207) Grimme, S.; Ehrlich, S.; Goerigk, L. *J. Comput. Chem.* **2011**, *32*, 1456–1465.

(208) Santra, G.; Sylvetsky, N.; Martin, J. M. *J. Phys. Chem. A* **2019**, *123*, 5129–5143.

(209) Stöhr, M.; Van Voorhis, T.; Tkatchenko, A. *Chem. Soc. Rev.* **2019**, *48*, 4118–4154.

(210) Engel, E.; Facco Bonetti, A.; Keller, S.; Andrejkovics, I.; Dreizler, R. M. *Phys. Rev. A* **1998**, *58*, 964–992.

(211) Casimir, H. B. G.; Polder, D. *Phys. Rev.* **1948**, *73*, 360–372.

(212) Grimme, S. *J. Comput. Chem.* **2004**, *25*, 1463–1473.

(213) Grimme, S.; Antony, J.; Ehrlich, S.; Krieg, H. *J. Chem. Phys.* **2010**, *132*, 154104.

(214) Becke, A. D.; Johnson, E. R. *J. Chem. Phys.* **2005**, *123*, 154101.

(215) Becke, A. D.; Johnson, E. R. *J. Chem. Phys.* **2006**, *124*, 014104.

(216) Grimme, S. *J. Chem. Phys.* **2006**, *124*, 034108.

(217) Goerigk, L.; Grimme, S. *Wiley Interdiscip. Rev. Comput. Mol. Sci.* **2014**, *4*, 576–600.

(218) Förster, A.; Visscher, L. *J. Comput. Chem.* **2020**, *41*, 1660–1684.

(219) Chai, J. D.; Head-Gordon, M. *J. Chem. Phys.* **2008**, *128*, 084106.

(220) Casanova-Páez, M.; Dardis, M. B.; Goerigk, L. *J. Chem. Theory Comput.* **2019**, *15*, 4735–4744.

(221) Kalai, C.; Toulouse, J. *J. Chem. Phys.* **2018**, *148*, 164105.

(222) Mester, D.; Kállay, M. *J. Chem. Theory Comput.* **2021**, *17*, 4211–4224.

(223) Mester, D.; Mihaly, K. *J. Chem. Theory Comput.* **2021**, *17*, 927–942.

(224) Bruneval, F.; Vast, N.; Reining, L. *Phys. Rev. B - Condens. Matter Mater. Phys.* **2006**, *74*, 045102.

(225) Hybertsen, M. S.; Louie, S. G. *Phys. Rev. B* **1986**, *34*, 5390.

(226) Larson, P.; Dvorak, M.; Wu, Z. *Phys. Rev. B - Condens. Matter Mater. Phys.* **2013**, *88*, 125205.

(227) Niquet, Y. M.; Gonze, X. *Phys. Rev. B - Condens. Matter Mater. Phys.* **2004**, *70*, 245115.

(228) Von Barth, U.; Holm, B. *Phys. Rev. B - Condens. Matter Mater. Phys.* **1996**, *54*, 8411–8419.

(229) Holm, B.; von Barth, U. *Phys. Rev. B - Condens. Matter Mater. Phys.* **1998**, *57*, 2108–2117.

(230) García-González, P.; Godby, R. W. *Phys. Rev. B - Condens. Matter Mater. Phys.* **2001**, *63*, 075112.

(231) Shirley, E. L. *Phys. Rev. B - Condens. Matter Mater. Phys.* **1996**, *54*, 7758–7764.

(232) Schöne, W. D.; Eguiluz, A. G. *Phys. Rev. Lett.* **1998**, *81*, 1662–1665.

(233) Caruso, F.; Rohr, D. R.; Hellgren, M.; Ren, X.; Rinke, P.; Rubio, A.; Scheffler, M. *Phys. Rev. Lett.* **2013**, *110*, 146403.

(234) Hellgren, M.; Caruso, F.; Rohr, D. R.; Ren, X.; Rubio, A.; Scheffler, M.; Rinke, P. *Phys. Rev. B - Condens. Matter Mater. Phys.* **2015**, *91*, 165110.

(235) Stan, A.; Dahlen, N. E.; Van Leeuwen, R. *Europhys. Lett.* **2006**, *76*, 298–304.

(236) Stan, A.; Dahlen, N. E.; van Leeuwen, R. *J. Chem. Phys.* **2009**, *130*, 114105.

(237) Ku, W.; Eguiluz, A. G. *Phys. Rev. Lett.* **2002**, *89*, 126401.

(238) Koval, P.; Foerster, D.; Sánchez-Portal, D. *Phys. Rev. B* **2014**, *89*, 155417.

(239) Bruneval, F.; Vast, N.; Reining, L.; Izquierdo, M.; Sirotti, F.; Barrett, N. *Phys. Rev. Lett.* **2006**, *97*, 267601.

(240) Bruneval, F.; Marques, M. *J. Chem. Theory Comput.* **2013**, *9*, 324–329.

(241) Caruso, F.; Dauth, M.; Van Setten, M. J.; Rinke, P. *J. Chem. Theory Comput.* **2016**, *12*, 5076–5087.

(242) Knight, J. W.; Wang, X.; Gallandi, L.; Dolgounitcheva, O.; Ren, X.; Ortiz, J. V.; Rinke, P.; Körzdörfer, T.; Marom, N. *J. Chem. Theory Comput.* **2016**, *12*, 615–626.

(243) Caruso, F.; Rinke, P.; Ren, X.; Scheffler, M.; Rubio, A. *Phys. Rev. B* **2012**, *86*, 081102(R).

(244) Caruso, F.; Rinke, P.; Ren, X.; Rubio, A.; Scheffler, M. *Phys. Rev. B* **2013**, *88*, 075105.

(245) Marom, N.; Caruso, F.; Ren, X.; Hofmann, O. T.; Körzdörfer, T.; Chelikowsky, J. R.; Rubio, A.; Scheffler, M.; Rinke, P. *Phys. Rev. B* **2012**, *86*, 245127.

(246) Richard, R. M.; Marshall, M. S.; Dolgounitcheva, O.; Ortiz, J. V.; Brédas, J. L.; Marom, N.; Sherrill, C. D. *J. Chem. Theory Comput.* **2016**, *12*, 595–604.

(247) Rostgaard, C.; Jacobsen, K. W.; Thygesen, K. S. *Phys. Rev. B* **2010**, *81*, 085103.

(248) Belić, J.; Förster, A.; Menzel, J. P.; Buda, F.; Visscher, L. *Phys. Chem. Chem. Phys.* **2022**, *24*, 197–210.

(249) Atalla, V.; Yoon, M.; Caruso, F.; Rinke, P.; Scheffler, M. *Phys. Rev. B - Condens. Matter Mater. Phys.* **2013**, *88*, 165122.

(250) Van Den Brink, J.; Sawatzky, G. A. *Europhys. Lett.* **2000**, *50*, 447–453.

(251) Van der Horst, J.; Bobbert, P. A.; de Jong, P.; Michels, M.; Brocks, G.; Kelly, P. *Phys. Rev. B - Condens. Matter Mater. Phys.* **2000**, *61*, 15817–15826.

(252) Molina-Sánchez, A.; Wirtz, L. *Phys. Rev. B - Condens. Matter Mater. Phys.* **2011**, *84*, 155413.

(253) Bhandari, C.; Lambrecht, W. *Phys. Rev. B - Condens. Matter Mater. Phys.* **2014**, *89*, 045109.

(254) Bhandari, C.; Lambrecht, W.; van Schilfgaarde, M. *Phys. Rev. B - Condens. Matter Mater. Phys.* **2015**, *91*, 125116.

(255) Baerends, E. J.; Gritsenko, O. V.; Van Meer, R. *Phys. Chem. Chem. Phys.* **2013**, *15*, 16408–16425.

(256) Körzdörfer, T.; Marom, N. *Phys. Rev. B - Condens. Matter Mater. Phys.* **2012**, *86*, 041110(R).

(257) Zhang, L.; Shu, Y.; Xing, C.; Chen, X.; Sun, S.; Huang, Y.; Truhlar, D. G. *J. Chem. Theory Comput.* **2022**, *18*, 3523–3537.

(258) Blase, X.; Attaccalite, C.; Olevano, V. *Phys. Rev. B* **2011**, *83*, 115103.

(259) Faber, C.; Janssen, J. L.; Côté, M.; Runge, E.; Blase, X. *Phys. Rev. B* **2011**, *84*, 155104.

(260) Blase, X.; Attaccalite, C. *Appl. Phys. Lett.* **2011**, *99*, 171909.

(261) Faber, C.; Attaccalite, C.; Olevano, V.; Runge, E.; Blase, X. *Phys. Rev. B* **2011**, *81*, 115123.

(262) Duchemin, I.; Deutsch, T.; Blase, X. *Phys. Rev. Lett.* **2012**, *109*, 167801.

(263) Boulanger, P.; Jacquemin, D.; Duchemin, I.; Blase, X. *J. Chem. Theory Comput.* **2014**, *10*, 1212–1218.

(264) Faber, C.; Boulanger, P.; Attaccalite, C.; Cannuccia, E.; Duchemin, I.; Deutsch, T.; Blase, X. *Phys. Rev. B* **2015**, *91*, 155109.

(265) Jacquemin, D.; Duchemin, I.; Blase, X. *J. Chem. Theory Comput.* **2015**, *11*, 3290–3304.

(266) Rangel, T.; Hamed, S. M.; Bruneval, F.; Neaton, J. B. *J. Chem. Theory Comput.* **2016**, *12*, 2834–2842.

(267) De Queiroz, T. B.; De Figueroa, E. R.; Coutinho-Neto, M. D.; Maciel, C. D.; Tapavicza, E.; Hashemi, Z.; Leppert, L. *J. Chem. Phys.* **2021**, *154*, 044106.

(268) Hashemi, Z.; Leppert, L. *J. Phys. Chem. A* **2021**, *125*, 2163–2172.

(269) Wilhelm, J.; Seewald, P.; Golze, D. *J. Chem. Theory Comput.* **2021**, *17*, 1662–1677.

(270) Ismail-Beigi, S. *J. Phys. Condens. Matter* **2017**, *29*, 385501.

(271) Choi, S.; Kutepov, A. L.; Haule, K.; van Schilfgaarde, M.; Kotliar, G. *npj quantum Mater.* **2016**, *1*, 16001.

(272) Kutepov, A. L.; Oudovenko, V. S.; Kotliar, G. *Comput. Phys. Commun.* **2017**, *219*, 407–414.

(273) Peter Kopietz, *Bosonization of Interacting Fermions in Arbitrary Dimensions, Chapter 1*; Springer: 1997.

(274) Klimeš, J.; Kresse, G. *J. Chem. Phys.* **2014**, *140*, 054516.

(275) Lee, Y.; Kotani, T.; Ke, L. *Phys. Rev. B* **2020**, *101*, 241409(R).

(276) Ke, S. H. *Phys. Rev. B* **2011**, *84*, 205415.

(277) Gui, X.; Holzer, C.; Klopper, W. *J. Chem. Theory Comput.* **2018**, *14*, 2127–2136.

(278) Marom, N.; Moussa, J. E.; Ren, X.; Tkatchenko, A.; Chelikowsky, J. R. *Phys. Rev. B - Condens. Matter Mater. Phys.* **2011**, *84*, 245115.

(279) Migani, A.; Mowbray, D. J.; Iacomino, A.; Zhao, J.; Petek, H.; Rubio, A. *J. Am. Chem. Soc.* **2013**, *135*, 11429–11432.

(280) Migani, A.; Mowbray, D. J.; Zhao, J.; Petek, H.; Rubio, A. *J. Chem. Theory Comput.* **2014**, *10*, 2103–2113.

(281) Marom, N.; Körzdörfer, T.; Ren, X.; Tkatchenko, A.; Chelikowsky, J. R. *J. Phys. Chem. Lett.* **2014**, *5*, 2395–2401.

(282) Tal, A.; Chen, W.; Pasquarello, A. *Phys. Rev. B* **2021**, *103*, 161104.

(283) Chantis, A. N.; van Schilfgaarde, M.; Kotani, T. *Phys. Rev. Lett.* **2006**, *96*, 086405.

(284) Svane, A.; Christensen, N. E.; Gorczyca, I.; van Schilfgaarde, M.; Chantis, A. N.; Kotani, T. *Phys. Rev. B - Condens. Matter Mater. Phys.* **2010**, *82*, 115102.

(285) Bruneval, F. *J. Chem. Theory Comput.* **2019**, *15*, 4069–4078.

(286) Bruneval, F. *Phys. Rev. B* **2019**, *99*, 041118(R).

(287) Bruneval, F.; Rodriguez-Mayorga, M.; Rinke, P.; Dvorak, M. *J. Chem. Theory Comput.* **2021**, *17*, 2126–2136.

(288) Faber, C.; Boulanger, P.; Duchemin, I.; Attaccalite, C.; Blase, X. *J. Chem. Phys.* **2013**, *139*, 194308.

(289) Ward, J. C. *Phys. Rev.* **1950**, *78*, 182.

(290) Dahlen, N. E.; van Leeuwen, R.; von Barth, U. *Phys. Rev. A - At. Mol. Opt. Phys.* **2006**, *73*, 012511.

(291) Langreth, D. C.; Perdew, J. P. *Phys. Rev. B* **1977**, *15*, 2884–2901.

(292) Romaniello, P.; Guyot, S.; Reining, L. *J. Chem. Phys.* **2009**, *131*, 154111.

(293) Pavlyukh, Y.; Stefanucci, G.; van Leeuwen, R. *Phys. Rev. B* **2020**, *102*, 045121.

(294) Mejuto-Zaera, C.; Vlček, V. *arXiv:2203.05029* **2022**.

(295) Reining, L. *Wiley Interdiscip. Rev. Comput. Mol. Sci.* **2018**, *8*, e1344.

(296) Golze, D.; Dvorak, M.; Rinke, P. *Front. Chem.* **2019**, *7*, 377.

(297) Mejuto-Zaera, C.; Weng, G.; Romanova, M.; Cotton, S. J.; Whaley, K. B.; Tubman, N. M.; Vlček, V. *J. Chem. Phys.* **2021**, *154*, 121101.

(298) Jiang, H.; Engel, E. *J. Chem. Phys.* **2007**, *127*, 184108.

(299) Ren, X.; Rinke, P.; Joas, C.; Scheffler, M. *J. Mater. Sci.* **2012**, *47*, 7447–7471.

(300) Irmler, A.; Gallo, A.; Hummel, F.; Grüneis, A. *Phys. Rev. Lett.* **2019**, *123*, 156401.

(301) Loos, P. F.; Romaniello, P.; Berger, J. A. *J. Chem. Theory Comput.* **2018**, *14*, 3071–3082.

(302) Nelson, W.; Bokes, P.; Rinke, P.; Godby, R. W. *Phys. Rev. A - At. Mol. Opt. Phys.* **2007**, *75*, 032505.

(303) Fernandez, J. J. *Phys. Rev. A - At. Mol. Opt. Phys.* **2009**, *79*, 052513.

(304) Singwi, K. S.; Tosi, M. P.; Land, R. H.; Sjölander, A. *Phys. Rev.* **1968**, *176*, 589–599.

(305) Hummel, F.; Grüneis, A.; Kresse, G.; Ziesche, P. *J. Chem. Theory Comput.* **2019**, *15*, 3223–3236.

(306) Møller, C.; Plesset, M. *Phys. Rev.* **1934**, *46*, 618-622.

(307) Smith, R. A. *Phys. Rev. A* **1992**, *46*, 4586–4597.

(308) Krien, F.; Kauch, A.; Held, K. *Phys. Rev. Res.* **2021**, *3*, 13149.

(309) Minnhagen, P. *J. Phys. C Solid State Phys.* **1974**, *7*, 3013–3019.

(310) Verdozzi, C.; Godby, R. W.; Holloway, S. *Phys. Rev. Lett.* **1995**, *74*, 2327–2330.

(311) Schindlmayr, A.; Godby, R. W. *Phys. Rev. Lett.* **1998**, *80*, 1702–1705.

(312) Schindlmayr, A.; Pollehn, T. J.; Godby, R. *Phys. Rev. B - Condens. Matter Mater. Phys.* **1998**, *58*, 12684–12690.

(313) Daling, R.; Unger, P.; Fulde, P.; van Haeringen, W. *Phys. Rev. B* **1991**, *43*, 1851–1854.

(314) De Groot, H.; Ummels, R.; Bobbert, P.; Haeringen, W. V. *Phys. Rev. B - Condens. Matter Mater. Phys.* **1996**, *54*, 2374–2380.

(315) Bobbert, P. A.; Van Haeringen, W. *Phys. Rev. B* **1994**, *49*, 10326–10331.

(316) Sole, R.; Reining, L.; Godby, R. *Phys. Rev. B* **1994**, *49*, 8024–8028.

(317) Ummels, R.; Bobbert, P. A.; van Haeringen, W. *Phys. Rev. B - Condens. Matter Mater. Phys.* **1998**, *57*, 11962–11973.

(318) Bechstedt, F.; Tenelsen, K.; Adolph, B.; Del Sole, R. *Phys. Rev. Lett.* **1997**, *78*, 1528–1531.

(319) Lewis, A. M.; Berkelbach, T. C. *J. Chem. Theory Comput.* **2019**, *15*, 2925–2932.

(320) Engel, G. E.; Farid, B. *Phys. Rev. B* **1993**, *47*, 15931–15934.

(321) Kurth, S.; Perdew, J. P.; Blaha, P. *Int. J. Quantum Chem.* **1999**, *75*, 889–909.

(322) Yan, Z.; Perdew, J. P.; Kurth, S. *Phys. Rev. B - Condens. Matter Mater. Phys.* **2000**, *61*, 16430–16439.

(323) Angyan, J. G.; Gerber, I. C.; Savin, A.; Toulouse, J. *Phys. Rev. A* **2005**, *72*, 012510.

(324) Janesko, B. G.; Henderson, T. M.; Scuseria, G. E. *J. Chem. Phys.* **2009**, *130*, 081105.

(325) Janesko, B. G.; Henderson, T. M.; Scuseria, G. E. *J. Chem. Phys.* **2009**, *131*, 034110.

(326) Toulouse, J.; Gerber, I. C.; Jansen, G.; Savin, A.; Ángyán, J. G. *Phys. Rev. Lett.* **2009**, *102*, 096404.

(327) Zhu, W.; Toulouse, J.; Savin, A.; Ángyán, J. G. *J. Chem. Phys.* **2010**, *132*, 244108.

(328) Toulouse, J.; Zhu, W.; Ángyán, J. G.; Savin, A. *Phys. Rev. A - At. Mol. Opt. Phys.* **2010**, *82*, 032502.

(329) Toulouse, J.; Zhu, W.; Savin, A.; Jansen, G.; Ángyán, J. G. *J. Chem. Phys.* **2011**, *135*, 084119.

(330) Bruneval, F. *Phys. Rev. Lett.* **2012**, *108*, 256403.

(331) Beuerle, M.; Ochsenfeld, C. *J. Chem. Phys.* **2017**, *147*, 204107.

(332) Ren, X.; Tkatchenko, A.; Rinke, P.; Scheffler, M. *Phys. Rev. Lett.* **2011**, *106*, 153003.

(333) Paier, J.; Ren, X.; Rinke, P.; Scuseria, G. E.; Grüneis, A.; Kresse, G.; Scheffler, M. *New J. Phys.* **2012**, *14*, 043002.

(334) Ren, X.; Rinke, P.; Scuseria, G. E.; Scheffler, M. *Phys. Rev. B - Condens. Matter Mater. Phys.* **2013**, *88*, 035120.

(335) Heßelmann, A.; Görling, A. *Mol. Phys.* **2011**, *109*, 2473–2500.

(336) Petersilka, M.; Gossmann, U. J.; Gross, E. K. *Phys. Rev. Lett.* **1996**, *76*, 1212–1215.

(337) Hellgren, M.; Von Barth, U. *Phys. Rev. B* **2007**, *76*, 075107.

(338) Hellgren, M.; Von Barth, U. *Phys. Rev. B - Condens. Matter Mater. Phys.* **2008**, *78*, 115107.

(339) Heßelmann, A.; Görling, A. *Mol. Phys.* **2010**, *108*, 359–372.

(340) Heßelmann, A.; Görling, A. *Phys. Rev. Lett.* **2011**, *106*, 093001.

(341) Bates, J. E.; Furche, F. *J. Chem. Phys.* **2013**, *139*, 171103.

(342) Bleiziffer, P.; Krug, M.; Görling, A. *J. Chem. Phys.* **2015**, *142*, 244108.

(343) Mussard, B.; Rocca, D.; Jansen, G.; Ángyán, J. G. *J. Chem. Theory Comput.* **2016**, *12*, 2191–2202.

(344) Erhard, J.; Bleiziffer, P.; Görling, A. *Phys. Rev. Lett.* **2016**, *117*, 143002.

(345) Olsen, T.; Patrick, C. E.; Bates, J. E.; Ruzsinszky, A.; Thygesen, K. S. *Nat. Comput. Mater.* **2019**, *5*, 106.

(346) Görling, A. *Phys. Rev. B* **2019**, *99*, 235120.

(347) Maggio, E.; Kresse, G. *Phys. Rev. B* **2016**, *93*, 235113.

(348) Holzer, C.; Gui, X.; Harding, M. E.; Kresse, G.; Helgaker, T.; Klopper, W. *J. Chem. Phys.* **2018**, *149*, 144106 (2018).

(349) Loos, P.-F.; Scemama, A.; Duchemin, I.; Jacquemin, D.; Blase, X. *J. Phys. Chem. Lett.* **2020**, *11*, 3536–3545.

(350) Trushin, E.; Thierbach, A.; Görling, A. *J. Chem. Phys.* **2021**, *154*, 014104.

(351) Fauser, S.; Trushin, E.; Neiss, C.; Görling, A. *J. Chem. Phys.* **2021**, *155*, 134111.

(352) Sottile, F.; Olevano, V.; Reining, L. *Phys. Rev. Lett.* **2003**, *91*, 056402.

(353) Adragna, G.; Del Sole, R.; Marini, A. *Phys. Rev. B - Condens. Matter Mater. Phys.* **2003**, *68*, 165108.

(354) Marini, A.; Del Sole, R.; Rubio, A. *Phys. Rev. Lett.* **2003**, *91*, 256402.

(355) Sharma, S.; Dewhurst, J. K.; Sanna, A.; Gross, E. K. *Phys. Rev. Lett.* **2011**, *107*, 186401.

(356) Chen, W.; Pasquarello, A. *Phys. Rev. B - Condens. Matter Mater. Phys.* **2015**, *92*, 041115(R).

(357) Reining, L.; Olevano, V.; Rubio, A.; Onida, G. *Phys. Rev. Lett.* **2002**, *88*, 066404.

(358) Botti, S.; Fourreau, A.; Nguyen, F.; Renault, Y. O.; Sottile, F.; Reining, L. *Phys. Rev. B - Condens. Matter Mater. Phys.* **2005**, *72*, 125203.

(359) Hung, L.; Bruneval, F.; Baishya, K.; Öğüt, S. *J. Chem. Theory Comput.* **2017**, *13*, 2135–2146.

(360) Grüneis, A.; Kresse, G.; Hinuma, Y.; Oba, F. *Phys. Rev. Lett.* **2014**, *112*, 096401.

(361) Cunningham, B.; Grüning, M.; Azarhoosh, P.; Pashov, D.; van Schilfgaarde, M. *Phys. Rev. Mater.* **2018**, *2*, 034603.

(362) Cunningham, B.; Gruening, M.; Pashov, D.; van Schilfgaarde, M. *arXiv:2106.05759v1* **2021**.

(363) Radha, S. K.; Lambrecht, W.; Cunningham, B.; Grüning, M.; Pashov, D.; van Schilfgaarde, M. *Phys. Rev. B* **2021**, *104*, 115120.

(364) Acharya, S.; Pashov, D.; Cunningham, B.; Rudenko, A. N.; Rösner, M.; Grüning, M.; van Schilfgaarde, M.; Katsnelson, M. I. *Phys. Rev. B* **2021**, *104*, 155109.

(365) Hirata, S.; Head-Gordon, M. *Chem. Phys. Lett.* **1999**, *314*, 291–299.

(366) Acharya, S.; Pashov, D.; Rudenko, A. N.; Schilfgaarde, M. V. *npj 2D Mater. Appl.* **2022**, *6*, 33.

(367) Kutepov, A. L.; Kotliar, G. *Phys. Rev. B* **2017**, *96*, 035108.

(368) Kutepov, A. L. *Phys. Rev. B* **2017**, *95*, 195120.

(369) Kutepov, A. L. *arXiv:1809.06654v2* **2018**.

(370) Kutepov, A. L. *Phys. Rev. B* **2021**, *104*, 085109.

(371) Kutepov, A. L. *Phys. Rev. Mater.* **2021**, *5*, 083805.

(372) Kutepov, A. L. *Phys. Rev. B* **2022**, *105*, 045124.

(373) Ness, H.; Dash, L. K.; Stankovski, M.; Godby, R. W. *Phys. Rev. B - Condens. Matter Mater. Phys.* **2011**, *84*, 195114.

(374) Van Leeuwen, R.; Dahlen, N. E.; Stefanucci, G.; Almbladh, C. O.; Von Barth, U. In *Time-Dependent Density Funct. Theory*, Marques, M. A., Ullrich, C. A., Nogueira, F., Rubio, A., Burke, K., Gross, E. K., Eds.; Springer Heidelberg: 2015, pp 185–217.

(375) Pavlyukh, Y.; Uimonen, A. M.; Stefanucci, G.; van Leeuwen, R. *Phys. Rev. Lett.* **2016**, *117*, 206402.

(376) Bruneval, F.; Sottile, F.; Olevano, V.; Del Sole, R.; Reining, L. *Phys. Rev. Lett.* **2005**, *94*, 186402.

(377) Hung, L.; da Jornada, F. H.; Souto-Casares, J.; Chelikowsky, J. R.; Louie, S. G.; Öğüt, S. *Phys. Rev. B* **2016**, *94*, 085125.

(378) Schmidt, P. S.; Patrick, C. E.; Thygesen, K. S. *Phys. Rev. B* **2017**, *96*, 205206.

(379) Wang, Y.; Rinke, P.; Ren, X. *J. Chem. Theory Comput.* **2021**, *17*, 5140–5154.

(380) Freeman, D. *Phys. Rev. B* **1977**, *15*, 5512–5521.

(381) Ren, X.; Marom, N.; Caruso, F.; Scheffler, M.; Rinke, P. *Phys. Rev. B - Condens. Matter Mater. Phys.* **2015**, *92*, 081104(R).

(382) Vlček, V. *J. Chem. Theory Comput.* **2019**, *15*, 6254–6266.

(383) Bruneval, F.; Dattani, N.; van Setten, M. J. *Front. Chem.* **2021**, *9*, 749779.

(384) Jansen, G.; Liu, R. F.; Ángyán, J. G. *J. Chem. Phys.* **2010**, *133*, 154106.

(385) Paier, J.; Janesko, B. G.; Henderson, T. M.; Scuseria, G. E.; Grüneis, A.; Kresse, G. *J. Chem. Phys.* **2010**, *132*, 094103.

(386) Grüneis, A.; Marsman, M.; Harl, J.; Schimka, L.; Kresse, G. *J. Chem. Phys.* **2009**, *131*, 154115.

(387) Phillips, J. J.; Zgid, D. *J. Chem. Phys.* **2014**, *140*, 241101.

(388) Williams, K. T. et al. *Phys. Rev. X* **2020**, *10*, 11041.

(389) Lochan, R. C.; Head-Gordon, M. *J. Chem. Phys.* **2007**, *126*, 164101.

(390) Neese, F.; Schwabe, T.; Kossmann, S.; Schirmer, B.; Grimme, S. *J. Chem. Theory Comput.* **2009**, *5*, 3060–3073.

(391) Kossmann, S.; Neese, F. *J. Phys. Chem. A* **2010**, *114*, 11768–11781.

(392) Grüneis, A.; Marsman, M.; Kresse, G. *J. Chem. Phys.* **2010**, *133*, 074107.

(393) Nguyen, B. D.; Chen, G. P.; Agee, M. M.; Burow, A. M.; Tang, M. P.; Furche, F. *J. Chem. Theory Comput.* **2020**, *16*, 2258–2273.

(394) Jung, Y.; Lochan, R. C.; Dutoi, A. D.; Head-Gordon, M. *J. Chem. Phys.* **2004**, *121*, 9793–9802.

(395) Lochan, R. C.; Jung, Y.; Head-Gordon, M. *J. Phys. Chem. A* **2005**, *109*, 7598–7605.

(396) Grimme, S. *J. Chem. Phys.* **2003**, *118*, 9095–9102.

(397) Szabados, Á. *J. Chem. Phys.* **2006**, *125*, 214105.

(398) Pitoňák, M.; Neogrády, P.; Černý, J.; Grimme, S.; Hobza, P. *ChemPhysChem* **2009**, *10*, 282–289.

(399) Sedlak, R.; Janowski, T.; Pitoňák, M.; Řezáč, J.; Pulay, P.; Hobza, P. *J. Chem. Theory Comput.* **2013**, *9*, 3364–3374.

(400) Sedlak, R.; Riley, K. E.; Řezáč, J.; Pitoňák, M.; Hobza, P. *ChemPhysChem* **2013**, *14*, 698–707.

(401) Goldey, M.; Head-Gordon, M. *J. Phys. Chem. Lett.* **2012**, *3*, 3592–3598.

(402) Goldey, M.; Dutoi, A.; Head-Gordon, M. *Phys. Chem. Chem. Phys.* **2013**, *15*, 15869–15875.

(403) Goldey, M. B.; Belzunces, B.; Head-Gordon, M. *J. Chem. Theory Comput.* **2015**, *11*, 4159–4168.

(404) Lee, J.; Head-Gordon, M. *J. Chem. Theory Comput.* **2018**, *14*, 5203–5219.

(405) Pittner, J. *J. Chem. Phys.* **2003**, *118*, 10876.

(406) Keller, E.; Tsatsoulis, T.; Reuter, K.; Margraf, J. T. *J. Chem. Phys.* **2022**, *156*, 024106.

(407) Engel, E.; Jiang, H. *Int. J. Quantum Chem.* **2006**, *106*, 3242–3259.

(408) Jiang, H.; Engel, E. *J. Chem. Phys.* **2006**, *125*, 184108.

(409) Daas, T. J.; Fabiano, E.; Della Sala, F.; Gori-Giorgi, P.; Vuckovic, S. *J. Phys. Chem. Lett.* **2021**, *12*, 4867–4875.

(410) Daas, T. J.; Kooi, D. P.; Grooteman, A. J. A. F.; Seidl, M.; Gori-Giorgi, P. *J. Chem. Theory Comput.* **2022**, *18*, 1584–1594.

(411) Goerigk, L.; Grimme, S. *J. Chem. Theory Comput.* **2011**, *7*, 291–309.

(412) Brémond, É.; Sancho-García, J. C.; Pérez-Jiménez, Á. J.; Adamo, C. *J. Chem. Phys.* **2014**, *141*, 031101 (2014).

(413) Mehta, N.; Casanova-Páez, M.; Goerigk, L. *Phys. Chem. Chem. Phys.* **2018**, *20*, 23175–23194.

(414) Riplinger, C.; Sandhoefer, B.; Hansen, A.; Neese, F. *J. Chem. Phys.* **2013**, *139*, 134101.

(415) Riplinger, C.; Neese, F. *J. Chem. Phys.* **2013**, *138*, 034106.

(416) Nagy, P. R.; Kállay, M. *J. Chem. Phys.* **2017**, *146*, 214106.

(417) Visscher, L.; Lee, T. J.; Dyall, K. G. *J. Chem. Phys.* **1996**, *105*, 8769–8776.

(418) Willow, S. Y.; Kim, K. S.; Hirata, S. *J. Chem. Phys.* **2012**, *137*, 204122.

(419) Willow, S. Y.; Kim, K. S.; Hirata, S. *J. Chem. Phys.* **2013**, *138*, 164111.

(420) Doran, A. E.; Hirata, S. *J. Chem. Theory Comput.* **2019**, *15*, 6097–6110.

(421) Backhouse, O. J.; Nusspickel, M.; Booth, G. H. *J. Chem. Theory Comput.* **2020**, *16*, 1090–1104.

(422) Scuseria, G. E.; Henderson, T. M.; Sorensen, D. C. *J. Chem. Phys.* **2008**, *129*, 231101.

(423) Scuseria, G. E.; Henderson, T. M.; Bulik, I. W. *J. Chem. Phys.* **2013**, *139*, 104113.

(424) Kutepov, A. L. *Phys. Rev. B* **2016**, *94*, 155101.

(425) Kutepov, A.; Haule, K.; Savrasov, S. Y.; Kotliar, G. *Phys. Rev. B - Condens. Matter Mater. Phys.* **2012**, *85*, 155129.

(426) Chu, I. H.; Trinastic, J. P.; Wang, Y. P.; Eguiluz, A. G.; Kozhevnikov, A.; Schulthess, T. C.; Cheng, H. P. *Phys. Rev. B* **2016**, *93*, 125210.

(427) Grumet, M.; Liu, P.; Kaltak, M.; Klimeš, J.; Kresse, G. *Phys. Rev. B* **2018**, *98*, 155143.

(428) Kutepov, A. L. *Comput. Phys. Commun.* **2020**, *257*, 107502.

(429) Singh, Y.; Wang, L. W. *Phys. Rev. B* **2020**, *101*, 235157.

(430) Foerster, D.; Gueddida, S. *Comput. Mater. Sci.* **2021**, *187*, 110078.

(431) Koval, P.; Ljungberg, M. P.; Müller, M.; Sánchez-Portal, D. *J. Chem. Theory Comput.* **2019**, *15*, 4564–4580.

(432) Kim, M.; Martyna, G. J.; Ismail-Beigi, S. *Phys. Rev. B* **2020**, *101*, 035139.

(433) Duchemin, I.; Blase, X. *J. Chem. Theory Comput.* **2021**, *17*, 2383–2393.

(434) Neuhauser, D.; Gao, Y.; Arntsen, C.; Karshenas, C.; Rabani, E.; Baer, R. *Phys. Rev. Lett.* **2014**, *113*, 076402.

(435) Vlček, V.; Rabani, E.; Neuhauser, D.; Baer, R. *J. Chem. Theory Comput.* **2017**, *13*, 4997–5003.

(436) Vlček, V.; Li, W.; Baer, R.; Rabani, E.; Neuhauser, D. *Phys. Rev. B* **2018**, *98*, 075107.

(437) Vlček, V.; Baer, R.; Rabani, E.; Neuhauser, D. *J. Chem. Phys.* **2018**, *149*, 174107.

(438) Weng, G.; Vlček, V. *J. Chem. Phys.* **2021**, *155*, 054104.

(439) Fujita, T.; Noguchi, Y.; Hoshi, T. *J. Chem. Phys.* **2019**, *151*, 114109.

(440) Rabani, E.; Baer, R.; Neuhauser, D. *Phys. Rev. B - Condens. Matter Mater. Phys.* **2015**, *91*, 235302.

(441) Ljungberg, M. P.; Koval, P.; Ferrari, F.; Foerster, D.; Sánchez-Portal, D. *Phys. Rev. B - Condens. Matter Mater. Phys.* **2015**, *92*, 075422.

(442) Marsili, M.; Mosconi, E.; De Angelis, F.; Umari, P. *Phys. Rev. B* **2017**, *95*, 075415.

(443) Fujita, T.; Noguchi, Y. *J. Phys. Chem. A* **2021**, *125*, 10580–10592.

(444) Bradbury, N.; Nguyen, M.; Caram, J. R.; Neuhauser, D. *ArXiv:2205.06690v1* **2022**.

(445) Billingsley, F. P.; Bloor, J. E. *J. Chem. Phys.* **1971**, *55*, 5178–5190.

(446) Baerends, E. J.; Ellis, D. E.; Ros, P. *Chem. Phys.* **1973**, *2*, 41–51.

(447) Whitten, J. L. *J. Chem. Phys.* **1973**, *58*, 4496–4501.

(448) Sambe, H.; Felton, R. H. *J. Chem. Phys.* **1975**, *62*, 1122–1126.

(449) Dunlap, B. I.; Connolly, J. W.; Sabin, J. R. *J. Chem. Phys.* **1979**, *71*, 3396–3402.

(450) Dunlap, B. I.; Connolly, J. W.; Sabin, J. R. *J. Chem. Phys.* **1979**, *71*, 4993–4999.

(451) Vahtras, O.; Almlöf, J.; Feyereisen, M. W. *Chem. Phys. Lett.* **1993**, *213*, 514–518.

(452) Feyereisen, M.; Fitzgerald, G.; Komornicki, A. *Chem. Phys. Lett.* **1993**, *208*, 359–363.

(453) Krykunov, M.; Ziegler, T.; Van Lenthe, E. *Int. J. Quantum Chem.* **2009**, *109*, 1676–1683.

(454) Merlot, P.; Kjærgaard, T.; Helgaker, T.; Lindh, R.; Aquilante, F.; Reine, S.; Pedersen, T. B. *J. Comput. Chem.* **2013**, *34*, 1486–1496.

(455) Hollman, D. S.; Schaefer, H. F.; Valeev, E. F. *J. Chem. Phys.* **2014**, *140*, 064109.

(456) Mejía-Rodríguez, D.; Köster, A. M. *J. Chem. Phys.* **2014**, *141*, 124114.

(457) Manzer, S. F.; Epifanovsky, E.; Head-Gordon, M. *J. Chem. Theory Comput.* **2015**, *11*, 518–527.

(458) Lewis, C. A.; Calvin, J. A.; Valeev, E. F. *J. Chem. Theory Comput.* **2016**, *12*, 5868–5880.

(459) Rebolini, E.; Izsák, R.; Reine, S. S.; Helgaker, T.; Pedersen, T. B. *J. Chem. Theory Comput.* **2016**, *12*, 3514–3522.

(460) Hollman, D. S.; Schaefer, H. F.; Valeev, E. F. *Mol. Phys.* **2017**, *115*, 2065–2076.

(461) Wirz, L. N.; Reine, S. S.; Pedersen, T. B. *J. Chem. Theory Comput.* **2017**, *13*, 4897–4906.

(462) Lin, P.; Ren, X.; He, L. *J. Phys. Chem. Lett.* **2020**, *11*, 3082–3088.

(463) Del Ben, M.; da Jornada, F. H.; Antonius, G.; Rangel, T.; Louie, S. G.; Deslippe, J.; Canning, A. *Phys. Rev. B* **2019**, *99*, 125128.

(464) Baym, G.; Mermin, N. D. *J. Math. Phys.* **1961**, *2*, 232–234.

(465) Han, X. J.; Liao, H. J.; Xie, H. D.; Huang, R. Z.; Meng, Z. Y.; Xiang, T. *Chinese Phys. Lett.* **2017**, *34*, 077102.

(466) Shinaoka, H.; Otsuki, J.; Ohzeki, M.; Yoshimi, K. *Phys. Rev. B* **2017**, *96*, 035147.

(467) Levy, R.; LeBlanc, J. P.; Gull, E. *Comput. Phys. Commun.* **2017**, *215*, 149–155.

(468) Pulay, P. *Chem. Phys. Lett.* **1980**, *73*, 393–398.

(469) Pokhilko, P.; Yeh, C. N.; Zgid, D. *J. Chem. Phys.* **2022**, *156*, 094101.

(470) Froese Fischer, C., *Hartree–Fock method for atoms. A numerical approach*; John Wiley and Sons, Inc.: New York, 1977.

(471) Franchini, M.; Philipsen, P. H. T.; Van Lenthe, E.; Visscher, L. *J. Chem. Theory Comput.* **2014**, *10*, 1994–2004.

(472) Zapata, F.; Luppi, E.; Toulouse, J. *J. Chem. Phys.* **2019**, *150*, 234104.

(473) Kronik, L.; Makmal, A.; Tiago, M. L.; Alemany, M. M.; Jain, M.; Huang, X.; Saad, Y.; Chelikowsky, J. R. *Phys. Status Solidi Basic Res.* **2006**, *243*, 1063–1079.

(474) Tiago, M. L.; Chelikowsky, J. R. *Phys. Rev. B* **2006**, *73*, 205334.

(475) E. C. Titchmarsh In Oxford University Press: Oxford, 1962.

(476) Shull, H.; Löwdin, P. U. *J. Chem. Phys.* **1959**, *30*, 617–626.

(477) Calderini, D.; Cavalli, S.; Coletti, C.; Grossi, G.; Aquilanti, V. *J. Chem. Sci.* **2012**, *124*, 187–192.

(478) Aquilanti, V.; Caligiana, A.; Cavalli, S. *Int. J. Quantum Chem.* **2003**, *92*, 99–117.

(479) Herbst, M. F.; Dreuw, A.; Avery, J. E. *J. Chem. Phys.* **2018**, *149*, 084106.

(480) Herbst, M. F.; Avery, J. E.; Dreuw, A. *Phys. Rev. A* **2019**, *99*, 012512.

(481) Steinborn, E. O.; Weniger, E. J. *Int. J. Quantum Chem.* **1977**, *11*, 516.

(482) Steinborn, E. O.; Weniger, E. J. *Int. J. Quantum Chem.* **1978**, *14*, 103–108.

(483) Bouferguene, A.; Fares, M.; Rinaldi, D. *J. Chem. Phys.* **1994**, *100*, 8156–8168.

(484) Ransil, B. J. *Rev. Mod. Phys.* **1960**, *32*, 239–244.

(485) Clementi, E.; Raimondi, D. L. *J. Chem. Phys.* **1963**, *38*, 2686–2689.

(486) Raffenetti, R. C. *J. Chem. Phys.* **1973**, *59*, 5936–5949.

(487) Van Lenthe, E.; Baerends, J. E. *J. Comput. Chem.* **2003**, *24*, 1142–1156.

(488) Hehre, W. J.; Stewart, R. F.; Pople, J. A. *J. Chem. Phys.* **1969**, *51*, 2657–2664.

(489) Jensen, F. *Wiley Interdiscip. Rev. Comput. Mol. Sci.* **2013**, *3*, 273–295.

(490) Averill, F. W.; Ellis, D. E. *J. Chem. Phys.* **1973**, *59*, 6412–6418.

(491) Te Velde, G.; Baerends, E. J. *Phys. Rev. B* **1991**, *44*, 7888–7903.

(492) Blum, V.; Gehrke, R.; Hanke, F.; Havu, P.; Havu, V.; Ren, X.; Reuter, K.; Scheffler, M. *Comput. Phys. Commun.* **2009**, *180*, 2175–2196.

(493) Zhang, I. Y.; Ren, X.; Rinke, P.; Blum, V.; Scheffler, M. *New J. Phys.* **2013**, *15*, 123033.

(494) Berlu, L.; Safouhi, H. *J. Phys. A. Math. Gen.* **2003**, *36*, 11791–11805.

(495) Lovrod, J.; Safouhi, H. *Mol. Phys.* **2020**, *118*, 1619854.

(496) Te Velde, G.; Bickelhaupt, F. M.; Baerends, E. J.; Fonseca Guerra, C.; van Gisbergen, S.; Snijders, J. G.; Ziegler, T. *J. Comput. Chem.* **2001**, *22*, 931–967.

(497) Caffarel, M. *J. Chem. Phys.* **2019**, *151*, 064101.

(498) Blum, V.; Gehrke, R.; Hanke, F.; Havu, P.; Havu, V.; Ren, X.; Reuter, K.; Scheffler, M. The Fritz Haber Institute ab initio molecular simulations package (FHI-aims), http://www.fhi-berlin.mpg.de/aims, 2009.

(499) Ren, X.; Rinke, P.; Blum, V.; Wieferink, J.; Tkatchenko, A.; Sanfilippo, A.; Reuter, K.; Scheffler, M. *New J. Phys.* **2012**, *14*, 053020.

(500) Klimeš, J.; Kaltak, M.; Kresse, G. *Phys. Rev. B* **2014**, *90*, 075125.

(501) Van Setten, M. J.; Weigend, F.; Evers, F. *J. Chem. Theory Comput.* **2013**, *9*, 232–246.

(502) Varandas, A. J. *Annu. Rev. Phys. Chem.* **2018**, *69*, 177–203.

(503) Helgaker, T.; Klopper, W.; Koch, H.; Noga, J. *J. Chem. Phys.* **1997**, *106*, 9639–9646.

(504) Cohen, A. J.; Handy, N. C. *J. Chem. Phys.* **2002**, *117*, 1470–1478.

(505) Watson, M. A.; Handy, N. C.; Cohen, A. J. *J. Chem. Phys.* **2003**, *119*, 6475–6481.

(506) Watson, M. A.; Handy, N. C.; Cohen, A. J.; Helgaker, T. *J. Chem. Phys.* **2004**, *120*, 7252–7261.

(507) Chong, D. P.; Van Lenthe, E.; Van Gisbergen, S.; Baerends, E. J. *J. Comput. Chem.* **2004**, *25*, 1030–1036.

(508) Schwartz, C. *Phys. Rev.* **1962**, *126*, 1015–1019.

(509) Hill, R. N. *J. Chem. Phys.* **1985**, *83*, 1173–1196.

(510) Kutzelnigg, W.; Morgan III, J. D. *J. Chem. Phys.* **1992**, *96*, 4484.

(511) Halkier, A.; Helgaker, T.; Jørgensen, P.; Klopper, W.; Koch, H.; Olsen, J.; Wilson, A. K. *Chem. Phys. Lett.* **1998**, *286*, 243–252.

(512) Dunning, T. H. *J. Chem. Phys.* **1989**, *90*, 1007–1023.

(513) Dyall, K. G. *Theor. Chem. Acc.* **1998**, *99*, 366–371.

(514) Dyall, K. G. *Theor. Chem. Acc.* **2002**, *108*, 335–340.

(515) Dyall, K. G. *Theor. Chem. Acc.* **2004**, *112*, 403–409.

(516) Dyall, K. G. *Theor. Chem. Acc.* **2006**, *115*, 441–447.

(517) Gomes, A. S. P.; Dyall, K. G.; Visscher, L. *Theor. Chem. Acc.* **2010**, *127*, 369–381.

(518) Autschbach, J.; Ziegler, T. *J. Chem. Phys.* **2000**, *113*, 9410–9418.

(519) Reeves, C. M.; Harrison, M. C. *J. Chem. Phys.* **1963**, *39*, 1–10.

(520) Silver, D. M.; Nieuwpoort, W. C. *Chem. Phys. Lett.* **1978**, *57*, 421–422.

(521) Ren, X.; Merz, F.; Jiang, H.; Yao, Y.; Rampp, M.; Lederer, H.; Blum, V.; Scheffler, M. *Phys. Rev. Mater.* **2021**, *5*, 013807.

(522) Schulz, G. J. *Rev. Mod. Phys.* **1973**, *45*, 423–486.

(523) Jordan, K. D.; Burrow, P. D. *Acc. Chem. Res.* **1978**, *11*, 341–348.

(524) Aflatooni, K.; Gallup, G. A.; Burrow, P. D. *J. Phys. Chem. A* **1998**, *102*, 6205–6207.

(525) Tozer, D. J.; Proft, F. D. *J. Phys. Chem. A* **2005**, *109*, 8923–8929.

(526) Kendall, R. A.; Dunning, T. H.; Harrison, R. J. *J. Chem. Phys.* **1992**, *96*, 6796–6806.

(527) Zheng, J.; Xu, X.; Truhlar, D. G. *Theor. Chem. Acc.* **2011**, *128*, 295–305.

(528) Chong, D. P. *Mol. Phys.* **2005**, *103*, 749–761.

(529) Schmidt, E. *Math. Ann.* **1907**, *63*, 433–476.

(530) Eckart, C.; Young, G. *Psychometrika* **1936**, *1*, 211–218.

(531) Myrsky, L. *Q. J. Math.* **1960**, *11*, 50–59.

(532) Schutski, R.; Zhao, J.; Henderson, T. M.; Scuseria, G. E. *J. Chem. Phys.* **2017**, *147*, 184113.

(533) Weigend, F.; Häser, M.; Patzelt, H.; Ahlrichs, R. *Chem. Phys. Lett.* **1998**, *294*, 143–152.

(534) Hättig, C.; Weigend, F. *J. Chem. Phys.* **2000**, *113*, 5154–5161.

(535) Beebe, N. H.; Linderberg, J. *Int. J. Quantum Chem.* **1977**, *12*, 683–705.

(536) Koch, H.; Sánchez De Merás, A.; Pedersen, T. B. *J. Chem. Phys.* **2003**, *118*, 9481–9484.

(537) Aquilante, F.; Lindh, R.; Bondo Pedersen, T. *J. Chem. Phys.* **2007**, *127*, 114107.

(538) Boman, L.; Koch, H.; Sánchez De Merás, A. *J. Chem. Phys.* **2008**, *129*, 134107.

(539) Aquilante, F.; Gagliardi, L.; Pedersen, T. B.; Lindh, R. *J. Chem. Phys.* **2009**, *130*, 154107.

(540) Kaplan, F.; Harding, M. E.; Seiler, C.; Weigend, F.; Evers, F.; Van Setten, M. J. *J. Chem. Theory Comput.* **2016**, *12*, 2528–2541.

(541) Wilhelm, J.; Seewald, P.; Del Ben, M.; Hutter, J. *J. Chem. Theory Comput.* **2016**, *12*, 5851–5859.

(542) Bruneval, F.; Rangel, T.; Hamed, S. M.; Shao, M.; Yang, C.; Neaton, J. B. *Comput. Phys. Commun.* **2016**, *208*, 149–161.

(543) Krause, K.; Klopper, W. *J. Comput. Chem.* **2017**, *38*, 383–388.

(544) Tirimbò, G.; Sundaram, V.; Çaylak, O.; Scharpach, W.; Sijen, J.; Junghans, C.; Brown, J.; Ruiz, F. Z.; Renaud, N.; Wehner, J.; Baumeier, B. *J. Chem. Phys.* **2020**, *152*, 114103.

(545) Van Setten, M. J.; Caruso, F.; Sharifzadeh, S.; Ren, X.; Scheffler, M.; Liu, F.; Lischner, J.; Lin, L.; Deslippe, J. R.; Louie, S. G.; Yang, C.; Weigend, F.; Neaton, J. B.; Evers, F.; Rinke, P. *J. Chem. Theory Comput.* **2015**, *11*, 5665–5687.

(546) Eichkorn, K.; Treutler, O.; Öhm, H.; Häser, M.; Ahlrichs, R. *Chem. Phys. Lett.* **1995**, *240*, 283–290.

(547) Weigend, F. *Phys. Chem. Chem. Phys.* **2006**, *8*, 1057–1065.

(548) Jackson, J. D., *Classical electrodynamics*, 3rd; John Wiley and Sons, Inc.: 1999, pp 841–842.

(549) Klahn, B.; Bingel, W. A. *Int. J. Quantum Chem.* **1977**, *XI*, 943–957.

(550) Löwdin, P. O. *Rev. Mod. Phys.* **1967**, *39*, 259–287.

(551) Kudin, K. N.; Scuseria, G. E. *Phys. Rev. B* **2000**, *61*, 16440–16453.

(552) Suhai, S.; Bagus, P. S.; Ladik, J. *Chem. Phys.* **1982**, *68*, 467–471.

(553) Kudin, K. N.; Scuseria, G. E.; Cancès, E. *J. Chem. Phys.* **2002**, *116*, 8255–8261.

(554) Lehtola, S.; Blockhuys, F.; Van Alsenoy, C. *Molecules* **2020**, *25*, 1218.

(555) Schipper, P. R.; Gritsenko, O. V.; Van Gisbergen, S. J.; Baerends, E. J. *J. Chem. Phys.* **2000**, *112*, 1344–1352.

(556) De Jong, G. T.; Visscher, L. *Theor. Chem. Acc.* **2002**, *107*, 304–308.

(557) Almlöf, J.; Faegri, K.; Korsell, K. *J. Comput. Chem.* **1982**, *3*, 385–399.

(558) Kaltak, M.; Klimeš, J.; Kresse, G. *J. Chem. Theory Comput.* **2014**, *10*, 2498–2507.

(559) Helmich-Paris, B.; Visscher, L. *J. Comput. Phys.* **2016**, *321*, 927–931.

(560) Duchemin, I.; Blase, X. *J. Chem. Phys.* **2019**, *150*, 174120.

(561) Levenberg, K. *Q. Appl. Math.* **1944**, *2*, 164–168.

(562) Gill, P. E.; Murray, W. *SIAM J. Numer. Anal.* **1978**, *15*, 977–992.

(563) Braess, D.; Hackbusch, W. *IMA J. Numer. Anal.* **2005**, *25*, 685–697.

(564) Takatsuka, A.; Ten-no, S.; Hackbusch, W. *J. Chem. Phys.* **2008**, *129*, 044112.

(565) Govoni, M.; Galli, G. *J. Chem. Theory Comput.* **2015**, *11*, 2680–2696.

(566) Umari, P.; Stenuit, G.; Baroni, S. *Phys. Rev. B* **2009**, *79*, 201104(R).

(567) Nguyen, H. V.; Pham, T. A.; Rocca, D.; Galli, G. *Phys. Rev. B* **2012**, *85*, 081101(R).

(568) Pham, T. A.; Nguyen, H. V.; Rocca, D.; Galli, G. *Phys. Rev. B* **2013**, *87*, 155148.

(569) Shao, M. Y.; Lin, L.; Yang, C.; Liu, F.; da Jornada, F. H.; Deslippe, J.; Louie, S. G. *Sci. China Math.* **2016**, *59*, 1593–1612.

(570) Vidberg, H. J.; Serene, J. W. *J. Low Temp. Phys.* **1977**, *29*, 179–192.

(571) Beach, K. S. D.; Gooding, R. J.; Marsiglio, F. *Phys. Rev. B* **2000**, *61*, 5147–5157.

(572) Golze, D.; Wilhelm, J.; Van Setten, M. J.; Rinke, P. *J. Chem. Theory Comput.* **2018**, *14*, 4856–4869.

(573) Golze, D.; Keller, L.; Rinke, P. *J. Phys. Chem. Lett.* **2020**, *11*, 1840–1847.

(574) Govoni, M.; Galli, G. *J. Chem. Theory Comput.* **2018**, *14*, 1895–1909.

(575) Kaplan, F.; Weigend, F.; Evers, F.; Van Setten, M. J. *J. Chem. Theory Comput.* **2015**, *11*, 5152–5160.

(576) Bergeron, D.; Tremblay, A. M. *Phys. Rev. E* **2016**, *94*, 023303.

(577) Otsuki, J.; Ohzeki, M.; Shinaoka, H.; Yoshimi, K. *Phys. Rev. E* **2017**, *95*, 061302(R).

(578) Gull, E.; Iskakov, S.; Krivenko, I.; Rusakov, A. A.; Zgid, D. *Phys. Rev. B* **2018**, *98*, 075127.

(579) Fournier, R.; Wang, L.; Yazyev, O. V.; Wu, Q. S. *Phys. Rev. Lett.* **2020**, *124*, 56401.

(580) Fei, J.; Yeh, C. N.; Gull, E. *Phys. Rev. Lett.* **2021**, *126*, 56402.

(581) Golub, G. H.; van Loan, C. F., *Matrix computations.* 4th; John Hopkins university press: Baltimore, 2013.

(582) Szabo, A.; Ostlund, N. S., *Modern quantum chemistry: introduction to advanced electronic structure theory*; Dover Publications INC. New York: 2012.

(583) Cances, E.; Le Bris, C. *ESAIM Math. Model. Numer. Anal.* **2000**, *34*, 749–774.

(584) Koutecký, J.; Bonačić, V. *J. Chem. Phys.* **1971**, *55*, 2408–2413.

(585) Bonačić-Koutecký, V.; Koutecký, J. *Theor. Chim. Acta* **1975**, *36*, 149–161.

(586) Kozuch, S.; Martin, J. M. *Phys. Chem. Chem. Phys.* **2011**, *13*, 20104–20107.

(587) Rodríguez-Mayorga, M.; Mitxelena, I.; Bruneval, F.; Piris, M. *J. Chem. Theory Comput.* **2021**, *17*, 7562–7574.

(588) Dancoff, S. *Phys. Rev.* **1950**, *78*, 382–385.

(589) I.E.Tamm, *Selected Papers*; Bolotovskii, B., Frenkel, V., Peierls, R., Eds.; Springer, Berlin Heidelberg: 1991, pp 157–174.

(590) Zhang, X.; Achilles, S.; Winkelmann, J.; Haas, R.; Schleife, A.; Di Napoli, E. *Comput. Phys. Commun.* **2021**, *267*, 108081.

(591) Winkelmann, J.; Springer, P.; Di Napoli, E. *ACM Trans. Math. Softw.* **2019**, *45*, 21.

(592) Fuchs, F.; Rödl, C.; Schleife, A.; Bechstedt, F. *Phys. Rev. B - Condens. Matter Mater. Phys.* **2008**, *78*, 085103.

(593) Alliati, I. M.; Sangalli, D.; Grüning, M. *Front. Chem.* **2022**, *9*, 763946.

(594) Haydock, R. *Comput. Phys. Commun.* **1980**, *20*, 11–16.

(595) Davidson, E. R. *J. Comput. Phys.* **1975**, *17*, 87–94.

(596) Stratmann, R. E.; Scuseria, G. E.; Frisch, M. J. *J. Chem. Phys.* **1998**, *109*, 8218–8224.

(597) Van Gisbergen, S. J.; Snijders, J. G.; Baerends, E. J. *Comput. Phys. Commun.* **1999**, *118*, 119–138.

(598) Stuke, A.; Kunkel, C.; Golze, D.; Todorović, M.; Margraf, J. T.; Reuter, K.; Rinke, P.; Oberhofer, H. *Sci. Data* **2020**, *7*, 1–11.

(599) Bruneval, F.; Maliyov, I.; Lapointe, C.; Marinica, M.-C. *J. Chem. Theory Comput.* **2020**, *16*, 4399–4407.

(600) Balasubramani, S. G. et al. *J. Chem. Phys.* **2020**, 184107.

(601) Deslippe, J.; Samsonidze, G.; Strubbe, D. A.; Jain, M.; Cohen, M. L.; Louie, S. G. *Comput. Phys. Commun.* **2012**, *183*, 1269–1289.

(602) Kresse, G.; Hafner, J. *Phys. Rev. B* **1993**, *47*, 558–561.

(603) Kresse, G.; Furthmüller, J. *Phys. Rev. B* **1996**, *54*, 11169–11186.

(604) Kresse, G.; Furthmüller, J. *Comput. Mater. Sci.* **1996**, *6*, 15–50.

(605) Maggio, E.; Liu, P.; Van Setten, M. J.; Kresse, G. *J. Chem. Theory Comput.* **2017**, *13*, 635–648.

(606) Gao, W.; Chelikowsky, J. R. *J. Chem. Theory Comput.* **2019**, *15*, 5299–5307.

(607) Kühne, T. D. et al. *J. Chem. Phys.* **2020**, *152*, 194103.

(608) Weigend, F.; Ahlrichs, R. *Phys. Chem. Chem. Phys.* **2005**, *7*, 3297–3305.

(609) Schwerdtfeger, P. *ChemPhysChem* **2011**, *12*, 3143–3155.

(610) Scherpelz, P.; Govoni, M.; Hamada, I.; Galli, G. *J. Chem. Theory Comput.* **2016**, *12*, 3523–3544.

(611) Krause, K.; Harding, M. E.; Klopper, W. *Mol. Phys.* **2015**, *113*, 1952–1960.

(612) Lange, M. F.; Berkelbach, T. C. *J. Chem. Theory Comput.* **2018**, *14*, 4224–4236.

(613) Wilhelm, J.; Del Ben, M.; Hutter, J. *J. Chem. Theory Comput.* **2016**, *12*, 3623–3635.

(614) Jensen, F. *J. Chem. Phys.* **2002**, *116*, 7372–7379.

(615) Kraus, P. *J. Chem. Theory Comput.* **2020**, *16*, 5712–5722.

(616) Dunlap, B. I.; Mei, W. N. *J. Chem. Phys.* **1983**, *78*, 4997.

(617) Monino, E.; Loos, P.-F. *J. Chem. Phys.* **2022**, *231101*, DOI: 10.1063/5.0089317.

(618) Staneke, P. O.; Groothuis, G.; Ingemann, S.; Nibbering, N. M. *Int. J. Mass Spectrom. Ion Process.* **1995**, *142*, 83–93.

(619) Van Lenthe, E.; Baerends, E. J.; Snijders, J. G. *J. Chem. Phys.* **1993**, *99*, 4597.

(620) Van Lenthe, E.; Baerends, E. J.; Snijders, J. G. *J. Chem. Phys.* **1994**, *101*, 9783–9792.

(621) Van Lenthe, E.; Snijders, J. G.; Baerends, E. J. *J. Chem. Phys.* **1996**, *105*, 6505–6516.

(622) Harris, C. R. et al. *Nature* **2020**, *585*, 357–362.

(623) Izmaylov, A. F.; Staroverov, V. N.; Scuseria, G. E.; Davidson, E. R.; Stoltz, G.; Canc‘s, E. *J. Chem. Phys.* **2007**, *126*, 084107.

(624) Krieger, J. B.; Li, Y.; Iafrate, G. J. *Phys. Lett. A* **1990**, *146*, 256–260.

(625) Chakravorty, S. J.; Gwaltney, S. R.; Davidson, E. R.; Parpia, F. A.; Fischer, C. F. *Phys. Rev. A* **1993**, *47*, 3649–3670.

(626) Gould, T.; Ruzsinszky, A.; Perdew, J. P. *Phys. Rev. A* **2019**, *100*, 022515.

(627) McCarthy, S. P.; Thakkar, A. J. *J. Chem. Phys.* **2011**, *134*, 044102.

(628) Bruneval, F. *J. Chem. Phys.* **2012**, *136*, 194107.

(629) Furche, F. *Phys. Rev. B* **2001**, *64*, 195120.

(630) Furche, F. *J. Chem. Phys.* **2008**, *129*, 114105.

(631) Eshuis, H.; Bates, J. E.; Furche, F. *Theor. Chem. Acc.* **2012**, *131*, 1084.

(632) Chen, G. P.; Voora, V. K.; Agee, M. M.; Balasubramani, S. G.; Furche, F. *Annu. Rev. Phys. Chem.* **2017**, *68*, 421–445.

(633) Chedid, J.; Ferrara, N. M.; Eshuis, H. *Theor. Chem. Acc.* **2018**, *137:158*, 1–11.

(634) Kreppel, A.; Graf, D.; Laqua, H.; Ochsenfeld, C. *J. Chem. Theory Comput.* **2020**, *16*, 2985–2994.

(635) Řezáč, J.; Hobza, P. *Chem. Rev.* **2016**, *116*, 5038–5071.

(636) Dobson, J. F. *Int. J. Quantum Chem.* **2014**, *114*, 1157–1161.

(637) Zhang, I. Y.; Grüneis, A. *Front. Mater.* **2019**, *6*, 00123.

(638) Goerigk, L.; Hansen, A.; Bauer, C.; Ehrlich, S.; Najibi, A.; Grimme, S. *Phys. Chem. Chem. Phys.* **2017**, *19*, 32184–32215.

(639) Knowles, P. J.; Handy, N. C. *Chem. Phys. Lett.* **1984**, *111*, 315–321.

(640) Knowles, P. J.; Handy, N. C. *Comput. Phys. Commun.* **1989**, *54*, 75–83.

(641) Richard, R. M.; Marshall, M. S.; Dolgounitcheva, O.; Ortiz, J. V.; Brédas, J. L.; Marom, N.; Sherrill, C. D. *J. Chem. Theory Comput.* **2016**, *12*, 595–604.

(642) Kang, W.; Hybertsen, M. S. *Phys. Rev. B - Condens. Matter Mater. Phys.* **2010**, *82*, 085203.

(643) Punya, A.; Lambrecht, W.; van Schilfgaarde, M. *Phys. Rev. B - Condens. Matter Mater. Phys.* **2011**, *84*, 165204.

(644) Botti, S.; Marques, M. *Phys. Rev. Lett.* **2013**, *110*, 226404.

(645) Bechstedt, F.; Seino, K.; Hahn, P. H.; Schmidt, W. G. *Phys. Rev. B - Condens. Matter Mater. Phys.* **2005**, *72*, 245114.

(646) Ranasinghe, D. S.; Margraf, J. T.; Perera, A.; Bartlett, R. J. *J. Chem. Phys.* **2019**, *150*, 074108.

(647) Henderson, T. M.; Scuseria, G. E. *Mol. Phys.* **2010**, *108*, 2511–2517.

(648) Peterson, K. A.; Kendall, R. A.; Dunning, T. H. *J. Chem. Phys.* **1993**, *99*, 9790–9805.

(649) Hönisch, B.; Hemming, G. N.; Archer, D.; Sidall, M.; McManus, J. F. *Science (80-.).* **2009**, *324*, 1548–1552.

(650) Røeggen, I.; Veseth, L. Interatomic potential for the X1g+ state of Be2, revisited, 2005.

(651) Chen, G. P.; Agee, M. M.; Furche, F. *J. Chem. Theory Comput.* **2018**, *14*, 5701–5714.

(652) Karton, A.; Daon, S.; Martin, J. M. *Chem. Phys. Lett.* **2011**, *510*, 165–178.

(653) Karton, A.; Rabinovich, E.; Martin, J. M. *J. Chem. Phys.* **2006**, *125*, 144108.

(654) Zhao, Y.; Lynch, B. J.; Truhlar, D. G. *Phys. Chem. Chem. Phys.* **2005**, *7*, 43–52.

(655) Zhao, Y.; González-Garda, N.; Truhlar, D. G. *J. Phys. Chem. A* **2005**, *109*, 2012–2018.

(656) Karton, A.; Martin, J. M. *J. Chem. Phys.* **2012**, *136*, 124114.

(657) Curtiss, L. A.; Raghavachari, K.; Trucks, G. W.; Pople, J. A. *J. Chem. Phys.* **1991**, *94*, 7221–7230.

(658) Hellgren, M.; Rohr, D. R.; Gross, E. K. *J. Chem. Phys.* **2012**, *136*, 034106.

(659) Verma, P.; Bartlett, R. J. *J. Chem. Phys.* **2012**, *136*, 044105.

(660) Bleiziffer, P.; Heßelmann, A.; Görling, A. *J. Chem. Phys.* **2013**, *139*, 084113.

(661) Voora, V. K.; Balasubramani, S. G.; Furche, F. *Phys. Rev. A* **2019**, *99*, 012518.

(662) Graf, D.; Ochsenfeld, C. *J. Chem. Phys.* **2020**, *153*, 244118.

(663) Yu, J. M.; Tsai, J.; Hernandez, D. J.; Furche, F.; Tsai, J.; Hernandez, D. J. *J. Chem. Phys.* **2021**, *155*, 040902.

(664) Hait, D.; Head-Gordon, M. *J. Phys. Chem. Lett.* **2018**, *9*, 6280–6288.

(665) Paier, J.; Janesko, B. G.; Henderson, T. M.; Scuseria, G. E.; Grüneis, A.; Kresse, G. *J. Chem. Phys.* **2010**, *133*, 2009–2011.

(666) Řezáč, J.; Riley, K. E.; Hobza, P. *J. Chem. Theory Comput.* **2011**, *7*, 2427–2438.

(667) Becke, A. D. *J. Chem. Phys.* **2014**, *140*, 18A301.

(668) Beuerle, M.; Graf, D.; Schurkus, H. F.; Ochsenfeld, C. *J. Chem. Phys.* **2018**, *148*, 204104.

(669) Doser, B.; Lambrecht, D. S.; Kussmann, J.; Ochsenfeld, C. *J. Chem. Phys.* **2009**, *130*, 064107.

(670) Pinski, P.; Riplinger, C.; Valeev, E. F.; Neese, F. *J. Chem. Phys.* **2015**, *143*, 034108.

(671) Nagy, P. R.; Samu, G.; Kállay, M. *J. Chem. Theory Comput.* **2016**, *12*, 4897–4914.

(672) Mezei, P. D.; Ruzsinszky, A.; Kállay, M. *J. Chem. Theory Comput.* **2019**, *15*, 6607–6616.

(673) Pluhařová, E.; Slavíček, P.; Jungwirth, P. *Acc. Chem. Res.* **2015**, *48*, 1209–1217.

(674) Klamt, A.; Schüürmann, G. *J. Chem. Soc. Perkin Trans. 2* **1993**, 799–805.

(675) Klamt, A. *J. Phys. Chem.* **1995**, *99*, 2224–2235.

(676) Klamt, A.; Jonas, V. *J. Chem. Phys.* **1996**, *105*, 9972–9981.

(677) Pye, C. C.; Ziegler, T. *Theor. Chem. Acc.* **1999**, *101*, 396–408.

(678) Lee, C.; Yang, W.; Parr, R. G. *Phys. Rev. B* **1988**, *37*, 785–789.

(679) Miehlich, B.; Savi, A.; Stoll, H.; Preuss, H. *J. Pediatr. Urol.* **1989**, *157*, 200–206.

(680) Deglmann, P.; Schenk, S. *J. Comput. Chem.* **2012**, *33*, 1304–1320.

(681) Pluhařová, E.; Jungwirth, P.; Bradforth, S. E.; Slavíček, P. *J. Phys. Chem. B* **2011**, *115*, 1294–1305.

(682) Pluhařová, E.; Schroeder, C.; Seidel, R.; Bradforth, S. E.; Winter, B.; Faubel, M.; Slavíček, P.; Jungwirth, P. *J. Phys. Chem. Lett.* **2013**, *4*, 3766–3769.

(683) Boese, A. D.; Martin, J. M. *J. Chem. Phys.* **2004**, *121*, 3405–3416.

(684) Mirkovic, T.; Ostroumov, E. E.; Anna, J. M.; Van Grondelle, R.; Govindjee; Scholes, G. D. *Chem. Rev.* **2017**, *117*, 249–293.

(685) Kasha, M.; Rawls, H. R.; El-Bayoumi, M. A. *Pure Appl. Chem.* **1965**, *11*, 371–392.

(686) Reimers, J. R. et al. *Biochim. Biophys. Acta - Bioenerg.* **2016**, *1857*, 1627–1640.

(687) Yin, S.; Dahlbom, M. G.; Canfield, P. J.; Hush, N. S.; Kobayashi, R.; Reimers, J. R. *J. Phys. Chem. B* **2007**, *111*, 9923–9930.

(688) Renger, T.; Schlodder, E. *ChemPhysChem* **2010**, *11*, 1141–1153.

(689) Sirohiwal, A.; Neese, F.; Pantazis, D. A. *J. Am. Chem. Soc.* **2020**, *142*, 18174–18190.

(690) Kitagawa, Y.; Matsuda, K.; Hasegawa, J. Y. *Biophys. Chem.* **2011**, *159*, 227–236.

(691) Polyakov, I. V.; Khrenova, M. G.; Moskovsky, A. A.; Shabanov, B. M.; Nemukhin, A. V. *Chem. Phys.* **2018**, *505*, 34–39.

(692) Reimers, J. R.; Cai, Z. L.; Kobayashi, R.; Rätsep, M.; Freiberg, A.; Krausz, E. *Sci. Rep.* **2013**, *3*, 2761.

(693) Frankcombe, T. J. *Phys. Chem. Chem. Phys.* **2015**, *17*, 3295–3302.

(694) Kavanagh, M. A.; Karlsson, J. K.; Colburn, J. D.; Barter, L. M.; Gould, I. R. *Proc. Natl. Acad. Sci. U. S. A.* **2020**, *117*, 19705–19712.

(695) Sen, S.; Mascoli, V.; Liguori, N.; Croce, R.; Visscher, L. *J. Phys. Chem. A* **2021**, *125*, 4313–4322.

(696) Tamura, H.; Saito, K.; Ishikita, H. *Chem. Sci.* **2021**, *12*, 8131–8140.

(697) López-Tarifa, P.; Liguori, N.; Van Den Heuvel, N.; Croce, R.; Visscher, L. *Phys. Chem. Chem. Phys.* **2017**, *19*, 18311–18320.

(698) Anda, A.; Hansen, T.; De Vico, L. *J. Phys. Chem. A* **2019**, *123*, 5283-5292.

(699) Cai, Z. L.; Crossley, M. J.; Reimers, J. R.; Kobayashi, R.; Amos, R. D. *J. Phys. Chem. B* **2006**, *110*, 15624–15632.

(700) Sirohiwal, A.; Neese, F.; Pantazis, D. A. *J. Chem. Theory Comput.* **2021**, *17*, 1858–1873.

(701) Saito, K.; Suzuki, T.; Ishikita, H. *J. Photochem. Photobiol. A Chem.* **2018**, *358*, 422–431.

(702) Shao, Y.; Mei, Y.; Sundholm, D.; Kaila, V. R. *J. Chem. Theory Comput.* **2020**, *16*, 587–600.

(703) Schirmer, J. *Phys. Rev. A* **1982**, *26*, 2395–2416.

(704) Schirmer, J.; Cederbaum, L. S.; Walter, O. *Phys. Rev. A* **1983**, *28*, 1237–1259.

(705) Christiansen, O.; Koch, H.; Jørgensen, P. *Chem. Phys. Lett.* **1995**, *243*, 409–418.

(706) Stanton, J. F.; Bartlett, R. J. *J. Chem. Phys.* **1993**, *98*, 7029–7039.

(707) Nooijen, M.; Bartlett, R. J. *J. Chem. Phys.* **1997**, *106*, 6441–6448.

(708) Nooijen, M.; Bartlett, R. J. *J. Chem. Phys.* **1997**, *107*, 6812–6830.

(709) Loos, P. F.; Lipparini, F.; Boggio-Pasqua, M.; Scemama, A.; Jacquemin, D. *J. Chem. Theory Comput.* **2020**, *16*, 1711–1741.

(710) Monino, E.; Loos, P. F. *J. Chem. Theory Comput.* **2021**, *17*, 2852–2867.

(711) Suomivuori, C. M.; Winter, N. O.; Hättig, C.; Sundholm, D.; Kaila, V. R. *J. Chem. Theory Comput.* **2016**, *12*, 2644–2651.

(712) Winter, N. O.; Hättig, C. *J. Chem. Phys.* **2011**, *134*, 184101.

(713) Send, R.; Kaila, V. R.; Sundholm, D. *J. Chem. Phys.* **2011**, *134*, 214114.

(714) Groot, M. L.; Pawlowicz, N. P.; Van Wilderen, L. J.; Breton, J.; Van Stokkum, I. H.; Van Grondelle, R. *Proc. Natl. Acad. Sci. U. S. A.* **2005**, *102*, 13087–13092.

(715) Romero, E.; Diner, B. A.; Nixon, P. J.; Coleman, W. J.; Dekker, J. P.; Van Grondelle, R. *Biophys. J.* **2012**, *103*, 185–194.

(716) Yoneda, Y.; Arsenault, E. A.; Yang, S.-J.; Orcutt, K.; Mazakazu, I.; Fleming, G. R. *Nat. Commun.* **2022**, *13*, 2275.

(717) Sirohiwal, A.; Berraud-Pache, R.; Neese, F.; Izsák, R.; Pantazis, D. A. *J. Phys. Chem. B* **2020**, *124*, 8761–8771.

(718) Sirohiwal, A.; Neese, F.; Pantazis, D. A. *Chem. Sci.* **2021**, *12*, 4463–4476.

(719) Wesolowski, T. A.; Warshel, A. *J. Phys. Chem.* **1993**, *97*, 8050–8053.

(720) Neugebauer, J.; Louwerse, M. J.; Baerends, E. J.; Wesolowski, T. A. *J. Chem. Phys.* **2005**, *122*, 094115.

(721) Gomes, S. P. A.; Jacob, C. R. *Annu. Reports Prog. Chem. - Sect. C* **2012**, *108*, 222–277.

(722) Manby, F. R.; Stella, M.; Goodpaster, J. D.; Miller, T. F. *J. Chem. Theory Comput.* **2012**, *8*, 2564–2568.

(723) Höfener, S.; Visscher, L. *J. Chem. Phys.* **2012**, *137*, 204120.

(724) Raghavachari, K.; Saha, A. *Chem. Rev.* **2015**, *115*, 5643–5677.

(725) Tölle, J.; Deilmann, T.; Rohl, M.; Neugebauer, J. *J. Chem. Theory Comput.* **2021**, *17*, 2186–2199.

(726) Neugebauer, J. *J. Chem. Phys.* **2007**, *126*, 134116.

(727) Höfener, S.; Visscher, L. *J. Chem. Theory Comput.* **2016**, *12*, 549–557.

(728) Leng, X.; Jin, F.; Wei, M.; Ma, H.; Feng, J.; Ma, Y. *J. Chem. Phys.* **2019**, *150*, 164107.

(729) Frähmcke, J. S.; Walla, P. J. *Chem. Phys. Lett.* **2006**, *430*, 397–403.

(730) Li, J.; Olevano, V. *J. Photochem. Photobiol. B Biol.* **2022**, *232*, 112475.

(731) Baerends, E. et al. ADF2022.1, locally modified development version, 2022.

(732) Sirohiwal, A.; Pantazis, D. A. *Angew. Chemie* **2022**, *134*, e202200356.

(733) Umena, Y.; Kawakami, K.; Shen, J. R.; Kamiya, N. *Nature* **2011**, *473*, 55–60.

(734) Gruber, E.; Kjær, C.; Nielsen, S. B.; Andersen, L. H. *Chem. - A Eur. J.* **2019**, *25*, 9153–9158.

(735) Dutta, A. K.; Neese, F.; Izsák, R. *J. Chem. Phys.* **2016**, *145*, 034102.

(736) Dutta, A. K.; Nooijen, M.; Neese, F.; Izsák, R. *J. Chem. Phys.* **2017**, *146*, 074103.

(737) Dutta, A. K.; Saitow, M.; Demoulin, B.; Neese, F.; Izsák, R. *J. Chem. Phys.* **2019**, *150*, 164123.

(738) Zamzam, N.; Van Thor, J. J. *Molecules* **2019**, *24*, 1–15.

(739) Loos, P. F.; Scemama, A.; Blondel, A.; Garniron, Y.; Caffarel, M.; Jacquemin, D. *J. Chem. Theory Comput.* **2018**, *14*, 4360–4379.

(740) Milne, B. F.; Kjær, C.; Houmøller, J.; Stockett, M. H.; Toker, Y.; Rubio, A.; Nielsen, S. B. *Angew. Chemie - Int. Ed.* **2016**, *55*, 6248–6251.

(741) Milne, B. F.; Toker, Y.; Rubio, A.; Nielsen, S. B. *Angew. Chemie - Int. Ed.* **2015**, *54*, 2170–2173.

(742) Cho, Y.; Bintrim, S. J.; Berkelbach, T. C. *J. Chem. Theory Comput.* **2022**, *18*, 3438–3446.

(743) Riemelmoser, S.; Kaltak, M.; Kresse, G. *J. Chem. Phys.* **2020**, *152*, 1–13.

(744) Loos, P. F.; Pradines, B.; Scemama, A.; Giner, E.; Toulouse, J. *J. Chem. Theory Comput.* **2020**, *16*, 1018–1028.

(745) Bruneval, F.; Hamed, S. M.; Neaton, J. B. *J. Chem. Phys.* **2015**, *142*, 244101.

(746) Duchemin, I.; Jacquemin, D.; Blase, X. *J. Chem. Phys.* **2016**, *144*, 164106.

(747) Li, J.; D'Avino, G.; Duchemin, I.; Beljonne, D.; Blase, X. *Phys. Rev. B* **2018**, *97*, 035108.

(748) Duchemin, I.; Guido, C. A.; Jacquemin, D.; Blase, X. *Chem. Sci.* **2018**, *9*, 4430–4443.

(749) Tirimbò, G.; De Vries, X.; Weijtens, C. H.; Bobbert, P. A.; Neumann, T.; Coehoorn, R.; Baumeier, B. *Phys. Rev. B* **2020**, *101*, 035402.

(750) Ramberger, B.; Sukurma, Z.; Schäfer, T.; Kresse, G. *J. Chem. Phys.* **2019**, *151*, 214106.

(751) Dyall, K. G.; Faegri, K. Introduction to Relativistic Quantum Chemistry, Oxford, 2007.

(752) Tomasi, J.; Mennucci, B.; Cammi, R. *Chem. Rev.* **2005**, *105*, 2999–3093.

(753) Rudberg, E.; Rubensson, E. H.; Sałek, P.; Kruchinina, A. *SoftwareX* **2018**, *7*, 107–111.

(754) Bruneval, F. *J. Chem. Phys.* **2016**, *145*, 234110.

Summary

The problem of many interacting electrons is hard to solve. Many-body perturbation theory is a set of techniques to reduce this problem to one of a single electron moving in an effective, energy-dependent potential. This potential is also called self-energy and can be represented as an infinite sum of terms describing the interaction of the single electron with the other electrons. In practice, one calculates only a few of these terms which are believed to be dominant for certain interaction patterns.

The self-energy can be used to calculate the single-particle Green's function whose poles can be identified with electron addition and removal energies. These can be probed in direct and inverse photo-emission spectroscopy. It also gives access to the 4-point vertex function which in turn can be used to calculate the interacting density-density response function whose poles describes the energies of electron-hole pairs. These can be probed in photo-absorption spectroscopy. Finally, electron-electron interaction energies can be obtained from the self-energy as well. Comparing the electron-electron interaction energies of different isomers is for instance useful to determine which isomer is most stable.

The most important terms in the self-energy are the Hartree contribution, describing the interaction of the electron with the average charge density produced by the other electrons, as well as the exchange term, accounting for the Fermionic structure of the wave functions. These terms already account for the majority of electron-electron interactions. However, for a realistic description of many-electron systems, additional terms need to be considered. The combined effect of these terms is called correlation. In a canonical method due to Hedin, the correlation part of the self-energy is expanded in powers of the screened electron-electron interaction.

The first-order term in this expansion is called GW term and truncating the self-energy after this term is called GW approximation. The GW approximation is a standard technique which is computationally feasible for systems with many hundreds of electrons. It rests on the assumption that the dominant source of electron-electron correlation is the screening of the electron-electron interaction by the presence of other electrons. This is a good approximation for processes which are dominated by long-ranged interactions, for instance when an electron is removed from a finite system. In case short-ranged interactions become important, additional terms, so-called vertex corrections, need to be considered. The $G3W2$ term is the next-to-leading order term in the expansion of the self-energy and it massively improves the description of short-range correlation.

In this thesis, we have implemented these techniques for finite systems and assessed their

precision and accuracy. Our implementation equips researchers with tools to describe spectroscopic properties of relatively large systems with good accuracy. We have demonstrated this *via* applications to the ionization of DNA oligomers as well as the low-lying excited states of the reaction center of photosystem II.

A more detailed summary of the research we have performed including an outlook on future work can be found in the conclusions of this thesis.

Samenvatting

De interactie tussen meerdere elektronen tegelijk is kwantitatief moeilijk in kaart te brengen. De veel-deeltjes storingstheorie is een verzameling technieken om dit probleem te herleiden tot dat van een enkel elektron in een effectieve, energie-afhankelijke potentiaal. Deze potentiaal wordt ook wel de zelf-energie genoemd en kan worden voorgesteld als een oneindige som van termen die de interactie van het enkele elektron met de andere elektronen beschrijft. In de praktijk berekent men slechts een aantal van deze termen, waarbij wordt aangenomen dat zij, op basis van bepaalde interactiepatronen, de rest in grootte overheersen. De zelf-energie kan worden gebruikt om de Greense functie voor een enkel deeltje te berekenen. De polen van deze functie kunnen worden geïnterpreteerd als de elektronenaffiniteit en de ionisatiepotentiaal. Experimenteel kunnen deze worden onderzocht met directe en inverse foto- emissiespectroscopie. Het geeft ook toegang tot de 4-punts vertexfunctie die op haar beurt weer kan worden gebruikt om de geïntegreerde dichtheid-dichtheid responsfunctie te berekenen. De polen van deze functie beschrijven de energieën van elektron-gat paren. Deze energieën kunnen worden onderzocht in foto-absorptie spectroscopie. Tenslotte kunnen ook interactie-energieën tussen elektronen worden verkregen uit de zelf-energie. Het vergelijken van de elektron-elektron interactie-energieën van verschillende isomeren is bijvoorbeeld nuttig om te bepalen welk isomeer het meest stabiel is.

De belangrijkste termen in de zelf-energie corresponderen met de zogenaamde Hartree-bijdrage. Deze beschrijft de interactie van het elektron met de gemiddelde ladingsdichtheid die door de andere elektronen wordt geproduceerd. Even belangrijk is de uitwisselingsterm, die volgt uit de fermionische structuur van de golffuncties. Deze termen zijn al goed voor het merendeel van de elektron-elektroninteracties. Voor een realistische beschrijving van meer-elektron-systemen moet echter rekening worden gehouden met extra termen. Het gecombineerde effect van deze termen wordt correlatie genoemd. In een canonieke methode van Hedin wordt het correlatiedeel van de zelf-energie geëxpandeerd in machten van de afgeschermde elektron-elektroninteractie.

De eerste-orde term in deze uitbreiding wordt de GW-term genoemd en het afkappen van de zelf-energie na deze term definieert de GW-benadering. De GW-benadering is een standaardtechniek die rekentechnisch haalbaar is voor systemen met vele honderden elektronen. Deze berust op de veronderstelling dat de dominante bron van elektron-elektroncorrelatie de afscherming is van de elektron- elektron interactie door de aanwezigheid van de andere elektronen. Dit is een goede benadering voor processen die worden gedomineerd door lange-afstandsinteracties, bijvoorbeeld wanneer een elektron uit een eindig systeem wordt verwijderd. Indien korte-afstandsinteracties

belangrijk worden, moet rekening worden gehouden met extra termen, de zogenaamde vertex-correcties. De $G3W2$ term is de opeenvolgende hogere orde term in de expansie van de zelf-energie en het verbetert de beschrijving van korte-afstand correlatie enorm.

In dit proefschrift hebben we deze technieken geïmplementeerd voor eindige systemen en hun precisie en nauwkeurigheid beoordeeld. Onze implementatie geeft onderzoekers middelen om spectroscopische eigenschappen van relatief grote systemen met goede nauwkeurigheid te beschrijven. We hebben dit aangetoond door de implementatie te gebruiken voor het beschrijven van de ionisatie van DNA-oligomeren en het berekenen van de laaggelegen aangeslagen toestanden van het reactiecentrum van fotosysteem II.

Een meer gedetailleerde samenvatting van onze bevindingen, inclusief een vooruitblik op toekomstig onderzoek, is te vinden in de conclusies van dit proefschrift.

Acknowledgements

I would like to thank my supervisor Lucas Visscher for supporting and mentoring me over the last 4 years. I am especially grateful that he encouraged me to work very independently right from the start and trusting me to bring in my own ideas and interests. Also, I would like to acknowledge the support of my co-promoter Klaas Giesbertz and the members of my thesis committee for the time they invested in reading my thesis and being present during my defense in Amsterdam.

I am also very grateful for the support I received from SCM: I would like to thank Stan van Giesbergen for trusting me with implementing the algorithms I developed here into ADF and for letting me use SCMs computational resources. I would also like to acknowledge many insightful discussion with Erik van Lenthe, whose support and guidance were decisive for the success of my PhD, Hans van Schoot for his patience when I started using the SCM cluster, and Mirko Franchini for his detailed explanations of many algorithms in ADF and his technical support especially during the first year of my PhD.

I would also like to acknowledge my colleagues and friends I made here at the VU: Jelena, Souloke, Ayush, Mauricio, Edoardo, Pierpaolo, Chandan, Mauricio, Dani, Lucas, Chima and potentially many more I might have forgotten. I especially would like to thank Chima and Roeland for helping my with writing the Dutch summary of this thesis. I also would like to thank Mauricio for many insightful discussions and helpful comments throughout my PhD; Souloke for his patience in explaining me the photophysics of Chlorophylls; and Jelena for the great time I had working on our joint paper.

Finally, I am immensely grateful to my master thesis supervisor Eberhard Engel who patiently taught me electronic structure theory, solid state physics, and scientific software development. Without my thesis work with him I would have never pursued this PhD project in the first place.

List of Publications

This dissertation is based on the following journal articles.

1. *A Quadratic Pair Atomic Resolution of the Identity Based SOS-AO-MP2 Algorithm Using Slater Type Orbitals*
   Arno Förster, Mirko Franchini, Erik van Lenthe, Lucas Visscher
   Journal of Chemical Theory and Computation, **2020**, 16 (2), 875-891

2. *Low-Order Scaling G_0W_0 by Pair Atomic Density Fitting*
   Arno Förster, Lucas Visscher
   Journal of Chemical Theory and Computation, **2020**, 16 (12), 7381–7399

3. *GW100: A Slater-Type Orbital Perspective*
   Arno Förster, Lucas Visscher
   Journal of Chemical Theory and Computation, **2021**, 17 (8), 5080-5097

4. *Low-Order Scaling Quasiparticle Self-Consistent GW for Molecules*
   Arno Förster, Lucas Visscher
   Frontiers in Chemistry, **2021**, 9:736591

5. *Exploring the statically screened G3W2 correction to the GW self-energy: Charged excitations and total energies of finite systems*
   Arno Förster, Lucas Visscher
   Physical Review B, **2022**, 105 (12), 125121

6. *Assessment of the Second-Order Statically Screened Exchange Correction to the Random Phase Approximation for Correlation Energies*
   Arno Förster
   Journal of Chemical Theory and Computation, **2022**, https://doi.org/10.1021/acs.jctc.2c00366

7. *Quasiparticle Self-Consistent GW-Bethe-Salpeter equation calculations for large chromophoric systems*
   Arno Förster, Lucas Visscher
   Journal of Chemical Theory and Computation, **2022**, https://doi.org/10.1021/acs.jctc.2c00531

Articles which are not part of this thesis.

8. *Double hybrid DFT calculations with Slater type orbitals*
   Arno Förster, Lucas Visscher
   Journal of Computational Chemistry, **2020**, 41 (18), 1660-1684

9. *Automated assessment of redox potentials for dyes in dye-sensitized photoelectrochemical cells*
   Jelena Belić, Arno Förster, Jan-Paul Menzel, Francesco Buda, Lucas Visscher
   Physical Chemistry Chemical Physics, **2022**, 24 (1), 197-210